Department of Exploration Geophysics

Sealing Potential of Shale Sequences through Seismic Anisotropy Analysis

Mohammad Hadi Nourollah

This thesis is presented for the Degree of
Doctor of Philosophy
of
Curtin University

June 2017

Declaration

To the best of my knowledge and belief this thesis contains no material previously published by any other person except where due acknowledgment has been made.

This thesis contains no material which has been accepted for the award of any other degree or diploma in any university.

Signature: …….

Date: ……26/06/2017……...

Dedication

To my parents

Abstract

The concept of the petroleum system embraces all the elements necessary for the accumulation of hydrocarbons to occur. If all the elements of the "petroleum system" of a basin are present, then there is a good chance of presence of hydrocarbon accumulations in that basin. Since evaluation of reservoir properties has a direct bearing on estimation of hydrocarbon volumes and deliverability, the focus on the reservoir has been far more significant. Seismic data have been primarily used to describe the geometry and stratigraphy of shales rather than their internal properties. However for a hydrocarbon accumulation to exist, the sealing capacity of shale is of critical importance.

This research investigates whether seismic anisotropy can be related to the sealing capacity of shales. Conventional approaches using Gassmann equations to model the shale (effective) porosity is not applicable due to the assumed effective connectivity of pore spaces which is not true in shales. Therefore an alternative approach is taken in this thesis. The rock physics model of the impact of incorporating capillary pipes to perfect shales is introduced. The potential impact of such variations on seismic data is then modelled. The model predicts that certain anisotropy parameters should show meaningful changes according to the changes in the sealing potential. Two case studies are then introduced as field tests of the proposed model. The study areas ate the Exmouth Sub-basin within the Carnarvon Basin of offshore Western Australia and the offshore Gippsland Basin in South Eastern Australia.

Clay-rich shales that have undergone at least typical compaction through burial are likely to be anisotropic, and often exhibit VTI (vertical transverse isotropy) medium symmetry. Well compacted, competent shale units typically show higher degree of anisotropy. Such shales show higher anisotropy due to a combination of well-developed platelets and grain elongation which both increase the rock stiffness in the bedding direction. This is reflected into the value of the fractional shale anisotropy Ɛ

(epsilon), where higher values of ε indicate better foliated shale. Both case studies show that to the first degree of approximation ε could be considered a seismic attribute related to the sealing capacity of shale formations.

In both cases seismic attributes were also calculated on the pre- and post-stack seismic data to investigate if a relationship between various attributes and the sealing potential of the sealing shales could be established. Different sets of attributes are analyzed carefully to reveal the most responsive attributes to the property under observation. In Gippsland Basin, the Trace Gradient shows a declining trend with increasing capillary pressure (P_c). However, in the Exmouth Sub-basin, lower relative values of Q factor with increasing sealing potential of the Muiron shale are observed. This might be related to different clay composition at the two sites. Still, seismic attributes may be valuable tools in identifying anomalies, seismic facies and character changes in seismic. The study aimed to identify the target attributes (classes) which could help in the evaluation of the sealing capacity. The proposed methodology is applied to a known gas chimney location offshore Gippsland Basin. Results obtained are in relatively good agreement with the previous studies and borehole data.

Modelled sealing capacities can be classified to different sealing categories to help better understand the capacity of the top seal and its lateral variability. This may help in a better risk estimate for hydrocarbon exploration and CO_2 sequestration projects.

Acknowledgements

I have to admit that a page for acknowledgements seemed too much at the start of my PhD! Now that I am getting close to the finish line, even three pages will not cover it.

First, I'd like to thank my supervisor, Dr. Milovan Urosevic, who helped me get started with the PhD and guided me through it. I understand how difficult it can be to give guidance and corrections to a student off-campus, yet being subtle enough. For all your efforts, I'd like to thank you.

Second, I like to thank my former colleague at 3D-Geo, Dr. Jeff Keetley who helped me with the logistics of my visits to Perth, the software and hardware required to complete this thesis. Jeff helped me with my career at 3D-Geo and was a good friend to me. I will never forget his kindness.

I like to take this opportunity to thank my good friend, Mike Hartley. Mike's assistance to get me out of some seismic processing loopholes was extremely important. He offered all such professional help without hesitation and for that I am indebted to him.

As a person who does not speak English as my mother tongue, I have always referred to my good friend and colleague James Preston to correct the papers and articles before getting published. I hope I will be able to repay his favors one day.

Last, but not least, I'd like to thank my supportive wife, Nga who stood next to me and coped with all the mood changes during this long journey. My two kids and their mother always gave me space to spend time over reading, writing and researching. Thank you.

Also, thanks to my parents, siblings and friends whose words of wisdom and encouragement were heart-warming during the course of my PhD. I acknowledge all of you and will remember your kindness.

Table of Contents

1 Chapter 1: Overview

1.1 Introduction

Exploration for hydrocarbon resources has gone through a long and interesting history. Geologists once had to rely on surface exposures and outcrops to map subsurface structures. Drilling wells was comparatively as expensive as today, based on far fewer data, and therefore riskier. Wildcat drilling was very common as it was the only means to tie/calibrate the proposed geological model. After gaining more experience and learning from failures (dry wells), more efficient exploration technologies and scientific approaches were introduced. Geologists developed the first cornerstones of what was later referred to as “The Petroleum System”.

The concept of the petroleum system (Perrodon and Masse, 1984) embraces all the elements necessary for the economic accumulation of hydrocarbons to occur. Through the geological history of a basin, source rocks that are capable of generating and expelling hydrocarbons (when under heat and pressure) will usually have been deposited. The porous and permeable reservoir rocks that will host the hydrocarbons, and the cap-rocks (Alsharhan and Nairn, 2003; Kaldi and Atkinson, 1997) that will impede their escape, are two further elements of the system. Usually the reservoir and its associated cap-rock (seal) are in a structural trap. The timing of the formation of the trap compared to the onset of expulsion of hydrocarbon out of the source rock is as important as the presence of any of the lithologies. If all the elements of the “petroleum system” of a basin are present, then there is a good chance of presence of hydrocarbon accumulations in that basin.

1.2 The Seal

The entry capillary pressure of the rock unit is the factor that determines how good a reservoir or seal the rock is (Vavra et al., 1992). Capillary pressure is a well-studied, physical phenomenon that

becomes relevant in a multi-phase fluid system of a tortuous, subsurface pore-space. Seal capacity of the sediments has been measured by a technique called MICP (Mercury Injection Capillary Pressure). This technique was developed by Purcell (1949), Picknell et al. (1966) and Wardlaw and Taylor (1976). The MICP measurement has remained the core calibration method of seal-capacity evaluation until this day.

Shales comprise a major part (more than 50%) of the sedimentary rocks (Boggs, 1992; Johnston and Christensen, 1995). Due to their low permeability, shales are known to be the common seal for the identified reservoirs (Aplin and Macquaker, 2011; Krushin, 1997). Despite their widespread existence, measurements of the geomechanical, hydraulic and elastic properties of shale faces certain challenges (Sarout and Guéguen, 2008a). The extremely low permeability in the highly porous shale is indicative of low connected porous space. Connectivity of the porous space, independence of the shear module of the rock and homogeneity of the rock are the assumptions of the Gassmann fluid substitution (Gassmann, 1951) that are all violated in shales (Josh et al., 2012). Presence of shales in the sand reservoir has been modelled to a certain degree of accuracy and was shown to impact the elastic and geomechanical properties of the shaly sand (Blangy et al., 1993; Dvorkin et al., 2007). However, the determination of the properties of wet shales and their elastic response under pressure is still under research (Aminul Islam and Skalle, 2013; Sayers and Boer, 2014).

Seal-evaluation has been the topic of many research papers that established the principles of hydrocarbon column-height and detection of seal-capacity (Fox, 1959; Sales, 1993; Schowalter, 1979). Most of these investigations were dependent on down-hole samples, and the results of the MICP tests that were performed on them. The greatest success of the use of seismic data has been in the evaluation of the geometry and integrity of the sealing units (Kaldi and Atkinson, 1997). Seismic data provides the opportunity to map detailed subsurface strata and relate their lithology to wells (Avseth et

al., 2008). Accurate subsurface maps of the sealing units were generated that helped identify pinch-outs, faults and unconformities (Bailey et al., 2006; Hoffman et al., 2012). Although the research showed promising advances in the evaluation of fault-seal and top-seal geometry and integrity, the use of seismic was limited to identifying bounding limits of sealing units. Researchers, however, identified seismic patterns and characters that are associated with top-seal failures (Kostenko et al., 2008; Sales, 1997). Identification of gas chimneys led to mapping of potential seal failure areas and reduction of exploration risks (Cartwright et al., 2007; Nourollah et al., 2010; Zhdanov et al., 2014).

1.3 Motivation

The wide range of the pore structure, size and origin in the mudrocks is a complex result of both depositional and diagenetic processes (Loucks et al., 2012). Shales are often found to be anisotropic (Winterstein and Paulsson, 1990). Their anisotropic seismic character and the impact on the time-depth relations were recognized by researchers (Levin, 1980). Shale sequences are also known for their significant reduction of seismic quality in comparison to other types of rocks (Barnes, 2016; Brown, 1996). Due to the complexities and variations of shale sequences, direct association of seismic attributes with the sealing capacity has not been attempted before.

Despite the difficulties in the measurements, the elastic properties of clay minerals were studied by several researchers (Katahara, 1996; Tosaya, 1982). However, the elastic response of shales is not just the result of the individual constituents of the shale, but the overall packing of the grains (Sayers, 2005; Ulm and Aboulseiman, 2006). On the other hand, the approach to model the inclusions in a solid should take the proper route of assigning zero elastic moduli and then reducing the size (Kachanov, 1992). The opposite direction of studying the elastic response of infinitesimal bodies faces some difficulties. Microstructural cracks and pores are limiting cases of inclusions and have been studied for the impact on the elastic response of the composites (Berryman, 1979; David and Zimmerman, 2011;

Hill, 1965). This may provide the bridge between what the seismic senses in shales and how shales are structured.

To analyse and characterize shales from seismic data, the family of the conventional seismic trace and sequence attributes needs to be further enriched. One idea is to introduce seismic anisotropy of shales as an additional parameter that hopefully could shed some new lights into seismic analysis of shale sealing properties. From their work of researchers (Amiri Besheli and Urosevic, 2006; Sarout and Guéguen, 2008b; Sayers, 1994a) it is clear that shales are too complex to be studied from the reflection data alone. Additional information is needed from core tests, logs and borehole seismic measurements. Moreover, the results of such measurements need to be analysed in the geological context of the basin investigated. Hence an empirical approach rather than explicit formulation is likely to be more effective.

1.4 Objectives

Seismic anisotropy has been used to produce more accurate images of subsurface, and to characterize the fractured reservoirs. Alkhalifah and Rampton (2001) published an example of using seismic anisotropy to identify shales. Shales are shown to have such an impact on their underlying reservoir units that they have masked the AVO signature of hydrocarbon-bearing sands (Amiri Besheli, 2006). Tutuncu (2010) discussed the anisotropic characters of shales in terms of reservoirs and seals. The anisotropic impact of presence of organic matter in shales was researched by Vernik and Nur (1992). The primary focus of this research is on the sealing aspect of the shales. I intend to investigate whether the seismic data is able to identify variations of sealing capacity and which parameter is likely to help us relate the elastic properties of shales to their sealing potential.

Such proposition was investigated with field data. The two locations studied are the Exmouth Sub-basin and the Gippsland Basin. They are both prolific (sub-) basins and have numerous wells drilled

within them. The proposed method is then applied and verified over a site of seal bypass system: a gas chimney.

1.5 Methodology

There are interesting cases in exploration and development of hydrocarbon reservoirs or carbon capture and storage (CCS) in which a relatively thin layer of shale is sealing a sizeable reservoir, while in other instances the same thicker unit is not as an effective seal (Bunch et al., 2009; Daniel, 2005). This is a well-known case in some areas such as the Gippsland basin that are of interest in CO2 sequestration. Investigating such cases through analysis of seismic data is of principal interest to this study.

To fully model the sealing capacity of a shale sequence in an area of a basin, numerous wells and samples would have been necessary. Hence this study aims to help this process by providing additional information of seismic data that could potentially help in understanding better the sealing capacity of shale in the basin under investigation. For that purpose I will aim to calibrate and cross-analyse laboratory measurements with various seismic attributes including the degree of seismic anisotropy. For assessment of seismic anisotropy I will be using logs, VSP and reflection seismic data. Hence the analysis is centered on the wells, while the findings are extrapolated away from the wells using surface reflection data to estimate the potential of prediction away from the wells. It is hoped that this method could reduce the number of core sample tests required for the shale property assessment. This research will attempt a detailed 3D modelling of sealing capacity of the shales across the areas of interest, to better understand the hydrocarbon potential (or CCS capacity) in the area of investigation. Understanding petroleum system in the area and interpreting measured data within this concept is one of the corner stones of this research.

1.6 Thesis lay-out

This thesis is divided to 8 chapters in order to take the readers through the course of the research and depict its progress and results.

Chapter *One* (current chapter) serves as a preface to the thesis and introduces the problem at hand, its significance and a brief history of the attempts that were made to solve the problem. It also mentions the objectives of the current research and the broad methodology that is proposed.

Chapter *Two* will be a summary of the background research that was completed to establish the foundations of this study. It will cover the basic concepts of the petroleum systems with special focus on the seal and how its capacity is measured. Seismic anisotropy and its classes, as well some of its attributes derived through inversion and AVO (Amplitude versus Offset), are introduced.

Chapter *Three* discusses the rock physics and the forward modelling procedure to understand shales and the effects of presence of capillaries in them. Effects of the disorder in the clay minerals and their impact on the seismic properties of shales are shown to be related to their sealing capacity. Seal capacity is then shown to relate to a potentially detectable seismic response.

Chapter *Four* introduces the case studies which were completed over the Exmouth Sub-basin, offshore Carnarvon basin and Gippsland Basin. This chapter will review the tectonics and stratigraphy of the areas of interest and discuss the properties of the shale sequences that will be studied.

Chapter *Five* presents the application of seismic anisotropy to evaluate the sealing potential. The seismic anisotropy is introduced as a potential co-variant that can provide a reasonable estimate to the sealing capacity of rocks over the two case studies. This chapter demonstrates the positive results of the proposed hypothesis of the relation between the anisotropy of shales and their sealing capacity.

Chapter *Six* reviews the results of seismic inversion and attributes studies over the two case studies from the Exmouth Sub-basin and the Gippsland Basin. This chapter depicts the challenges and shortcomings of the conventional approaches towards relating the seismic and well logs to the sealing capacity of shales. Despite such difficulties, there are some very promising results introduced for each case study.

Chapter *Seven* reviews the results of the case studies both in terms of seismic anisotropy and the seismic attributes. Analysis of the results show why the two case studies differ in their sealing potential and how such difference can provide a bound for future studies.

Chapter *Eight* introduces a case study for the application of the proposed method. A gas chimney site that has seen exploration interests in the petroleum industry is studied for the sealing capacity. Findings of the previous case studies and the theoretical modelling were directly applied.

Chapter *Nine* is the final part of this thesis where the conclusions and results are summarized. The results of the case studies over Exmouth Sub-basin and Gippsland Basin are discussed. Recommendations are also made for potential future studies.

2 Chapter 2: Background

Determination of a petroleum system within an area of study depends on our knowledge of source, reservoir and seal. Failure of any of the key elements of the petroleum system causes a failure in a discovery or further development. In order to have a productive field, all five elements of a petroleum system must exist. Presence of source, reservoir, seals and trap along with appropriate timing is key to the creation of a commercial field.

2.1 Petroleum System

Despite the abundance of oil and gas in some basins, the story behind the formation of hydrocarbons is complicated. Any sedimentary basin that hosts hydrocarbons will require several lithological, tectonic and temporal elements to work together in an organized manner so that a producible hydrocarbon play forms (Perrodon and Masse, 1984).

2.1.1 Source

Source rocks are sedimentary rocks that contain a considerable amount of organic material. Source rocks may form in various depositional environments such as marine deep water, delta-plains or lakes. Their environment of deposition, and the total organic matter within them, greatly contributes to the amount and type of hydrocarbon they are capable of generating.

Shale units are the most common sources for hydrocarbon generation. When buried deep enough and subjected to heat and pressure, they can produce oil and gas. Based on the type of hydrocarbon they are most likely to produce, source rocks are classified as oil-prone and gas-prone.

If an oil-prone source is buried to depths greater than what is favorable to the production of oil (this is called the *oil-generative window*), it can ultimately expel gas, since the components of

unexpelled oil will crack to form gas. If the burial continues further, the gas molecules will continue to break down, and the extreme end result will be methane and CO_2.

Another mechanism for production of gas is through fermentation. When favorable conditions exist for bacterial activity (such as low reservoir temperatures resulting from shallow depth of burial), bacteria can degrade the reservoir hydrocarbons (consume the light components of oil) and form biogenic gas. This type of gas is generally referred to as *Secondary Biogenic Gas*.

2.1.2 Reservoir

Reservoir rocks are generally sedimentary rocks that can host hydrocarbon. Such rocks have favorable porosity and permeability to allow hydrocarbons to occupy their porous space. There are different classifications of the reservoir rocks depending on which aspect is being studies. Reservoirs can be clastic (such as sandstone) or carbonate (such as dolomite and chalk) reservoirs based on the environment of deposition.

2.2 Seal

Sedimentary rocks that have a sealing potential can cap a reservoir (impede the upward movement of hydrocarbon) have long been of interest to the industry. Shaley formations are by far the best-known seals for hydrocarbon reservoirs.

Determination of sealing potential is not necessarily a straight-forward procedure. The first practical hurdle is to obtain samples of the shale unit. It is a tendency of the industry not to core shale units. This seems intuitive as we would like to determine the properties of the reservoir, which most of the time is not a shale unit. Another reason is that coring of shales can be difficult, and they tend not to be acquired with high recovery. Furthermore, there is always the argument of having disturbed the original condition of the sample through coring. The consequence of this is that data are more often collected through petrophysical well-log analysis.

Seal potential is generally investigated by three factors: *Geometry*, *Integrity* and *Capacity*. Although referring to separate elements of sealing, these categories are not necessarily independent of each other.

- **Geometry**: This is the study of the thickness and lateral extent of the unit. This is generally determined through mapping of the reservoir and seal unit on seismic data.
- **Integrity**: The lithological type and distribution, the presence of faults and fractures, define the integrity of the sealing unit. Preferred lithologies are shale or other fine-grained units. Identification of hydrocarbon build-ups and breaching faults and their associated fractures is part of this criterion.
- **Capacity**: This is the measurement of pore sizes of the target unit and the entrance capillary pressure. This criterion determines hydrocarbon column-height a unit can hold (as a membrane seal) before it starts leaking (due to the extra pressure above the entry threshold pressure). The Capillary pressure measurements are performed on cuttings or core samples in laboratory.

2.2.1 Capillary pressure

Capillary pressure is the difference in pressure across the interface between two immiscible fluids and is defined as (Bear, 1972):

$$P_c = P_{non-wetting} - P_{wetting} \quad (1)$$

Wetting and non-wetting phases originate from our everyday understanding of how something gets *wet*. When we soak our clothes with water, they get *wet*. The physical reason behind this is the **interfacial tension**. Molecules of water have higher interfacial tension with cloth fabrics than with the air. Therefore they *wet* the fabrics of your clothes. The opposite happens when mercury is spilled on the floor. It forms little drops and it doesn't wet the floor. The reason is that

the interfacial tension between the mercury molecules is less than air's molecules (oxygen, nitrogen, etc.).

If we look at the interaction of wetting and non-wetting phases with the target material under the microscope, we can envisage the wetting phase tends to cover the surface of the substance. This is opposed to the non-wetting phase that shows a larger contact angle (θ) in comparison with the wetting phase (Figure 1).

From the definition above, we can see that wettability is a relative measure. A non-wetting phase to a substance can be a wetting one in the presence of more non-wetting phases. This all depends on the interfacial tension between the phases and the substance, and the contact angle they form.

Surface tension of fluids is a result of cohesion that exists between the molecules of the fluid. While the molecules inside the fluid volume are subjected to cohesive forces from all directions, the molecules at the surface of the fluid have one free side (in vacuum) or adhesive forces acting (the attraction between molecules of two different substances). Surface tension results when cohesion is greater than adhesion.

The Young-Laplace equation describes the capillary pressure difference across the interface between two static fluids. This equation states that the capillary pressure is related to the surface tension and the shape of the surface.

$$\Delta P_c = -\gamma \nabla . \hat{n} = \gamma \left(\frac{1}{R_1} + \frac{1}{R_2} \right) \quad (2)$$

Where γ is the surface tension, $\hat{n}$ is the unit normal pointing out of the surface and R_1 and R_2 are the principal radii of curvature.

We can approximate the (connected) porosity of rocks to a bunch of narrow tubes with circular cross-sections. The meniscus that is formed between two fluids is approximated to a sphere, and the pressure across the fluid surfaces is:

$$\Delta P = \frac{2\gamma}{R} \tag{3}$$

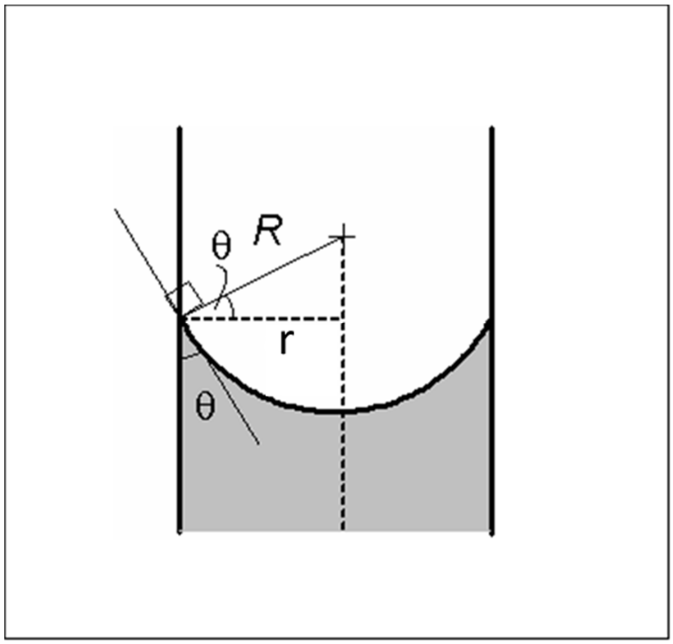

Figure 1. Wetting and non-wetting phase share the capillary space according to their surficial tension.

The radius of the sphere is related to the contact angle, θ through

$$R = \frac{r}{cos\theta} \tag{4}$$

Therefore ΔP can be written as

$$\Delta P = \frac{2\gamma cos\theta}{r} \tag{5}$$

The interfacial tension causes the capillary pressure that in turn drives the fluid up the capillary tube. The fluid rises in the tube until the weight of the fluid equates to the capillary pressure (ΔP) where hydrostatic equilibrium occurs. Therefore:

$$\Delta P = \rho g h \tag{6}$$

Or

$$\frac{2\gamma cos\theta}{r} = \rho g h \tag{7}$$

From this equation, we can calculate the height of fluid column (h) that rises in a capillary tube.

2.2.2 Capillary pressure in petroleum reservoirs

Let's imagine a conventional hydrocarbon reservoir where the reservoir zone is filled with gas, oil and water. Due to their buoyancy difference, gas stands on top, oil occupies the middle part of the reservoir and water will lie underneath. (Figure 2)

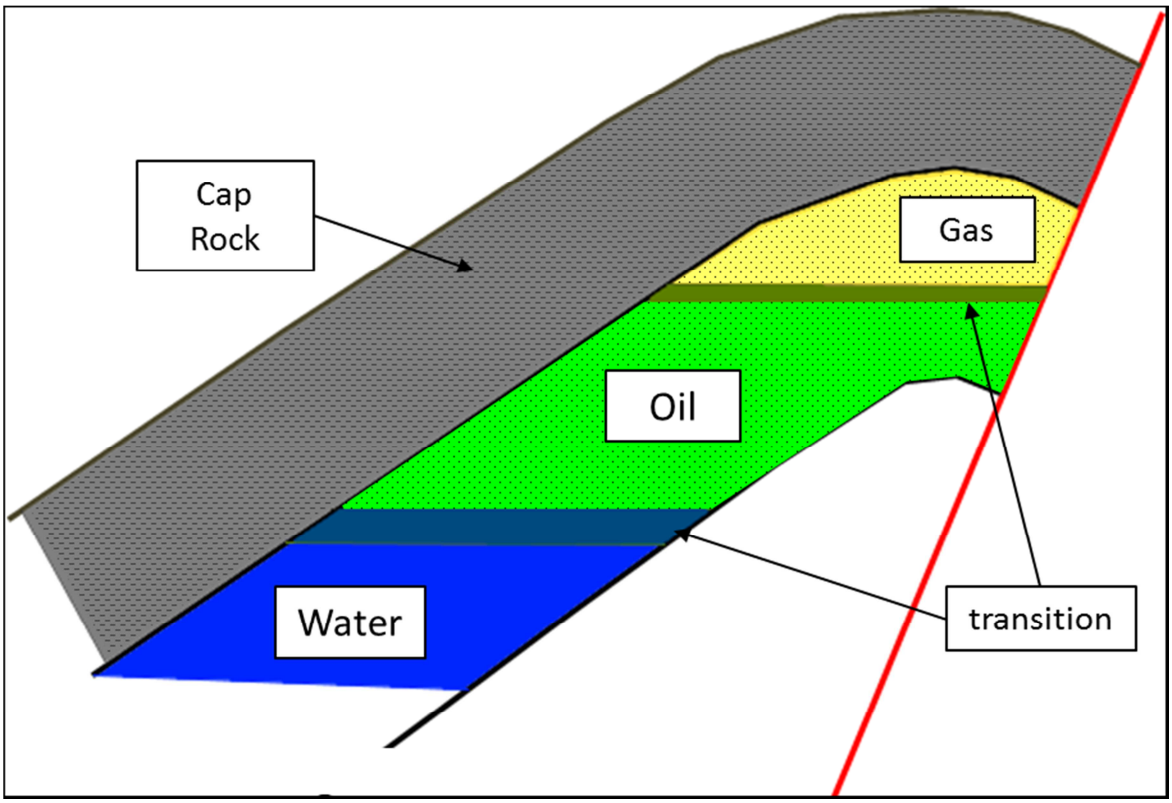

Figure 2. A schematic of a common reservoir setting where a mixture of dip and fault closures form the structure. The cap rock acts as the top seal while the fault stands as the lateral seal. Gas-oil and oil-water contacts are not sharp boundaries and form transition zones.

In reality, the contacts between fluid phases in the reservoir are not as simple as a straight line. The porous space of the rocks is where fluids have room to move to. Such space is similar to narrow straws that create a capillary effect. This means that the separation between oil and water, or oil and gas, is no longer a sharp line but a zone.

Capillary pressure is inversely related to the radius of the tube. A rock unit with low porosity and permeability has marginally connected conduits. Such host rock will cause a transition zone of tens of meters, depending on the densities of fluids. On the other hand, if rock pore spaces are large and well connected, the capillary effect is minimal.

Low capillary effect is the signature of good reservoir rocks where highly porous rocks with considerable permeability have minimal transition zone.

Sealing units such as shale and anhydrite essentially show noticeable capillary effects. This means a considerable buoyancy pressure is required to enable the non-wetting phase (hydrocarbon) to displace the wetting phase (water).

Capillary pressure of rock samples is measured in the lab using Mercury Injection Capillary Pressure Measurement (MICP). In this technique, the rock sample is dried to make sure that its pore space is filled with air. Here, the air represents the wetting phase since it covers the surface of the rock in the pore space. A typical non-wetting phase is mercury, since it has a high cohesion among its molecules and in presence of water or air will be a definite non-wetting phase.

The mercury is then injected incrementally to the rock. The injection will be done under pressure since the non-wetting phase is replacing the wetting phase. The percentage of the pore space filled with mercury is constantly monitored and is recorded with the corresponding pressure reading. The result is usually the plot of saturation (of mercury) versus the pressure. (Figure 3)

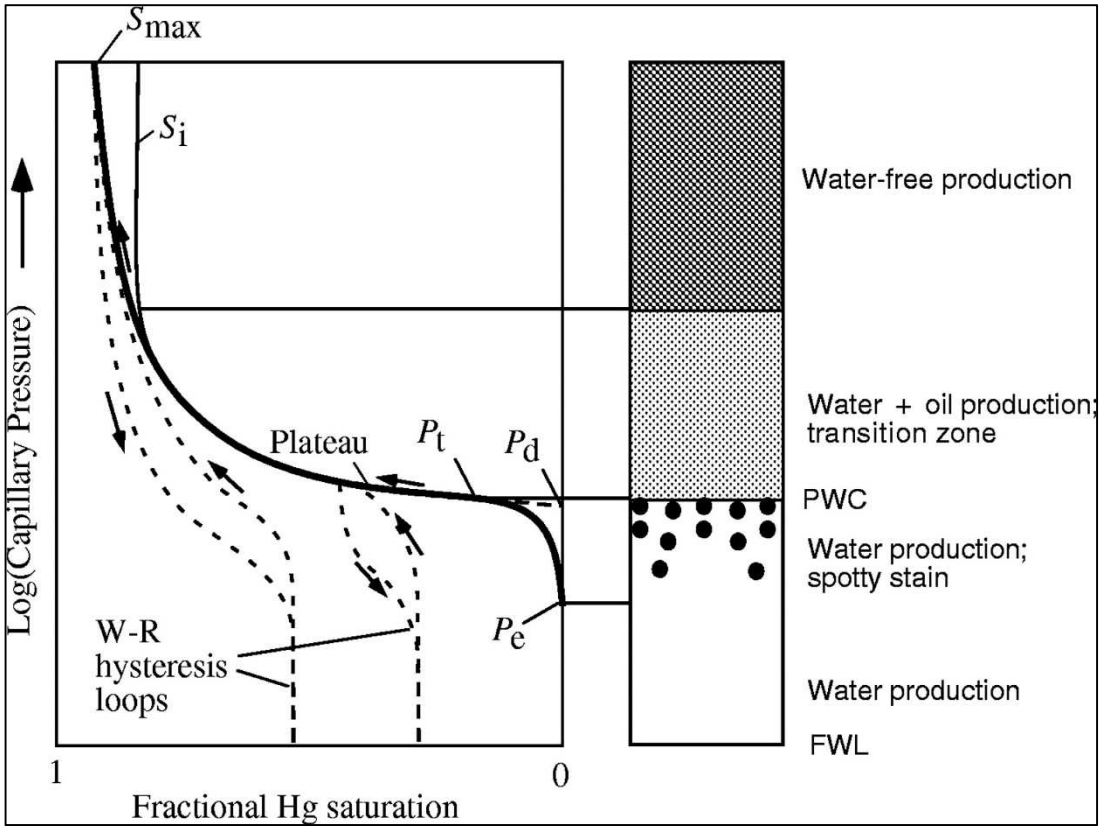

Figure 3. Diagram of Pressure versus Saturation of non-wetting phase on a Mercury Injection plot. The panel on the right shows how each part of the plot relates to the actual hydrocarbon in the reservoir (Brown, 2003).

The shape of the mercury injection plot reveals a lot of information about the rock type, its permeability, pore space and its sealing/reservoir potential.

The plot usually shows an initial pressure value at which the mercury starts to move in and displaces air. This pressure is called "entry" or P_e. By increasing the pressure level, more mercury enters the pore chambers and then the curve shows a more or less stable phase (Plateau). A reading of the lower parts of the plateau, which usually happens at around 7.5% saturation, is called the "displacement" pressure, or P_d. P_d and P_e are indicative of whether a rock can be considered a seal or a

reservoir. These two values are fairly low for reservoir rocks while they are substantially larger for seals (Dewhurst et al., 2002b; Kaldi and Atkinson, 1997; Sneider et al., 1997).

The shape of the plateau indicates the structure of pore spaces. If a rock has large pore throats and well-connected pores, mercury will easily saturate most of the space through a relatively low increase of pressure. On the other hand, if the rock is not well sorted, it will require a large increase in pressure for mercury to displace most of the air (Figure 3). Such rock might be categorized as reservoir due to a low P_d, but it will have high transition zone and will produce hydrocarbon with difficulty. Numerous experimental laboratory and field studies have been reported for such behavior (Jennings, 1987; Moriya, 2011; Vavra et al., 1992).

Based on the above, we can expect a seal to have large values for P_d and a steeply-shaped curve where the plateau occurs. More details on the method including sampling and corrections is provided in the Appendix 1.

2.3 Anisotropy

A medium is anisotropic when measurements of this property depend on the direction in which such measurements are done (Winterstein, 1990). Anisotropy should be distinguished from *heterogeneity* and *homogeneity*. We live in a heterogeneous world. It is a matter of convenience or the exactness of our measurement that we consider something otherwise, i.e. homogeneous. Geological models are typical examples. On field scale what appears to be clinoforms can be investigated at a close look to form sub-parallel layers of sediments within which they will have smaller scale sedimentary features such as hummocky cross-beds or ripples. Within those ripples, we can see layers of sediment particles and palaeo-biological activities such as burrows.

It is because of our limited ability to measure such heterogeneity, or its importance in the objectives of the project, that we must assume, at least for practical purposes, a homogeneous system.

Suppose we see the prograding system of a delta that is depicted on seismic data by sets of clinoforms. If we are interpreting the seismic to identify sequences, we will most probably stop at calling the clinoforms a delta, and distinguishing the delta-fronts and pro-delta and mouth bar areas where we can have “sands” and “shales”. However, if the project at hand is to measure how the fluids are moving through the rock frame, and we need to use a finer scale. Such a scale is below seismic resolution. However, seismic reflection can detect any rock parameter or property which exhibits uniformity (alignment) over a large scale. This is where “equivalent media” is important to understand since the seismic responses to even micro scale changes (Gurevich, 2003).

Seismic anisotropy can be measured at different scales. For example a layered system (“layer cake”) such that individual units (constituents) are much thinner that seismic wavelet (less than 1/8th of dominant seismic wavelet, (Backus, 1962; Postma, 1955)) will appear anisotropic to seismic wave propagation. The fastest velocities will be recorded along the symmetry plane (bedding plane), slowest along the axis of symmetry (Normal to bedding plane). Such anisotropy is referred to as TIV (transverse isotropy with vertical axis of symmetry) or equivalently VTI. Shales fall into this type of symmetry and will be further discussed in this chapter.

Another system that we can consider is anisotropic at all scales, despite the host rock itself is homogeneous and isotropic. Consider a sandstone unit that is fractured and that fractures are aligned in certain direction that is azimuth. This may happen with asymmetric horizontal stresses. The bigger the difference between the two principal horizontal stresses the higher is potential for significant fracturing. This fracturing can be at pore scale level or at the level of joints (Crampin, 1994). In any case the fracturing is likely to occur orthogonal to the minimum stress direction. The effect on the seismic waves will be measurable if the fractures open (not cemented). Such case is likely to exist as long as the weight of sediments is keeping them open ($\sigma_v > \sigma_H$). Again, the fast direction is dependent on what we call the

plane of symmetry, and, in the case of the described sandstone, is parallel to major orientation of the fractures. We can see that seismic velocity is faster parallel to the orientation of fractures and slower across them. In this case we have anisotropy that is referred to as TIH (transverse isotropy with horizontal axis of symmetry) or equivalently HTI. This has been studied by many researchers (Crampin, 1994; Helbig, 1984; Laubach et al., 2004).

Real rocks typically possess lower order of symmetries than the simple TIH or TIV. For example a thinly layered system pervaded by a set of vertical fractures will exhibit orthorhombic symmetry, requiring 4 elastic parameters more than VTI or HTI media that require only 5. In general it should be emphasized that alignments of properties of a medium at any scale will cause seismic anisotropy. Multiple alignments in different directions will lower the symmetry. Opposite to that is the case of a rock pervaded by randomly oriented fractures. Because there is no alignment of the properties in any particular directions such rock would be isotropic to seismic wave propagation. Therefore anisotropy is caused by some form of alignment of the medium properties. We can likewise say that ordered heterogeneity on a micro-to large scale results in anisotropy on macro-scale (Grechka, 2009).

2.3.1 Shale Anisotropy

Seismic anisotropy in a rock is caused by numerous geological processes which as discussed previously can be classified into three main categories: intrinsic, thin layering, and fracture-induced anisotropy (Crampin et al., 1984). Of particular interest to this study is the shale anisotropy.

Unlike other rocks shale exhibit intrinsic anisotropy which comes from preferred orientation of elongated mineral grains (Thomsen, 1986). This is often reinforced by the micro-alignment of plate-like mineral grains due to compaction, stresses or sedimentation during deposition hard bands (platelets) which are oriented also parallel to the bedding plane. This type of anisotropy is widespread since it is typically found in shales which comprise 70% of all sedimentary rocks (Slater, 1997). Thus shale

anisotropy is the result of a combined effect of platelets and elongated grains as they are both increasing stiffness of the rock parallel to bedding plane. Intrinsic anisotropy of shales can be further enhanced by the presence of thin layering (Thomsen, 2002).

As previously mentioned, one of the common lower symmetries also found in real rocks is orthorhombic. This one can be pictured as a combination of VTI and HTI, or, say, as a "fractured shale" or "fractured thin bed" model. In practice orthorhombic symmetries can be often decimated into VTI and HTI components through a two-step analysis (Grechka and Kachanov, 2006; Jenner, 2011). Orthorhombic symmetries can be effectively used to explain most of in situ measured phenomena (Sayers and Kachanov, 1995; Schoenberg and Sayers, 1995).

2.4 Stress and Strain

In order to utilise seismic anisotropy for this study we need to look into rock symmetries and accordingly wave propagation through such systems. The second law of Newton can be viewed as governing how elastic waves and material particles interact with each other. In a simplistic way, a wave-front will exert some type of force to the particles which will cause motion in them. As long as this interaction of force and motion is within the elastic tolerance of the matter, a reversible acceleration of particles will occur as expressed by the second law of Newton:

$$F = (mass).(Acceleration) \tag{8}$$

Adopting the same scheme for our purpose, we can relate the stress field caused by the seismic waves to the particle motions:

$$\nabla . T = \rho \frac{\partial^2 u}{\partial t^2} \tag{9}$$

Where T is the stress field and u is the particle displacement field (Auld, 1973).

Experimental observation has revealed that strain is linearly proportional to stress as long as the deformation is small. Beyond a certain amount of deformation, the stress and strain are no longer linearly proportional, but follow a higher-order polynomial relation. However, by removing the stress, the strain will go back to zero. This is called the *elastic deformation*. Beyond the region of elastic deformation, a permanent footprint of stress will remain that is called *plastic deformation* (Figure 4).

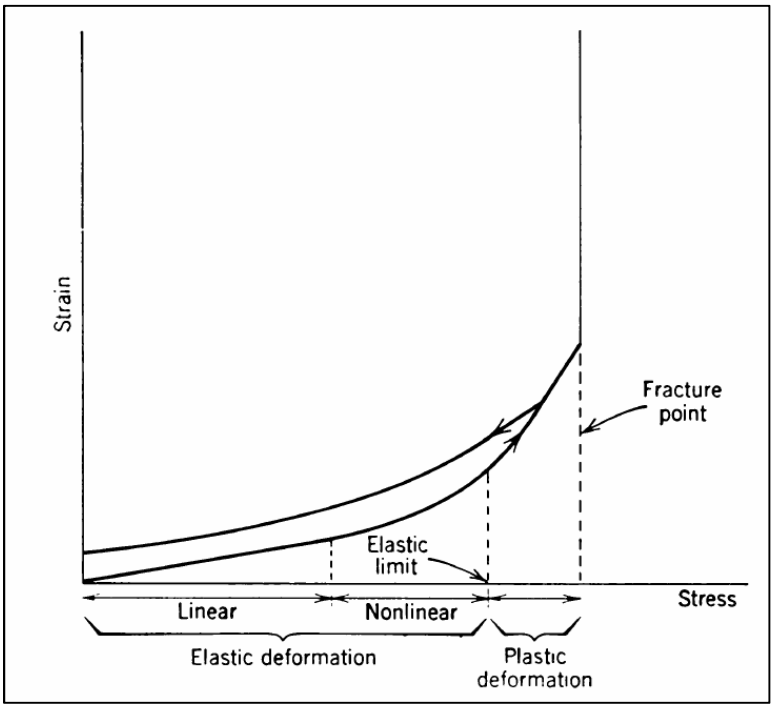

Figure 4. General plot of stress versus strain for elastic materials (or elastic behavior) (Auld, 1973). Seismic waves and the impact on the rocks is generally considered and elastic (and usually linear) deformation.

Most of the interactions of the seismic waves with materials fall within the elastic deformation part of the curve; hence seismic waves (of our topic) are also called *elastic waves*.

The observation that, for small amounts of strain, strain and stress are linearly related was first stated as a law by Hooke; hence it was named after him. Hooke's law is mathematically expressed by writing each component of stress as a general linear function of all the strain components. In general:

$$T_{ij} = c_{ijkl} S_{kl} \tag{10}$$

Where $i, j, k, l = x, y, z$

This general equation states that any stress component exerted on each surface will result in strain in all directions. The constants c_{ijkl} are "microscopic spring constants". These constants are larger for rigid materials compared to easily deformed ones. Not all 81 possible cases for *c* are unique. We know that

$$c_{ijkl} = c_{jikl} = c_{ijlk} = c_{jilk} \tag{11}$$

And

$$c_{ijkl} = c_{klij} \tag{12}$$

which will reduce the total number of independent constants to 21. This is the maximum number of constants for any medium. Usually the number of constants is further reduced by the symmetry of the material over one or more axes.

The inconvenience of using the full subscripts for the stiffness constants, plus the fact that there is no way to distinguish between terms such as $c_{xyxy}S_{xy}$ and $c_{xyyx}S_{yx}$, an abbreviation method has been introduced. In this scheme known as the Voigt notation:

I	ij
1	xy
2	yy
3	zz
4	yz,zy

5	xz,zx
6	xy,yx

Therefore, for example $c_{xxyy}=c_{12}$ and $S_{yy}=S_2$.

2.5 Symmetry Classes

There are many cases in which certain stiffness constants of materials are practically zero, or equal to each other. This is very much the same as the symmetry classes of crystals (which is in fact the origin of the entire stiffness components and symmetries), where we have symmetry axes and planes. As a result, the crystals are classified as orthormbic, hexagonal, tetrahedral, etc.

If a rock is asymmetric (has no symmetry), it possesses *triclinic* symmetry. However, for any triclinic stiffness tensor **c**, there exists such a coordinate frame where (Helbig, 1994, P. 116)

$$C_{34} = C_{35} = C_{45} = 0 \tag{13}$$

As a result the maximum possible number of stiffness constants (21) that was discussed in the previous section will reduce to 18. Measuring all 18 tensors will require a lot of measurements and is a time-consuming task, but it is possible. However, a lot of sediments show some degree of symmetry and therefore will have fewer non-zero tensors.

In general terms we can write:

$$\begin{bmatrix} T_1 \\ T_2 \\ T_3 \\ T_4 \\ T_5 \\ T_6 \end{bmatrix} = \begin{bmatrix} c_{11} & c_{12} & c_{13} & c_{14} & c_{15} & c_{16} \\ c_{12} & c_{22} & c_{23} & c_{24} & c_{25} & c_{26} \\ c_{13} & c_{23} & c_{33} & c_{34} & c_{35} & c_{36} \\ c_{14} & c_{24} & c_{34} & c_{44} & c_{45} & c_{46} \\ c_{15} & c_{25} & c_{35} & c_{45} & c_{55} & c_{56} \\ c_{16} & c_{26} & c_{36} & c_{46} & c_{56} & c_{66} \end{bmatrix} \begin{bmatrix} S_1 \\ S_2 \\ S_3 \\ S_4 \\ S_5 \\ S_6 \end{bmatrix} \tag{14}$$

2.5.1 Orthorhombic Symmetry

Orthorhombic media have three mutually orthogonal planes of mirror symmetry. If we assume the three planes of XY, XZ and ZX along these mirror planes, we can see that the stiffness tensor for the orthorhombic can be written as:

$$c = \begin{bmatrix} c_{11} & c_{12} & c_{13} & 0 & 0 & 0 \\ c_{12} & c_{22} & c_{23} & 0 & 0 & 0 \\ c_{13} & c_{23} & c_{33} & 0 & 0 & 0 \\ 0 & 0 & 0 & c_{44} & 0 & 0 \\ 0 & 0 & 0 & 0 & c_{55} & 0 \\ 0 & 0 & 0 & 0 & 0 & c_{66} \end{bmatrix} \quad (15)$$

The higher order of symmetry in this media indicates that it can be fully described with 9 independent stiffness tensors. An example of such media is a layered sandstone unit that has fractures perpendicular to its bedding.

Symmetries lower than orthorhombic are rarely considered due to great difficulties in relation to acquiring or measuring all the necessary elastic constants.

2.5.2 Transverse Isotropy

This class of symmetry is in widespread use in seismic processing and imaging. The simplicity of the stiffness tensor compared to the previous classes, i.e. the number of independent coefficients, makes this class a practical solution to model the anisotropy of rocks.

Transverse isotropy or TI is defined as a media that has an axis of symmetry with a polar symmetry. In other words, this axis of symmetry is of order of ∞. If the axis of symmetry is vertical, the media is named *Vertical Transverse Isotropic*.

Geological characteristics of sediments make this class of symmetry a convenient approach. Fine layering of units and shale sequences are typical examples were a VTI medium can be assigned to their seismic response. The VTI stiffness tensor can be written as:

$$c = \begin{bmatrix} c_{11} & c_{12} & c_{13} & 0 & 0 & 0 \\ c_{12} & c_{11} & c_{13} & 0 & 0 & 0 \\ c_{13} & c_{13} & c_{33} & 0 & 0 & 0 \\ 0 & 0 & 0 & c_{55} & 0 & 0 \\ 0 & 0 & 0 & 0 & c_{55} & 0 \\ 0 & 0 & 0 & 0 & 0 & c_{66} \end{bmatrix} \quad (16)$$

This class of anisotropy has found wide application in the petroleum industry and has been discussed by many authors (Grechka, 2009; Sayers, 1994b; Thomsen, 1986).

2.5.3 Isotropy

The highest class of symmetry which is considered the ideal case in seismic modelling is isotropic media. Although real isotropy can rarely exist, it has been widely assumed to model the behavior of rocks for decades. Only technological advances have persuaded the exploration and production companies to utilize/support the use of anisotropic media in their models.

An isotropic medium has the simplest stiffness tensor. The famous *Lamé* constants are defined as part of the isotropic tensor:

$$c = \begin{bmatrix} \lambda + 2\mu & \lambda & \lambda & 0 & 0 & 0 \\ \lambda & \lambda + 2\mu & \lambda & 0 & 0 & 0 \\ \lambda & \lambda & \lambda + 2\mu & 0 & 0 & 0 \\ 0 & 0 & 0 & \mu & 0 & 0 \\ 0 & 0 & 0 & 0 & \mu & 0 \\ 0 & 0 & 0 & 0 & 0 & \mu \end{bmatrix} \quad (17)$$

2.6 Thomsen Parameters

Exact equations for anisotropic media are complicated and non-intuitive. While some sedimentary rocks such as shale can show a significant anisotropy at macro level (Johnston and Christensen, 1995; Sondergeld and Rai, 2011), most cases can be studied under the assumption of weak anisotropy when seismic waves are the measurement criteria. This means when surface seismic is used

to measure such properties, the rock units depict much less anisotropy compared to core samples (Sayers, 1994b; Thomsen, 1986).

Thomsen (1986) recognized such weak anisotropy and ignored the higher order terms of small quantities and generated a set of phase velocity equations:

$$v_p(\theta) = \alpha_0(1 + \delta sin^2\theta cos^2\theta + \varepsilon sin^4\theta) \tag{18}$$

$$v_{sv}(\theta) = \beta_0[1 + \frac{\alpha_0^2}{\beta_0^2}(\varepsilon - \delta) sin^2\theta cos^2\theta] \tag{19}$$

$$v_{sh}(\theta) = \beta_0(1 + \gamma sin^2\theta) \tag{20}$$

Where he introduced parameter δ that is defined as

$$\delta = \frac{(c_{13} + c_{44})^2 - (c_{33} - c_{44})^2}{2c_{33}(c_{33} - c_{44})} \tag{21}$$

ε defines the relation between vertical and horizontal v_p:

$$\varepsilon = \frac{v_p(90°) - v_p(0°)}{v_p(0°)} \tag{22}$$

Although not a complete definition, parameter ε is a good reference to the anisotropy of a unit that is being studied.

Parameter δ appears to be less intuitive to understand from its definition above. However, it plays an important role in how P waves propagate (and hence shape of wave front) in the near-vertical.

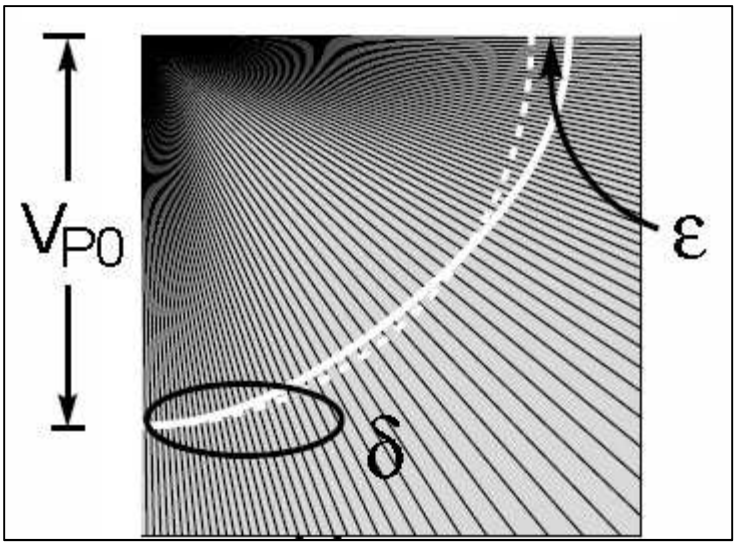

Figure 5. Anisotropic parameters δ and ε affect the shape of seismic wavefield in near and far offsets respectively.

2.7 Move-out Correction

One of the fundamental steps in seismic processing is the application of normal move-out. When the seismic source emits energy, the waves travel downward (in a half space) through the layers of the Earth. Whenever the seismic waves sense a new (acoustic) layer, part of the downward-travelling wave field reflects upward and reaches the geophones/hydrophones. The phones are spread away from the source to offsets of up to several thousands of meters.

The travel time of sound waves through earth versus the offsets of the geophones is not a straight line or a simple curve, but a complicated higher-order polynomial. Our desirable image of the subsurface is a zero offset time image. The Taylor series can be used to describe the behavior of the reflection times with respect to offset (x) (Bolshikh, 1956; Taner and Koehler, 1969):

$$t^2 = A_0 + A_2 x^2 + A_4 x^4 + \cdots \quad (23)$$

Where $A_0 = t^2|_{x=0}$,

$$A_2 = \frac{d(t^2)}{d(x^2)}|_{x=0},$$

$$A_4 = \frac{1}{2}\frac{d^2(t^2)}{d(x^2)^2}|_{x=0}$$

Traditionally, the Earth was assumed to be isotropic due to the limitations in computer hardware and software, keeping seismic processing flows practical. Furthermore, the depth of investigation in exploration and production was not very deep and long offset spreads of geophones were rare. As a result, the first two terms of the Taylor's expansion of travel time-offset series was adequate for most exploration and development purposes.

Use of the two-term normal move-out equation has an implicit assumption of isotropic strata in it. The A_2 term is the famous V_{nmo} and the variation of travel time with offset is described as a hyperbola.

This approach has been quite successful through the history of exploration with the more easily identifiable petroleum targets being discovered. Consequently, with more complex geological targets, the seismic processing methodology was advanced with greater precision within the workflow, to assist explorers. The inclusion of higher orders of NMO (Normal Move-Out) equations that allows better flattening of far offset data, where the depth to reflector is less than the recorder's offset, has been attempted. Higher orders of equation (23) will describe the characteristics of the subsurface lithology and its fluid contents. However, higher orders of the expanded NMO equation (equation (23)) generate instability and are difficult to model. The current industrial practice finds the 4^{th} order to be sufficient to describe the earth's behavior to an acceptable accuracy.

The Taylor's expansion of the NMO equation is not very user-friendly when used in higher orders. The industry standard software suits are well-equipped to measure the A_2 term in equation (23).

However, the rest of the parameters (A_n) represent composed effects of too many rock properties to be handled easily. Alkhalifah (1997) introduced the constant η to help calculate the 4th order NMO equation. Alkhalifah and Tsvankin (1995) simplified Equation 2 and reformatted the results into a more usable equation:

$$t^2 = {t_0}^2 + \frac{x^2}{V_{nmo}^2} - \frac{2\eta x^4}{V_{nmo}^2[t_0^2 V_{nmo}^2 + (1+2\eta)x^2]} \tag{24}$$

where parameter η (eta) is picked to best predict (hence flatten) the variation of reflectors' times for large offsets.

The parameter η is not a pure measure of the seismic anisotropy. Although researchers have associated its higher values with more shaly lithologies (Alkhalifah, 2011), higher η values do not necessarily indicate more anisotropic rock layers. In fact, the η in equation (24) is an effective η ($\eta_{effective}$) that is a combination of isotropic long offset move-out and the contribution of rock properties (anisotropy). The process of evaluating η is sometimes referred to as "ETA analysis".

η is best understood when specified as a combination of Thomsen's anisotropic parameters (Thomsen, 1986) epsilon "ε" and delta "δ". Alkhalifah et al. (1996) described such relationship as:

$$\eta = \frac{\varepsilon - \delta}{1 + 2\delta} \tag{25}$$

Thomsen's anisotropic coefficient δ can be approximately estimated from short offset velocity analysis at the borehole location.

The NMO velocity is related to vertical velocity through the equation(Grechka, 2009)

$$V_{nmo} = V_0\sqrt{1+2\delta} \tag{26}$$

V_o can be obtained through sonic integration or from zero offset VSP surveys, and NMO velocities are calculated from short offset seismic velocity analysis. Hence at a borehole location we can infer elastic parameters of an assumed TI system.

The calculation of move-out velocity is an important processing step to generate a stack section. Stacked seismic is the backbone of seismic interpretation. The move-out velocity further contributes to accurate depth-conversion and well-tie analysis.

2.8 Seismic Amplitude versus Offset

Seismic reflection data have been traditionally used for identifying appropriate structural shapes and stratigraphic plays which are likely to host hydrocarbons. Amplitude variation with offset (AVO) analysis (Ostrander, 1982-1984) was initially proposed as a technique for validating seismic amplitude anomalies associated with gas sands. Years before this technique was applied to find hydrocarbon reserves, researchers realized that seismic amplitude signature varies with offset. The initial exact solution was provided by Zoeppritz (Koefoed, 1955).

The difficulty with the solutions provided by Zoeppritz is that his equations are not linear and as such are not readily usable in reflection seismology. We are measuring incidence angle, offset, velocities, densities and travel time to events, as well as the variations of amplitudes at boundaries. Any relationship should readily relate these measurements with the variations of amplitude. In the ideal case we want a function of the form

$$\nabla . F(A) = G(offset, Velocity, density, time) \tag{27}$$

where “A” denotes amplitude.

Many successful developments were achieved through linearization of Zoeppritz equations. Such modifications started from the simplest approximations to the original equations and matured in

their complexities over years. Researchers tried to model the amplitude response by using two- and three-term AVO equations (Aki and Richards, 1980). Higher-order approximations had potential to reveal more information about the reservoir, but were more prone to errors. Researchers showed that solutions to the isotropic AVO can produce significant errors in presence of anisotropy (Teng and Mavko, 1996), and hence significantly distort the results produced by the conventional AVO analysis (Banik, 1987; Kim et al., 1993).

2.8.1 Isotropic AVO Equations

To reveal the information content of Zoeppritz equations, several authors (Aki and Richards, 1980; Bortfeld, 1961; Hilterman, 2001) formulated two-term approximations. An intuitive approach to approximation of AVO response of interfaces can state that such a response is a combination of two terms a vertical reflection component and the contribution from the non-zero offsets. In this case we are writing the total reflectivity as:

$$R(\theta) = R_p + G.sin^2(\theta) \tag{28}$$

Where R_p is the P-wave intercept and G is the "gradient". Theoretically the second term (G. $sin^2\theta$) represents the non-zero offset.

The above equation was first introduced by Bortfeld (1961) as a practical approximation to full Zoeppritz equations. However, the validity of the above equation was severely limited by the incidence angle. In reality, considering that all rocks are anisotropic, its accuracy started degrading beyond 30 degrees incidence angle.

Shuey (1985) introduced a practically viable approximation of for the three-term AVO as

$$R_p^{iso} = A + Bsin^2\theta + Csin^2\theta\, tan^2\theta \tag{29}$$

Where

$A = \frac{1}{2}\left(\frac{\Delta v_p}{\Delta \overline{v}_p} + \frac{\Delta \rho}{\overline{\rho}}\right) = \frac{1}{2}\frac{\Delta Z}{\overline{Z}}$ is the normal incident

$B = -2\left(1 - \frac{\overline{\sigma}}{1-\overline{\sigma}}\right)A - \frac{1}{2}\frac{1-3\overline{\sigma}}{1-\overline{\sigma}}\frac{\Delta v_p}{\overline{v}_p} + \frac{\Delta \sigma}{(1-\overline{\sigma})^2}$ is the AVO gradient

$C = \frac{1}{2}\frac{\Delta v_p}{\overline{v}_p}$ is the curvature term

The main advantage of this formulation is that each term is dominant in a different angular range.

The coupling between transverse and longitudinal waves for oblique incidence angles manifests itself in the dependence of the P-wave AVO on the shear-wave velocity (Shuey, 1985). However, the opposite is not true and the S_v-wave AVO gradient is independent of the compressional wave velocities. Overall, all three-term isotropic approximations have their limitations and fail to predict the behavior of the AVO curves well beyond 40 degrees or when approaching the critical angle (Figure 6).

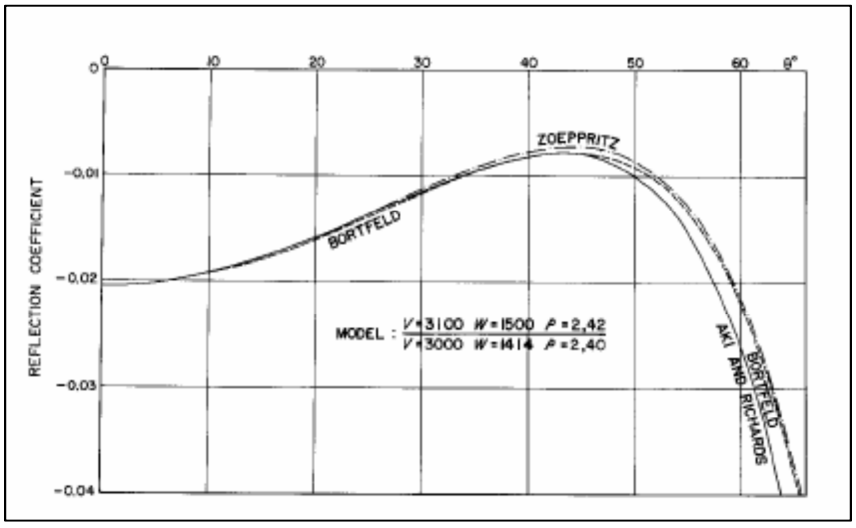

Figure 6. Comparison of the accuracy of Bortfeld Aki &Richards and Zoeppritz in predicting the AVO effects for different offsets/angles.

The most critical issue with the three-term AVO approximations is their initial assumption of isotropy. By adding more terms to the AVO, we are trying to measure smaller quantities, but the magnitude of the errors can much exceed variations produced by the rock itself. It is also important to notice that AVO studies are actually AVA) studies. In isotropic media, offset is nearly equivalent to angle while in anisotropic media there could be a notable difference between the two as the direction of energy propagation may not be orthogonal to the wavefront (Schoenberg and Douma, 1988).

Although AVO analysis is not the primary focus of this thesis, it will be mentioned multiple times during the analysis of each case study. The basic understanding of the concept will assist in better definition of the workflow and data QC.

2.9 Model-based approach to determine anisotropy

Variation in the anisotropy parameters of the earth limits our approach to evaluate it. An effective method (Amiri Besheli and Urosevic, 2006) is to model the anisotropy parameters and their response from well information and compare the various realizations with the measured surface seismic and find out the best match. The effect of VTI overburden can change reflection response for small angles of incidence (<20) even for weakly anisotropic case. A combination of cross-dipole sonic (DSI) log, image log and a VSP survey can be used to determine the presence of anisotropy in sediments at well location (Pevzner et al., 2010). Walk-away VSP can greatly help elaborate the dimensions of any existing anisotropy (Dewangan and Grechka, 2003). To evaluate the feasibility of surface seismic data for measuring azimuthal anisotropy in reservoirs, the elastic parameters should be derived from anisotropic Gassmann fluid replacement analysis (Gurevich, 2003). However, most of the scientific efforts were concentrated around the reservoir rock. This poses an important question: How could surface seismic help us with another component of the petroleum system: “the seal”? If we can answer this question, we can help find the relationship between presently known hydrocarbon accumulations and sealing rock

(shale) quality or its parameters, such as structure, composition, state of stress, etc. Similarly, we may be able to understand the relationship between the poor quality of the shales and partially discharged fields as found offshore NWS (Northwest Shelf).

Microstructural inhomogeneities which are modelled within the larger background matrix must be properly represented in the overall elastic response. To identify the microstructural properties of interest involves understanding the shape factor of the inclusion and the elastic nature of the matrix (Kachanov and Sevostianov, 2005). Such analysis usually needs the expression of the target properties in form of tensors. Many classical works tried to address various aspects of the "inclusion problem" which focuses on the evaluation of mechanical/elastic properties of a solid with inclusions. Most of the early work considered the problem of spherical holes and isotropic background (e.g. (Mackenzie, 1950)). Further insights were cast on to the overall inhomogeneities/anisotropies of the composite containing various types of inclusions (Berryman, 1979; Hill, 1963, 1965; Morris, 1970; Taya and Chou, 1981). The base of all the micromechanical approaches to solving an inclusion problem is to find an approximation to the Eshelby's tensor (Eshelby, 1957) of the target. The problem will then convert to incorporate the right proportion of this inclusion to the matrix. Various methods have been devised to solve for the overall elastic properties of a composite material. Depending on the cases, individual or combinations of these approaches may be used to evaluate the elastic components of a composite (Hornby, 1998; Matthies, 2012; Nishizawa and Yoshino, 2001).

2.9.1 The inclusion

Let's consider a homogenous solid with linear elastic constant C_{ijkl}. Suppose a sub-volume of this solid body undergoes permanent deformation (like phase deformation) and is then removed from the matrix. The sub-volume (inclusion) will then retain a non-zero uniform strain e_{ij}^{*}. Eshelby (1957) introduced the term *eigenstrain* for the stress-free state of the removed inclusion and introduced the

solution for the stress, strain and displacement fields of the inclusion and the matrix. Using the superposition principle of linear elasticity and the Green functions (Mura, 1987) Eshelby showed the strain inside the inclusion is related to its eigenstrain:

$$e_{ij}^{c} = S_{ijkl} e_{kl}^{*} \tag{30}$$

Where S_{ijkl} is often called the Eshelby's tensor.

The Eshelby's tensor satisfies minor symmetries $S_{ijkl}=S_{jikl}=S_{ijlk}$, but does not have major symmetries, i.e. $S_{ijkl}\neq S_{klij}$. For an ellipsoidal inclusion in a homogeneous matrix, the Eshelby's tensor is constant tensor (Mura, 1987; Weinberger and Cai, 2004). Appendix 1 further elaborates on the components and calculations of the Eshelby's tensor.

2.9.2 Effective Medium Theory

The complexity of some structures and combinations of multiple ingredients have challenged the physicists and mathematicians for long. One method to determine the behavior of heterogeneous materials is to build a fictitious homogenous medium that has the equivalent properties of the original complex heterogeneous medium. The Effective Medium Theory is the method(s) which describes such process. The averaging procedure for the heterogeneous material was described by (Hill, 1963):

$$\sigma_{ij}^{*} = \frac{1}{V}\int_{V} \sigma_{ij}(x) dV \tag{31}$$

Where * denotes the average stress (σ) over the entire volume V.

Hornby et al. (1994) explain that for a sub-volume of fraction v_n, a tensor K^n (Hudson and Knopogg, 1989) that relates the applied stress <σ> can be related to the average strain in each inclusion e^n. The expression for the effective compliances of the composite is:

$$s^* = s^0 - \sum_{n=1}^{N} v_n (s^0 c^n - I) K^n \tag{32}$$

Where s^* is the tensor of compliance of effective material that we wish to estimate. "c" is the stiffness tensor and superscript "0" indicates "average".

2.9.3 The self-consistent approximation

If a spherical region from a stress-free homogenous matrix is removed and is subjected to the deformation e^p_{tv}, the inclusion would need a surface traction applied so that it gets restored to its original shape (Eshelby, 1957). Therefore once a long-field uniform stress is applied to the composite, the total stress of the inclusion is $e^G_{nw}$and has the following relationship to the applied stress:

$$\sigma_{lm} = C_{lmnw}(e^G_{nw} - e^p_{nw}) \tag{33}$$

Where C_{lmnw} is the stiffness constant of the matrix.

If the inclusion is now replaced with a single crystal (with elastic constant C^{crs}_{lmnw} which undergoes the same hypothetical procedure above, is subject to stress; we will have (Morris, 1970):

$$\begin{gathered} \sigma = C : (u + I) : \bar{e} \\ u = -(c^{crs} - C + C : w)^{-1} : (C^{crs} - C) \end{gathered} \tag{34}$$

Where ":" denotes double inner production of tensors, $\bar{e}$ is the elastic deformation, w is the approximation of Eshelby's tensor and "I" is the unity tensor.

The solution for $\bar{u} = 0$ over principal elastic constants C^{pr} is:

$$u = [C^{pr} - C + E^{-1}]^{-1} E^{-1} - I \tag{35}$$

Where $E=w^{-1}$:S and S is the compliance tensor.

While this theory is essential for understanding wave propagation in effective anisotropic media its practical use is limited by the measured data. Consequently, we often combine macro properties such as kinematic anisotropic component with some other attribute based on the amplitude or frequency change of seismic waves, measure on a sample by sample basis (instantaneous attribute) or across entire rock unit (sequence attribute).

3 Chapter 3: Shales Anisotropy and Sealing

Shales comprise a major component of the sedimentary rocks. Their contribution to the lithologies of the sedimentary basins has been estimated to up to 50% (Boggs, 1992). A major part of the shales is composed of phyllosilicates or clay minerals such as Illite, Muscovite, Kaolinite, Chlorite and Smectite. Upon sedimentation, the dynamics of the process of deposition encourages the phyllosilicates to lie on their flat side. Later diagenesis and compaction will encourage this preferred orientation of clay minerals. Indeed most shales are known to be seismically anisotropic (Banik, 1984; Levin, 1980; Winterstein and Paulsson, 1990). Hence their influence on exploration methodology may be significant.

3.1 Anisotropy of Shales

Seismic velocities of shales have increasingly been the subject of studies over the past decades (Johnston and Christensen, 1995; Kaarsberg, 1959; Sondergeld and Rai, 2011; Vasin et al., 2013). Jones and Wang (1981) investigated the Cretaceous shales of the Williston Basin and showed that those shales are transversely isotropic. Indurated shale samples of the Devonian-Mississippian formations (Chattanooga shale, New Albany Shale and Antrim Shale) were studied by Johnston and Christensen (1995).

In order to conduct direct measurements of the seismic velocities, core samples (2-5 cm in diameter) are taken perpendicular and parallel to the bedding of the shales. Sending and Receiving transducers are connected to the polished end of the samples and compressional (P) and Polarized Shear waves (V_{sh} and V_p) are emitted to the sample. Three directions of measurements (perpendicular, parallel and 45degrees to the bedding) are required as minimum to establish the five elastic constants of the VTI medium. The following equations will then be used (Auld, 1973; Hearmon, 1961):

$$C_{11} = \rho V_{p\,(par)}^2 \tag{36}$$

$$C_{12} = C_{11} - 2\rho V_{sh}^2$$

$$C_{33} = \rho V_{p\,(per)}^2$$

$$C_{44} = \rho V_s^2$$

$$C_{13} = -C_{44} + [4\rho^2 V_{p\,(45)}^4 - 2\rho V_{p\,(45)}^2 (C_{11} + C_{33} + 2C_{44})$$

$$+ (C_{11} + C_{44})(C_{33} + C_{44})]^{\frac{1}{2}}$$

However clay measurement is very tedious as the saturation changes take many weeks to accomplish and even then we can only consider "wet" clay rather than dry clays (Dewhurst et al., 2007; Sarout and Guéguen, 2008a). The velocities measured depend on many factors; one of the most important is the mineral composition of the clays. To study the clay composition and mineral alignment X- Ray Diffraction (XRD) is probably the best way (Kanitpanyacharoen et al., 2015). Illite planes tend to show the best results in the alignment studies since the 002 and 110 planes of this mineral are almost perpendicular to each other (Kaarsberg, 1959). A normalized ratio of the reflectance of these two planes reveals the preferred orientation of the clay minerals. Illite is a common clay mineral and its elastic properties are close to Muscovite. Although Illite contents are different in shales, a very silty shale will exhibit low anisotropy even if all clay minerals are perfectly aligned (Johnston and Christensen, 1995).

Scanning Electron Microscope (SEM) is also used in the description of shale samples (Johnston and Christensen, 1995; O'brien, 1986) and can be qualitatively used to estimate the orientation index (alignment of clay minerals) of the constituents of the sample. This type of study is sometimes used to supplement the X-ray diffraction method. Samples taken from perpendicular and parallel to the bedding of the shale are the ideal samples to be studied. XRD and SEM are important in understanding the clays composition and mineral alignments. However for their sealing properties we need additional assessments.

3.2 Seal Capacity of shales

Sealing capacity of shales is directly related to the pore space size and connectivity. The larger these pores, the larger are the radii of the capillary tubes and easier it is for the fluid to pass through. Standard Mercury Injection tests measure the largest connected pore and assign the corresponding capillary pressure or withstanding column pressure as the sealing capacity of the sample. If shale sequences were made purely of shales, the sealing capacity of them would be much higher than the observed. One of the best explanations for the formation of the capillary pipes or "escape" passes was offered by Sneider et al. (1997). They suggested that the passages within the shales are created by grains that disturb the perfect alignment of phyllosilicates. The clay platelets will give way to some open space in the vicinity of quartz, pyrite or any other such grains and if such spaces happen frequently (i.e. presence of such disturbances by grains), it is likely that they are connected. These connected spaces will cause leakage (Figure 7).

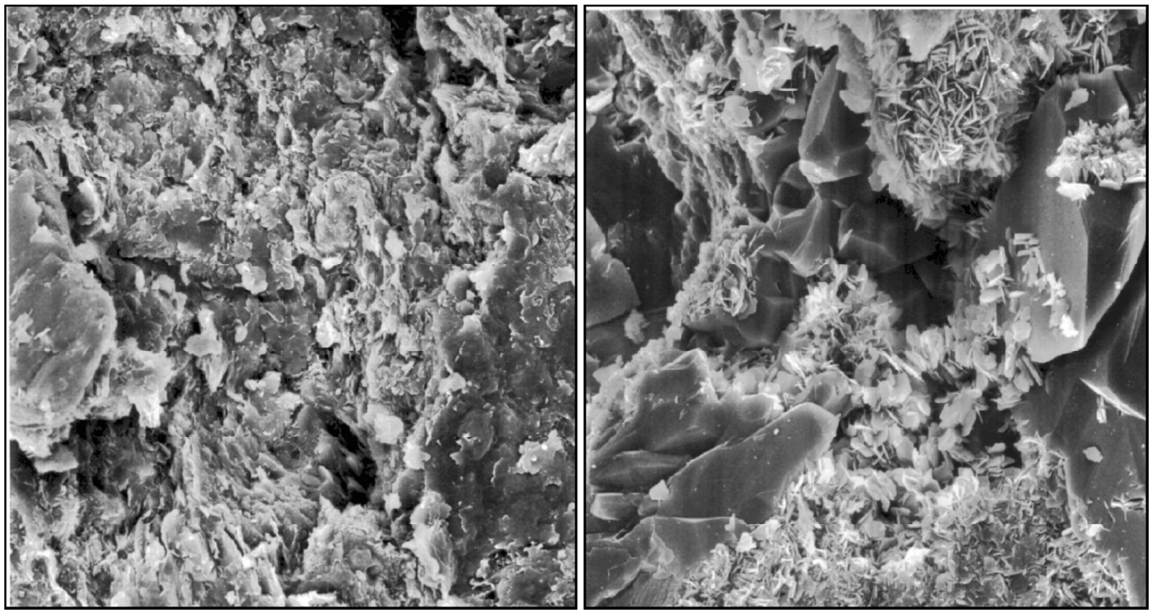

Figure 7. Comparison of two SEM photomicrographs taken from two seals: good (type A) on the left and weak (type D) on the right. Notice the presence of grain-supported fabric in the poorer seal. Picture is taken from Figure 9 of Sneider et al. (1997)

Intra-platelet spaces than can act as capillary pipes are actually low aspect ratio pores that are connected across the platelets. A shale sample with perfectly aligned clay minerals parallel to the bedding and compacted on top of each other is a very good seal. Such seal is unlikely to let any noticeable amount of fluid to pass. The anisotropy of such shales has been studied. A leaking seal can be imagined as perfectly aligned seal platelets plus capillary pipes across this "domain". Capillary pipes can be considered connected low-aspect-ratio pore spaces (Figure 8). The strength of a seal to withstand the fluid pressure depends on the radii of the capillaries (blue pipes in Figure 8) as well as the abundance within the sample. The shale shown in Figure 9b is likely to exhibit lower apparent VTI anisotropy as the faster direction (bedding plane) will be slowed down by the intercepting capillary pipes. This is one of the founding elements for this study.

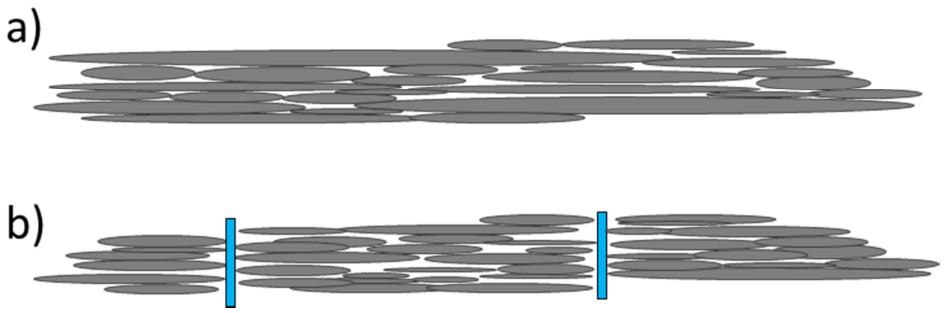

Figure 8. Schematic representation of a shale with all clay particles perfectly aligned along the bedding which forms a very good seal (top) and a leaking seal (bottom). Leakage pipes or capillary pipes are represented in blue low aspect ratio connected pores across the bedding.

3.3 Shale-capillary composite

To approach a realistic model for the sealing/leakage mechanism it is essential to start with a simple model. Figure 8 serves as a representation of the idea of the leakage and is a useful concept to model the capillaries in the shales. In the simplest scenario (Model 1), the leaking shale can be envisaged as perfectly aligned platelets forming a VTI medium and a bunch of straight vertical tubes penetrating through it (Figure 9). This simplification will help understanding the potential impact on the

compressibility and anisotropy of the shale. A VTI medium is defined by five independent compressibility constants $C_{11}=C_{22}$, C_{33}, $C_{12}=C_{21}$, $C_{13}=C_{31}=C_{23}=C_{32}$, $C_{44}=C_{55}$, $C_{66}= (C_{11}-C_{12})/2$. Water filled capillaries will bring the isotropic compressibility (K) and rigidity (μ) of water in the mix.

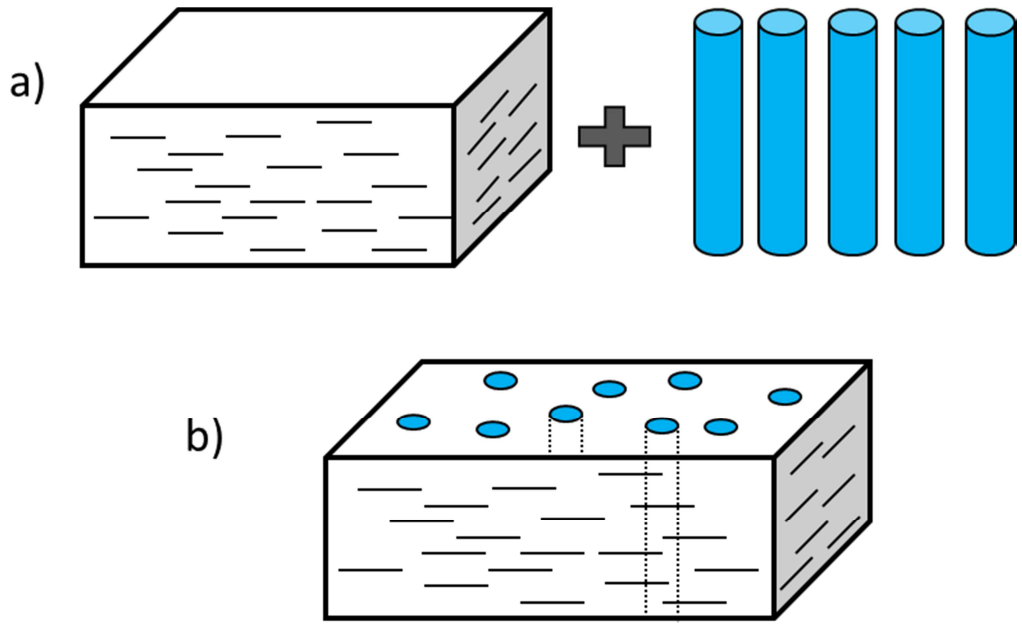

Figure 9. Schematic representation of the simplest case (Model 1) of capillary pressure in a VTI (shale) medium. The capillaries (blue pipes) and the undisturbed shale (a) will form the VTI medium with vertical capillaries (b).

The analytic solution to the changes of the elastic properties of mixture of materials is introduced by Hill (1963) and is applicable on the model 1 that is represented in Figure 9. The mixed (reinforced) compressibility (K) will lie somewhere in between the ingredients. Using a typical compressibility measurements for shales from laboratory measurements by Jones and Wang (1981) and comparing it with the compressibility of water (k_w=2.2GPa, μ=0), a huge difference is observed (Table 1). The addition of water filled pipes (capillaries) to a block of shales will essentially reduce C_{11} without having much impact on C_{33}. It essentially means that squeezing the shale samples without the vertical pipes along the horizontal axes (where $C_{11}=C_{22}$ come to play) is more difficult than squeezing the sample with the capillaries along the same axes. However, the loading capability of shale along the vertical axis (C_{33}) will not be affected as much as the horizontal loading.

C_{ij}	GPa
C_{11}	34.3 ±1.4
C_{33}	22.7 ±0.9
C_{44}	5.4 ±0.8
C_{66}	10.6 ±1.6
C_{13}	10.7 ±5.4

Table 1. The five independent elastic components of a shale sample measured by (Jones and Wang, 1981).

Impinging seismic wavefront on the "clay+pore" medium inflicts the stress which will be sensed (according to the effective medium theory (Berryman, 1992; Jakobsen et al., 2000; Nishizawa and Yoshino, 2001)) by the boundaries of vertical (or perpendicular to the horizontal coordinate system fixed parallel to bedding) capillary pipes. This change is more noticeable is the horizontal direction due to the introduction of excess horizontal compliance compared to the unchanged vertical one. Also, the capillary pipes are far thicker than the inter-platelet pore spaces. Typical intra clay spacing is 1-5^{nm} while any noticeable seal breach happens well beyond tens of nanometers.

Although Model 1 introduces the concept of adding capillaries to the shales in a simplified manner, it faces serious challenges in the real world. The real shales almost never show a nicely vertical porous phase running perpendicular to the bedding. The capillary pipes themselves are very rarely in a shape of vertical undisturbed pipes. Furthermore, the shale platelets are not all aligned in the bedding direction in the real world. There is also the problem of the huge reduction of stiffness components that is resulted from such combination. Numerical modelling of such impact was performed over the well-studied Kimmeridge Shale (Hornby, 1998; Vasin et al., 2013) and shows the unrealistic drop in the stiffness components of the mixed medium where the capillary tubes are perpendicular to the bedding. Despite all these shortcomings, Case 1 introduces an upper bound to the sealing/leakage modelling. It

shows that the reduction in C_{11} is faster than the reduction in C_{33} due to the introduction of (near) vertical low-aspect-ratio pores. From Equation 22 we can see than the anisotropy parameter ε should decrease with increasing portion of capillary pipes.

3.4 Excess compliance

A more realistic situation for the capillary pipes that were shown in Figure 9 is to consider the tractions perpendicular and parallel to these pipes (Model 2). The capillary tubes are more likely to have varying diameter along their length and they will adapt some traction as the impinging seismic wave causes some stress change. Sayers and Kachanov (1995) and Sayers (1999) have shown that there is excess compliance along/across the bedding-parallel pore shapes. Figure 10 shows a modified and more realistic depiction of the capillary pipe that will run across (or perpendicular to) the bedding of the shale. The incident seismic wave on the surface will cause some stress and as a result some traction will occur along the boundary. For our case, the surfaces of interest are perpendicular to the bedding plane (and clay platelets).

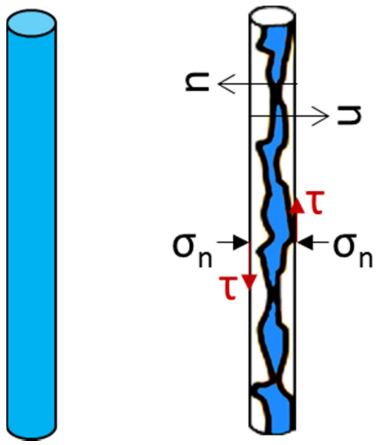

Figure 10. More realistic representation of a capillary pipe (left) is shown on the right where the thickness of the pipe is not constant and traction may happen along the pipe sides (modified after Sayers (1994a)).

The excess compliance that results from the normal and shear compliances of low-aspect-ratio pores was shown (Sayers, 1999) to be:

$$\Delta S_{ijkl} = \frac{1}{4}\left(\delta_{jk}\alpha_{jk} + \delta_{il}\alpha_{jk} + \delta_{jk}\alpha_{il} + \delta_{jl}\alpha_{ik}\right) + \beta_{ijkl} \tag{37}$$

Where

$$\alpha_{ij} = \frac{1}{V_{solid}}\sum_{r=1}^{N} B_T^{(r)} n_i^{(r)} n_j^{(r)} S^{(r)} \tag{38}$$

$$\beta_{ijkl} = \frac{1}{V_{solid}}\sum_{r=1}^{N} \left(B_N^{(r)} - B_T^{(r)}\right) n_i^{(r)} n_j^{(r)} n_k^{(r)} n_l^{(r)} S^{(r)} \tag{39}$$

B_N and B_T are effective normal and shear compliances for the r^{th} grain boundary.

The assumption of the clay sheets align perfectly and the pores/capillaries are perpendicular to them implies that $n_3=0$ and $n_1=n_2$. This also means that $\Delta S_{3333}=0$ and the only non-zero component of α_{ij} and β_{ijkl} are α_{11} and β_{11}. This will have immediate impact on anisotropy parameter ε:

$$\epsilon' = \frac{C_{11} + [\Delta S_{1111}]^{-1} - C_{33}}{2C_{33}} \tag{40}$$

Where $\Delta S_{1111}=\Delta S_{11}=\alpha_{11}+\beta_{1111}$

With the axes rotation to fit the perpendicular pore/tubes, we have

$$\alpha_{11} = \frac{1}{V_{solid}}\sum_{r} B_T^{(r)} A^{(r)}$$
$$\beta_{1111} = \frac{1}{V_{solid}}\sum_{r} B_N^{(r)} - B_T^{(r)} A^{(r)} \tag{41}$$

The normal compliance of shales is much smaller than their shear compliance so that

$$(\zeta = \frac{B_N}{B_T}) \ll 1 \quad (42)$$

From equations (40) and (41), we can see that the compliance variation $[\Delta S_{1111}]^{-1}$ along the clay sheets is a negative value. Therefore ε' will be a smaller figure compared to ε. In fact the presence of fluids lowers the values of B_N and the term β_{iiii} becomes important(Sayers, 1999). On the other hand, the thinner the capillary tube is, the higher the chance of grain-contacts and the higher B_N will be. Thinner tubes mean lower chance of compliance excess and the reduction in α_{ii}.

3.5 Disordered domains

Model 2 sufficiently presents the decrease in ε with increasing presence of capillary pipes. However, there is still the oversimplification of assigning leakage to vertical capillary tubes and the rapid reduction of ε as result of such engagement. The problem goes back to the assumption that was made to have all the clay particles aligned with the bedding. Katahara (1996) observes the huge discrepancy between the mode velocities of the clay minerals and shales. The calculated mode velocities were up to two times larger than their corresponding velocities in shales measured by Han et al. (1986); Tosaya (1982) and Castagna et al. (1985). Such discrepancy can also be made comparing the measured stiffness constants of clay mineral and those of the shales. Within a range, the measured stiffness values for shales (Ortega et al., 2007; Ulm and Aboulseiman, 2006) are close to the values (Table 2) reported by Jones and Wang (1981). However, the reported C_{ij} values for Illite (and muscovite) are much larger (Table 2).

C_{ij}	**GPa**
C_{11}	178
C_{33}	54.9

C_{44}	12.2
C_{12}	42.4
C_{13}	14.5

Table 2. Stiffness values reported for Illite by Alexandrov and Ryzhova (1961)

Such discrepancy can be explained by the effects of disorder of clay platelets in shales (Sayers, 2005). An orientation Index that was obtained from the X-Ray studies was shown (Johnston and Christensen, 1995) to be indicative of the VTI nature of the shales and the alignment of the clay platelets. Better alignment of clay minerals means higher anisotropy which in turn means the stiffness tensor of the shale changes to get closer to that of the clay minerals. It was shown by Ulm and Aboulseiman (2006) and Ortega et al. (2007) that the mechanical properties of shales are determined by the contact regions between the clay particles rather than the stiffness and compliances of the clay platelets themselves. They also concluded that the anisotropy of shales is the result of sedimentary feature that is driven by depositional processes and not the intrinsic anisotropy of the clay minerals. In fact, a number of clay sheets that share the same orientation and are stacked together act as basic brick to construct the overall elastic properties of the shale. Such regions are referred to as a domain (Aylmore and Quirk, 1960).

To describe the order within a shale sample an orientation function is described. The orientation function shows the general alignment of the domains within the overall sample. If y_{ijk} describe the coordinate system that is fixed within each domain, then the orientation of the domain within the shale unit having the fixed coordinate of X_{ijk} can be described by Euler angles (Figure 11). The orientation distribution function (ODF) of a domain will help provide the amount of clay in the fractional space of $(\zeta+d\zeta,\psi+d\psi,\phi+d\phi)$

$$clay\ content = W(\zeta, \psi, \varphi) d\zeta d\psi d\varphi$$
$$\zeta = \cos\theta \tag{43}$$

Where θ, ψ and ϕ are the Euler angles between X_3-y_3, X_2-y_2 and X_1-y_1 pairs respectively (Roe, 1965). The elastic stiffnesses of the shale are obtained by integrating the stiffnesses of clay domains (in the Voigt approximation) using the distribution function of the domains. The integrals were simplified by Roe (1965) using a generalized Legendre functions $Z_{lmn}(\zeta)$:

$$W(\zeta, \psi, \varphi) = \sum_{l=0}^{\infty} \sum_{m=-1}^{1} \sum_{n=-1}^{1} W_{lmn} Z_{lmn}(\zeta) e^{-im\psi} e^{-in\varphi} \tag{44}$$

Details of the Legendre Expansion can be found in Appendix 3.

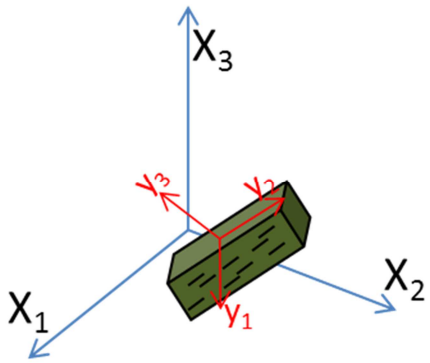

Figure 11. The orientation of a domain with its local coordinates can be described to the fixed coordinate system.

The table of calculated W_{lmn} for 4th rank tensors is provided in detail by Morris (1969). Out of the orientation coefficients W_{lmn} that are predicted by equation (43), only two are required to describe the anisotropic behavior of shales (Sayers, 1994a). W_{400} and W_{200} are the two parameters that can describe the spatial orientation of the domains to predict their stiffness values. Alternatively, the stiffness values of shales can be used to calculate W_{400} and W_{200}. A total chaotic and random orientation of the domains means W_{400}=W_{200}=0 while a completely ordered shale particles will result in $W_{200\text{-}max}$=0.04005 and $W_{400\text{-}max}$=0.05373 (Sayers, 1989). Most shales have their $W_{400}/W_{200} \leq (W_{400\text{-}max}/W_{200\text{-}max})$. Disorder in the

orientation of shale domains will cause a reduction in W_{400} faster than W_{200} as W_{400} is of a higher order compared to W_{200}.

The stiffness coefficients of the shale averaged over the domains can be written as (Sayers, 2005):

$$\bar{C}_{11} = C_{22} = \lambda + 2\mu + \frac{8\sqrt{10}}{105}\pi^2 a_3 W_{200} + \frac{4\sqrt{2}}{35}\pi^2 a_1 W_{400} \tag{45}$$

$$\bar{C}_{33} = \lambda + 2\mu - \frac{16\sqrt{10}}{105}\pi^2 a_3 W_{200} + \frac{32\sqrt{2}}{35}\pi^2 a_1 W_{400} \tag{46}$$

$$\bar{C}_{12} = \lambda - \frac{8\sqrt{10}}{315}\pi^2 (7a_2 - a_3) W_{200} + \frac{4\sqrt{2}}{35}\pi^2 a_1 W_{400} \tag{47}$$

$$\bar{C}_{13} = \lambda + \frac{4\sqrt{10}}{315}\pi^2 (7a_2 - a_3) W_{200} - \frac{16\sqrt{2}}{105}\pi^2 a_1 W_{400} \tag{48}$$

$$\bar{C}_{44} = \mu - \frac{2\sqrt{10}}{315}\pi^2 (7a_2 + 2a_3) W_{200} - \frac{16\sqrt{2}}{105}\pi^2 a_1 W_{400} \tag{49}$$

Where

$$a_1 = C_{11} + C_{33} - 2C_{13} - 4C_{55} \tag{50}$$

$$a_2 = C_{11} - 3C_{12} + 2C_{13} - 2C_{55} \tag{51}$$

$$a_3 = 4C_{11} - 3C_{33} - C_{13} - 2C_{55} \tag{52}$$

Disturbance to the alignment of clay platelets (or domains) is caused by silt and pore inclusions, as well as low-aspect-ratio pores or capillary pipes. The presence of pore space escapes through the shales essentially means a higher disturbance compared to the perfect alignment case of the domains. Perfect alignment of the clay minerals leaves little room for any capillary pipe to form and let the fluid pass through tightly compacted clay domains. According to Sayers (2010) any shale's stiffness tensor can be calculated using the base values from the Williston Basin studied by Jones and Wang (1981)(Table 1)

and the right combination of W_{200} and W_{400}(Figure 12). Obviously, better alignment of clay particles will result in higher W_{200} and W_{400} values and consequently the anisotropy parameter ε.

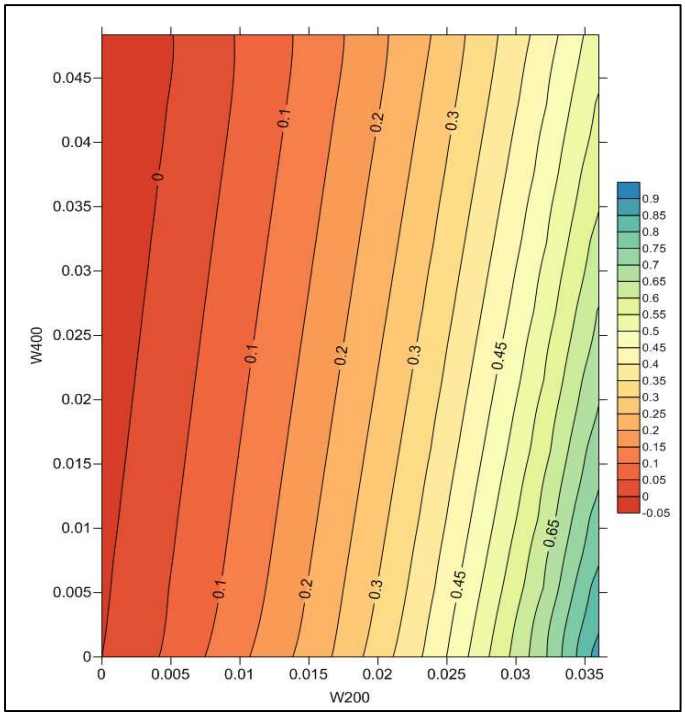

Figure 12. Variation of ε with W200 and W400.calculated using Voigt approximation. The input data are taken from Table 1 which reports a shale sample from Williston Basin (Jones and Wang, 1981). General increase of ε with the increase of W200 and W400 is visible.

3.6 Modelling

Figure 13 depicts a schematic of a shale sample with some misalignment of the clay particles (or domains). Such disturbances are responsible for the large difference between the stiffness of the clay minerals and a shale. The orientation of domains will direct how the capillary pipes are connected through the thickness of the shale. If the domains were perfectly aligned, the capillary pipes would have to go right past them and be near vertical. This is geologically unusual as explained in the conceptual model above. The domains, however, get pushed around by silts and lie at a misaligned angle to the

general isotropy surface of the shale (Figure 13). The angle ϕ denotes both the direction of a segment of the capillary pipe and the nearby shale domain. As a result ratio (W_{400}/W_{200})/ ($W_{400\text{-}max}/W_{200\text{-}max}$) is related to ϕ. The higher is W_{400}/W_{200}, the better-ordered shale it is, and the closer ϕ comes to zero.

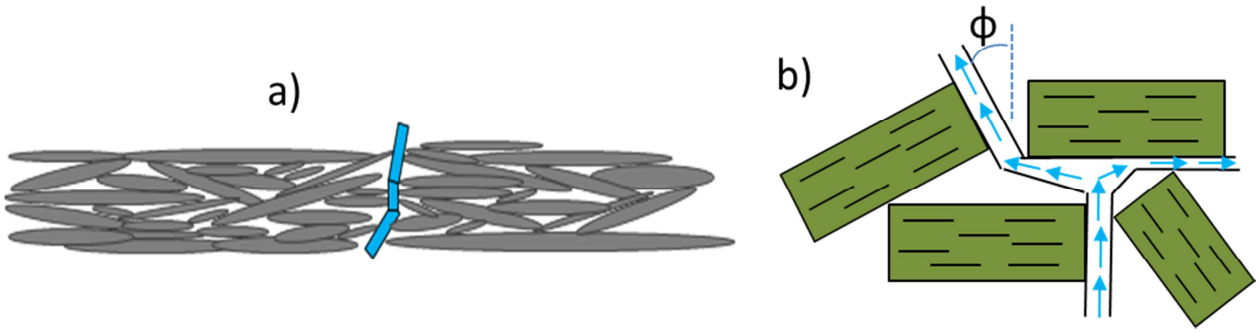

Figure 13. Misalignment of clay platelets and domains within a shale sample affects the elastic characteristics of shales (a). The arrangement of the platelets will have direct impact on the orientation and shape of the capillary pipes. Such misalignment is closely related to the capillary path. ϕ is the angle between the axis of symmetry(vertical) and the normal to a domain (b).

The elastic properties of a composite can be explained via two well-known models of Voigt (Voigt, 1887) for parallel connection between the phases and Reuss (Reuss, 1929) for a series connection of the phases. They are stated as:

$$E_{parallel} = E_1 f_1 + E_2 f_2 \tag{53}$$

$$E_{series} = \left(\frac{f_1}{E_1} + \frac{f_2}{E_2}\right)^{-1} \tag{54}$$

Where E is the elastic property and f_i is the fraction of the phase in the composite.

A system of (sub-) vertical capillary pipe is necessary for the leakage to happen. Assuming the capillary pipes are saturated with water (K_w=2.2 GPa), the horizontal stiffness of a 'shale domain-

capillary pipe' is a series composite while the vertical stiffness is a parallel one. Combining Equations (53), (54) into (45) to (52) to extract the ε value of the new composite, we will get:

$$\varepsilon' = \frac{K_w \bar{C}_{11} - \left(\frac{\bar{C}_{33}}{\varphi} + K_w - \bar{C}_{33}\right)\left(\bar{C}_{11} - K_w + \frac{K_w}{\varphi}\right)\varphi^2}{2\left(\frac{\bar{C}_{33}}{\varphi} + K_w - \bar{C}_{33}\right)\left(\bar{C}_{11} - K_w + \frac{K_w}{\varphi}\right)\varphi^2} \tag{55}$$

Where $\bar{C}_{ij}$ are defined in equations (45) to (52).

Equation (55) takes into account the misalignment of shale domains as well as the capillary pipe inclusions in the leaking shale composite. It can be simplified by ignoring the parallel composite impact of capillary pipes on C_{33} in comparison with the effect on C_{11} .Such simplification reveals that the decline in ε due to the increase of capillary porosity is a function of 1/φ. Equations (53) to (55) define the upper and lower bounds (Hill, 1963) of the introduction of capillary pipes to an elastic shale system. In order to unify the comparison criteria for the shale orientation, an orientation Index is defined based on the relative values of W_{200} and W_{400} to their corresponding maximums. The index runs from 0 (lowest order) to 10 (highest order):

$$I_w = \left(\frac{W_{200}}{0.04005}\right) \times 9.9 + \left(\frac{W_{400}}{0.05373}\right) \times 0.1 \tag{56}$$

Figure 14 shows the variations of ε with capillary porosity for several configurations of shale platelets.

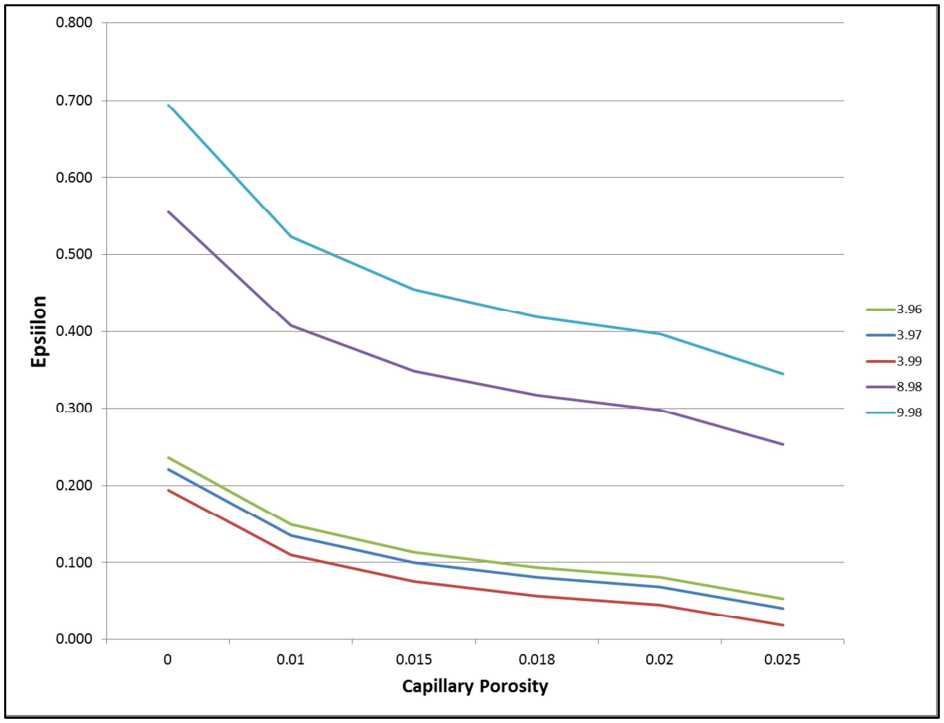

Figure 14. Variation of Epsilon with capillary pressure for a number of combinations of W_{200} and W_{400} combinations to represent a variation of highly aligned to highly randomized shale domain orientations.

The effect of variations of compliance due to introduction of capillary pipes can be modelled using equation (41) for the two cases of X_3 and X_1 axes (also refer to Appendix 4). The capillary pipes from Figure 13b can be modelled as a series of vertical and horizontal pipes which upon integration will form the real pathway. Therefore, the two excess compliances to be calculated are $\Delta S_{11}=\alpha_{11}+\beta_{1111}$ and $\Delta S_{33}=\alpha_{33}+\beta_{3333}$. Following Sayers and Kachanov (1995) and per Nye (1985), the inverted compliance matrix for C_{ij} values as:

$$\Delta C_{11} = \frac{(S_{11}^0 + \alpha_{33} + \beta_{3333})}{D} + \frac{1}{S_{11}^0 - S_{12}^0 + \alpha_{11} + \frac{2\beta_{1111}}{3}} - C_{11} \tag{57}$$

$$\Delta C_{33} = \frac{S_{11}^0 + S_{12}^0 + \alpha_{11} + \frac{4}{3}\beta_{1111}}{D} - C_{33} \tag{58}$$

where

$$D = (S_{11}^0 + \alpha_{33} + \beta_{3333})\left(S_{11}^0 + S_{12}^0 + \alpha_{11} + \frac{4}{3}\beta_{1111}\right) - 2(S_{12}^0 + \beta_{1133})^2 \tag{59}$$

$$C = C_{33}(C_{11} + C_{12}) - 2(C_{13})^2$$

$$2S_{11}^0 = \frac{C_{33}}{C} + \frac{1}{C_{11} - C_{12}}$$

$$2S_{12}^0 = \frac{C_{33}}{C} - \frac{1}{C_{11} - C_{12}}$$

ΔC_{11} and ΔC_{33} will be the variation of stiffness due to presence of capillary pipes and will be combined with equations (45) and (46) to compute the new ε.

The capillary pipes are most likely filled with water (or a fluid with K≠0), therefore $B_N << B_T$. This means α_{ij} and β_{ijkl} will have opposite signs. The reduction of B_N is directly proportional to the radius of the capillary pipe. This means the thicker the capillaries are, the lower the ration B_N/B_T is. Following equations (40) to (42), we will have

$$2C'_{11} = \frac{S_{33}}{S_{33}(S_{11} + \alpha_{11} + \beta_{1111} + S_{12}) - 2[S_{13}]^2} + \frac{1}{C_{11} - C_{12}} \quad (60)$$

The new value of C_{11} is then used to recalculate equations (45) to (52). Figure 15 depicts the variation of parameter ε with the same range of W_{200} and W_{400} as in Figure 12. A noticeable decrease is visible in ε values. The calculations can be repeated for various B_N/B_T ratios to represent the capillary radius, but the general trend is to decrease ε.

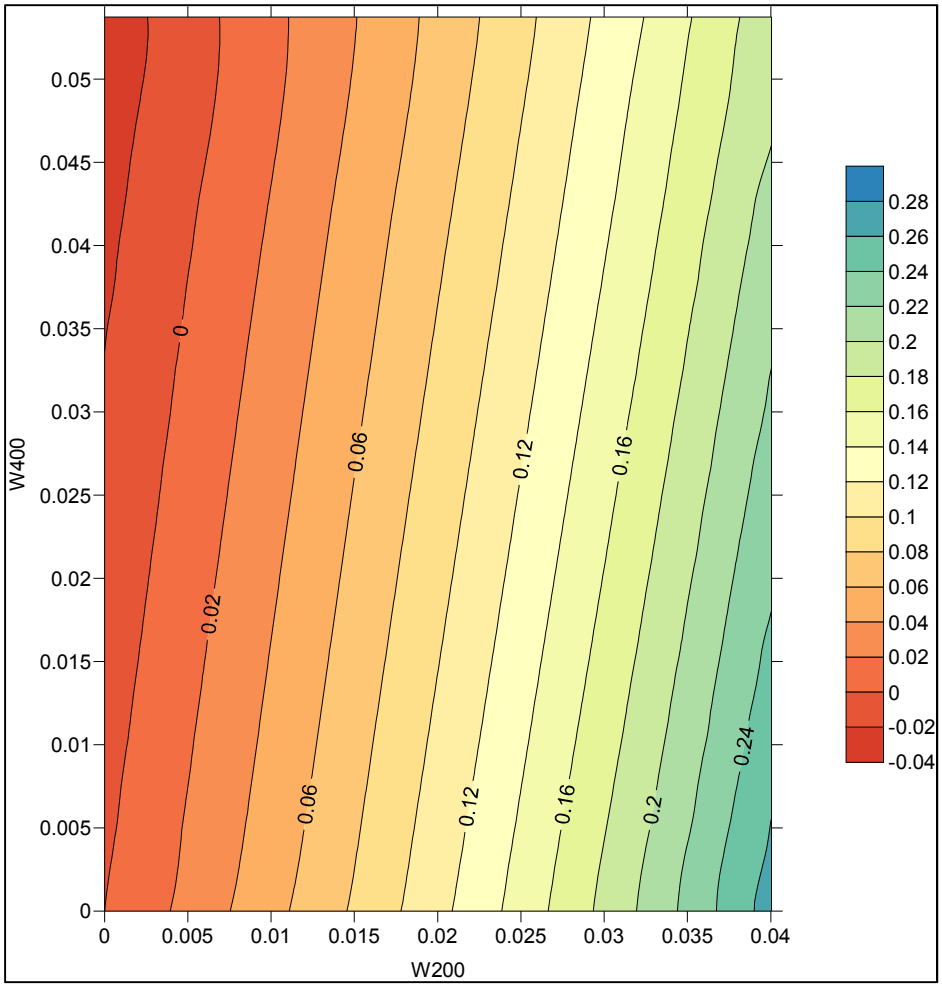

Figure 15. Variations of epsilon with W_{200} and W_{400} for B_N/B_T=0.3.

Presence of capillary pipes is due to intergranular spaces that were left open during (partial) compaction or presence of hard buttresses such as silt grains. Therefore, one-one-one comparison of Figure 12 and Figure 15 might be misleading. Capillary pipes are almost certainly associated with lower values of W_{400} and W_{200}. Also not all the shale domains have a similar size capillary pipe associated with them. In reality the capillary pipes cover a range of radii. Horne (2013) has collected a large amount of measured ε for all shales around the globe. His statistical review shows that the distribution of ε has a mean of 0.25 with standard deviation of 0.19 and the median of 0.21. This means values of ε>0.4 are

rare. Therefore, perhaps more than 10% of the shale domains have some kind of associated capillary pipe.

The radiuses of the capillary pipes have direct relationship with the B_N/B_T ratio. This means that if the capillary pipe that is next to a shale domain is very thin ($r_c \rightarrow 0$), the B_N/B_T increases to close to the dry shale (or its maximum). On the other hand, when the r_c increases, the ratio B_N/B_T falls. For saturated Muscovite, figures as low as 0.19 are reported for ratio of normal to shear compliance (Sayers, 2008). Laboratory measurements can help with the distribution histogram of the capillary pipes in a shale sample. One such example is presented by Dewhurst and Hennig (2003) for the Muderong Shale of the Carnarvon Basin, Australia. The Muderong shale sample studied by Dewhurst and Hennig (2003) shows a high degree of alignment of the platelets and the stiffness coefficients that were measured relate to high calculated W_{200} and W_{400} values (Equations (45) to (52)). Figure 16 show the volumetric distribution of the diameters of the pore throats in the shale sample. Although a higher fit could be achieved using a fourth order polynomial function, a linear trend line has a high enough correlation and is much easier to perceive. The linear decline in the cumulative volumes of the pore radii is almost intuitive: larger pores are rarer. However, Figure 16 can be thought of as an approximation to the rate of decline in the ratio of B_N/B_T as the pore throats get larger.

Based on the discussion above and the ranges of $\zeta = B_N/B_T$ that are found for dry and wet shales by Sayers (1999), Figure 16 reveals that for the Muderong Shale:

$$\zeta = -1.555 r_c + 0.493 \tag{61}$$

Where $0.26 < \zeta < 0.47$.

Regardless of the distribution, the average function of the ratio of compliances can be built:

$$f_{average} = \frac{1}{r_{c-max} - r_{c-min}} \int_{r_{c-min}}^{r_{c-max}} f(\zeta)\, dr_c \tag{62}$$

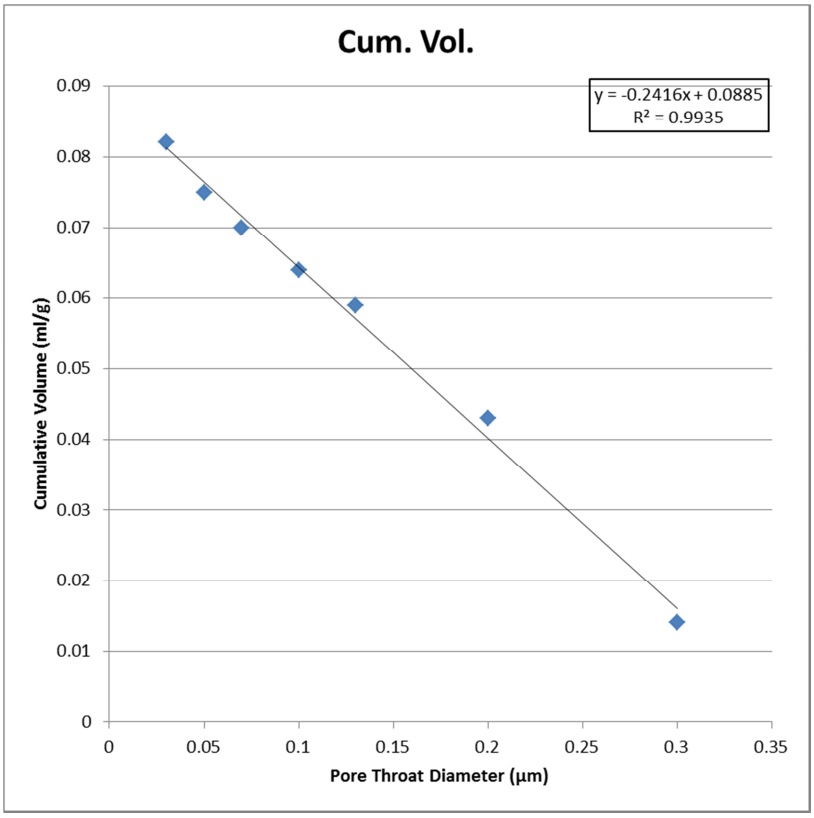

Figure 16. The volumetric distribution of pore throat size in a sample of the Muderong shale, Carnarvon Basin, Australia (modified after Dewhurst and Hennig (2003)).

For the Muderong shale sample, the average value of ζ is 0.36. The Muderong Shale has close to 60% of its composition being the clay minerals of Illite, Smectite and Kaolinite. At ambient conditions, the MICP test revealed a 17% porosity for the sample (Dewhurst et al., 2002a). Therefore an excess compliance equivalent to ζ=0.36 should be applied to at least 17% of its volume. Using these values, ε values for a range of W_{200} and W_{400} is calculated for the shale sample from Williston Basin (Figure 12) are shown in Figure 17. A comparison of Figure 17 and Figure 12 shows the obvious decline in epsilon values.

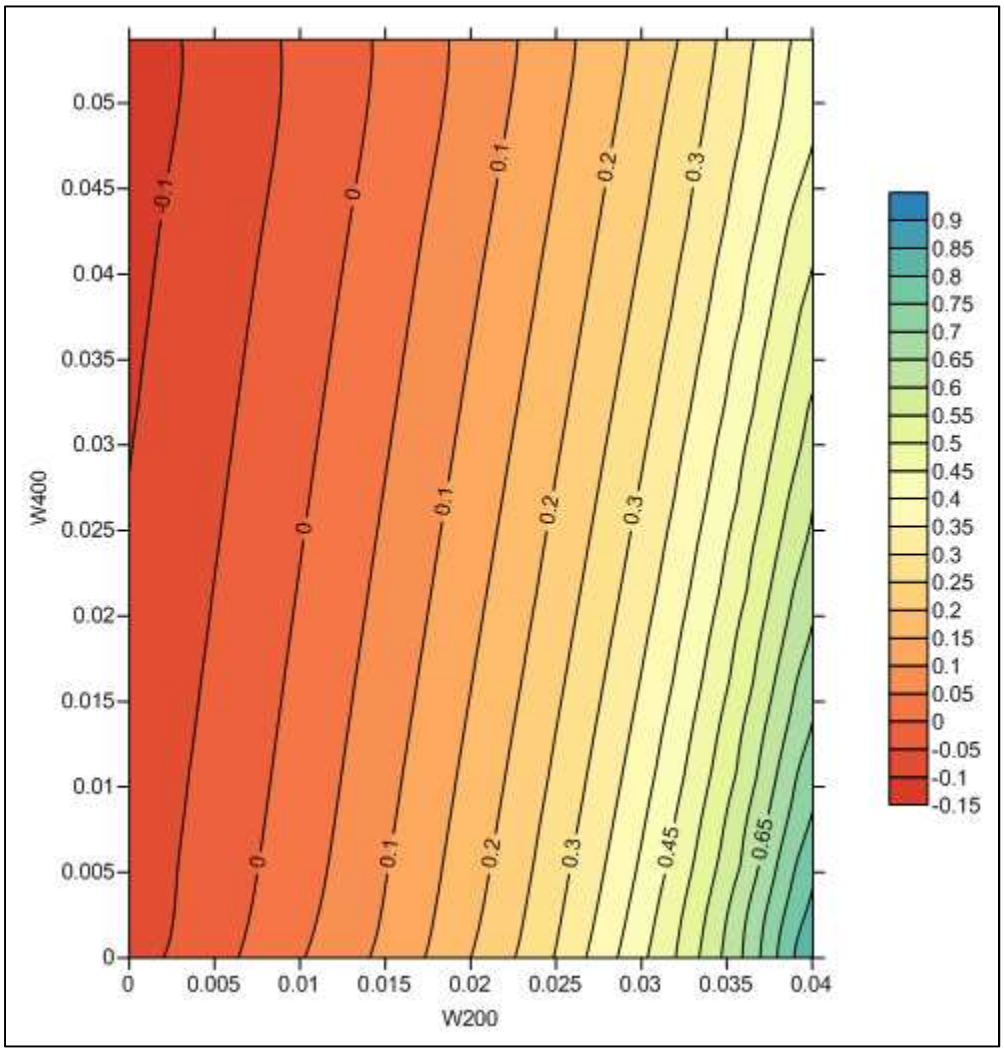

Figure 17. Variations of ε with the orientation parameters W_{200} and W_{400} for the Williston Shale. An excess compliance for B_N/B_T=0.36 is applied for the capillary space. Compare with Figure 12.

Figure 17 reveals some interesting points:

- Introduction of saturation to shales makes a general bulk shift of ε towards lower values. The saturated values are more consistent with seismically measured mean,

median and ranges of ε as suggested by Horne (2013). This observation complies with the fact that shales in are saturated in the basins.

- The reduction in ε is not uniform and is dependent on the B_N/B_T ratio which in turn is related to the capillary radii. Thinner capillary pipes get smaller reduction in their ε values. These smaller reductions happen closer to higher W_{200} regions (green contour fills in Figure 17) which are associated with better oriented shale domains. Therefore better-oriented domains mean less likely presence of capillary pipes (or thinner ones).

In summary, it appears that the presence of wider capillary pore spaces is associated with the relevant excess in the compliance of the shale domains as well as the reduction in the ordered setting of the platelets. Such disturbances seem to have an impact on ε that is one of the seismic properties of a VTI medium. This hypothesis will be tested with the field data in the following chapters.

4 Chapter 4: Case Studies

In order to field test the theoretical foundations that were described in the previous chapter, two well-studied basins in Australia are put forward for this thesis to investigate their sealing characters and its relation with the seismic anisotropy. They are both prolific basins that have been of interest for exploration and development activities and have accumulated significant number of wells, well logs, velocity surveys, seismic data and seal studies. These two areas are the Exmouth Sub-basin within the Carnarvon Basin of offshore Western Australia, and the offshore Gippsland Basin in offshore South Eastern Australia.

4.1 Exmouth Sub-basin

The area of interest is located 45 kilometers north of the city of Exmouth, in the Exmouth Sub-basin, within the overall Carnarvon Basin, NW of Australia (Figure 18). The water depth over the area varies from 250 to over 1000 meters. Exmouth Sub-basin is located in the northern Carnarvon Basin, and has been the subject of a number of studies for seismic anisotropy (Amiri Besheli and Urosevic, 2006). Economic discoveries of hydrocarbon in the area and a number of important producing fields such as Enfield, Muiron and Vincent has historically encouraged the industry to drill numerous wells to test prospective areas.

As a result of years of exploration and production in the area, a considerable amount of data has been accumulated. Case studies conducted on Stybarrow and Enfield show significant anisotropy in the reservoir unit (Amiri Besheli, 2006; Duncan et al., 2013; Glinsky et al., 2005). Attempts have been made to measure the anisotropy of the shale units and subtract their impact on the AVO signature of the reservoir unit (Amiri Besheli, 2006). Several wells drilled in the area have the shale unit assessed for its sealing potential for hydrocarbon (Cruse, 2004a; James, 2004). Such data will provide the calibration and validation points.

4.1.1 Geology

The Exmouth Sub-basin is the southernmost of the four Jurassic rift basins in the Carnarvon Basin (Glinsky et al., 2005). The north-south-trending Triassic high of the Alpha Arch marks the eastern boundary of the Exmouth Sub-basin and separates it from the Barrow Sub-basin (Figure 18). The western margin of the Exmouth Sub-basin is bounded by northeast-southwest-trending Resolution Arch, which separates the sub-basin from the broad, faulted Triassic platform of the Exmouth Plateau (Tindale et al., 1998). Development of the Resolution Arch commenced during the Campanian and was enhanced during the Oligocene and possibly the Miocene. The rapid inversion along the Resolution Arch created a zone of instability, resulting in significant slumping and channeling over the western Exmouth Sub-basin (Scibiorski et al., 2005). Development of this latter structure commenced in the early Santonian and continued into the Oligocene, overprinting, reactivating and causing the erosion of earlier Valanginian structures (Scibiorski et al., 2005; Tindale et al., 1998). To the south of the Novara Arch, the ENE-WSW-trending Ningaloo Arch formed during the Valanginian uplift, reactivating Triassic to Jurassic faults (Figure 18).

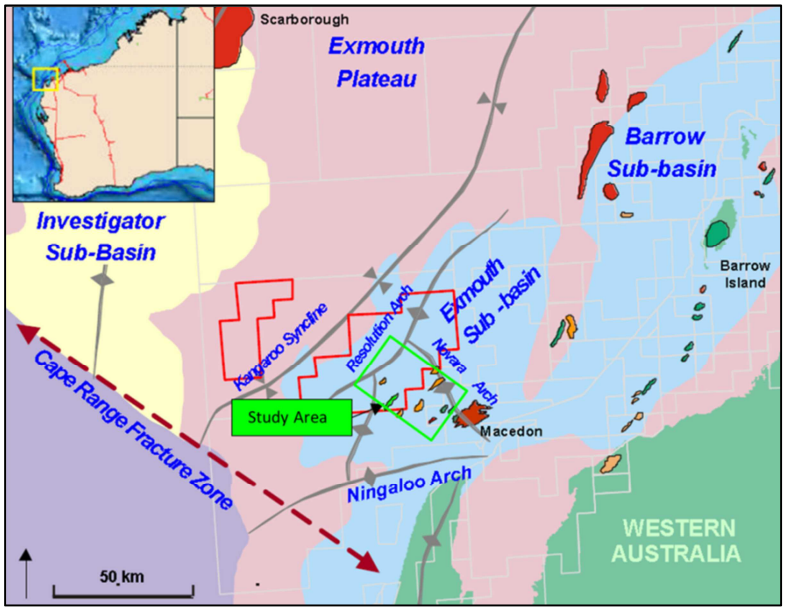

Figure 18. Exmouth Sub-basin location map (after Glinsky et al. (2005)).

4.1.2 Depositional History

Along with the Barrow, Dampier and Beagle sub-basins, the Exmouth Sub-basin formed as a series of NE-SW-trending, en echelon structural depressions during the Pliensbachian to Oxfordian (Tindale et al., 1998). These sub-basins are Jurassic depocentres representing a failed rift system that developed during the early syn-rift phase of breakup of the northwestern Australian continental margin (Longley et al., 2003).

The pre-rift section in the Exmouth Sub-basin consists of a sequence of Permian and Early-to-Middle Triassic sediments. Pennsylvanian (Late Carboniferous) to Early Permian rifting and subsequent Triassic thermal subsidence resulted in the formation of a wide basin. The Locker Shale was deposited in shallow shelf environments during a widespread Early Triassic marine (Longley et al., 2003). The Locker Shale is overlain by a thick succession of mainly fluvio-deltaic to marginal marine sediments of the Mungaroo Formation (Figure 4 of Tindale et al. (1998)).

A narrow basin, formed during the Early-Middle Jurassic rifting between Australia and Greater India, resulted in the deposition in an open marine environment of the Dingo Claystone, the main source rock of the region (Figure 19). Extensional reactivation followed in the Late Jurassic and Early Cretaceous as Greater India separated from Australia. Rift-related uplift to the south of the Exmouth Sub-basin provided the sediment source for the main reservoir units in the area (Bailey et al., 2006). These lie within the Barrow Delta which prograded northward over the Exmouth Sub-basin and the southern and central Exmouth Plateau. The delta had covered the Alpha Arch by the mid-Berriasian (Smith et al, 2003) and extended into the Barrow Sub-basin as far as the southern end of the Gorgon field (Figure 18). NE-SW-trending syn-sedimentary faults affect the Barrow Group sediments and can provide local combined structural and stratigraphic traps.

Continued separation of Greater India from Australia in the Valanginian (Veevers, 1988) is correlated with major structural inversion which resulted in the uplift of the Ningaloo Arch, with associated erosion of the Barrow Group and older Jurassic sediments across much of the sub-basin (Figure 4 and Figure 5a; Tindale et al, 1998). The delta sediments were reworked and re-deposited in the parasitic deltaic wedges of the Zeepaard and Birdrong formations (Figure 4; Arditto, 1993; Tindale et al, 1998). This resulted in the formation of complex trapping architecture within the Late Berriasian arch that extends in a north-northeast direction across the western edge of the sub-basin (e.g., Eskdale structure).

A regional marine transgression during the Hauterivian marked the beginning of thermal relaxation during the post-rift stage, and resulted in the deposition of the main regional seal for the Carnarvon Basin, the Muderong Shale (Figure 19). This formation thins to the south of the study Area where it onlaps the Ningaloo Arch, which was a positive feature at the time of deposition (Tindale et al, 1998). The Muderong Shale is overlain by the Windalia Radiolarite. Above the radiolarite, the Lower Gearle Formation, which consists of a thick sequence of Albian to mid-Cenomanian claystones and siltstones, is deposited in an outer-shelf environment and is considered to be an effective top-seal for some accumulations in the sub-basin (e.g., Pyrenees and Macedon fields; Bailey et al, 2006). Uplift began in the early Santonian and overprinted and reactivated previously formed structures (Tindale et al, 1998).

The latest phase of tectonism is recorded in the Late Miocene by gross tilting of the margin to the west due to progradation of a thick Tertiary carbonate wedge and fault reactivation. During this interval, a renewed phase of compression enhanced the Pyrenees/Macedon structure and is interpreted to have tilted many structures to the south and west and is likely to have modified existing hydrocarbon accumulations (Tindale et al, 1998). The Upper Cretaceous to Holocene passive margin sedimentary

section in the Exmouth Sub-basin is dominated by deep-water fine-grained carbonate, including calcilutite and marl (Figure 19).

A thick (up to 5 km) sequence of deep marine shales (the Locker shale) overlain by a fluvio-deltaic sequence (the Mungaroo Formation) is a typical pre-rift Mesozoic succession in the area (Barber 1982). In the Late Triassic to Early Jurassic, subsidence had become localized, with the development of the Exmouth Sub-basin rift basin. This basin formed in response to two rifting events, the rifting and breaking away of Argo Land north of the Exmouth Plateau in the Early to Mid-Jurassic and the rifting and breaking away of Greater India to the west and south of the Exmouth Plateau in the Early Cretaceous.

During Jurassic basin development, predominantly fine-grained, deep water deposition occurred, and by the end of the Jurassic and the first rift phase, a remnant basin topography remained. The Barrow Delta was then deposited from the south filling the Exmouth and Barrow Sub-basins. The Early Cretaceous rifting then inverted the Exmouth Sub-basin. Post-rift sedimentation was effectively terminated in the late Berriasian as the Indian Plate finally separated from Western Australia. This caused the sequence boundary of the Early Cretaceous.

By the end of the Berriasian the Barrow delta had built out to a roughly east-west front and was substantially eroded on the Arch, and across the Long Island Fault System (Arditto 1993). With clastic input decreased, the whole delta top was subsequently reworked to form the thin, highly glauconitic, shallow marine Mardie Greensand Member of the Muderong Formation (Stybarrow 1, well completion report).

The Barrow group is target zone for exploration and development in the area, with several field produce hydrocarbon from it. Within the Barrow group the deep-water turbidites called the Macedon sandstone have been proved to be holding hydrocarbons. The Macedon sandstone is generally sealed by the Macedon Shale (or Muiron member) of the Barrow Group.

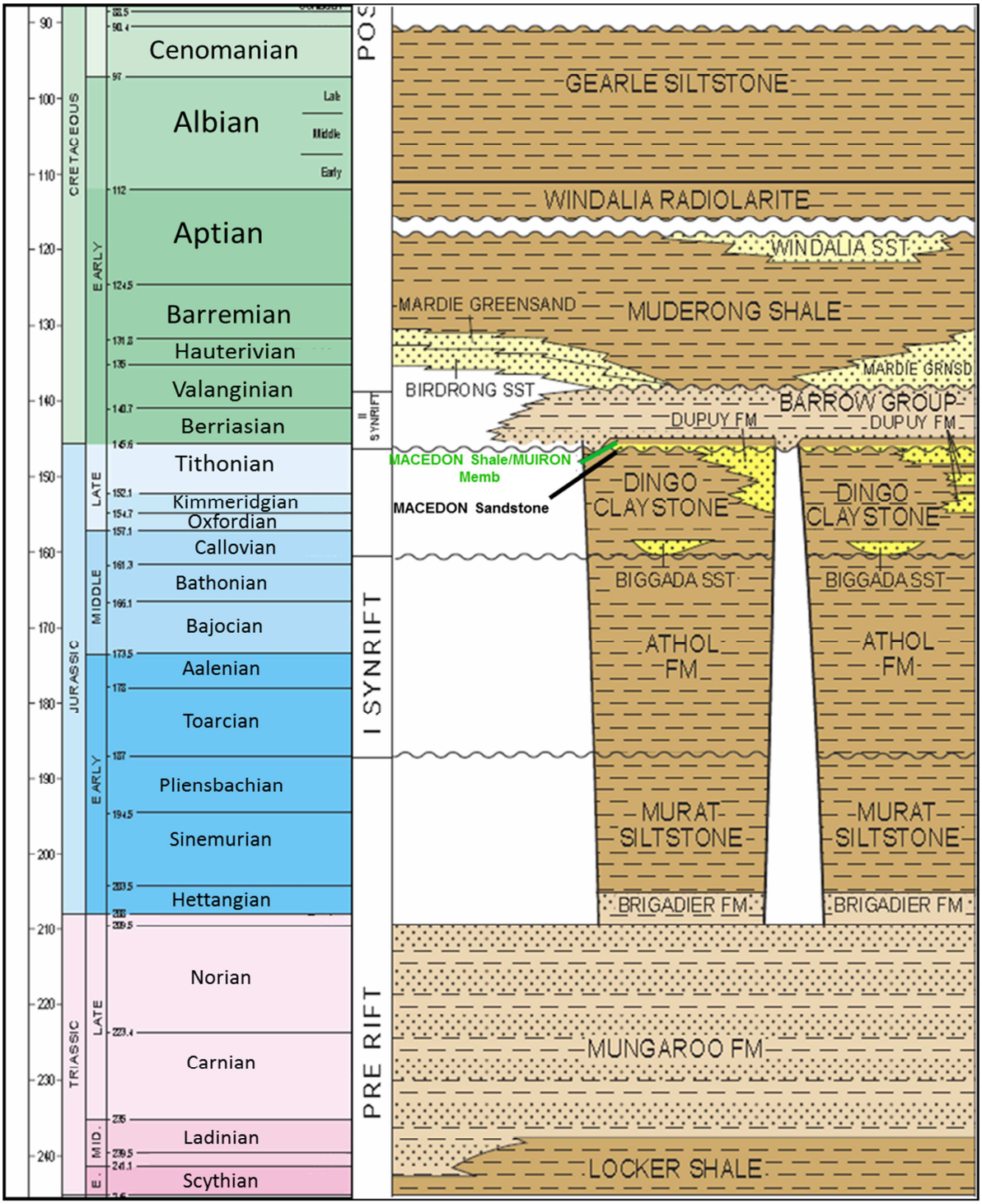

Figure 19. Stratigraphic column of Exmouth sub-basinn for Late Jurassic to Late Cretaceous (after Woodside 1999)

4.1.3 Data

Five seismic cubes exist in the area of study, Vincent 3D, HA2002, Enfield 4D, HC93 and Vincent 4D. Two of these volumes were the primary source of seismic for the interpretation stage (Vincent 3D and HCA2002) since they cover the majority of the area of the study. The south-eastern corner of the study area is covered by HC93. Enfield 4D and Vincent 4D volumes are dedicated seismic data to explored fields and overprint Vincent 3D and HCA202. (Figure 20)

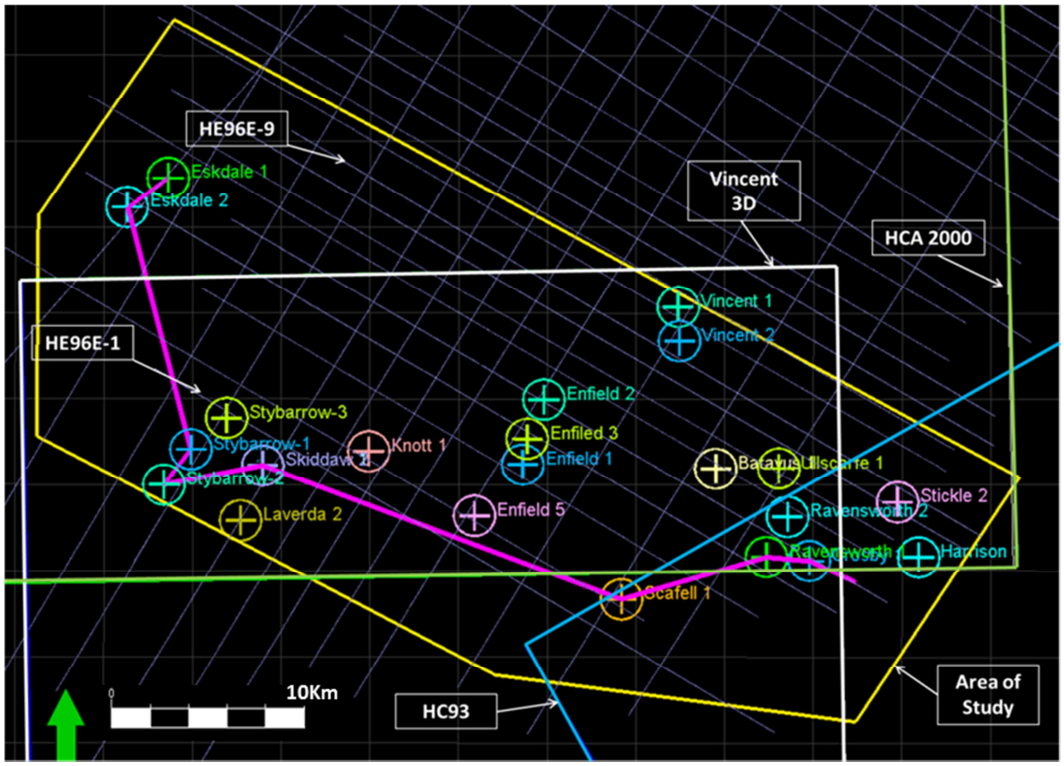

Figure 20 The location of seismic surveys, the area of study (yellow polygon) and cross section (pink line).

4.1.3.1 Seal

The two well-studied seal in the area of study are the Muderong Shale and the Macedon/Muiron member of the Barrow Group. The Muderong shale comprises the regional top seal in the Northern Carnarvon Basin (Longley, et al., 2002). It is the result of post-rift transgressional sea deposition in the deep marine environment (Westpahal and Aigner 1997). The thickness of Muderong

shale varies between 5 and 70 meters in the area of study. However, its thickness can reach 800m in the Carnarvon basin.

The geomechanical properties of the Muderong Shale have been studied by Dewhurst and Hennig (2003). Their study reveals that although the shale samples were weak in their cohesive strength (2.75MPa and a coefficient of friction of 0.34 – on the plot of Mohr envelope) relative to other rock types, they were not at the risk of developing fractures that could lead to seal failure. In fact, the in-situ effective stress was shown to be well below the Mohr stress failure criteria.

Underneath the Muderong shale lies the Barrow Group, a deltaic sequence that hosts one of the prolific reservoirs of the Carnarvon Basin. As is usual for deltaic sequences, the Barrow Group is comprised of local members and formations that form reservoir and seal combinations. Two members of the deltaic Barrow sequence are the Macedon sandstone and the Macedon shale (also known as Muiron member). Macedon sandstones are one of primary targets in the area of study and form the producing reservoir of the Stybarrow and Enfield fields.

4.1.3.2 Seal geometry

The Vincent field to the north of the area of study depicts a typical section of the Muderong shale. Vincent-1 encountered just over 17^{m} of the Muderong shale and registered an oil and gas column in the lower Barrow reservoir. The Muderong Formation maintains more or less the same thickness across the area of study (Figure 21). Although the Muderong Shale is the prominent top seal for the Barrow Group, it is not the only sealing component. The Windalia Radiolarite and Gearle Siltstone can act as secondary (or even primary seals) for top Lower Barrow reservoirs (Cruse, 2004b; Willis, 1999). Figure 22 shows the thin layer of the Muderong Formation that acts as the top seal of the Barrow reservoir at the Vincent field.

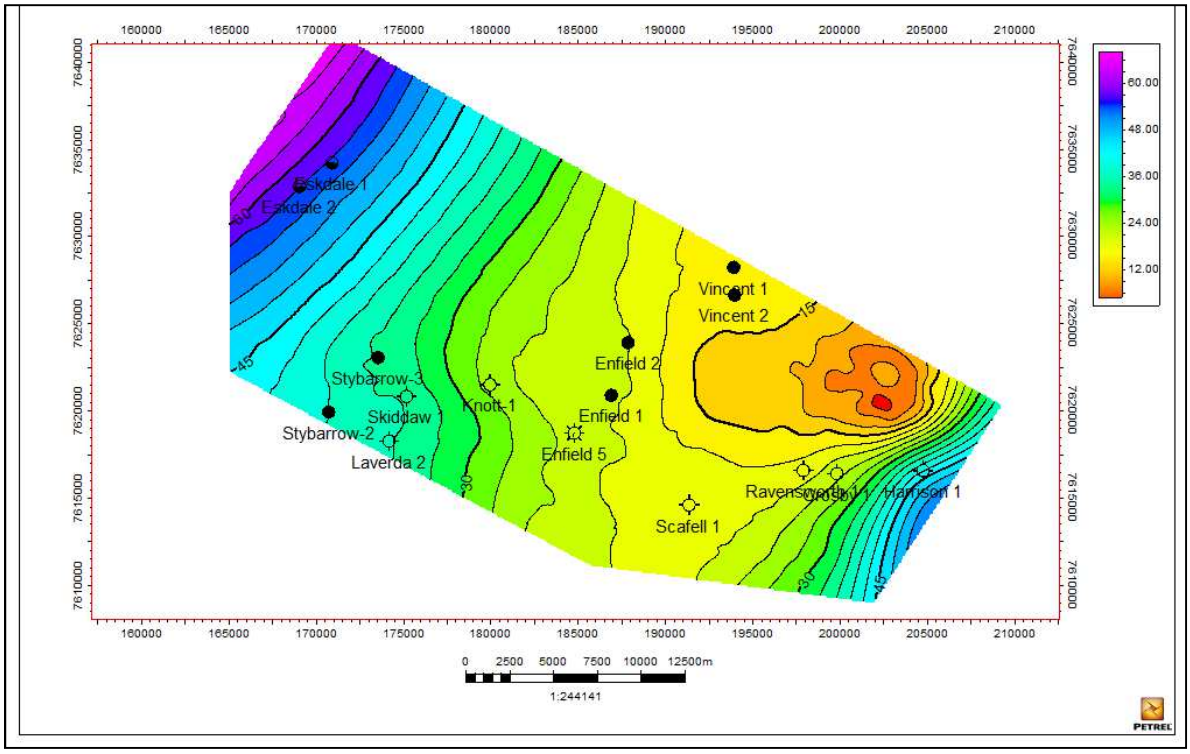

Figure 21. Isochron of the Muderong shale in the area of study reveals two mild depo centers to the SE and NW.

Faults are dominant features within the Late Jurassic and Early Cretaceous sediments, sometimes re-activated later in the tectonic history and penetrating through the Muderong and Gearle Siltstone package (Figure 22). This certainly adds to the risk of cross-fault sealing capability of the Muderong shale in the area of study should it be the sole sealing sequence. However, as mentioned above, the Gearle silts are competent enough (at least locally) to provide an average seal for reservoirs that contain small columns of hydrocarbon (BHP Billiton, 2004).

Furthermore, the offset of the faults that penetrated the Muderong shale is minimal compared to the largest offset of the same faults. Therefore, cross-fault leakage is unlikely as the good quality sands of the Barrow Group are juxtaposed against the Muderong shales or Gearle Silts.

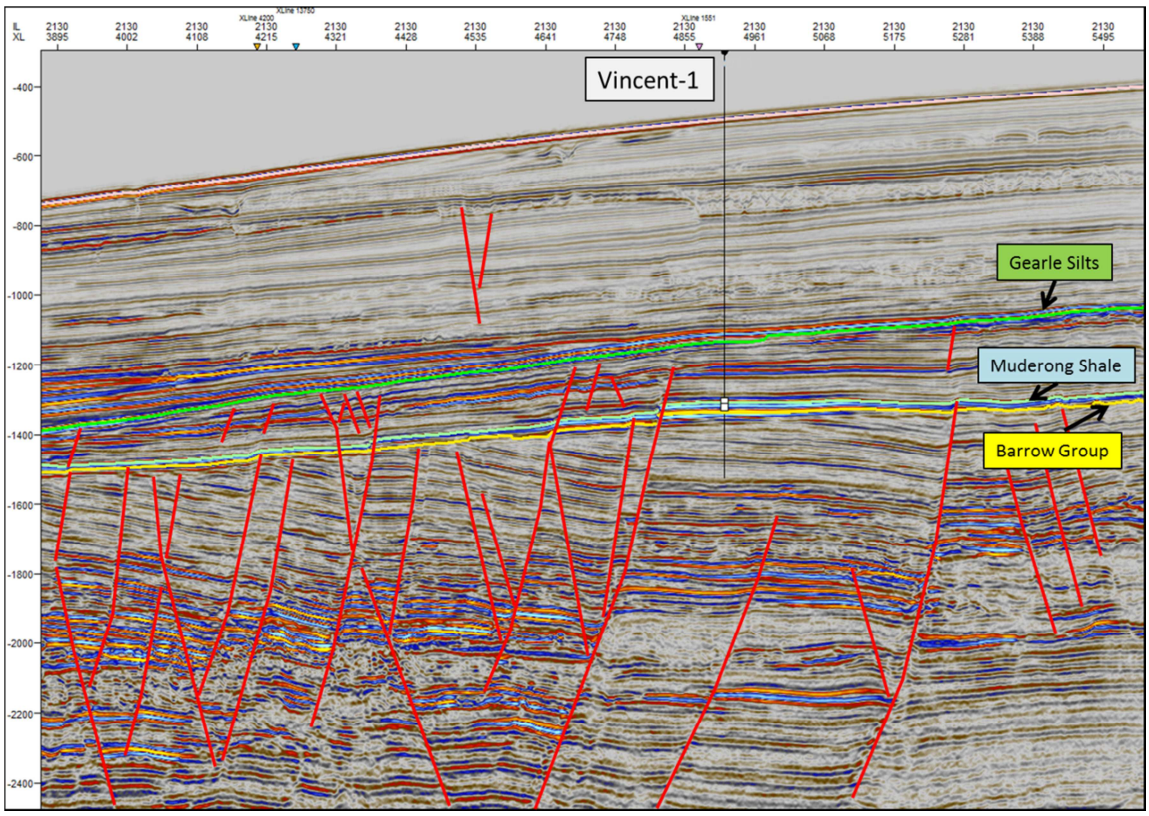

Figure 22. Inline 2130 of the Vincent 3D that is nearby Vincent-1 well. Interpretation shows a thin layer of Muderong Shale sealing the Lower Barrow reservoir sands. The early Cretaceous tectonic activities is manifested by extensional faults.

An important intra-formational seal in the area of study is the Macedon Shale (Muiron Member). It is identified by an increase on the gamma-ray log, and is composed of yellowish-grey to grey silty claystone. The bland seismic character on top of the outstanding strong reflection for the Macedon sands is an indication of the soft and shaley character of this zone (Figure 23). The Early Cretaceous sediments are heavily faulted due to the extensional rift tectonics. The faults breach the thickness of the Macedon shale and offset the blocks for tens of meters. This causes compartmentalization of reservoir zones and juxtaposition of reservoir sands against poorer quality seals.

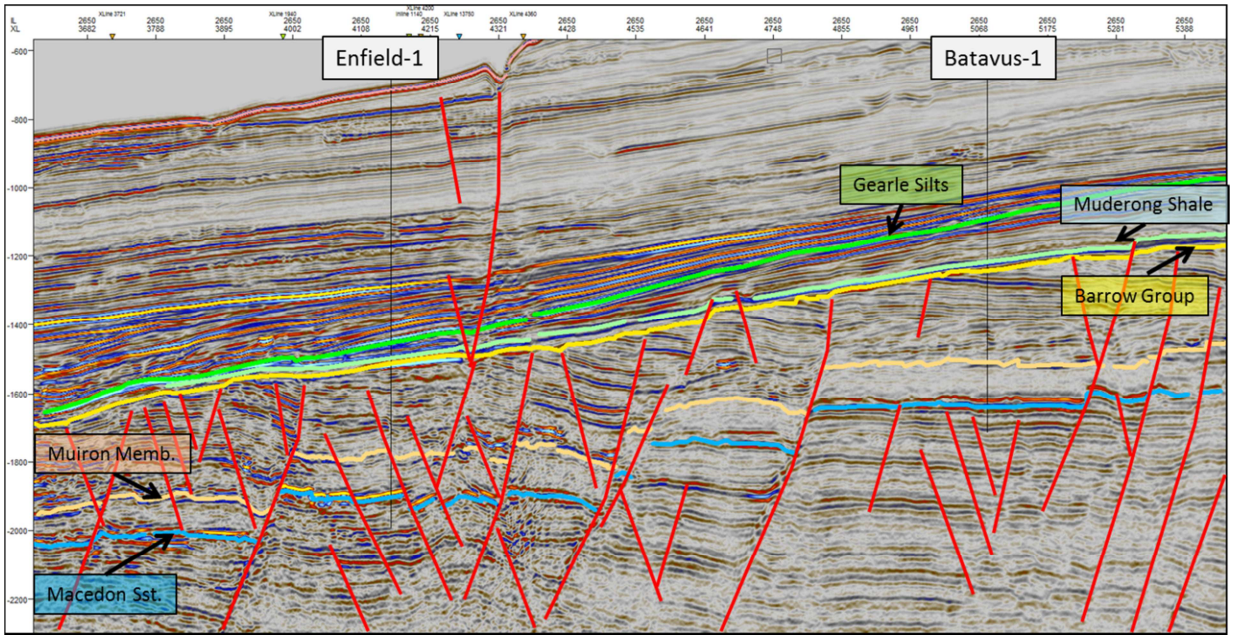

Figure 23. Inline 2650 of the Vincent 3D. The primary reservoir and seal units for Enfield are intra-formational members of Macedon sst and shale. Note the relative characterless seismic signature of the Muiron member in comparison to the underlying Macedon Sandstone.

Unlike the nearly constant thickness of the Muderong shale, the Muiron Member varies in thickness across the area of study (Figure 24). Both stratigraphic and tectonic factors contribute to such variation. The NE-SW stripes of almost zero thickness are caused by the extensional faulting that offsets the Muiron member against the younger units.

Although the seismic character of the Barrow Group clearly depicts the deltaic origin of the sediments (including the Macedon shale), the stratigraphic thickness change is not only caused by wedging out. Underlying tectonic uplifting to the south and erosion of the top Barrow group on the local high caused the stripping of the Muiron member (Figure 24). Such areas are high risk in terms of the geometry of the seal.

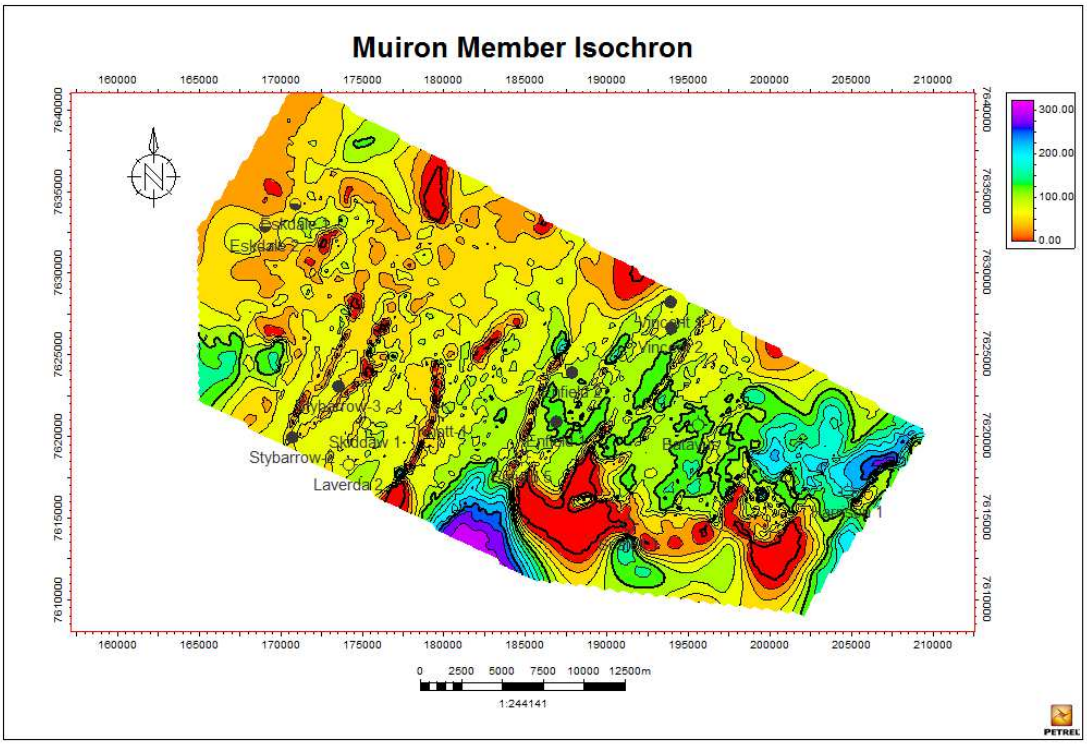

Figure 24. Time thickness map of the Macedon shale shows a wide range of variation across the area of study. The NE-SW trending streaks of near-zero thickness areas are the result of faults. Some thin (high risked) seal coverage can be seen towards the south and southeast.

Despite the wide variation in its thickness, the Muiron Member provides a competent seal in terms of seal geometry, as it benefits from reasonably high thickness within the fault blocks. Presence of commercial hydrocarbons in the area of study (such as Stybarrow and Enfield) is evidence to the working top seal and petroleum system.

4.1.3.3 Seal capacity

Seal capacity that reflects the difficulty that any type of fluid (typically hydrocarbons) will face to penetrate and run though the rock is related to its capillary pressure. Mercury injection tests are conducted on the rock samples to measure the pressure at which the rock leaks. The value at saturation 7.5% (of non-wetting phase) is often used to indicate the point where the hydrocarbon phase in the seal rock is continuous enough to cause the seal to leak (Sneider et al., 1997).

The two sealing sequences that are identified in the Exmouth Sub-basin (Muderong/Windalia formations and the Muiron member of the Barrow group) are sampled for MICP tests. There are 82 samples of P_c from 9 wells spread across the area (Table 3). Since the primary target and the producing reservoir in the area of study was the Macedon sandstone, its sealing unit (Muiron member) was sampled more frequently. However, there are some MICP samples and its relevant petrographic studies that can provide insight to the behavior of the Muderong shale sealing sequence.

Well Name	Number of Samples
Eskdale-1	13
Eskdale-2	8
Stybarrow-1	18
Stybarrow-2	1
Skiddaw-1	8
Skiddaw-2	4
Scafell-1	14
Ravensworth-1	10
Crosby-1	6

Table 3. Mercury injection samples for each well in the area of study.

The sequence that provides the top seal for the Barrow reservoir consists of the Windalia Radiolarite and the Gearle Siltstone. A typical sealing capacity measurement from the Windalia formation was performed on the sample from Crosby-1, a radiolarite with siliceous skeletons (Figure 25), which was tested to be very impervious (permeability of 0.455 mD) and provided the highest seal capacity among the samples from this well (Cruse, 2004b). The reported mercury pressure at 7.5% saturation is reported to be 355^{psi}. This is still a class C seal in Sneider's classification.

Other samples from the Muderong shale in the area of study provide even higher seal capacity measurements. The highest measured figure belongs to Eskdale-1 with 2646^{psi}. It is interesting to note that samples that are taken from meters away from each other in a particular well sometimes report a very different threshold pressure, as is the case among the samples of Muderong shale in Eskdale-1.

The Gearle Formation proves to be an important seal, as the sample from Ravensworth-1 measures one of the highest readings of mercury pressure for the sealing threshold (reading 3204 psi at 7.5% saturation). The sample is a claystone that shows a uniform and mild alignment of grains along the bedding. Most of the clay-rich matrix is composed of mica flakes (Figure 26).

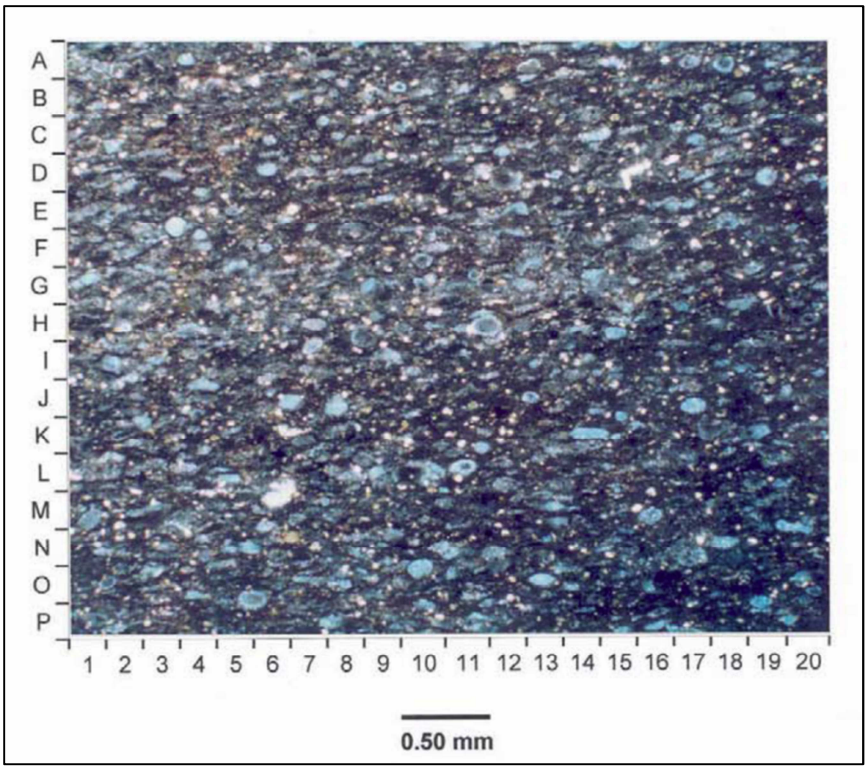

Figure 25. A sample from the Windalia Radiolarite formation under microscope. Skeletons of radiolarian (light blue circular to oval particles) sets in an argillaceous matrix. Silt size quartz particles are white (Cruse, 2004b).

Due to the higher number of samples that were taken from the Macedon shale, higher weight is given to the modelling of its sealing capacity. Furthermore, the clay-rich Muiron member is a thicker sequence compared to the Muderong shale (Figure 24 and Figure 21).

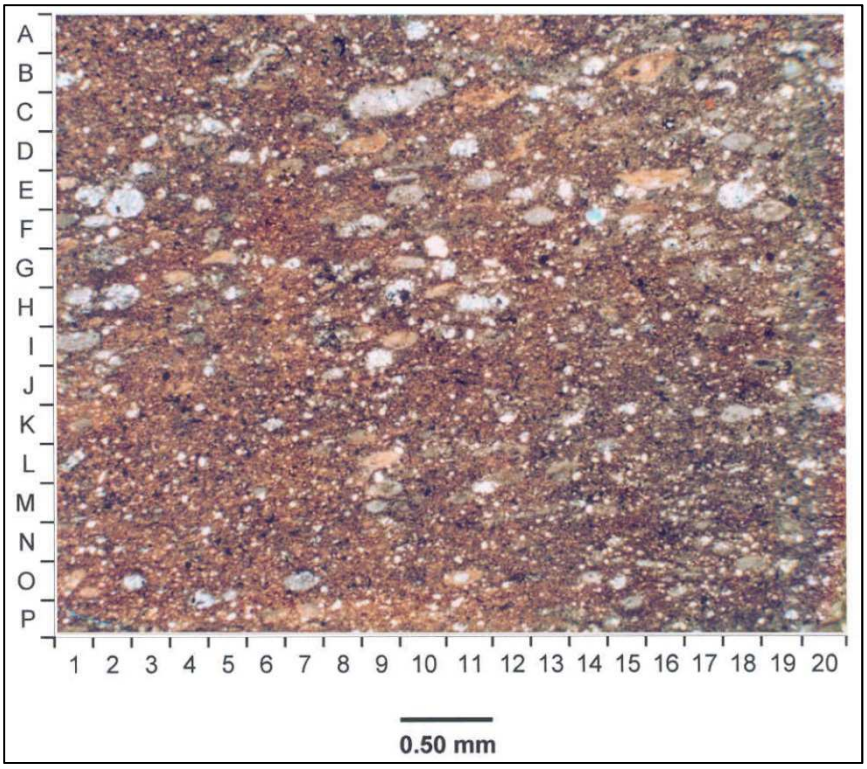

Figure 26. A clay-rich sample of the Gearle formation under microscope. The sample was taken from Ravenworth-1. Sand-sized glauconite are mostly oxidized to brownish colour. Pyrite particles are black and pore spaces are blue.

It is typical of sealing sequences, especially if they are of deltaic origin, that their sealing capacity varies among the samples of a single well. The deltaic environment is active and relatively high-energy, with shaley particles deposited in different dynamic conditions, causing some variations in their sealing potential. Furthermore, there is no guarantee that each sample is taken from the same exactly chronologically equivalent shale across the field. As the delta progresses/regresses, the dynamics of deposition vary over a certain point. Therefore, the sediments that are stacked on top of each other will have different sealing capacities.

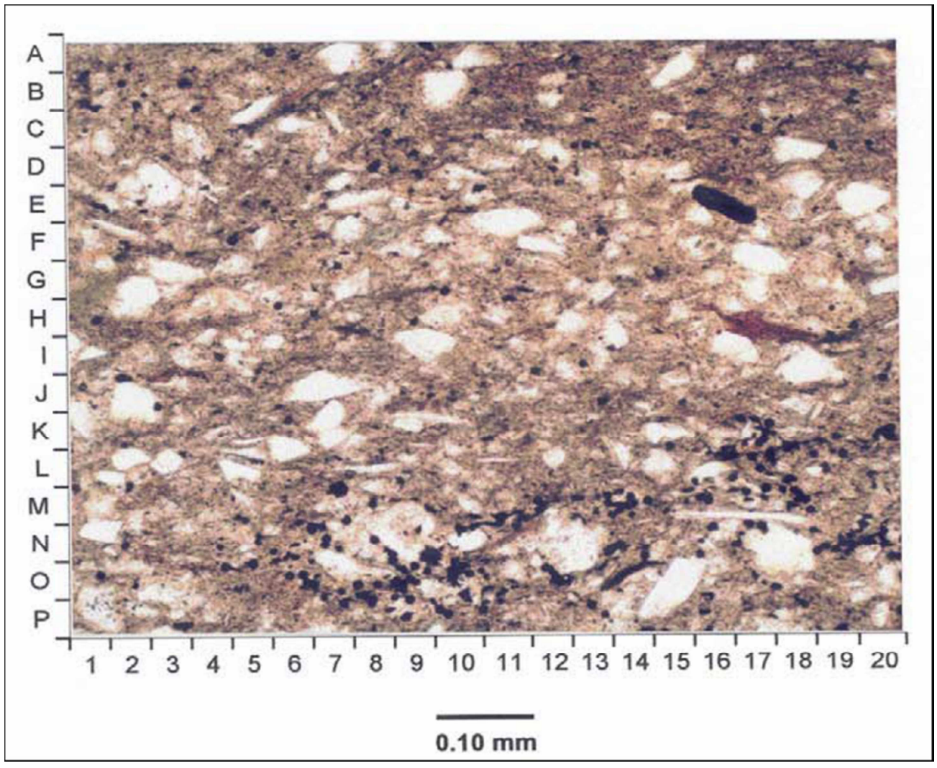

Figure 27. Photomicrograph of a shale sample from Eskdale-1. It belong to the very bottom of Muiron member just right on top of Macedon sand. Lamination and orientation of clay particles (even silts) is obvious. The matrix is clay with small black particles representing pyrite. Elongate mica particles are also visible (James, 2004).

The Muiron Member samples are generally bioturbated argillaceous silty claystones that were deposited at the distal end of the "Macedon Delta" (Cruse, 2004a; James, 2004). The samples are normally brownish to olive-grey with moderate sorting.

Such variation in sealing capacity is observed among the samples that are taken from Muiron Member in the Eskdale-1 (Figure 28). The range varies from 359^{psi} to 2070^{psi} which equates to 40m to 231m of a typical gas column in the area. However, this is enough evidence that the seal over the Eskdale-1 is competent enough (in terms of capacity) to hold a large hydrocarbon column. The lack of hydrocarbons should be explained through other mechanisms such as cross-fault leakage or biodegradation.

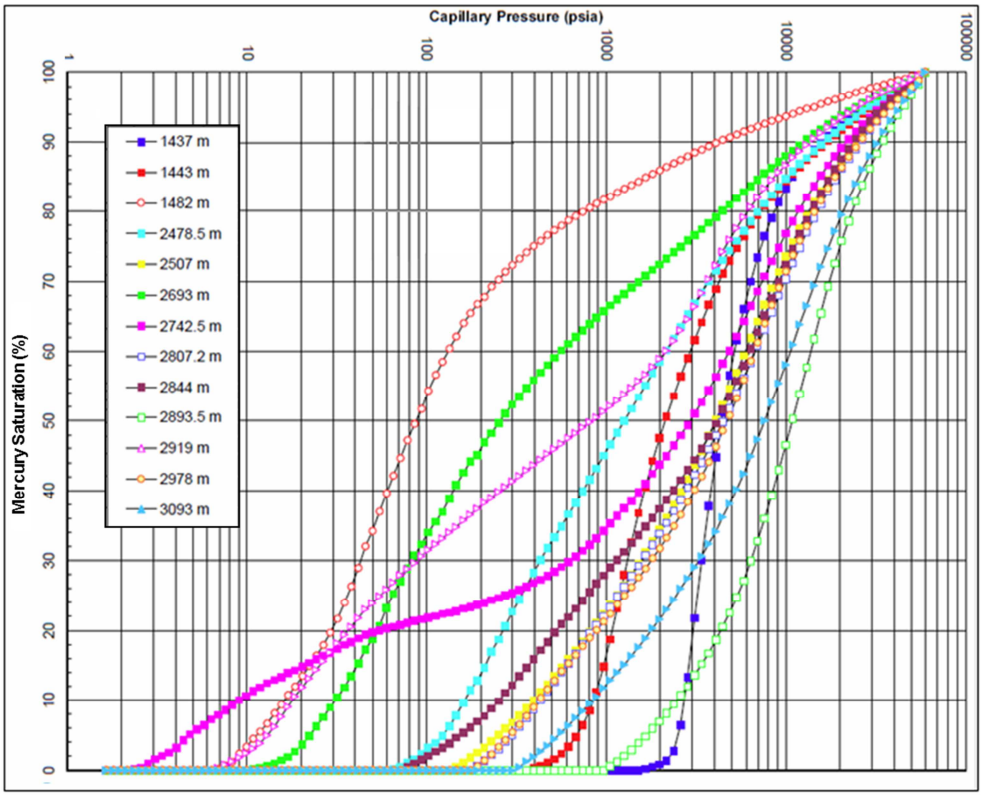

Figure 28. MICP measurements on samples from Eskdale-1. The Muiron Member samples are taken from 2807m to 2893m in depth.

Interestingly, the samples that have seal capacity values close to each other appear to be similar in the degree of alignment of their particles (Figure 29). The general amount of non-shale particles is roughly the same, which explains the nuclei that create openings close to them. These opened-up microscopic spaces are the reasons siltier shales can have lower breakthrough/threshold capillary pressure (Sneider et al., 1997).

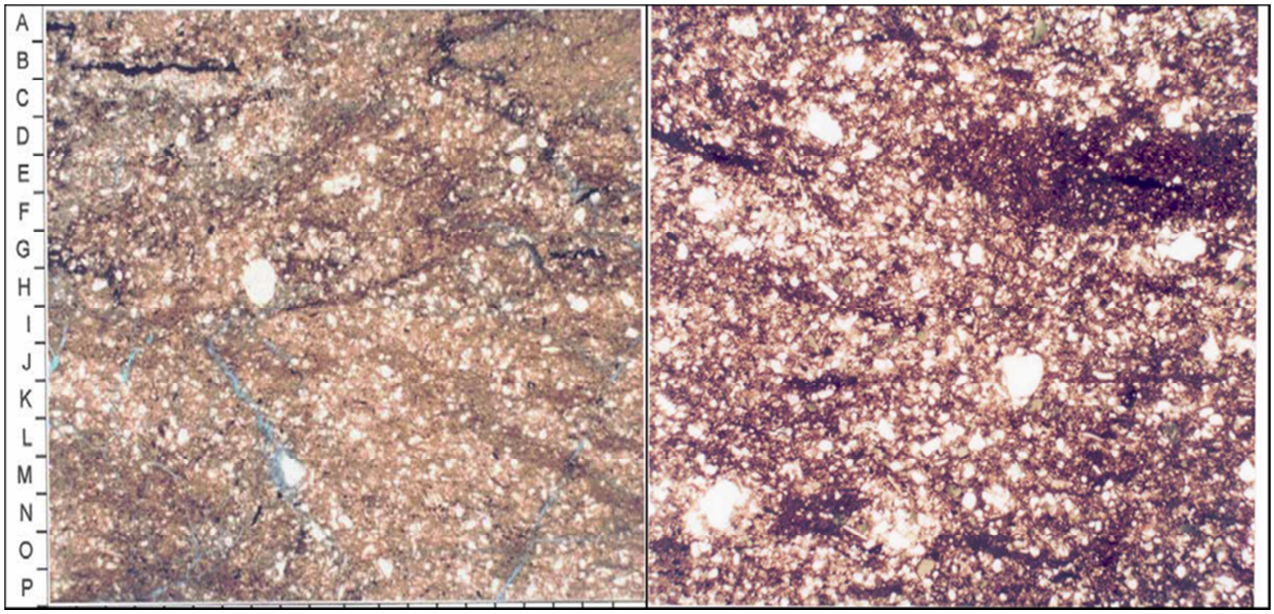

Figure 29. Comparison of the samples of Muiron Member from Eskdale-1 (left) and Skidaw-1 (right). Both samples have the similar sealing capacity.

4.2 Gippsland Basin

The Gippsland Basin is located approximately 200 km east of Melbourne, Victoria, in south-eastern Australia (Figure 30). The basin has both onshore and offshore elements. Large oil and gas fields are located in the offshore portion of the basin. In the Latrobe Valley onshore, extensive deposits of brown coal are present and these are used to supply the majority of the State's electricity.

Due to its prolific nature, this basin has been the subject of multiple studies. A recent trend in the Australian energy industry focused on the CO_2 sequestration. The CarbonNet project was established to investigate the potential of the Gippsland Basin for carbon capture and storage (CCS). Targeted seismic surveys were shot in the southern Gippsland area and mercury injection tests were conducted on selected wells to evaluate the sealing potential of Lakes Entrance Formation. Such historical accumulation of geological and geophysical data helps establish a good background to investigate the relationship between the sealing potential and anisotropy of the sediments.

The vast majority of the discoveries are reservoired within the siliciclastics of the Late Cretaceous to Palaeogene Latrobe Group, and almost all of the currently producing fields are located offshore in shallow water (at depths of less than approximately 100 m). Onshore, the Wombat, North Seaspray and Gangell gas fields within the Seaspray Depression are reservoired in the older Strzelecki Group. The area of study for this part of the project is the southern offshore Gippsland that is covered by a recent 2D seismic survey.

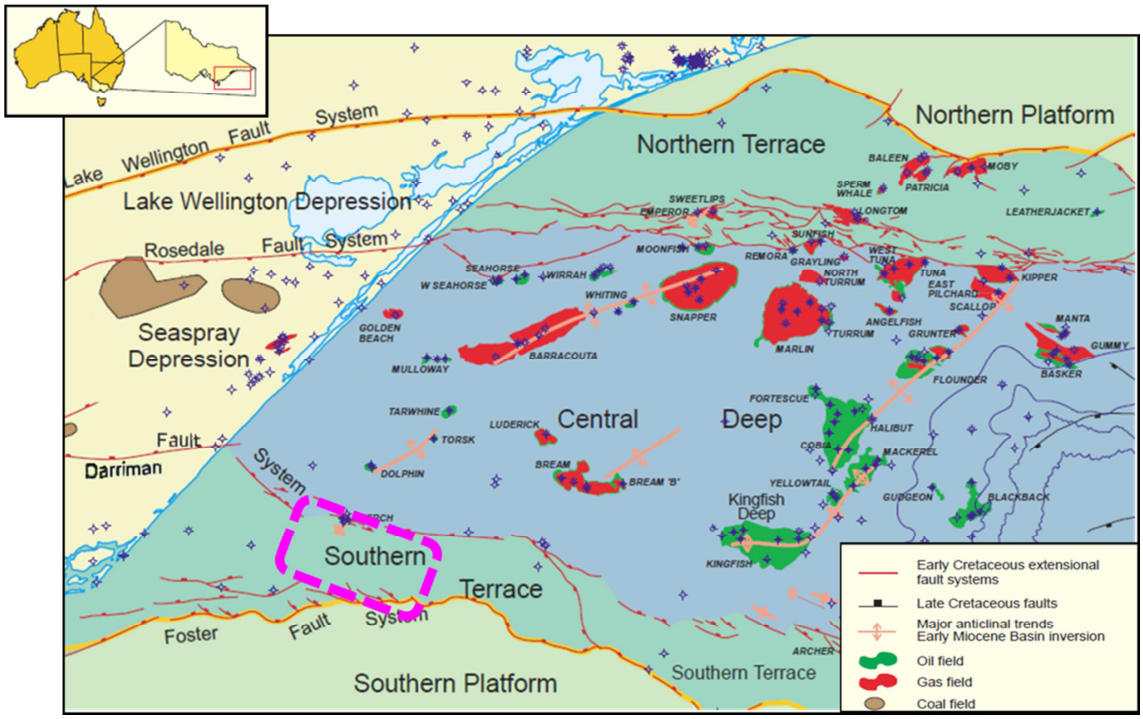

Figure 30. The Gippsland basin (modified after Goldie Divko et al. (2010b)) is shaded in yellow. The dashed purple square marks the area of interest for the seal capacity analysis.

4.2.1 Geology

The Gippsland Basin is an east-west trending feature that formed as a consequence of the break-up of Gondwana in the Mesozoic (Norvick et al., 2001; Rahmanian et al., 1990). The basin's evolution is recorded by three major depositional sequences ranging from Early Cretaceous to Recent in age, and the overall tectonic control on the sedimentary systems of the basin is manifested by a series

of angular unconformities. Extension was directed approximately north-south, with the rift system extending along the southern margin with NW to NE trending growth-faults bounding the half-grabens. Gippsland faults trend NE to E-W and control deposition of the Strzelecki Group. Faulting gradually waned towards the end of the period, and regional subsidence or sag dominated the tectonics. A short episode of folding may have occurred just before the next phase of extension.

E-W extension along what became the present-day east coast of the continent eventually led to sea floor spreading and creation of the Tasman Sea. Extension was most likely accompanied by N-S to NNE trending faulting and regional uplift (Duddy & Green, 1992) along the east coast of Tasmania (Figure 33), the eastern portion of the Early Cretaceous Gippsland Basin and the coast of NSW.

Regional NE-SW directed extension, accompanied by WNW- to NW-trending faults, led to the formation of the Otway and Sorell Basins in western Victoria and along the west coast of Tasmania, the Bass Basin between Tasmania and Victoria, and the present offshore portion of the Gippsland Basin. The coincidence of this extension and subsidence related to the beginning of Tasman Sea spreading resulted in transgression into the Gippsland Basin and deposition of the Latrobe Group.

A second phase of rifting occurred from the Late Cretaceous to Eocene, associated principally with Tasman Sea spreading, and this produced a classic extensional basin geometry comprising a depocentre (the Central Deep) flanked by platforms and terraces to the north and south. The Darriman and Foster fault systems on the southern basin margin, and the Rosedale and Lake Wellington fault systems on the northern margin, define these areas. The onshore basin architecture is comprised of the Alberton, Seaspray and Lake Wellington (including the Latrobe Valley) depressions, which are the onshore extensions of the Central Deep, Northern Terrace and Southern Terrace respectively, and the Lakes Entrance Platform to the north of the Lake Wellington Fault System. In the west of the basin, a

compressional event uplifted the Strzelecki Group to form the Narracan and Balook blocks, which now form the Strzelecki Ranges (Bernecker and Partridge, 2001).

The second phase of rifting provided the accommodation space within which the Latrobe Group was deposited. This rifting phase was punctuated by a series of minor uplift events that led to the development of local unconformities (those recognised between the four subgroups of the Latrobe Group - the Emperor, Golden Beach, Halibut and Cobia subgroups), followed by a period of drift. The Baragwanath Anticline and related structural fabric of the prominent NE to ENE-trending anticlines (Smith, 1988), which form the main hydrocarbon traps offshore, developed as a result of Late Eocene uplift and compression. The regional sealing facies of the Oligocene Seaspray Group was deposited during the post-rift sag phase following the conclusion of Tasman Sea rifting in the Eocene and the onset of rapid seafloor spreading between Australia and Antarctica.

During Early-Mid Tertiary there was continued subsidence and transgression in the Gippsland Basin. Possible pulses of NW-SE directed compression in the Early Eocene and Oligocene, lead to structural inversion along NE-trending normal faults. Major NW-SE directed compression resulted in the growth of anticlines related to inversion of mainly NE to E-W trending Early Cretaceous growth faults during the Mid to Late Miocene. There was continued deposition of coal measures onshore, partly controlled by the shoreline position and the growing folds (Norvick et al., 2001). Tectonism has continued to overprint the basin as documented by localized uplift during the Late Pliocene to Pleistocene. This is also reflected in the uplift of Pliocene sediments on the Barracouta, Snapper and Marlin anticlines, as well as around Lakes Entrance.

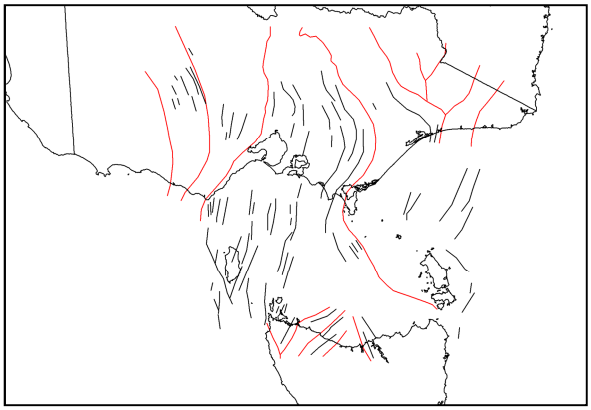

Basement Boundaries and Trends

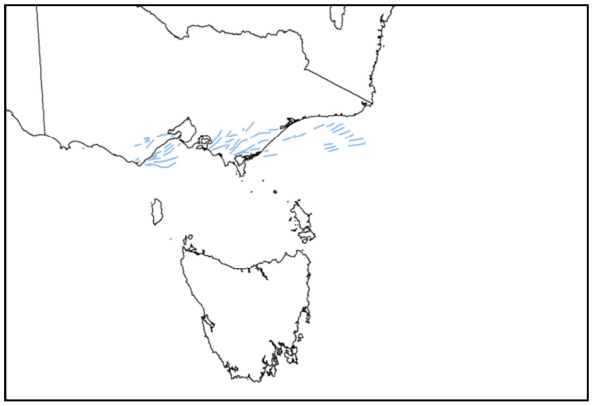

Early Cretaceous Normal Faults

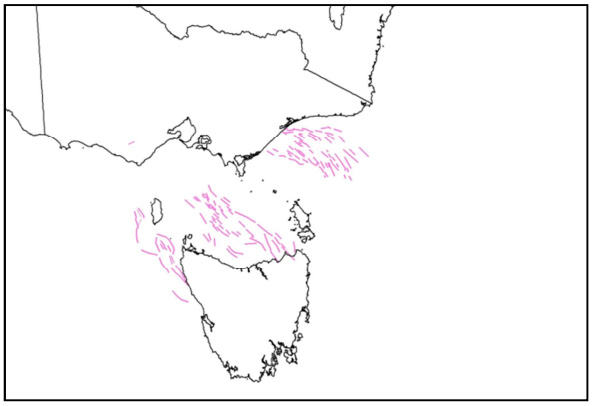

Late Cretaceous Normal Faults

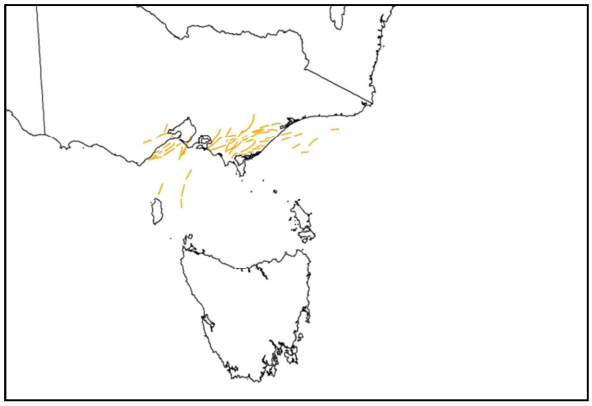

Late Tertiary Reverse Faults

Figure 31. A series of diagrams showing the types of faults present within the Torquay, Bass and Gippsland Basins during the Early Cretaceous to the Tertiary (3D-Geo internal client report-used by permission, (Goldie Divko et al., 2009b; Norvick et al., 2001; Ruth et al., 2006)).

4.2.2 Stratigraphy

The sediments in the Gippsland Basin consist of the Early Cretaceous Strzelecki Group, the Late Cretaceous to Tertiary Latrobe Group and the Tertiary Seaspray Group (Figure 32).

Basement has not been encountered within the Central Deep of the Gippsland Basin, but has been drilled along the northern and southern terraces where it is either granite or folded Devonian metasediments. The undrilled basement under the central part of the Gippsland Basin is presumed to be similar. Basement is generally recognised by fast sonic and/or high density values, whether granite or metasediments, although a weathered zone of intermediate values may overlie basement.

The *Strzelecki* Group is mostly non-reservoir volcaniclastic fluvial sediments but contains quartzose potential reservoirs in places (Holdgate and Mcnichol, 1992). The Strzelecki is mainly Early Cretaceous, but may be Late Jurassic at its base. It consists of fine-to-medium-grained volcaniclastic sandstones, claystones and some coals. The sandstones are fluvial, deposited by meandering to braided rivers subject to major floods, and the claystones were deposited on floodplains where soils developed under widespread forests. The stratigraphy of the Strzelecki Group is based on spore-pollen palynology (Constantine, 2001) because most of the sediment is non-marine.

The *Latrobe* Group is mostly fluvial to coastal sediments, consisting of quartzose reservoir sandstones interbedded with coals and carbonaceous claystones, but also includes shallow-marine glauconitic sediments deposited seawards of the coast forming a transgressive veneer over the non-marine parts of the Latrobe Group. The Top-Latrobe unconformity is a composite surface made up of local ravinement surfaces formed during the transgressive deposition of the Latrobe Group. The Latrobe Group has been divided into the Emperor, Golden Beach, Halibut and Cobia subgroups (Partridge et al., 2012). The subgroups have been identified from biostratigraphy, though there are also some mineralogical differences. The original definitions indicate that the subgroups are separated by basin-wide unconformities, but it is also possible that unconformities exist only along the basin margins and over the hydrocarbon fields which have been periodically uplifted with erosion or non-deposition.

The regional sealing facies of the Oligocene *Seaspray* Group is mostly marine sealing claystones overlain by bioclastic limestones, but includes coastal sandstones and fluvial sediments with coals in the Latrobe Depression onshore. It consists of lower coastal plain, coastal and marine portions, with the coastal zone under the present onshore. The lower coastal plain portion is the Latrobe Valley Subgroup which is similar to the Halibut and Cobia Subgroups of the Latrobe Group but contains thicker coals. The coastal sandstones belong to the Balook Formation. The marine portion consists mainly of the Lakes Entrance Formation overlain by the Gippsland Limestone and extends from the present day onshore to the offshore.

The Lakes Entrance Formation is widely recognized as the sealing unit in the offshore Gippsland basin (Goldie Divko et al., 2010a; Partridge et al., 2012; Rahmanian et al., 1990). However, the Lakes Entrance Formation itself is a representative term for the top seal and its stratigraphy is more complex. Partridge et al. (2012) introduced the the Bassian Rise units within the general Lakes Entrance Formation and Seaspray Group. Along with the Early Oligocene Wedge (EOW), the fifth (and oldest) Bassian Rise Unit (BR5) forms the top seal for the offshore Gippsland. The EOW has a prominent presence in the southern platform of the Gippsland Basin (Blevin et al., 2013) and is distinguished from the top BR5 (top Late Oligocene) which represents the top Lakes Entrance (Figure 32).

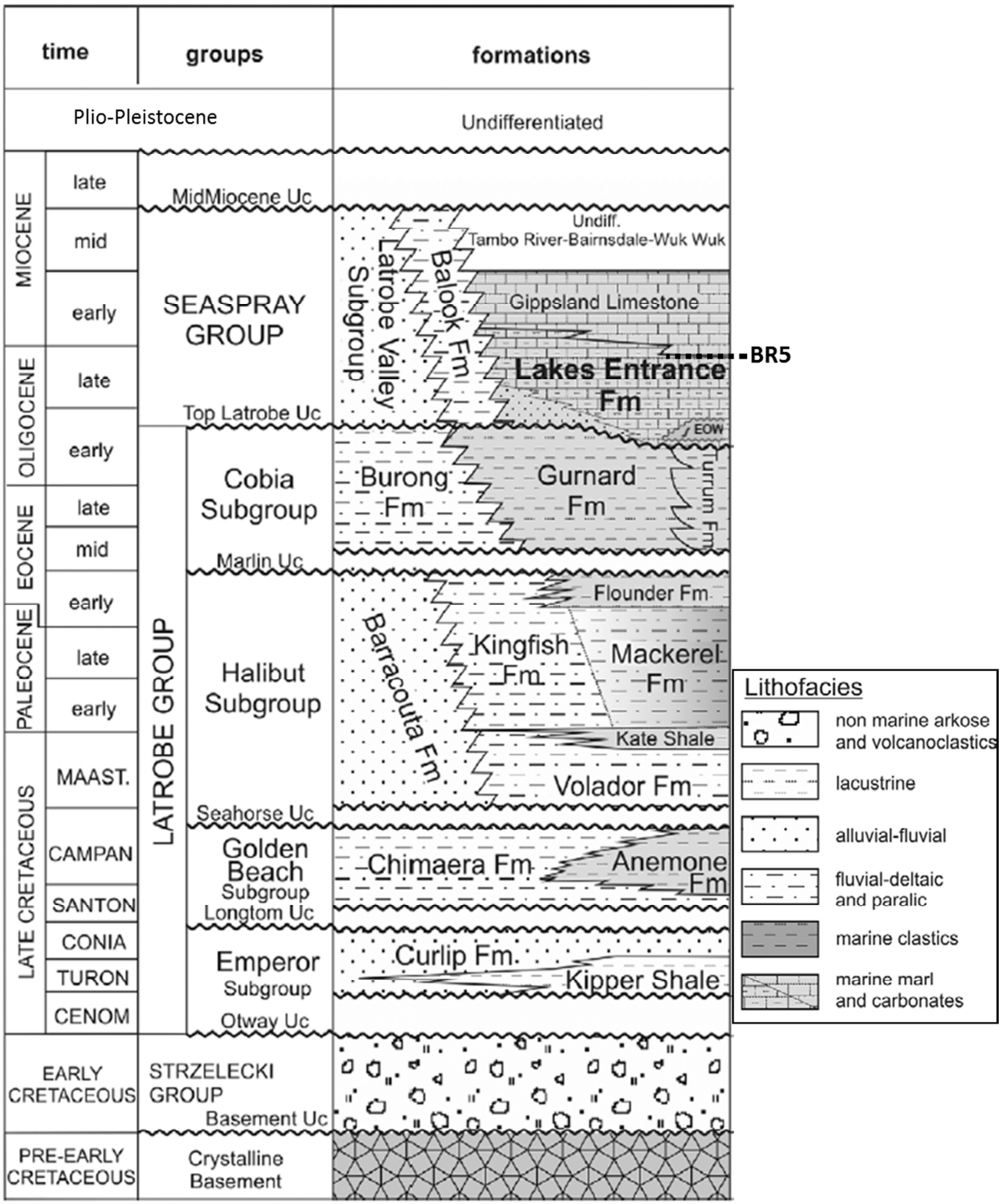

Figure 32. Gippsland basin Stratigraphy modified after Ciftci et al. (2014). The Lakes Entrance Formation is the primary sealing unit in the Gippsland Basin.

4.2.3 Data

The southern terrace of the Gippsland basin (Figure 30) has been a target for exploration since 1970s. Early seismic surveys that covered the area had to comply with the well data that indicated a shallow basement. Numerous 2D surveys were acquired over the next decades to establish the limited potential for the existence of a thick reservoir and charge. However, it was also revealed that minor sub-basins appeared to exist within the basement high of the southern terrace.

The investigations for the potential CO_2 sequestration of the Gippsland Basin brought attention to better delineate the southern terrace. The then existing surveys were not of enough coverage or in the best orientation to complete such studies. As a result, the former Victorian Department of Primary Industries shot a 2D seismic survey (GDPI10) in, and perpendicular to, the orientation of the maximum horizontal stress. To avoid the potential HTI effects on the seismic waves, the preferred direction of the seismic survey should be in the plane of isotropy which is the same as the maximum horizontal stress. This orientation for the Gippsland basin is 120 degrees (Müller et al., 2012).

There are 32 wells and boreholes in the area of study. Most of these wells are drilled on the southern margin of the central trough where a thicker reservoir and better access to the charge system is more plausible. The rest of the wells are situated around the north western margin of the area of study. Groper-1 and 2 wells are the only wells that provide subsurface data from the central and western side of the area (Figure 33).

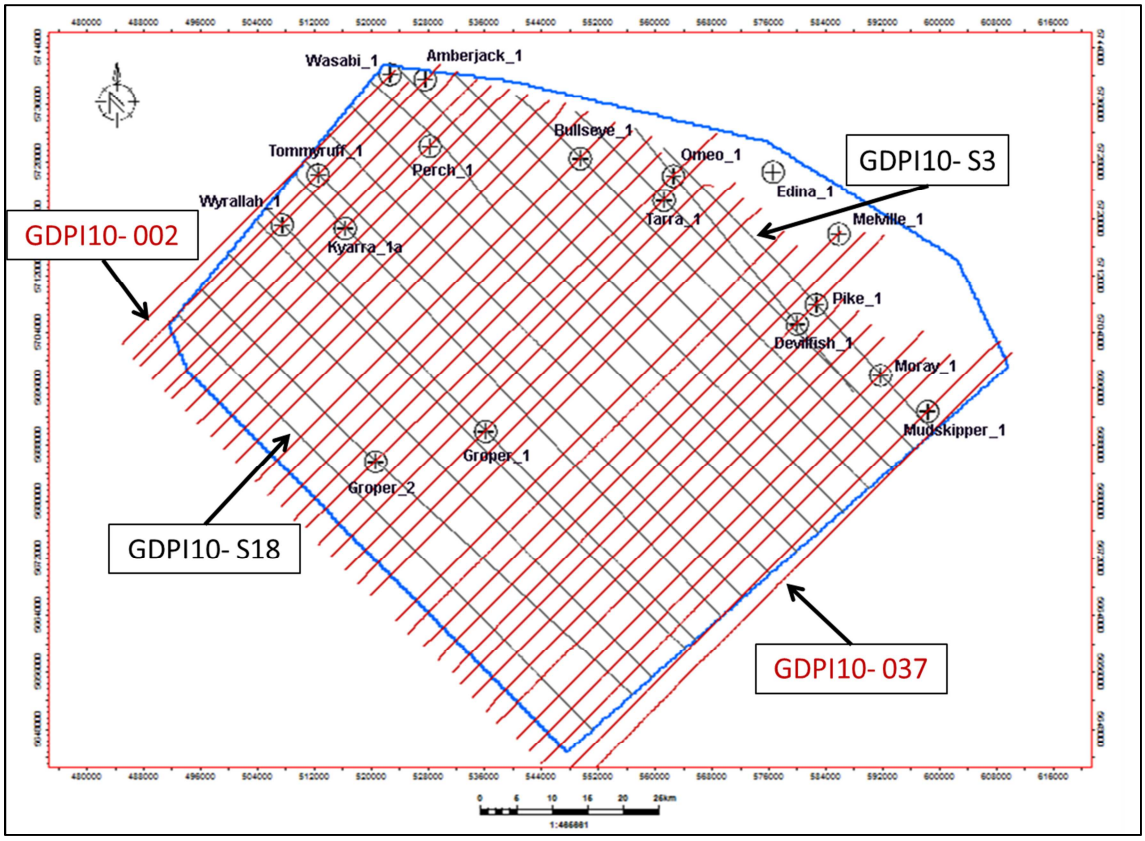

Figure 33. The area of study (blue Polygon) is located in the offshore of the southern Gippsland Basin. The area is covered by an orthogonal grid of 2D seismic lines. Dip lines (002-037) are colored brown and strike lines (S3-S18) are grey.

The GDPI10-2D is the selected seismic survey that fully covers the area of study. The strike lines of this seismic survey are oriented in the desired orientation of 120 degrees. All 18 strike lines were used for this study (Figure 33). Out of the 32 wells, 12 provide sealing data for the Lakes Entrance Formation. They are spread all across the area of study which is an important element in the spatial verification of the modelling. Although Melville-1 and Edina-1 are not covered by an adjacent 2D strike line, their velocity and sealing data can be helpful in the calibration and 3D modelling process.

4.2.3.1 Seal Potential of the Lakes Entrance

Goldie Divko et al. (2010a) reports that samples from the deeper measured depths have higher smectite content and cite this as the reason for their higher sealing capacity. Smectite is the most prevalent clay mineral in the Lakes Entrance Formation samples that have been studied in the Gippsland

basin (Goldie Divko et al., 2009a). Depth of burial was reported as a likely factor in the alignment of smectite minerals that helped forming better seals. Where more quartz granules were present in the samples, they disrupted the alignment of clay minerals and opened up micro-spaces next to themselves. Such openings are micro-scale reasons for lower leakage threshold.

The seal potential of the Lakes Entrance group was evaluated through the mercury injection tests that were performed on samples from various wells within the area of study. The source some of the data points are the Victorian government report no 1 (Goldie Divko et al., 2009a). The rest are open file and are mentioned in the GDPI10 interpretation report (Blevin et al., 2013), but were not included in the appendices due to their confidentiality at the time of publication. These wells are now public domain data. The MICP measurements for Devilfish-1, Kyarra-1a, Melville-1, Mudskipper-1a, Pike-1a and Tummy-Ruff-1 were performed by Adelaide University. The data for these wells were in part-interpreted state and needed finalization. These measurements were obtained and interpreted to estimate the sealing capacity of the Lakes Entrance formation.

The group of wells that came in with the lab measurements over the MICP samples has two wetting/non-wetting phase injection and withdrawal curve that are also referred to as drainage and imbibition respectively. The injection of mercury results in the measurement of pore volume in the sample. When the injection (drainage) and the incremental pore volume curves are plotted together, they can reveal several features about the sample such as pore size, their distribution and connectivity.

Depending on the lithology and the amount of fissures and cracks on the surfaces of the sample, the mercury injection process “feels” two sets of pore spaces to invade. The first “easy-to access” bunch of pore spaces is the surface cavities and fissure and micro-fractures. The invaded pore space either plateaus or increases slightly before it encounters the second mound of porous space. The latter pores

space is the actual inter-granular pore space that is invaded by the non-wetting phase through driving the wetting phase (water or air) out.

Not all the samples show the same amount of micro-cracks and fissures. Some of the samples show homogeneity for the mercury injection in a sense that the surface fissures and cavities get quickly filled and a quick jump in the mercury saturation depicts the onset of the drainage process (Figure 34).

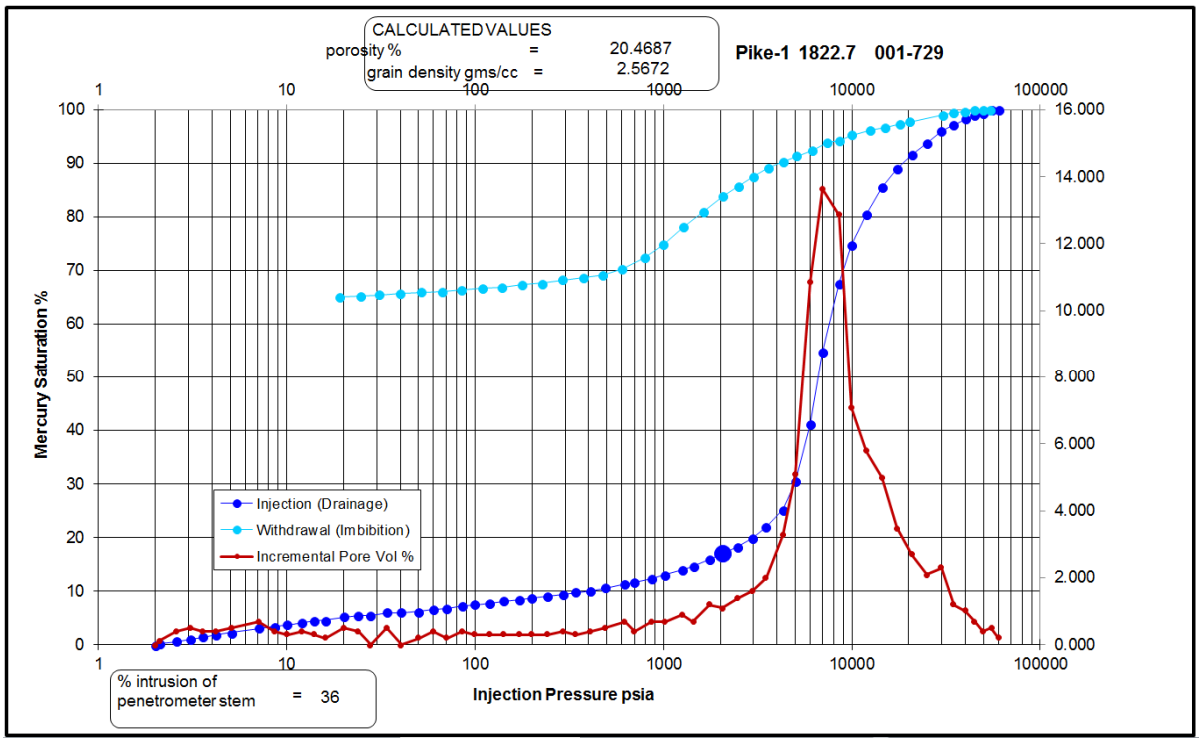

Figure 34. The MICP plot for Pike-1. Microfissures and crack are negligible in the sample and their effect is minimal on the pore volume curve (Red in color). Likely points for the invasion phase of mercury are depicted by larger blue circles.

Before this MICP plot can be used for seal capacity evaluation, some further correction was applied to the lab data. The data have seen general laboratory corrections applied. The lab measurements also delineated the inflection point for the data so that the conformance correction can be applied.

4.2.3.2 Seal Capacity

The industry standard practice is to designate the corresponding pressure value of 7.5% mercury saturation as the seal capacity of the sample (Sneider et al., 1997). Table 4 shows a summary of the sealing capacity of the Lakes Entrance Formation samples that were used in this study. When viewed altogether, a relatively wide range of sealing capacity exists within the samples from the area of study. However, the highest P_c value as the sealing criteria for the Lakes Entrance formation still puts it as a class C seal type according to Sneider's scheme (Sneider et al., 1997).

Well	Depth of Sample (m)	Sealing P_c value (psi)	Formation/Unit
Devilfish-1	1593	600	Lakes Entr.
Groper-1	909.15, 926.1, 932	1688, 435, 290	EOW
Groper-2	747.86	75	EOW
Kyarra-1	980	1470	EOW
Melville-1	2190	1340	Lakes Entr.
Mudskipper-1	1470	2256	EOW
Omeo-1	2175	2930	EOW
Omeo-2A	2169	2263	EOW
Pike-1	1822.7	3900	EOW/Slump
Tommy Ruff-1	880	642	EOW
Wasabi-1	1250	823	EOW

Table 4. Mercury injection capillary pressure values from samples in the AOI of southern Gippsland

Goldie Divko et al. (2010a) reported that the samples from the deeper measured depth have higher smectite content and cite this as the reason for their higher sealing capacity. Smectite is the most prevailing clay mineral in the Lakes Entrance Formation samples that have been studied in the Gippsland

basin (Goldie Divko et al., 2009b). Depth of burial was reported as a likely factor in the alignment of smectite minerals, helping to form better seals. Where more quartz granules were present in the samples, they disrupted the alignment of clay minerals and opened up micro-spaces next to themselves. This is likely to increase the sealing risk.

5 Chapter 5: Sealing Potential and Seismic Anisotropy

Seismic anisotropy is an attribute of the seismic that is a direct outcome of the sedimentological or tectonic settings of the subsurface. In this chapter, the two case studies are investigating possible relationship between the magnitude of VTI seismic anisotropy and the sealing potential of shales.

5.1 VTI or Orthorhombic

In order to infer VTI component of in situ anisotropy measurements have to be conducted in a specific way. We also need to have logs and/or VSP data. The surface seismic data can then be analysed for VTI anisotropy in the plane of symmetry which is in the direction of maximum horizontal stress. In that way we minimize any other "component" of anisotropy. For example if we have in situ orthorhombic anisotropy which seems to be often the case in sub-horizontally layered systems, analysis in the direction of σ_{max} which is one of the symmetry planes will allow for investigation of shale (VTI) anisotropy. Shale formations are often assumed as possessing VTI anisotropy. Hence to analyze the seals that are mostly shale, the direction of the seismic lines should not matter. This would assume an isotropic stress field. Are there any other factors of importance for anisotropy analysis of shales?

The answer lies in the geology and the structural history of the formation that is subject to the study. A shale formation that is generally a VTI medium can undergo fracturing and turn into an orthorhombic isotropy. The degree and effectiveness of such stress regime determines whether the produced fractures are significant enough to imprint the seismic response. Geological intuition tells us that a relatively recently formed shaly formation that has undergone minimal stress can still act as a VTI medium, while a deeply buried and well solidified shale that has seen multiple episodes of varying stress regime (perhaps in different orientations) is very likely to have open fractures that turn its underlying VTI condition into orthorhombic.

Li (1999) demonstrated how intersecting seismic lines that are shot in different azimuths can be used to detect the orientation of the fractures. This method relies on the fact that the seismic velocities are faster in the direction parallel to the strike of the fractures (isotropy plane).

In general, there are three methods that are available to detect the orientation (or existence) of fractures though seismic data:

- Velocity
- Residual move-out
- Amplitude

The "velocity" method compares the NMO velocity of intersection seismic lines (over a single location) and assigns the fast velocity to be in (or close to) the direction of the fractures. The "residual velocity" method compares the far offset move-outs of the target horizon (corrected by the same velocity) and determines the orientation of fractures. The amplitude method compares the variations of the amplitude of far offset seismic in different orientations and deduces the most likely strike orientation of fractures. This method is not used in our analysis as it is beyond the scope of this study.

5.1.1 Gippsland Basin

In order to investigate the degree of fracturing in the Lakes Entrance Formation, several intersections of orthogonal seismic lines were analyzed. Priority was given to the northern margin of the study area where the Lakes Entrance Formation is thickest.

5.1.1.1 V_{nmo} method

The stacking velocities of the GDPI10 survey were divided into two groups: the first group is along azimuth 135 (parallel to $\sigma_{h\text{-}max}$) and the second group is along azimuth 45 (orthogonal to $\sigma_{h\text{-}max}$). The values for each group are up-scaled and interpolated within the structural model. The two models

are then subtracted from each other to produce a difference volume. The values of the difference volume can be queried along surfaces that are parallel to base Lakes Entrance Formation (Figure 35).

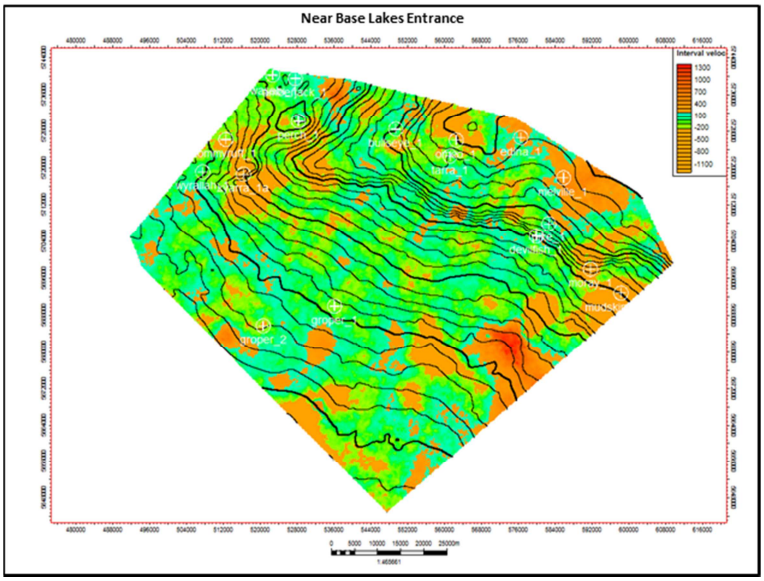

Figure 35. The difference in Interval velocity of dip and strike lines at near base Lakes Entrance. The Average Interval velocity for the zone is 2700m/s. Values higher than 5% of average interval velocity are colored in red.

The difference volume shows that the majority of the velocity values fall within 5% of the average interval velocity for the Lakes Entrance Formation. This indicates that there is not much change in the V_{nmo} velocity of the sealing formation between the orthogonal seismic lines. Therefore, the Lakes Entrance Formation is effectively a VTI medium.

A better qualitative understanding of values in Figure 35 is given when we calculate the same values for the more likely fractured Latrobe Group. Figure 36 shows that for the same normalization range (5%) of the average interval velocities, the Latrobe Group shows much more anisotropy.

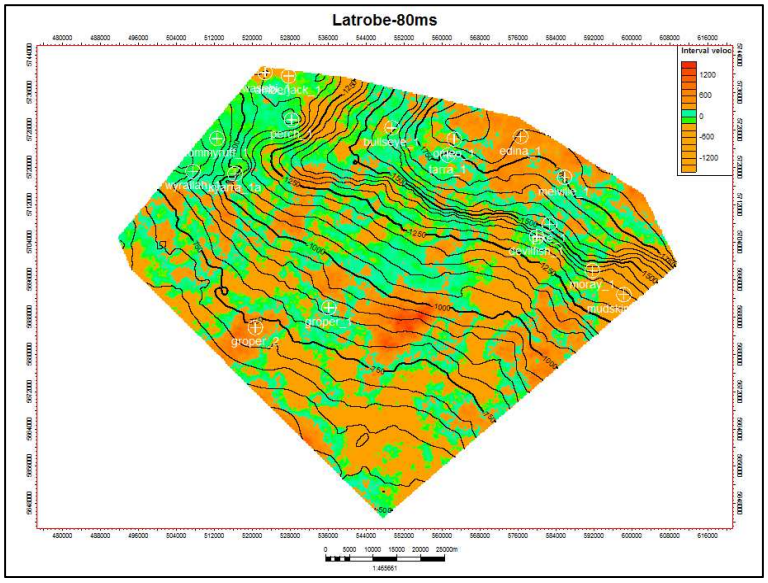

Figure 36. The difference in the interval velocity of Dip and strike seismic lines in the Latrobe group. The orange-red colour zones depict the values outside 5% of the average interval velocity of the Latrobe group.

5.1.1.2 Residual Move-out

The seismic velocities of a VTI medium are independent of the azimuthal orientation. Hence, the residual time difference at far offsets between the same events (for the bottom of a zone of interest) observed over orthogonal seismic lines is negligible for VTI medium and noticeable when HTI effects are present. This method provides a more reliable way to detect the presence of fractures in a formation.

Figure 37 below shows the corrected gathers for the intersection of line S05 (left) and D28 (right). The line S05 is parallel to the isotropy plane and would have faster velocities in the presence of HTI effects to flatten the events. The picked horizon is the Top Latrobe, which shows minimal difference between the two directions for similar velocity values. If the Lakes Entrance Formation had significant fracturing, the residual move-out of the long offsets between the two orthogonal lines would be different. Of interest is the event below Top Latrobe (around 1470msec). For similar velocity corrections, there is a visible difference between the two directions in the far offsets. This can serve as a calibration point to show the analysis is working correctly for the reference offset. We have to remember that the

faults within the Latrobe group are not oriented in relation to the current state of stress ($\sigma_{h\text{-}max}$). The faults and fractures in the Latrobe Group are oriented in the azimuth of ~105 degrees (Ciftci et al., 2014). As a result, the line S05 (Azimuth 135 degrees- Figure 33) shows some HTI effect on it for the Latrobe group, but comparatively less than Line D28 (Azimuth 44 degrees).

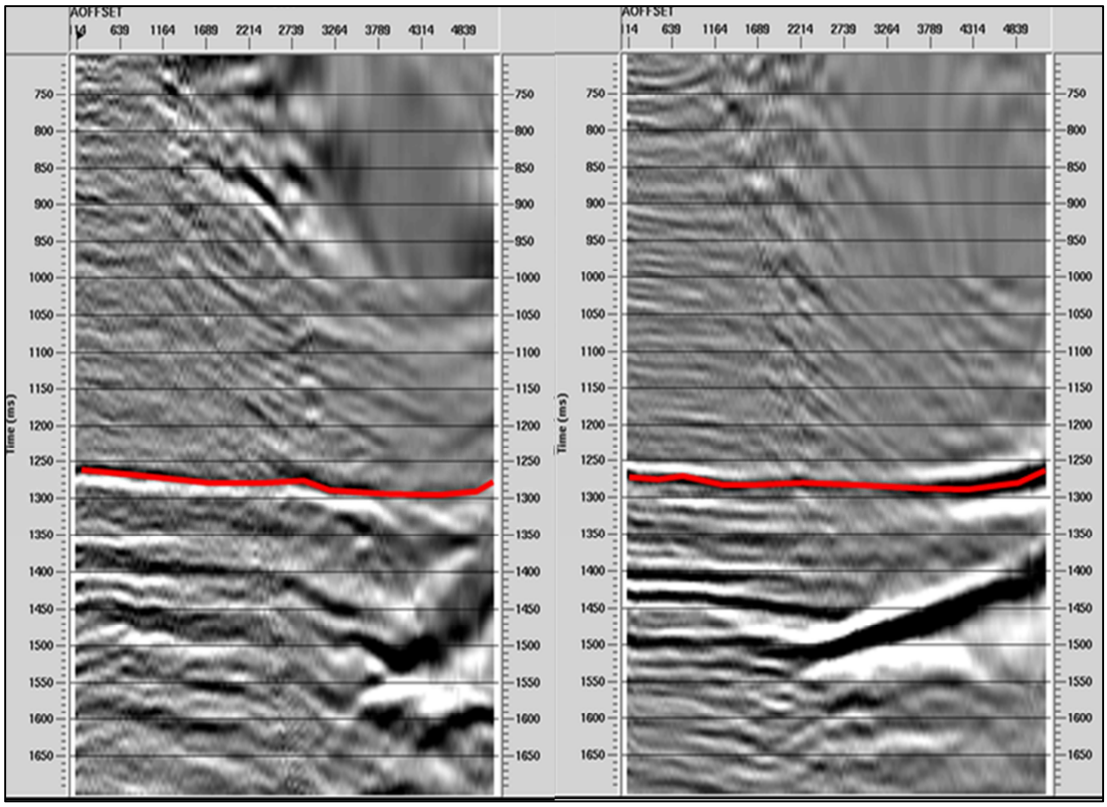

Figure 37. Comparison of two CMP gathers on the same location at orthogonal orientations. Both lines are NMO corrected with the same velocity function and eta value (0.02).

This proves that the Lakes Entrance Formation fits well with the description of the VTI medium, and the orientation of the seismic line will not influence the derived anisotropy parameters (at least in the area of study). This result fits well with the geological settings of the Lakes Entrance Formation that is relatively young, the depth of burial rarely exceeding 1500^{m} in the Gippsland Basin. The tectonic regime to which the Lakes Entrance Formation has been subjected (Chapter 2) is also more or less in the same direction of the present-day maximum horizontal stress.

5.1.2 Exmouth Sub-basin

Given that the "residual time" method produces more reliable results, it was chosen to investigate the effectiveness of fractures in the sealing sequence. Figure 38 shows a comparison of the CDPs from the same location taken from two orthogonal lines. Both CDPs are move-out corrected with a similar velocity function. However, while the line that is orthogonal to the isotropy plane (HE96-32) shows a good flattening of events around target level (red horizon in Figure 38), the line that is in the isotropy plane requires a higher velocity value in order to be flattened.

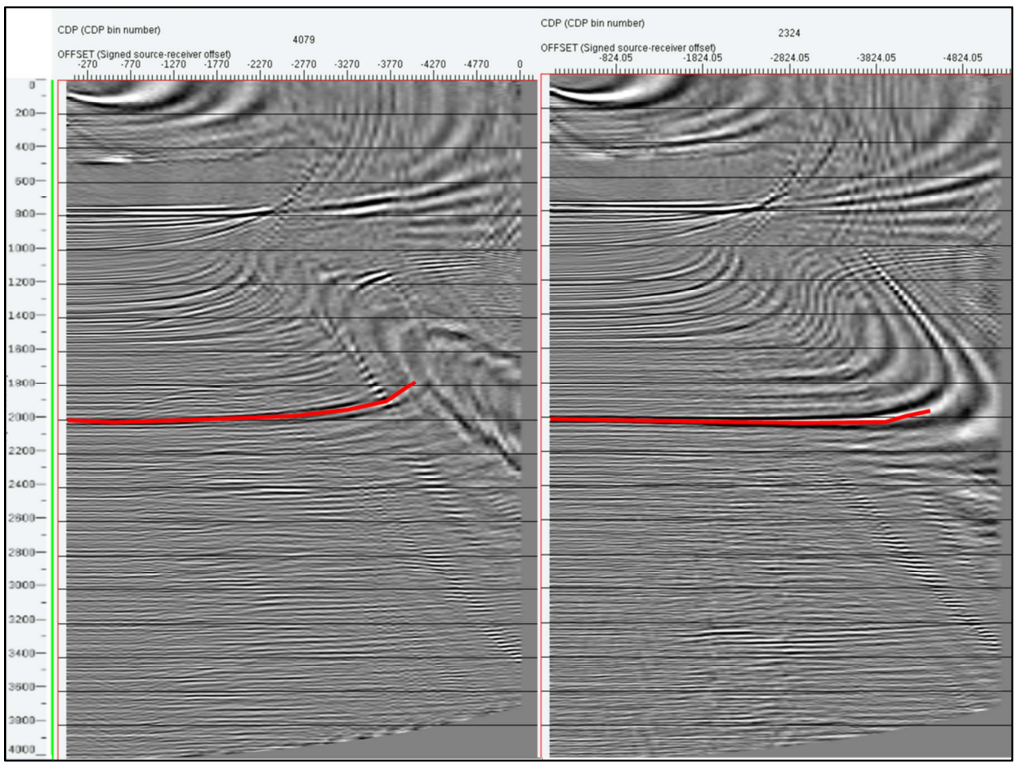

Figure 38. The residual time test between two orthogonal seismic lines: HE96-4 (Left) and HE96-32 (right). The interpreted horizon (Red) is the Base Muiron Member (Top Macedon Sandstone).

This analysis shows that the level of fracturing in the Muiron Member is significant enough that has caused significant residual time difference between the orthogonal seismic lines (the isotropy plane and orthogonal to it). This essentially means that the Muiron Member is an orthorhombic media, and to eliminate the impact of the fractures the seismic lines need to be oriented in the isotropy plane. This

choice will reduce the number of independent stiffness values to 5 (which is the same as the VTI medium).

The fact that the Muiron Member is best described as an orthorhombic medium (as opposed to the Lakes Entrance in Gippsland) is best explained through the complexity of its tectonic history. The Muiron Member of the Barrow Group was deposited in the Cretaceous (as compared to Lakes Entrance, which is Tertiary in age) and is buried significantly deeper. The effect of burial history on the anisotropy of shales has been the subject of many studies (Bachrach, 2011; Delle Piane et al., 2015; Kanitpanyacharoen et al., 2011; Pervukhina and Rasolofosaon, 2017). Different episodes of tectonic stress have likely created a network of fractures in the Muiron Member well after it was solidified.

5.2 Exmouth Sub-basin

5.2.1 Interpretation

The area of interest includes three producing fields of Enfield, Stybarrow, the southern part of Vincent and nearby exploration wells (Figure 20). There are 28 wells within the study area, of which 18 wells have checkshot/VSP data. The area of interest is covered by three 3D seismic surveys: Vincent 3D, HCA 2000 and Macedon 3D (HC93), with other smaller field-specific 3D seismic surveys associated with the Enfield and Vincent fields. A number of 2D seismic surveys exist in the area of study. Most of these surveys either partially cover the area or do not have closely spaced seismic lines. HE96 survey is the only 2D seismic survey that provides a reasonable coverage of the area.

In order to cover the entire area of study with interpretation of target units, the three seismic 3D volumes were included in the post-stack interpretation. Well tops and logs from all the wells were loaded to Petrel or Techlog software suites, and were unified and interpreted. Most wells have the complete set of logs including sonic DT, gamma ray, neutron density and bulk density. Shear wave sonic

is common and some wells benefit from a cross-dipole shear sonic that is of great help is the evaluation of anisotropy.

Seismic interpretation of the area was conducted to build the necessary structural and stratigraphic framework that is used in the modelling and mapping of rock properties such sealing capacity and anisotropy. To do so, faults were interpreted first to define the structural framework and the horizons were then picked and tied to the wells.

The entire Exmouth Sub-basin area is characterized by normal faults. Extensional faulting that occurred during Early Cretaceous plays an important role in defining the reservoir boundaries, hydrocarbon pathway and lateral seal. Most of these faults are terminated by the Early Cretaceous disconformity of Muderong shale deposition that defines their upper extent. Faults are interpreted based on the juxtaposition of the seismic reflectors where a stable trend can be pursued. Higher weight was assigned to the faults with larger offset since they are more likely to have an impact on the sealing character of the fault blocks.

Interpretation of faults has a direct impact on the building of water-tight 3D model. The 3D model will be the framework that will guide the calculated properties and separate geological segments. Faults are also important to delineate zones where ETA (η) analysis is likely to return less reliable results.

Faults were interpreted and correlated in 3D. A map view of the strike of the fault planes (Figure 39) reveals that the majority of these faults are oriented in the NNE-SSW direction (Azimuth 30-40 degrees). This observation means that the orientation of the maximum stress over the zone of study (Early Cretaceous) is around 120 degrees.

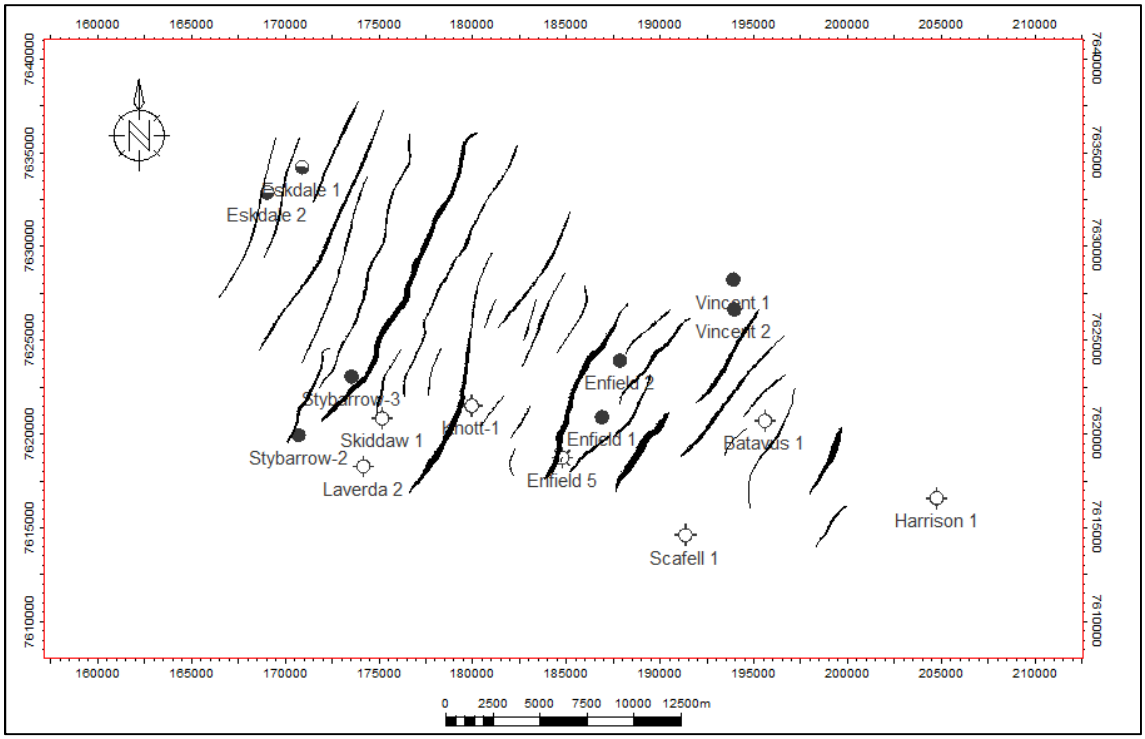

Figure 39. The orientation of the major faults are NE-SW that is orthogonal to the orientation of maximum stress.

The ultimate purpose of seismic interpretation is to build a framework in which attributes can be assigned or extracted over target horizons. Since the seal units are of most interest in this study, the primary goal was to interpret them. Muderong shale and Macedon shale are the two known seal units that cap Lower Barrow Formation and the Macedon sandstone unit respectively.

The contact between the shale and sand is usually a more easily identified seismic reflector. This is due to the velocity and density contrast between the two units. This is not always the case for the top seal unit. I therefore decided to interpret the top reservoirs to help complete the top-seal pick. Such seismic picks will also define the bottom seals and will help in building isopach maps of the seals. Hence, top Lower Barrow formation and Top Macedon sandstone units were picked. Seabed and some accessory horizons were also picked to help build a water-tight model and complete the depth-conversion process.

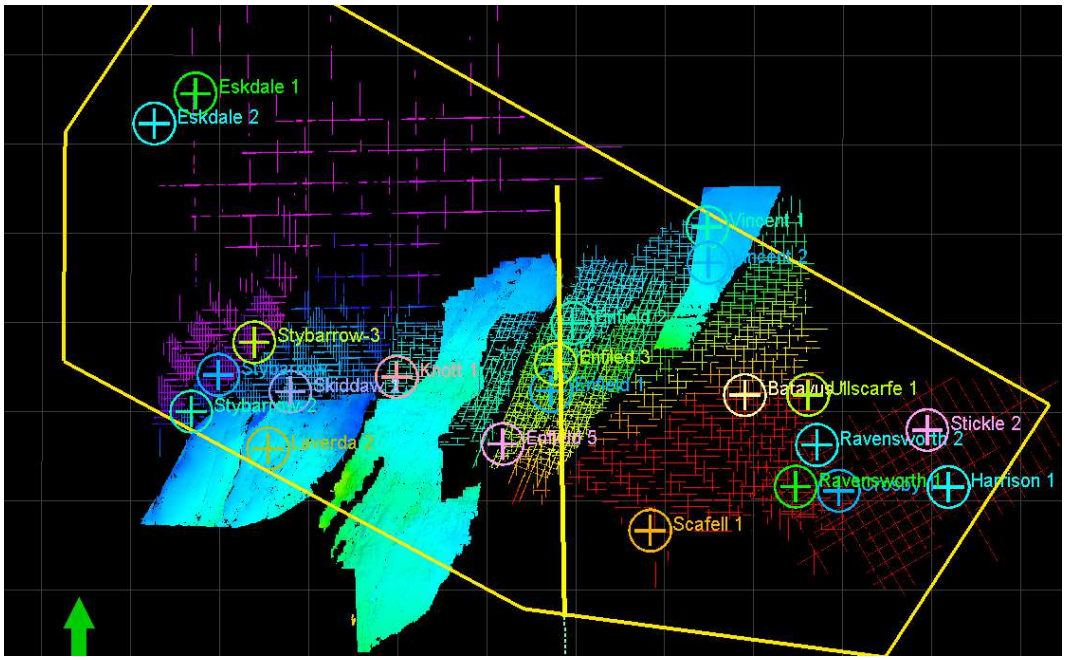

Figure 40. The extent of interpretation on Macedon Sandstone. Several 3D seismic vintages were collated together to cover the area of study.

5.2.2 Depth Conversion

The target in this project is to investigate the relationship between anisotropy and the seal potential of shale sequences using seismic data. The nature of seismic recording makes it time-domain data. Our velocity and ETA analysis are also performed in time-domain. Although the time-domain data have their own limitations in depicting the depth-domain, it will not concern us much, since the calibration points are in the vicinity of wells and the structures are simple enough to be addressed in time-domain processing. However, depth-domain processing is also discussed later in the project for its superior imaging powers and the wealth of anisotropy parameters it provides.

Since the majority of the data is in time-domain (seismic-interpretation, modelling), it makes the analysis easier to convert the well tops/logs to their equivalent TWT values. The calibration points such as checkshots and VSP data serve as important ingredient of the velocity model.

Depth-conversion plays an important role when structural maps are output. Unlike seismic data, geology is recorded in depth. Maps with attributes of any kind should ultimately be output in depth since the depth to target is what matters in exploration and development.

The horizontal velocities vary in the area of the study. Therefore, a simple compaction curve (which honors the vertical velocity changes) is not the best representative of the depth-conversion process in the area. Presence of fault blocks and structural variations across the area of study urges us to incorporate our interpretation of the seismic in the depth-conversion process. One of the most accurate velocity modelling approaches that is practiced in the petroleum industry is adopted in this area. This approach will comprise the perceived geology of the area through utilizing the seismic interpretation and 3D modelling. It will also honor the lateral and vertical velocity variations within formations through using VSPs and stacking velocities. The 3D structural framework (which was built from the seismic interpretation tied to well tops) acts as the base of the velocity model. The checkshot and VSP velocity data are then fed to the model (along the well trajectories). The stacking velocities are conditioned and are added to the 3D geocellular model to act as the weighing points in the interpolation of the velocity data from the wells. The final result was smoothed and QC'ed for irregularities. Unless the depth conversion results were not in the acceptable range (<1m), residual velocity surfaces and models (to the target well tops) were made (iteratively) and applied to the model. The incorporation of all well and seismic derived data into a structural 3D volume will make a water-tight 3D velocity model.

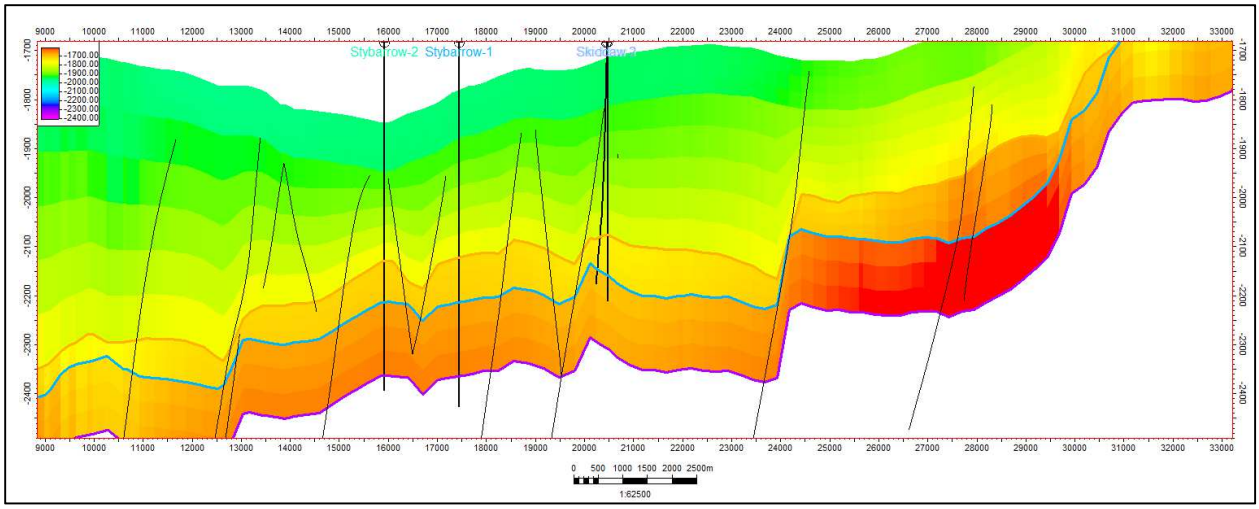

Figure 41. An arbitarary section through the velocity model of the area of study. Lateral velocity variations can be envisaged in the model and within each structural zone.

5.2.3 Anisotropy and Seal Potential

Clay-rich shales that have undergone at least typical compaction through burial are likely to be anisotropic, and are typical examples of a VTI (vertical transverse isotropy) medium, i.e. vertical ≠horizontal seismic velocity. Well-developed shale sequences have fissile fabric that tends to show anisotropy on seismic and dipole-shear sonic logs. Studies on core samples of such shales show their elastic anisotropy (Sondergeld and Rai, 2011), and can be associated with AVO (amplitude versus offset) signatures (Amiri Besheli and Urosevic, 2006; Rüger, 1996).

Seismic data provide a window into the subsurface, allowing the geometry and integrity of deformed formations such as shales, to be mapped, identifying sequence boundaries and structural stability. Researchers have been developing methods to extract more geology out of seismic data using pre-stack attributes and seismic anisotropy (Alkhalifah and Rampton, 2001; Kendall et al., 2007).

Using equations (Chapter 2- Equations 25 and 26), ε, which is the fractional P-wave anisotropy, can be calculated. The latter resembles intrinsic shale anisotropy, and as such could be linked to the internal structure of the shale. In simpler terms, ε indicates the ratio of horizontal and vertical P-wave

velocity. This means that higher values of ε indicate better foliated shale (Lonardelli et al., 2007). The next step is to investigate the possible relationship between ε and the capillary pressure measurements. We propose that ε from seismic data can serve as a good proxy attribute for sealing capacity from capillary pressure measurements.

Core plugs of analyzed shale from the Floyd Shale in Alabama have exhibited moderate to strong seismic anisotropy (Sondergeld and Rai, 2011). Similar scale-dependent results were found when analyzing field data from the Carnarvon Basin (Amiri Besheli and Urosevic, 2006; Urosevic et al., 2004). In this study, we look at the entire problem from the viewpoint of the effective-medium theory. The effects measured by seismic are not due to some change in the shape of pore-space under stress or local alignment of micro-cracks. Such effects have to happen over significant volume to affect seismic wave propagation. According to this theory, the seismic anisotropy measured in perfectly isotropic sands that are exposed to asymmetric stress field is comparable to the anisotropy we see in our area of study. This is indeed the phenomenon we are looking for when it comes to relating the "sealing quality" or the sealing capacity of the shales to their intrinsic anisotropy. It is well known that the vertical and horizontal velocities are distinct in layered/laminated materials (such as shale). Therefore, through measurement of the degree of shale anisotropy in space, we can, to the first degree of approximation, estimate its sealing capacity. The assumption is that good sealing shale will have well-developed platelets and well packed grains (Figure 1). These two together will to a great degree control shale elastic properties and hence degree of intrinsic shale anisotropy. Mineralogy, of course, enters into this equation: if it is variable over the Fresnel zone, it will cause errors in our predictions. Therefore, borehole control is essential.

5.2.4 Data Analysis

The Vincent and HCA2000 3D surveys were shot at an azimuth of 90 degrees, therefore not complying with the optimum direction for our analysis. In order to align the analysis along the maximum horizontal stress, $\sigma_{max,}$ (to avoid azimuthal anisotropy contribution, which reduces the medium symmetry to effectively VTI for that purpose), the HE96-2D survey was selected as it runs at an azimuth of 120 degrees. This is the azimuth of the maximum horizontal stress (Müller et al., 2012). The HE96 survey also benefits from longer streamer offsets compared to the 3D surveys. The area of interest is covered by lines 1 to 9 of HE96 survey (Figure 20). The target lines were processed by the standards of the relatively deep water of the area of interest (Appendix 10).

5.2.5 Estimation of η and ε

Once the near trace or V_{nmo} velocities are determined, the full offset gathers were examined to calculate the η value that will flatten the seismic reflectors. This procedure was essentially iterative as to determine the best CDP gather requires modifications to both V_{nmo} and η.

The computed η values were used to compute Thomsen's parameters at well locations, and then up-scaled to the 3D model so that attribute maps could be extracted over mapped horizons (Figure 42). These figures were then tied to the nearest wells, and using equations (Chapter2) 3 to 5, ε was calculated.

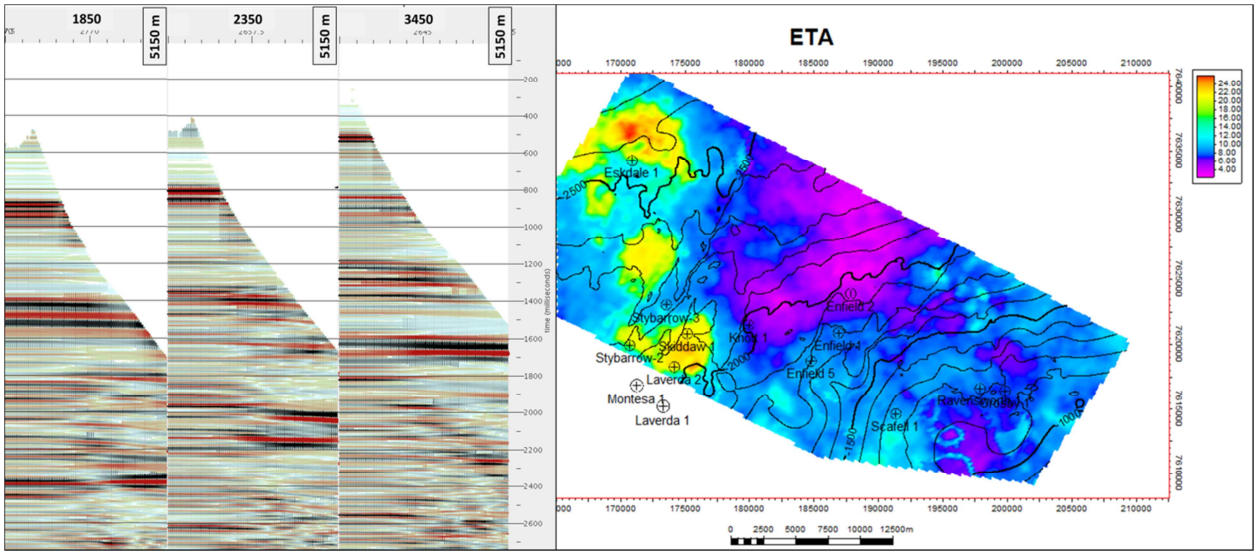

Figure 42.Supergathers along HE96E-3 (left) and map of Eta (η) on top Muiron member (right).

The MICP values (Table 3) were up-scaled using a mathematical mean to their corresponding cells in the 3D model. Up-scaling of η and P_c values should be done with care as the sampling rates for them are different. η values are calculated in time and normally over 50-100 msec intervals. Capillary pressure samples were acquired over the measured depth axis of the wells, and needed to be converted to time. A 3D velocity model was built using interpreted horizons, VSP data and V_{nmo} to help convert the time-domain to depth and vice versa.

In the model, a minimum 5 meter layering thickness was chosen to accommodate the occasional close-sampling of P_c. Capillary pressure samples that were acquired in closer spacing than 5 meters were amalgamated into one cell. The up-scaled cells of ε at well locations were plotted against P_c values, and show a reasonable correlation. This means that, in general terms, the increase in capillary pressure cells is matched by the same trend in ε values.

ε values calculated from seismic were cross-plotted against capillary pressure measurements (Figure 43). A linear trend with reasonable correlation (70%) can be assigned to the plot. It might initially seem reasonable that a linear regression line could be fitted to map P_c from ε. However, we should

remember that Figure 6 depicts a statistical relation between two groups. It implies that higher values of P_c (better seals) in our study area are probably associated with better foliated shales (hence higher ε values).

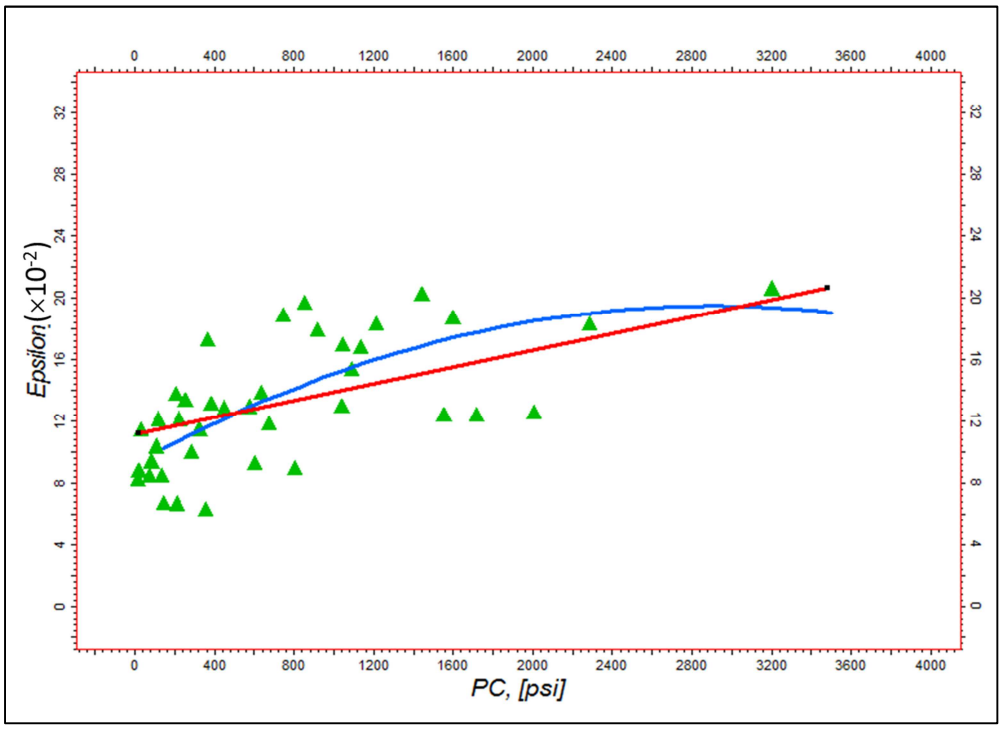

Figure 43. Plot of Pc versus Ɛ shows a general increase of anisotropy parameter ε with increasing the sealing capacity (measured through P_c). A linear regression (red line) and a second-order polynomial (blue curve) are shown as reference.

It is perhaps safe to assume that for this spectrum of Pc values, the trend is more or less linear. We have attempted a second-order polynomial, and it gave slightly higher regression values of 74% (Figure 43, the blue trend curve). Remembering the lessons every geophysicist learns while depth-converting time maps, we know that using a trend blindly can quickly deteriorate the prediction powers of the curve, e.g. the time-depth relationship does not stay linear or hyperbolic, and the trend almost plateaus beyond a certain time. An analogous scenario can be visualized here. As shales become more compacted and develop higher foliage and alignment of the platelets, the ratio of V_{hor}/V_{ver} (or 1+ε) increases. Beyond a certain degree of such alignment of platelets, the ratio of increasing of ε should

slow down, as observed on Figure 6. This is probably why a second-order polynomial generates a slightly better regression.

Field measurements are prone to errors and the values should be understood in relative sense, not absolute. Considering that previous work on the shale anisotropy in this region (Amiri Besheli, 2006) put ε values up to 0.4, our several rounds of interaction with the data limited the errors for delta (δ) and epsilon (ε) at a maximum of 50%. In order to make the analysis easier, the initial model is built in time. This will make comparison of interpretations, seismic characters and velocities easier. Using the available VSPs and NMO velocities, a 3D structural velocity model is built. Depth-conversion is then applied to the final volumes and maps.

5.2.6 3D Modelling

Using the established relationship between ε and P_c, we can propagate the up-scaled well measurements into the 3D structural model. The cornerstones of the model are built on the up-scaled P_c values at wells. Next, the entire 3D volume is given weight according to the scaled ε cells. The goodness of propagation in the vicinity and between wells is checked by portraying the target property (P_c) on well sections (Figure 44). The Muiron unit therefore appears to be a good seal in the cross-section between Eskdale and Stybarrow (Figure 44), but it is not a very promising seal towards Ravensworth-1 and Crosby-1. This is coincident with the geometry of the Muiron Member, which is reduced to almost zero around Scafell-1 and may present lower-quality seal for Macedon sandstone. Once the entire 3D volume is populated with P_c values, we can extract the sealing potential along the mapped P_c values on the Muderong shale and Muiron Member (Figures Figure 45 and Figure 46). Hence we can observe that more competent sealing units form top seals over the existing reservoirs.

Further calibration can be applied in the 3D modelling by defining reject zones, e.g. non-sealing units. There are a number of wells from which we have no P_c data, but other logs, such as gamma ray or

density, are available. These logs can help identify sand zones where the sealing potential is close to zero. Such zones can be incorporated in the model to help the propagation of targeted properties, i.e. sealing versus non-sealing.

Once the shale units are classified according to their sealing potential, we can extract their properties at the fault zones. A preliminary approach used to check for fault leakage is to construct an Allan diagram. This diagram essentially reflects where a shale unit is juxtaposed against a sand unit. Although there are reported sand-versus-sand fault seals (Bouvier et al., 1989; Yielding et al., 1997), juxtaposition of sand against sand is generally considered unfavorable and is a potential leakage. A juxtaposition diagram can be more descriptive if facies modelling of rock units is done based on seismic. Using the proposed method, we can better identify shales based on their seismic character, which in turn will high-grade our juxtaposition diagrams. Also, shales can be sub-categorized according to their potential sealing capacity, and windows of sand against shale can either be sand against high-sealing shale, or sand against poor-sealing shale. Such juxtaposition analysis can offer a first step approach as to how some faults may be hydraulic seals.

With the analysis technique introduced in this paper, we propose a methodology to assign a degree of sealing (or class) to shale units and faults. This may be considered as having an additional parameter to help characterize shales rather than an explicit measure of the shale sealing capacity. Therefore, we will have more tools in describing top seal, bottom seal, lateral seal and fault seal within a field and away from wells (Figures Figure 45 and Figure 46). An example output of this analysis is seen in Figure 47 in which the bounding fault near Knott-1 has juxtaposed a low capacity sealing unit (depicted in red) against a reservoir quality unit; hence a potentially leaky window emerged.

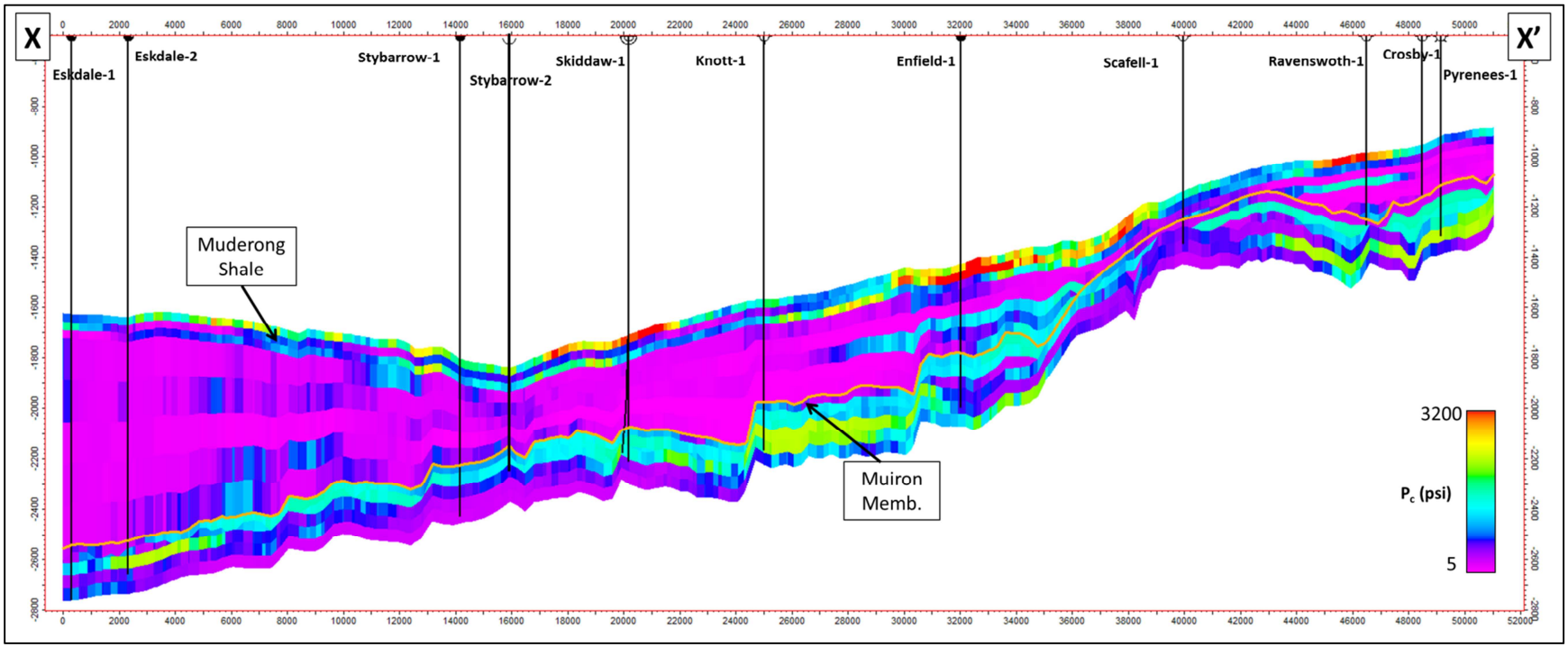

Figure 44. Cross section through the predicted Pc volume. Both Muderong Shale and the Muiron Member show a relatively high sealing capacity. However, their capacity varies within the area of study. Location of the section is on Figure 20.

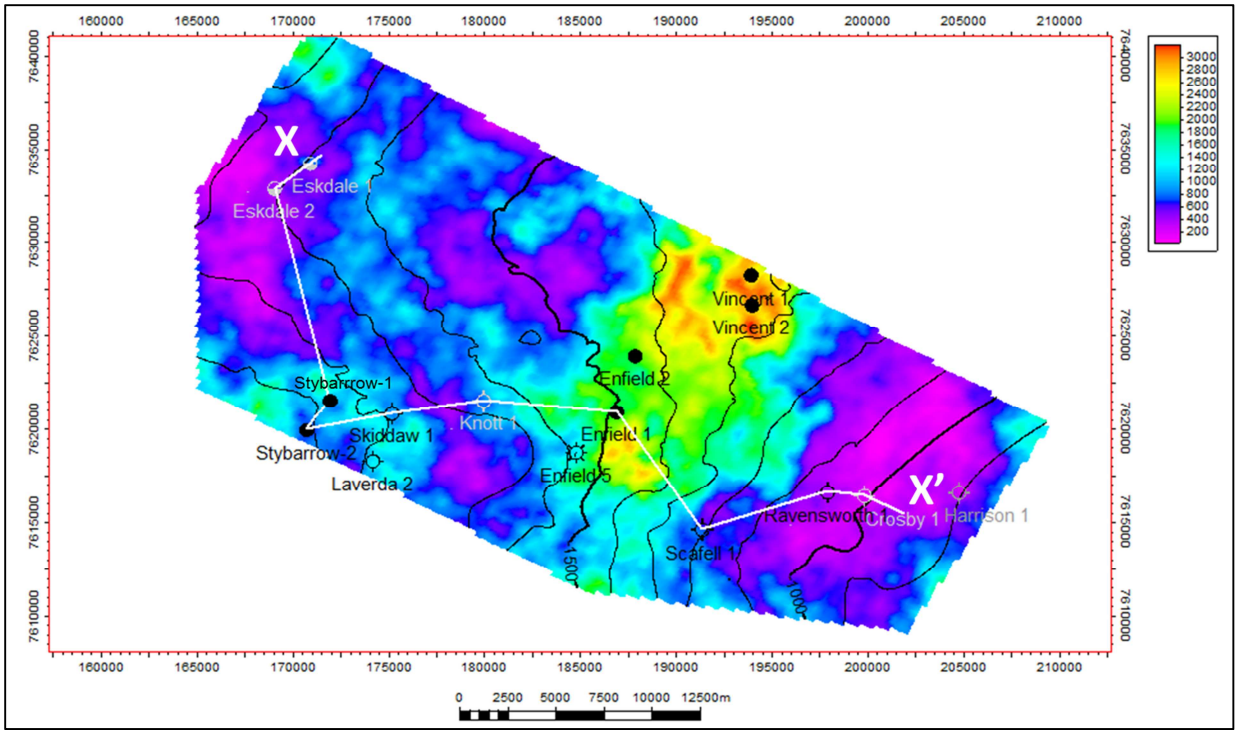

Figure 45. Map of Pc over Muderong Shale. Vincent shows good seal quality for the Barrow reservoir.

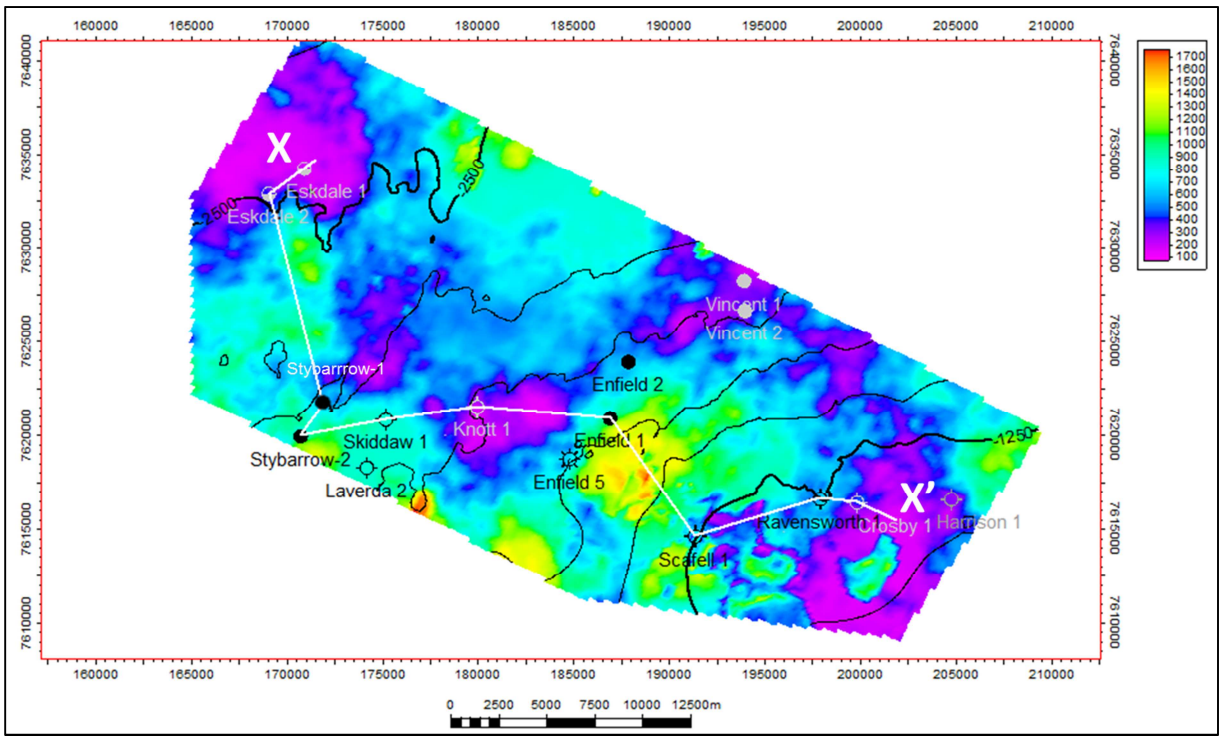

Figure 46. Map of Pc over Muiron Member. High seal quality is observed over Enfield which has a gas cap.

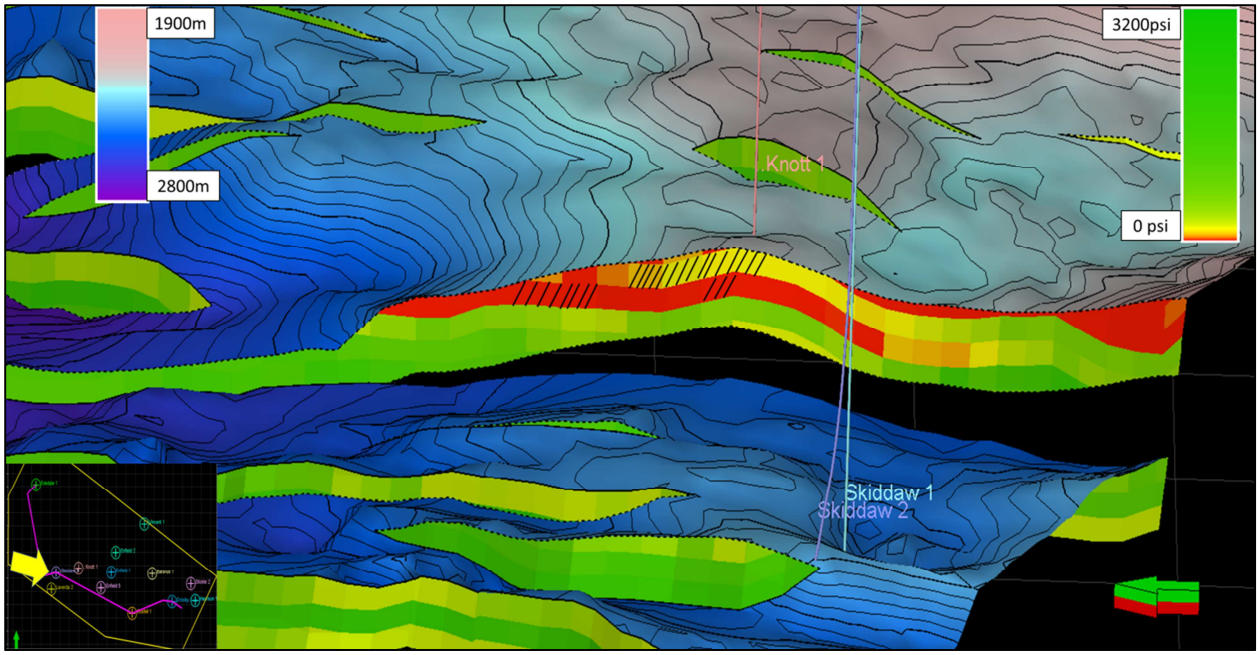

Figure 47. 3D perspective view of Macedon Sandston horizon with the Pc mapped on fault planes. If the fault seal was dependent on juxtaposition only (and not shale smearing), low sealing capacity shales (hashed cells on the fault surface) are potential leak areas.

5.2.7 Discussion

When completing this type of anisotropic analysis, it is important to choose the correct orientation of seismic lines with appropriate acquisition orientation/parameters, ideally in the orientation of the σ_{Hmax} (maximum horizontal stress). Fractures and stress-caused cracks form along the axis of maximum horizontal stress. Orthogonal to the maximum horizontal stress direction (minimum horizontal stress), pre-existing fractures are closed. The isotropy axis lies parallel to the maximum horizontal stress. Therefore, it is best to calculate the η along the axis that is isotropic with regards to the fracturing.

A reality check is taken from the nearby fields such as Enfield and Vincent. The Enfield and Vincent Fields both produce from the Barrow Group, but have different sealing units. The Macedon Shale/Muiron Member of the Lower Barrow Group is the sealing unit for Enfield, while Muderong Formation serves as seal in Vincent (Figures Figure 45 and Figure 46). In order to keep every step of the

analysis consistent, a depth model was built based on the VSP and stacking velocities and the structural interpretation of the area, and was used to depth-convert the results.

There are no apparent gas chimneys in the area of study, which means there has been no active leakage of gas in the area, or at least it has not been sufficient to be detected on seismic. However, not all seal failures are associated with gas chimneys, and leakage of oil will most probably leave no trace on seismic records. Laverda-1 and Harrison-1 have been the location of potential leakage with a lower capacity top seal (BHP Billiton, 2005; Woodside, 2001), in contrast to Knott-1 that has additional risk, due to low fault seal capacity (Figure 47). In a proven productive petroleum system, one of the reasons that may have caused such failures is a weak sealing system.

The size of the up-scaled cells should be determined with due diligence, as too small a size can have adverse effects on the interval velocities and will result in erroneous ε values. It is equally important to quality-control the input values, and decide whether they are geologically sensible. For example, if the calculations indicate some cells have unusually high values of ε (greater than 1), they have to be investigated as they contradict the basic assumption of weak anisotropy.

The computed linear regression equation, while valid for the Muiron and Muderong shales within surrounding areas, should not be considered as a global function. Variation in shales composition, diagenesis and sedimentological settings will affect the anisotropy of the units involved and alter the correlation between anisotropy and sealing potential. For invariant shale mineralogy, it appears that the capacity to seal may be related to the magnitude of VTI anisotropy measured. This has to be taken as relative measure only and needs calibration with measured P_c values. Its predictive value is solely in lateral variations of shale anisotropy that can be associated with the variations in the “seal quality”.

Care should also be taken not to over-interpret the data. There are seal units that are not necessarily anisotropic or foliated (such as anhydrite). Such seals are simply tight zones that have very tiny pore throats. Our proposed method is expected to have poor prediction capability for such seals.

Extracted maps from the 3D model should always be interpreted in concert with the 3D model. Extracted attributes on maps can help adjust the best representative horizons for a geological event. Figure 44 shows that good seal for Top Muiron was encountered in the Eskdale-1 well, while the attribute map of P_c over the interpreted horizon shows a relatively low-quality seal in that area (Figure 46). Comparing the two figures reveals that in order to follow a quality sealing part of the Muiron Member, the interpreted seismic horizon for Top Muiron should have been deeper near Eskdale-1 (Figure 44); in other words, not the entire Muiron Member is a high quality seal.

Faults should be treated with care, as VTI anisotropy values within the fault zone tend to be erroneous. It is best to initially reduce the effect of faulting on velocity analysis through processes such as DMO (Dip Move Out) (Yilmaz, 2001). Furthermore, major faults are best to be avoided when selecting the η analysis location. Fault zones, including jointed areas, introduce HTI (Horizontal Transverse Isotropy) and thus act against VTI anisotropy (Jenner, 2011), aiming to reduce it as typically having an orthogonal axis of symmetry with respect to the VTI system. Hence, to some degree behavior of anisotropic parameters at the location of the fault will indirectly provide additional information about the fault itself. The anisotropy values can be extracted on the interpreted fault planes that provide significant and meaningful fault seal data for risking. This analysis could be further improved through the use of cross-well-seismic, walkaway VSPs, and sophisticated acquisition, and provide support data on cross-fault sealing.

A more time-consuming, but more accurate method to estimate the anisotropy parameters ε and δ is to reprocess seismic data to pre-stack depth migration (PSDM). The only way to truly separate

the effect of non-hyperbolic velocity from anisotropy (and to model ε and δ) is to perform anisotropic pre-stack depth migration (APSDM).

Although our proposed method is to high-grade the description of shales in the 3D model and across fault surfaces/zones, it is not a replacement for advanced algorithms that estimate fault seals (such as shale gouge ratio and smearing) (Bretan et al., 2003; Yielding et al., 1997). A better knowledge of the sealing potential of shale units can enhance the existing techniques and algorithms in their approach to fault seal analysis.

5.3 Gippsland Basin

5.3.1 Seismic Interpretation

The primary focus of the seismic interpretation was to delineate the sealing sequence in the area of study. The Lakes Entrance Formation is known to be the sealing unit over the well-known reservoir sands of the Latrobe Group. Therefore the Top Latrobe and Top Lakes Entrance formations were interpreted as the lower and upper boundaries of sealing unit.

The relatively shallow depth of burial (especially on the southern platform) for Lakes Entrance, relaxed the intensity of required horizons for modelling. No major seismic event is visible in the sediments above the Top Lakes Entrance except for the seabed. Most of the sediments are laid in near horizontal bedding (Figure 48).

The Top Latrobe is generally a well-defined seismic reflector. It represents a local hard kick which forms the top of an erosional unconformity (Figure 48). The Top Latrobe is a complex surface despite its relatively distinctive seismic reflector. In some areas, glauconitic sands, known as greensands, are deposited on the reworked sands of the Top Latrobe erosion (e.g. Gurnard Formation).

The top of the Lakes Entrance Formation is not consistently picked in the wells. Most wells have reported the first lithology that is significantly shaly below the Gippsland Limestones as the Lakes Entrance. The Lakes Entrance is therefore not as well defined as the Top Latrobe. However, the reported Top Lakes Entrance does not necessarily indicate the top of the potential sealing sequence (Nourollah, 2011). Complications arise when the Top Lakes Entrance is modified by slumps and channels. Such features modify the already transitional boundary for the top of the seal and make the seismic interpretation challenging. The key to have a consistent top seal interpretation is to alter the view that the top seal is not just a lithological boundary, but a sedimentary feature. Blevin et al. (2013) have made such an attempt to redefine what was considered as the Top Lakes Entrance as the progradational Early Oligocene Wedge (EOW).

Faults are not a prevailing feature for post-Miocene sediments (i.e younger than Top Latrobe). However, local re-activation has caused some older faults to penetrate the Lakes Entrance sediments. The offset for such faults is not large enough to breach the integrity of the top seal (Figure 49).

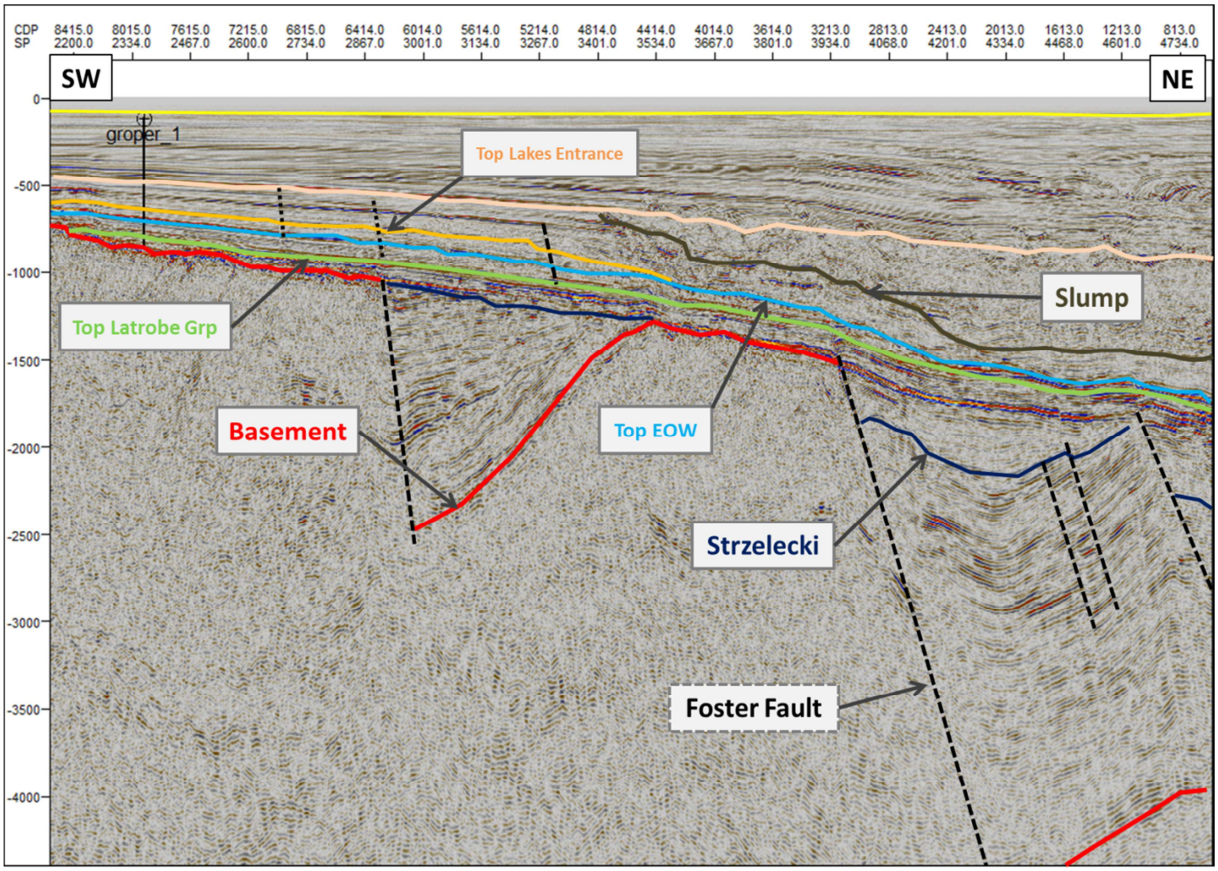

Figure 48. Section of seismic line GDPI-20 shows the veneering of sediments on the southern terrace basement high. A half-graben is visible in the centre. Blue horizon represents top Early Oligocene Wedge and Top Lakes Entrance is coloured Orange. Interpretation is modified after Blevin et al. (2013).

Similar method as the Exmouth case study was adopted for this area to maintain all the data in time-domain. Building an accurate velocity model was necessary to convert values that were measured in depth. Checkshot and VSP data of the wells were combined with stacking velocities of the processed seismic lines (GDPI10) and was utilized in the 3D structural model. The structural model was built from the interpreted seismic horizons.

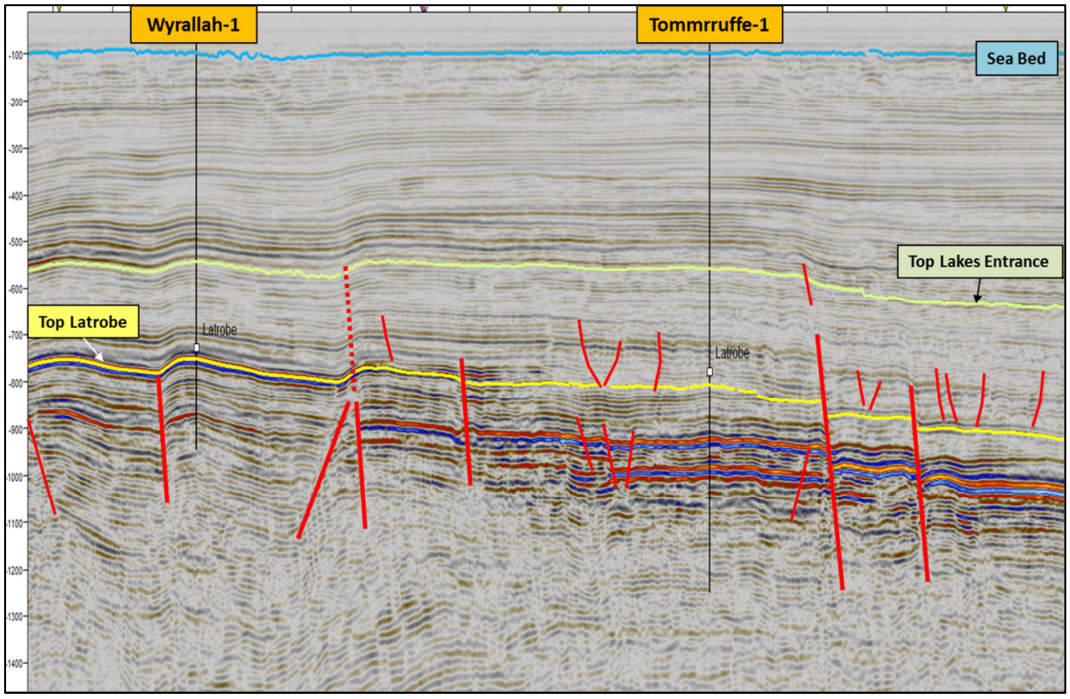

Figure 49. Locally re-activated faults are generally no threat to the top seal integrity in the area of study (Line GDPI10-4).

5.3.2 Well Calibration

A total number of 32 wells were included in the area of study. The wells provided depth and time well ties for Top Lakes Entrance and Top Latrobe (seal and reservoir formations). Some of the wells had their shale samples analyzed for seal capacity and were used for the calibration of the capillary pressure. Most of the wells were drilled in 1970s and 1980s, except for Wasabi-1 which was drilled in 2008. The vintage well data should be treated with care and should pass a careful QC. Sonic (DT), gamma-ray (GR) and caliper logs from the above-mentioned wells were loaded to Petrel and QC-ed. Although some of the wells did not have capillary pressure data, their vertical velocity logs (checkshot/VSP) were used to help define the variation of V_0 across the area (Figure 50).

The sonic log will provide the velocity of the target formations (Lakes Entrance/seal) under ideal conditions. It is important to be aware of the validity of the sonic logs since the diameter of the well

might have changed (cave-in or wash-out), and the sonic tool was measured (or was adversely affected) by the mud. This is partly true for the zone of invasion of drilling mud as the permeability of the formations decide how far the formation liquids are displaced by the mud. Since the sealing formations have generally minimal permeability, the latter effect was assumed to be negligible.

The validity of the information from the DT log has been doubted in some instances, especially where sonic data is run in a portion of the well (and not the entire length) without calibration to checkshots. If a sonic velocity log is run continuously from surface to a target depth, it provides valuable information with regards to the compaction and potentially anisotropy of the formations. However, few of the DT logs (and none in the area of study) have such condition. Therefore, their most important input is to high-grade the time-depth values through synthetic seismograms and well-seismic ties. When needed, DT logs were up-scaled to the seismic wavelength using Backus-averaging (Backus, 1962).

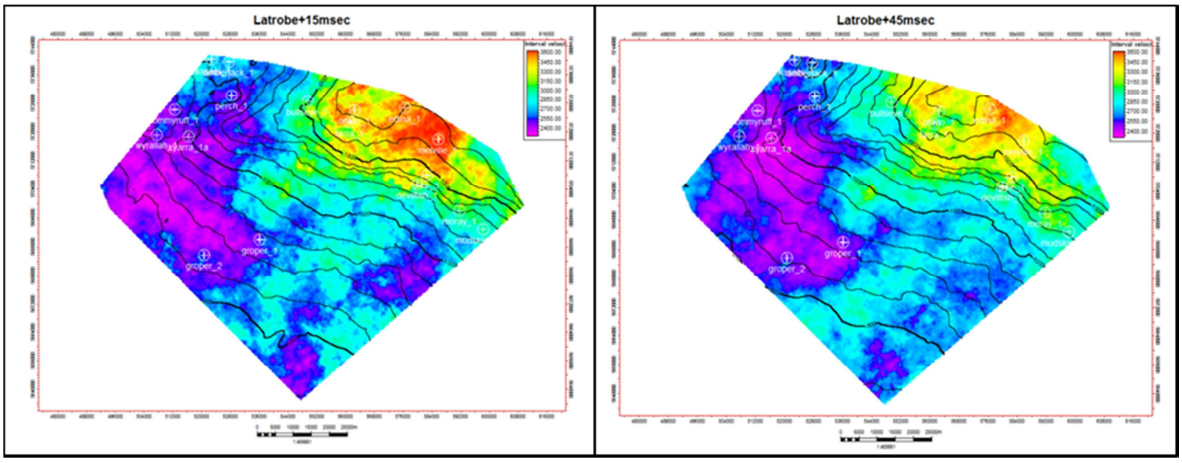

Figure 50. Variation of V_0 through the Lakes Entrance formation. Two horizon slices (Latrobe+15msec on the left, Latrobe+45msec on the right) are shown above.

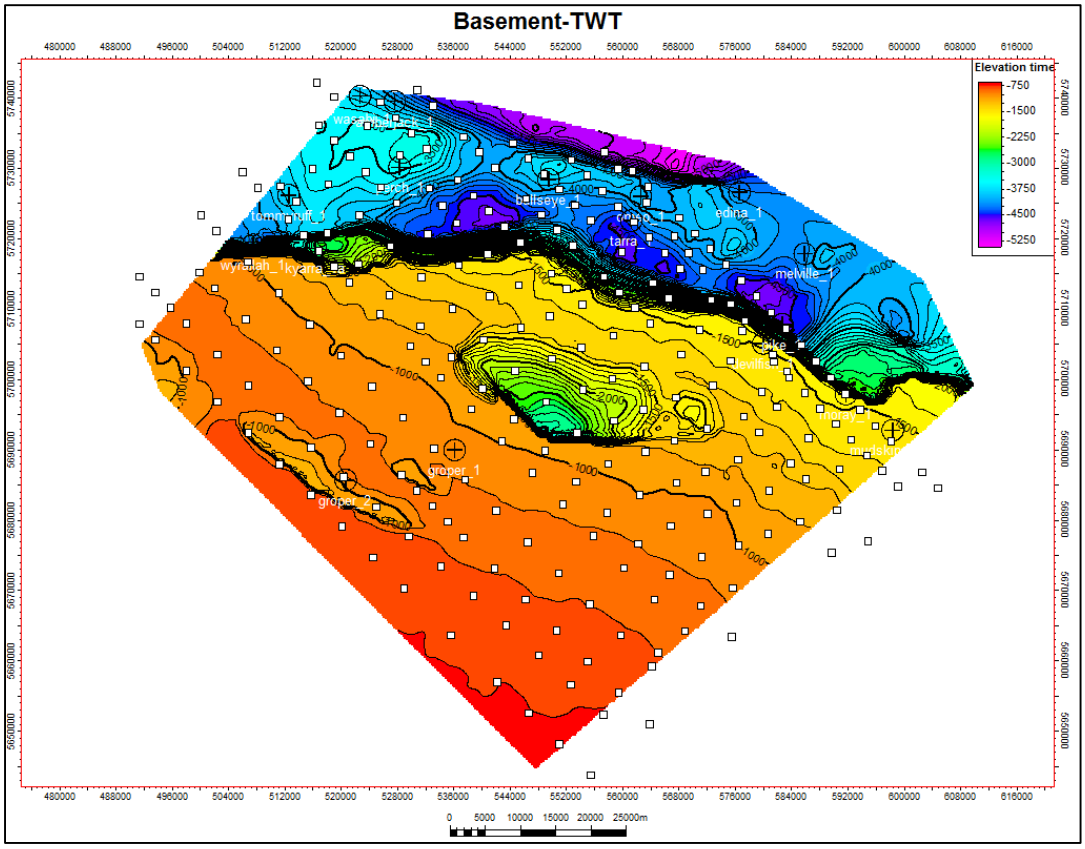

Figure 51. TWT map of basement. The white squares represent the locations where V_{nmo} and η were estimated from 2D seismic lines.

5.3.2.1 Estimation of Thomsen's parameters

Thomsen's parameters are simplified representations of elastic anisotropic parameters, i.e. how the wave front behaves while travelling through an anisotropic or so-called transversely isotropic rocks. The underlying motivation to derive these parameters is to make anisotropy easy to understand and compute. A step further in the applicability of his theory is the assumption that most rocks exhibit "weak anisotropy". This further simplifies formulations and make them more acceptable by a wider geophysical audience.

The anisotropy parameter, δ (a weak approximation of exact parameter δ*), and ε can be estimated once the V_0, V_{nmo} and eta are calculated (using equations 25 and 26 from Chapter 2). The

underlying assumption in such calculation is the relative simplicity of the subsurface structures (in terms of seismic). Such assumption is relatively satisfied for the Lakes Entrance Formation. Once up-scaled and modelled into the 3D model, maps and sections can be extracted to QC the results and deduce possible geological meanings (Figure 52).

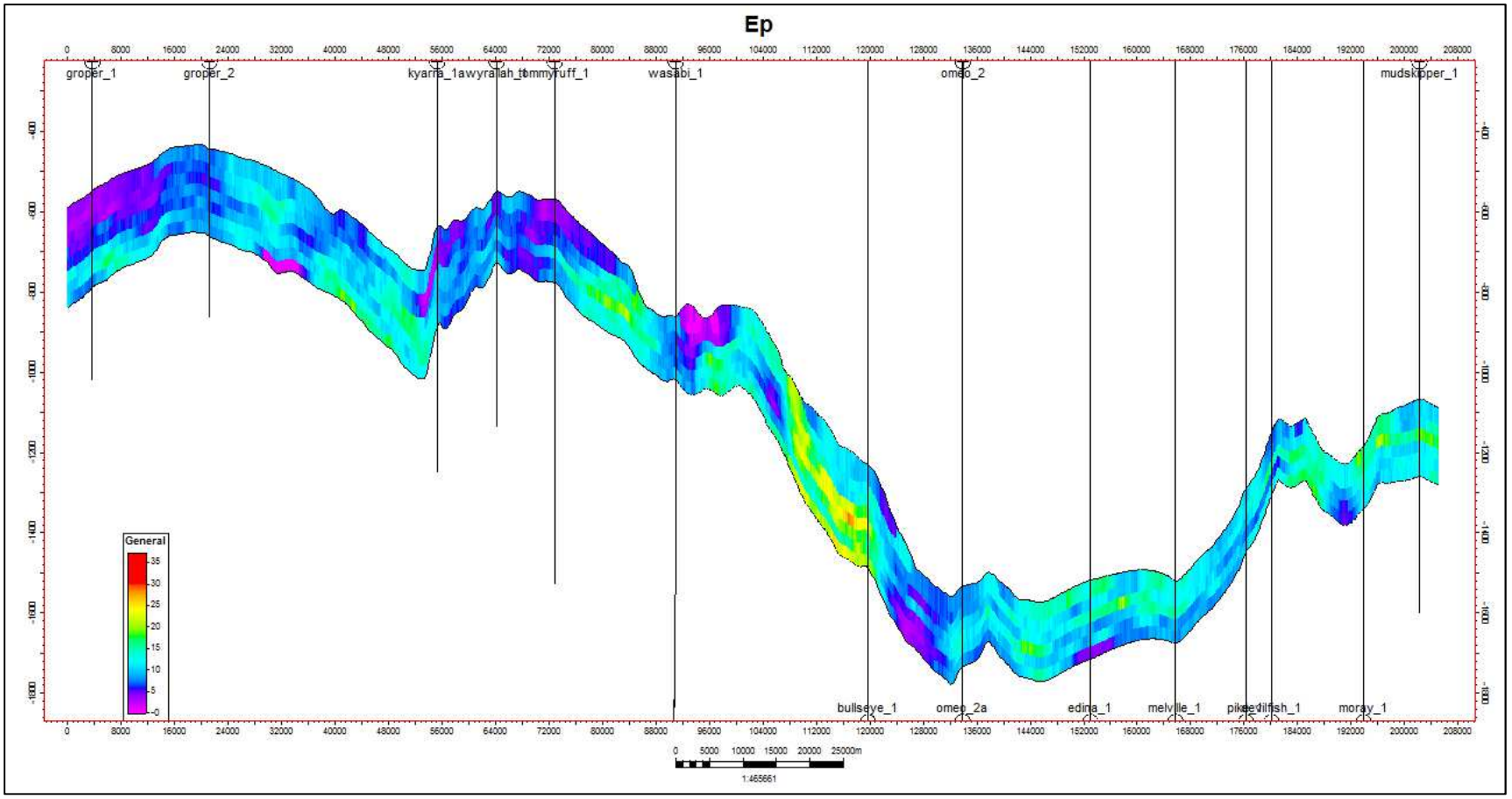

Figure 52. Distribution of epsilon within the Lakes Entrance Formation along cross section X-X'.

5.3.3 Ɛ and Sealing Potential

A comparison between interpolated volume of P_c values and ε along arbitrary sections and maps can be tempting. However, such comparison is not very accurate as the capillary pressure values are measured at wells and should be compared with their equivalent seismic values (which come at a different scale). The case study of Exmouth sub-basin leads us to test the relationship between the capillary pressure and ε (Nourollah et al., 2015). Figure 53 shows that similar trends exist between the two, as increasing P_c values correspond with higher ε ones.

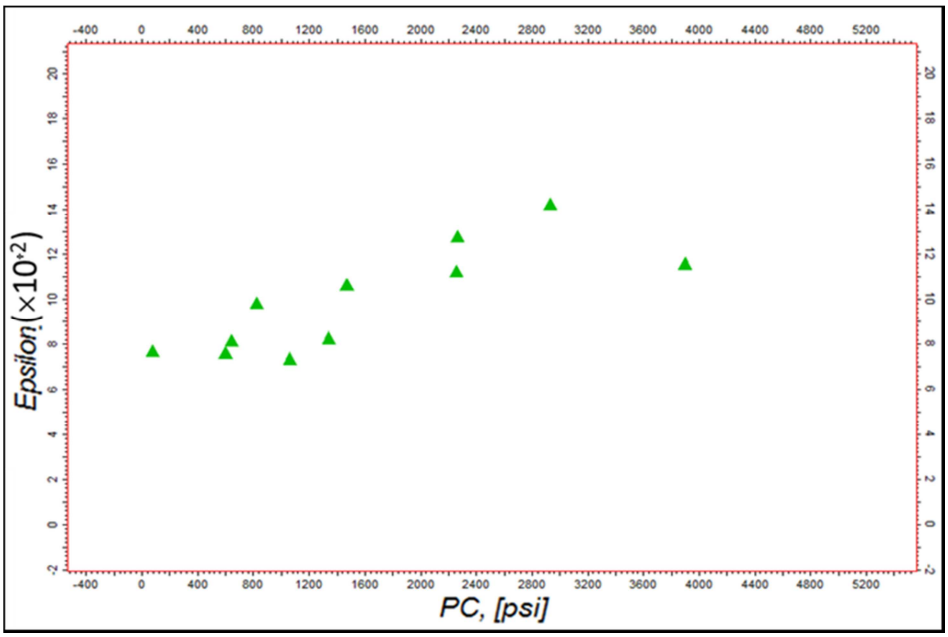

Figure 53. Plot of Capillary pressure values versus their corresponding epsilon in the Lakes Entrance formation.

Just like the case study from Exmouth, we can see an increasing trend for ε with rising P_c. However, the dip angle of the trend is not gentle. The ε ranges between 7 and 17 while P_c varies between 75 to nearly 4000 psi. Although the ε values are lower in comparison to the Exmouth case study, the general observation is that Ɛ increases with increasing P_c. Linear or a polynomial fit could be attempted for the data of Figure 53. The linear curve (red in Figure 54) will return a regression value of 80%, while a second-order polynomial will yield a value of 84%. The seal capacity corresponding to

nearly 4000psi is closing on the maximum measured value in the Gippsland Basin. Higher capacity is unlikely to be followed by a decreasing Ɛ. It is possible that the values of Ɛ would plateau for further increase in seal capacity.

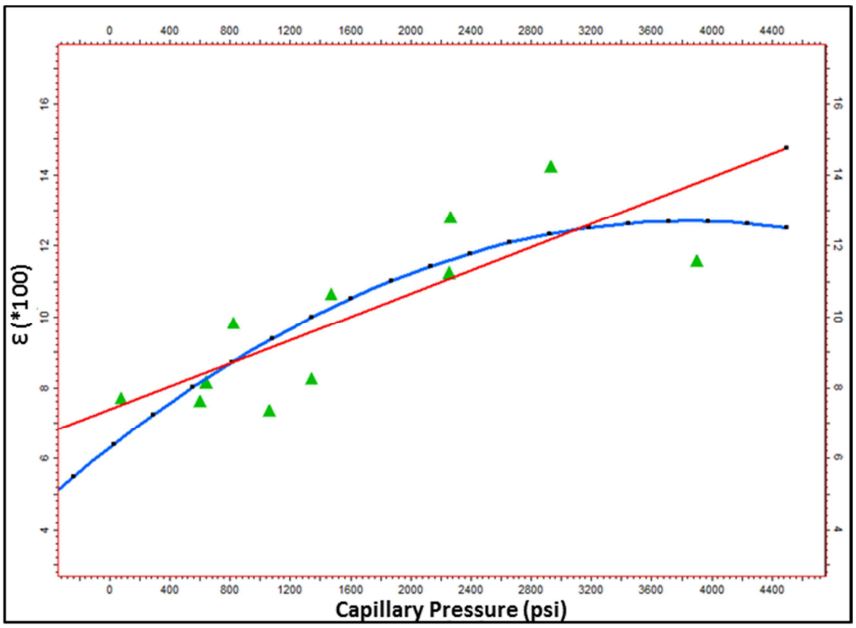

Figure 54. Two possible curve-fits to the distribution of epsilon and capillary pressure values.

The capillary pressure value of 3900 psi belongs to Pike-1. This point on the ε-P_c curve is almost a singularity that is placed at a crucial position on the chart. Unfortunately there was no more seal capacity measurements in the same range to compare and reduce the uncertainty of the predictive curve. However, this point indicates that the rate of increase of ε has slowed down.

5.3.4 Stiffness constants

The stiffness constants of rocks will require extensive measurements on core samples to be accurately determined. Sondergeld and Rai (2011) showed an example in their paper on evaluation of anisotropic properties of a shale core sample. Another method that has fewer requirements is to assume weak anisotropy of sediments for common seismic frequencies and convolve it with well

measurements to extract Thomsen parameters. These parameters are dependent on the stiffness constants in the first place.

For a VTI medium, the total number of independent stiffness constants will reduce to five. With our five extracted values of V_{p0}, V_{s0}, δ, ε and γ, plus the density (ρ), we should be able to estimate the stiffness constants through equations (36). Rock stiffness parameters have been shown to be of importance in evaluation of the behavior of reservoirs (Collet and Gurevich, 2013; Djikpesse, 2015). There appears to be no direct relationship between any of the stiffness parameters of the Lakes Entrance and its sealing potential. However, when constructing a three-component cross-plot of Ɛ, P_c and C_{11}, we can see that higher ranges of C_{11} coincide with high values of P_c and ε (Figure 55). This matches the results that were obtained in Chapter 3.6 where presence of connected capillary pipes will cause a drop in the C_{11} values quicker than C_{33}.

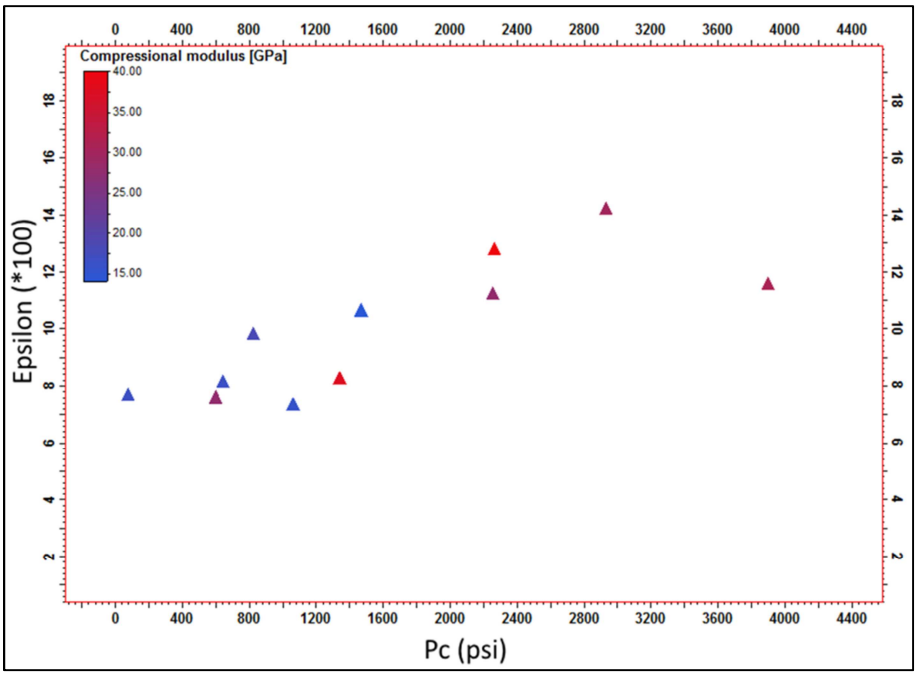

Figure 55. Plot of P_c versus epsilon. The cross plot stations are coloured based on their stiffness modulus C_{11}.

5.3.5 3D Modelling

The model building was mainly conducted in time and was based on the horizons that were interpreted on processed seismic lies. Since most of the MICP samples are taken from the Lakes Entrance Formation, the model was built to cover the temporal extent of this formation. A quick review of density of the sampling per well reveals that most wells have only one MICP sample. Therefore, the up-scaling process is less concerned about averaging adjacent values. A minimum 10 meter vertical spacing seemed accurate enough to account for the variations of sealing potential.

To utilise both seismic-based trends (Trace Gradient and Epsilon) to help evaluate the sealing potential, a neural network process was designed. The unsupervised neural network utilised the existing data for training and validation from the predicting input trends (Trace Gradient and Epsilon). Figure 56 shows an average map of the predicted capillary pressure for the Lakes Entrance Formation projected on top basement map. It shows that on average the sealing capacity of the shales are much higher towards the north. While still at acceptable values towards the west, the sealing capacity drops in the southern part of the area of study. This is where we have no calibration well, therefore the result are of interest, but should be treated with due diligence. Although Figure 56 suggests that the risk of sufficient seal is higher towards the southern part of the area of study, it does not reject the possibility of its existence. A consistent but relatively thin layer of good quality seal can still be very effective. This can be investigated with a 3D view of the subsurface seal.

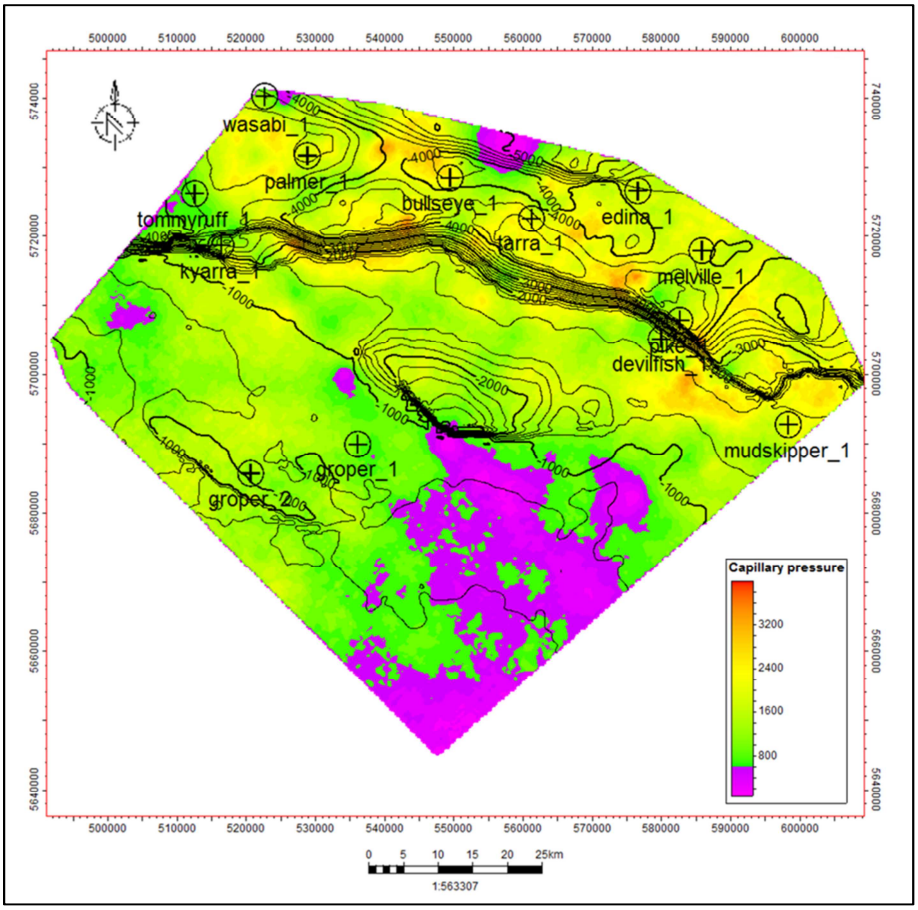

Figure 56. Average sealing potential of the lakes Entrance Formation projected on Top Basement Map.

The minimum consistent seal capacity value is important to evaluate the potential for the maximum hydrocarbon column or CO_2 (for sequestration). Figure 57 shows a 3D volume that is filtered to retain the capillary pressure values above 1300psi. This value is the highest threshold pressure value that can fully cover the mini sub-basins. Compared with Figure 56, it shows the lack of consistent sealing shale in southern areas. Using wells outside of the area of study (in the south), Blevin et al. (2013) produced maps indicating the lower sealing quality in an area that roughly coincides with the purple-coloured areas of Figure 56. The introduction of extra clastic material during the deposition of the seal was concluded as the likely reason (Blevin et al., 2013).

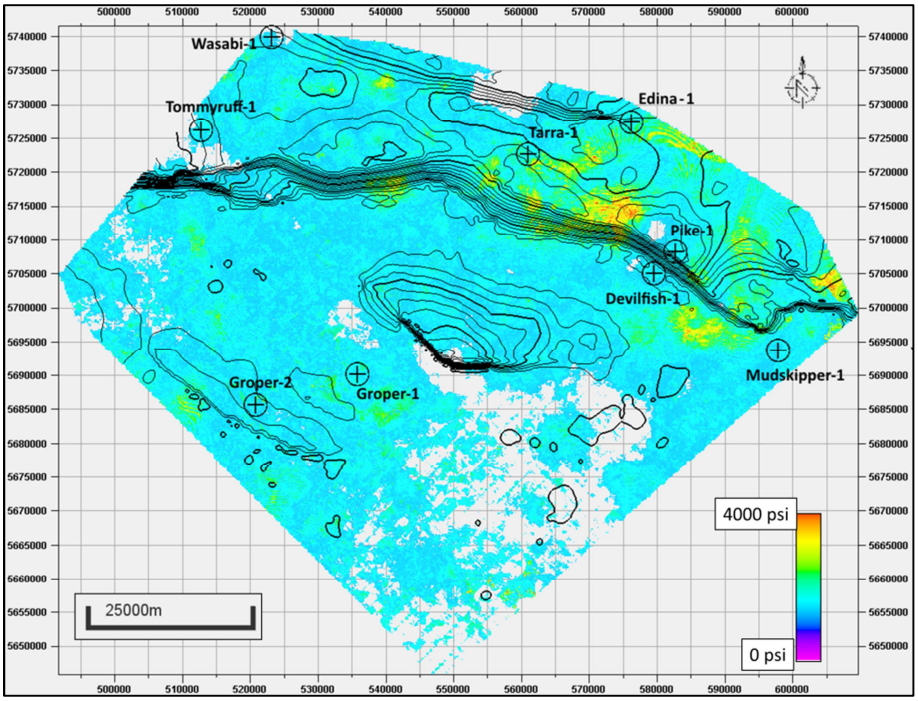

Figure 57. Top view to the 3D volume of seal capacity. Capillary pressure values lower than 1300psi are filtered out. Contours show a Basement to top Latrop thickness.

6 Chapter 6: Seismic Attributes and Sealing Potential

In this chapter, I will investigate the power of the familiar approach of *seismic attributes* to extract information from the seismic data for the purpose of evaluating the sealing potential. It attempts to identify the attributes which are useful in the investigation and narrow down the search criteria based on the findings.

6.1 Seismic attributes Analysis

An established method of connecting geological properties to their seismic signature is through the calculation of seismic attributes via calibration with borehole data (Chen and Sidney, 1997; Ciz et al., 2005; Nourollah et al., 2010; Urosevic et al., 2002). Different geological features of interest may be highlighted or better defined by specific attribute or sets of attributes. For example, to highlight the frequency shadows related to the presence of gas in pore space, frequency-based attributes are most effective. Sub-seismic discontinuities are best detected by waveform attributes. Seismic attributes are derived from analytic representation of seismic trace. There are many different attributes that could be related to various rock properties, lithology, and structural elements. Analyzed jointly, attributes are used to perform both qualitative and quantitative (when calibrated with well data) studies. Mapping of variations in the character of attributes (such as across chimney) are examples of qualitative uses of attributes, while estimation of reservoir properties like porosity and permeability are the subject of quantitative studies. Many attributes introduced in the industry are generally utilized in empirical ways and are hence often a debating subject.

Seismic attributes were calculated on the pre- and post-stack seismic data to investigate any relationship between such attributes and the sealing potential of the sealing shales. In general, it was investigated whether

- Seismic attributes could be related to the sealing potential of shales
- Identify the (class) of attributes which are likely identifiers of the sealing capacity

In this research, dip-steered attributes are also used to show continuity, or lack of it, in 3D, and make it easier to map complex discontinuities. Methodical approach was utilized to investigate the association of the most likely sub-category of the seismic attributes (Barnes, 2016; Chopra and Marfurt, 2007) with the target property (sealing potential).

6.2 Gippsland Basin

The starting point in relating the well data to the sealing potential can be the famous "shale identifier" well log: *Gamma Ray*. Shales are generally recognized by their characteristic high GR value. The assigned values are relative and can vary widely from shale to shale. However, within a specific unit/area, the range is usually confined to some limits. The gamma radiation that is detected on the well logs is due to Uranium, Thorium or Potassium particles in the minerals or organic matters. The high gamma signature of shale is generally due to their higher potassium content. Although higher readings on the GR log are a strong indication of a shaly unit, it does not necessarily tell us about the internal structure of the shale or its sealing capabilities. Figure 58 shows that there is no meaningful correlation between the shaliness of the Lakes Entrance Formation (as measured from GR log) and the corresponding capillary pressure measurements of the samples.

Shales of the Lakes Entrance Formation are of hemipelagic origin, which means they have marine organic input with some terrestrial influence. While distinct from the clean sands of the underlying Latrobe Group, their typical GR reading is not very high (between 50-90API). In fact, Figure 58 shows two classes of P_c measurements. Each group shows increasing values of GR readings correspond with increasing values of capillary pressure. However, the rates of increase are not identical for the two families. The separation of these two classes is somewhere around PC=1200^{psi}.

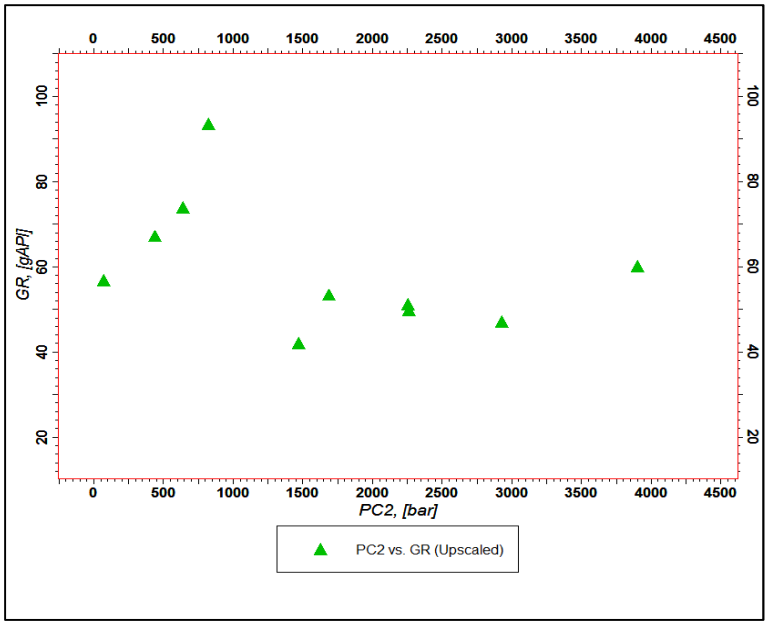

Figure 58. Up-scaled capillary pressure measurements and GR show little correlation.

The variation of the GR log readings within the shale package is indicative of the relative sea levels changes that affect the environment of deposition of the shale and their composition. Figure 59 shows some upward-fining packages within the Lakes Entrance Formation (indicated by decreasing GR readings upward) that are indicative of shallowing upwards of the depositional environment within each para-sequence. Such variations are visible in most of the wells in the area of study. Blevin et al. (2013) observe that the samples taken from the EOW have generally a higher sealing capacity. They discuss that the deeper samples from Groper-1 that have lower quality seal come from the Gurnard Formation and not the EOW part of the Lakes Entrance Formation. This observation fails for the Groper-2 sample that is taken from the EOW and reports the lowest record of MICP in the area of study. There is also the sample from Devilfish-1 that is taken from the shallower sections of the Lakes Entrance Formation (and not within EOW). Although it does not report a high capillary pressure measurement, it is not as low as the measurement from Groper-2. Figure 59 shows the relative location of the MICP samples from the sealing sequence. Interestingly, the readings on the Capillary Pressure values (P_C) do not correspond

with the location of the sample within the parasequence. In fact, some of the lowest quality seals samples come from the base of para-sequences (Groper-2) while the highest P_c measurement (Pike-1) is read close to the base of EOW sequence. From the prediction standpoint, GR is not a direct identifier of the sealing potential. It is observed that our best-sealing shales are not amongst the highest GR readings.

The gamma ray signature of a shale unit can help us with the mineralogy of it. “Shale” is a very compact term which refers to a large class of rocks and their various minerals. Although there are many similarities between the shakes, not all shales have a similar petrophysical, mineralogical or geomechanical properties. It is not difficult to imagine that mineralogy of shale may have an impact on its sealing potential. From this standpoint, better knowledge of the GR variations may be important to the sealing potential. It was mentioned that the gamma ray readings are a composite of the Thorium, Uranium and Potassium particles. A subclass of GR logs separates each band and can help whether the source is from a clay mineral (Potassium), heavy minerals (Thorium) or organic matter (Uranium).

Seismic attributes can be used to estimate well logs. In this case, we need to extract some attributes of seismic that can be utilized to estimate gamma ray. Hampson (Hampson et al., 2001) suggested a method that, through combining the original seismic and its relative attributes, an estimation of a target well log can be computed from the seismic traces. Any number of attributes can be input to this analysis, and the method determines the most relevant and the best number of combined attributes to be selected. This approach can be useful in tracing the lithology changes away from wells after the seismic-to-well tie has been completed.

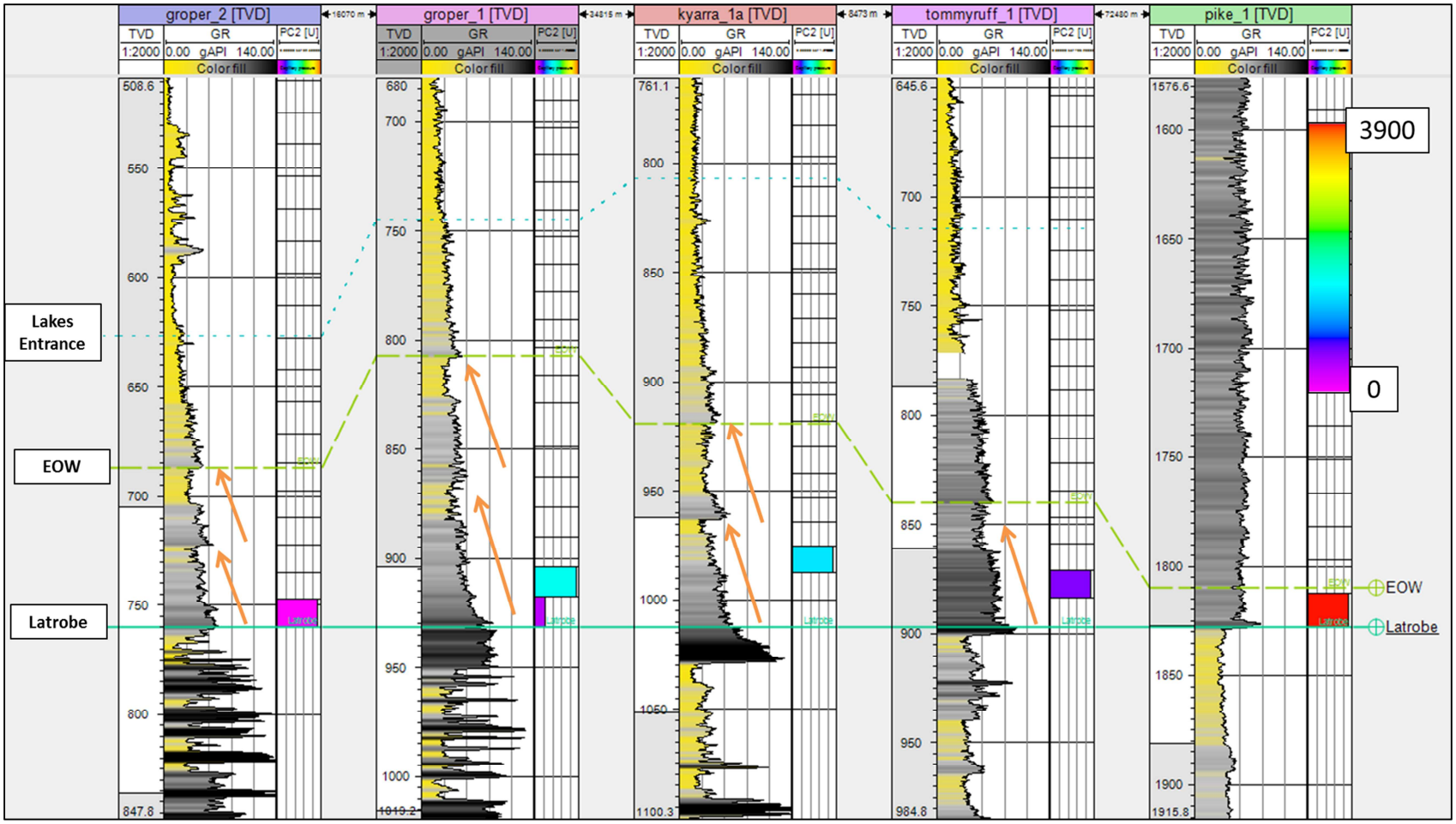

Figure 59. An arbitrary cross section between the wells on the southern platform shows the Para-Sequences within the EOW of the Lakes Entrance formation. The wells north of the Foster and Darriman faults (Tommyruff-1 and Pike-1) lose the prograding signature of the top seal (orange arrows). The MICP measurements were shown on the right hand column. The colour bar shows the ranges of Pc.

A select number of waveform shape, frequency domain (instantaneous and windowed) and spectral decomposition attributes are computed for this purpose and run through the process. The analysis (Figure 60) shows that the multi-attribute analysis can tie the input seismic and its attributes to the GR log with a maximum error of ~16API when using minimum 5 attributes and a three-point combination. This error is relatively high, especially for the GR signature of the Lakes Entrance formation that varies between 30 and 85 API. The results can still be used as a first-order indicator to sub-define the Lakes Entrance Formation and be calibrated with its local mineralogy. The predicted GR (computed off the seismic traces) was then input to Neural Network pattern recognition. The Neural Network attempts to separate those GR values that correspond to a certain range of mineralogy (identified by density, sonic, core samples, acoustic Impedance. The predicted Capillary Pressure (P_C) values show a meaningful correlation with the target PC which ensure the soundness of the Neural Network process.

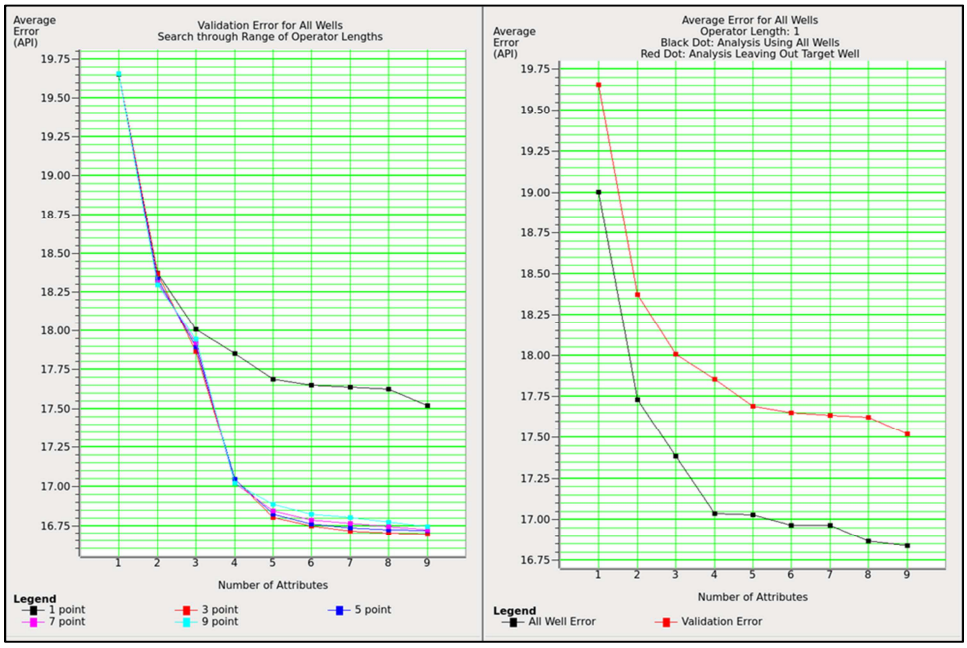

Figure 60. Multi-attribute analysis to estimate GR from seismic trace. The number of attributes which are engaged in the prediction process is tested (left) with the corresponding error of prediction to the target value (right). After a certain number of attributes, their linear dependence renders the addition of further attributes of limited use.

Using the potential ability of the predicted gamma ray in identifying shales and their mineralogy, further logs may help narrow the search for better seals. The seismic reflections are the result of a contrast between the product of density and velocity of the two layers in contact. Although one-to-one plot of density versus PC, or sonic and PC, do not reveal a clear trend, a XYZ plot of GR, P_C and density/DT values (Figure 61) shows some interesting features. Figure 61 is the same as Figure 58 except for the corresponding values of density (taken from RHOB log) and Sonic velocity (DT) are plotted as Z-values. The plot shows that, among the two shale families, the most competent ones have the highest recorded density and sonic values (orange to red colored). Therefore, the product of velocity and density (acoustic impedance, Z_p) should stand out on the GR-selected background. This will then correspond to the higher capillary pressure values. A cross plot of GR, PC and Zp shows the target values (Figure 62).

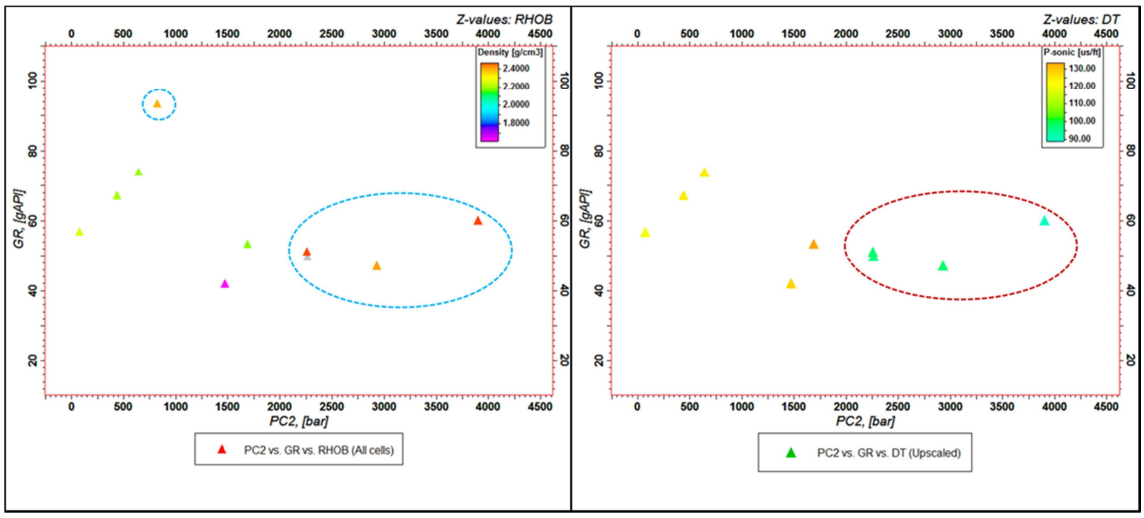

Figure 61. Pseudo 3D plot of GR, Capillary Pressure and Density (left) and the same plot for sonic velocity on the right. Outstanding areas on high sonic velocity and high density can form joint criteria for seismic to identify good seals.

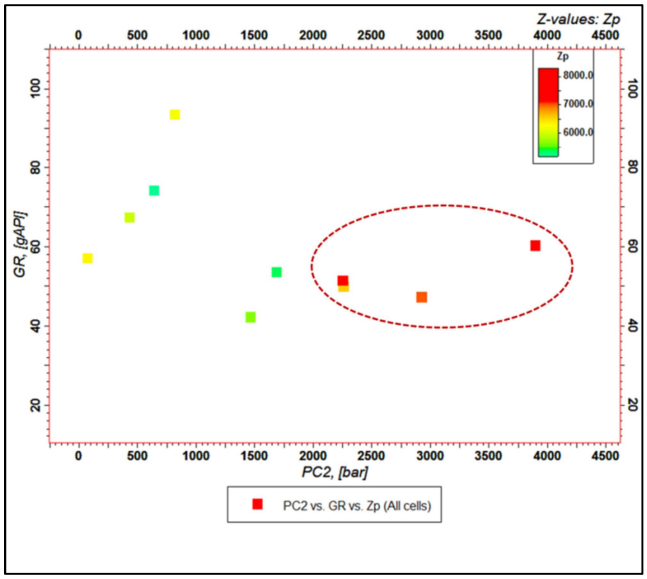

Figure 62. Pseudo 3D cross plot of GR, PC and Zp. A subset of the GR- families joined with the high compressional Impedance values correspond to good sealing potential

6.2.1 Pre-stack attributes

Pre-stack attributes require the conditioned CDP gathers and interpretation of seismic horizons on the pre-stack (CDP) domain. The advantage of calculating seismic attributes in the pre-stack domain is to add an extra domain (offset) to data, which highlights a wider range of rock physics properties of sub-surface. Disadvantage relates to lower signal-to-noise ratio compared to post-stack data.

Seismic inversion methods are well-established to study pre-stack seismic data. Seismic inversion attempts to extract the basic rock properties such as compressional and shear velocities and densities after seismic data were tied (calibrated) to logs. The seismic data were inverted within the target time window centered on the seal (Lakes Entrance shale). All the wells in the area of study had the minimum well logs to be incorporated in the inversion process except for Mellvile-1. Most wells have compressional sonic and density log runs within the zone of interest; however, only Wasabi-1 has shear sonic.

The pre-stack seismic inversion process requires the S-wave velocity of the rocks. Since only one of the wells in the AOI (Wasabi-1) has shear velocity data, the shear logs can be estimated at other locations using empirical relations such as Castagna (Castagna et al., 1985) or forward modelling through rock physics. The disadvantage of using a Castagna's method, however, is that the Z_s-Z_p relationship follows linear trend with errors that may not be always acceptable, as is shown in Figure 63.

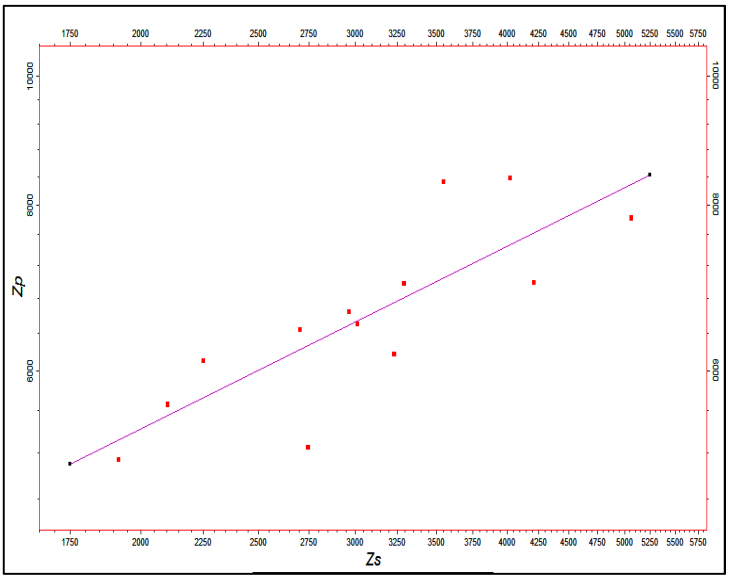

Figure 63. When Shear wave is estimated from the P-wave, Zs (Shear Acoustic Impedance) is not independent of Zp.

Therefore, in this area of study, Z_p is the main output of the seismic inversion process. However, analysis of this parameter shows that it has a very weak to non-existing relation to the sealing potential in this area of study (Figure 64). This initially contradicts the results of Figure 62 where relatively higher values of acoustic impedance were associated with higher sealing potential. The reason behind this was the third element that was used to construct the Pseudo-3D plot of Figure 62 (GR). Gamma ray was shown to have little reliability in predicting the sealing capacity and its prediction from seismic is not very reliable (Figure 60). A high range in the predicted values of GR (gamma ray) for the Lakes Entrance Formation will leave limited use for it to take part in any prediction algorithm dependent upon it. Further explanation is the variations of the density log over the range of the capillary pressure which will

impose further doubt (in the inversion model) over the validity of acoustic impedance as a proxy to estimate P_c.

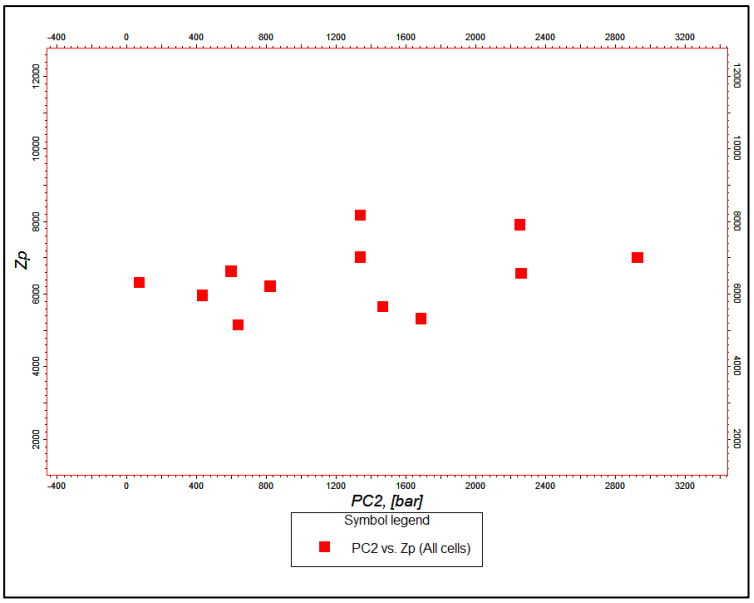

Figure 64. Acoustic Impedance (Compressional) shows little correlation with the sealing potential of the Lakes Entrance formation.

6.2.2 Post-stack attributes

Numerous post-stack seismic attributes exist, and to try every individual one randomly is an exhaustive task. In order to reduce the wasted CPU time and increase the efficiency of the search to find the correct class of attributes, selected group of attributes were given higher weight. However, without a walk-away VSP survey, trial and error within the selection of attributes is inevitable (Miller Douglas and Spencer, 1994). Apart from laboratory measurements (which are performed on small samples), VSP surveys are very useful in estimation of anisotropy parameters (Armstrong et al., 1995; Dewangan and Grechka, 2003; Pevzner et al., 2010).

"Stratigraphy-related" attributes (Such as Chaos) show better internal characters of the seismic character, which is related to the geology of the rock (such as lithology, facies, etc), in contrast to structural ones (dip, azimuth and curvature), and were tested first. Any one of the features of interest

(anisotropy, lithology or sealing potential) may be revealed by different attributes, such as Chaos, Sweetness, instantaneous and/or waveform attributes. The P_c measurements come from well samples that potentially represent thin layers of lithology with a different class of sealing potential within the shale sequence. The seismic waves may be affected by such changes in lithology, and represent such changes in waveform attributes or frequency content. Identifying such changes with attributes may enable us to indirectly estimate their sealing potential.

Of particular importance was to test frequency-based attributes that can be related to the intrinsic attenuation of the rock. Indeed, Lakes Entrance is a carbonaceous shale unit that displayed apparent attenuation of seismic signal, above the Top-Latrobe unconformity. Since competent sealing strata are not uniformly spread within the Lakes Entrance Formation, waveform attributes were also tested to detect sub-seismic discontinuities within the unit.

The attributes were calculated on the 2D seismic line grids of GDPI10 in the area of study. In order to interpolate the values of attributes between the lines, seismic was resampled (at 4msec) and up-scaled to the constructed 3D model. The up-scaled seismic attribute cells were then interpolated through geostatistical methods. Because of the abundance of data points and their range, pixel based algorithms can run more efficiently and honor the spatial geostatistics of data (Nourollah, 2011; Pyrcz and Deutsch, 2014). Random Gaussian Simulation was used as the algorithm of choice to complete the interpolation. At first, both dip and strike seismic lines are considered to ensure a smoother distribution of modelled geostatistical facies. However, the results were also compared with the same attributes calculated on dip, and strike lines separately.

The seismic signature of the Lakes Entrance Formation is distinguished from the underlying sandy Latrobe by a characteristic drop in the relative amplitude and lower frequency content. While *Instantaneous Q* shows no correlation with the sealing capacity, the *Trace Gradient* shows a declining

trend with increasing P_c (Figure 65). The result shows potentially smaller groups of trends on the plot. Such trends can be of further use in establishing the better relation between the seismic and the sealing potential. These sub-trends could be caused by the change in shale composition, but may also be caused by insufficient SNR.

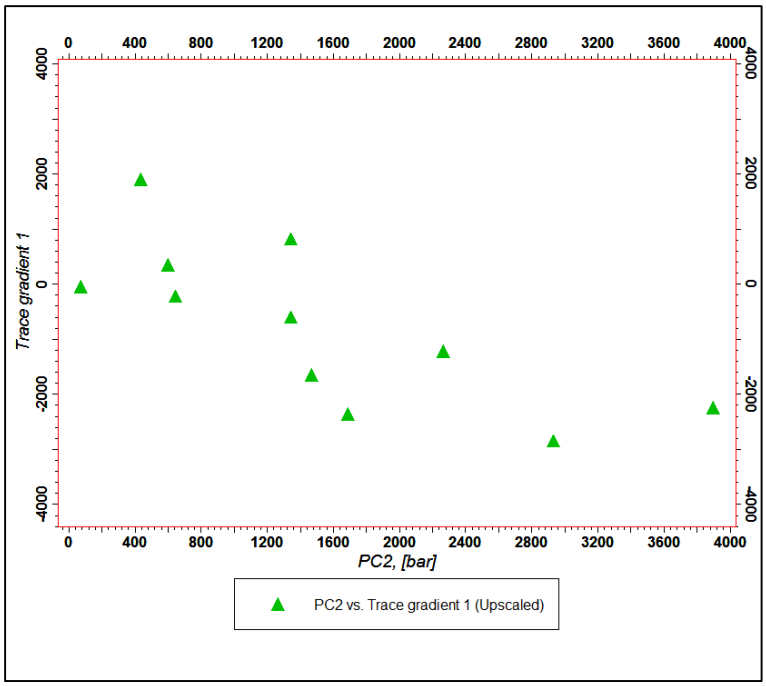

Figure 65. A steady decline in the trace gradient attribute is visible against the corresponding Pc values in the Lakes Entrance formation.

When superimposed on the original seismic, the target attributes can highlight specific features of the original seismic. This is demonstrated in Figure 66, where instantaneous Q and Trace Gradient are shown together with the amplitude section. While instantaneous Q brings the frequency content forward and highlights local variations, the Trace Gradient shows distinct global "texture" that provides some idea of lithology. It is clear that different sets of attributes have to be analyzed carefully to reveal the most responsive attributes to the property under observation. Such process can take significant time unless put in context of the geological setting of the area under investigation.

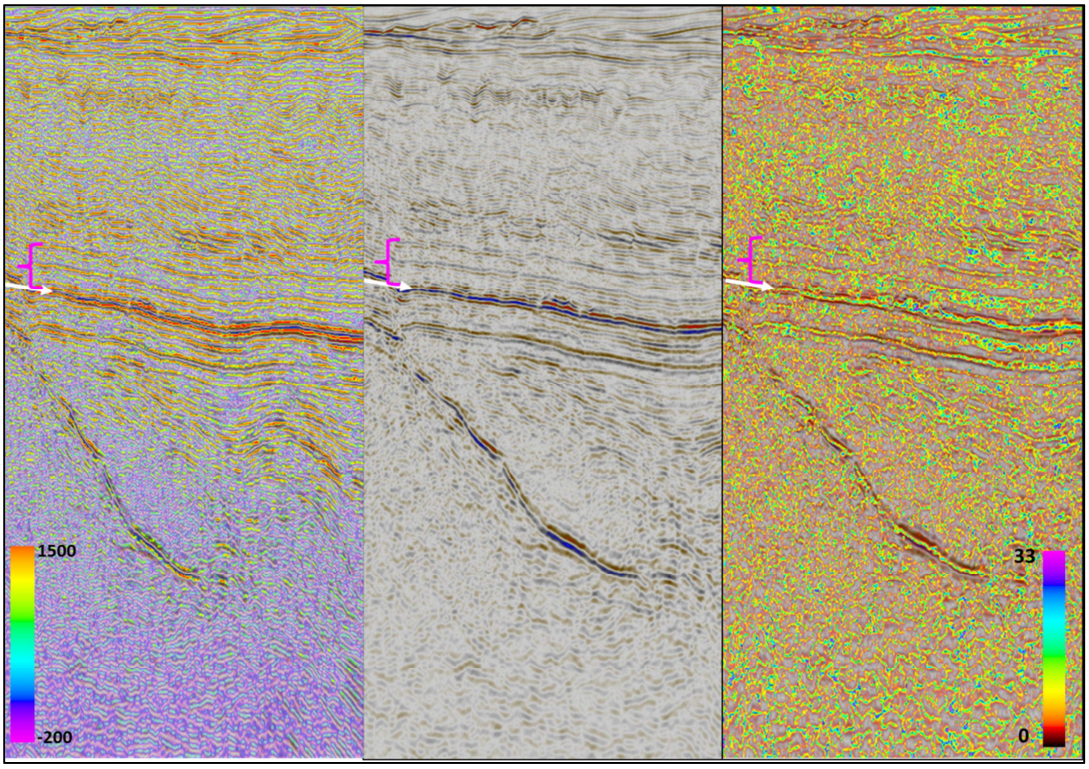

Figure 66. A section of GDPI10-S3 (middle) with overlays of the Trace Gradient (left) and the Instantaneous Q (right). The white arrow indicates the top of the reservoir (top Latrobe Group) and the pink bracket shows the top seal package.

The calculated Trace Gradient attribute was used as a trend to interpolate between the P_c measurements at wells. Figure 67 displays the extracted map of the sealing potential on the lower Lakes Entrance shales (immediately above the Latrobe).

It appears that seismic attributes which relay information about the seismic quality factor (or its variations) are better candidates in identifying the changes of sealing capacity of shales. Attempts to predict V_{shale} from GR using the seismic data faces difficulties and shows little predictive power.

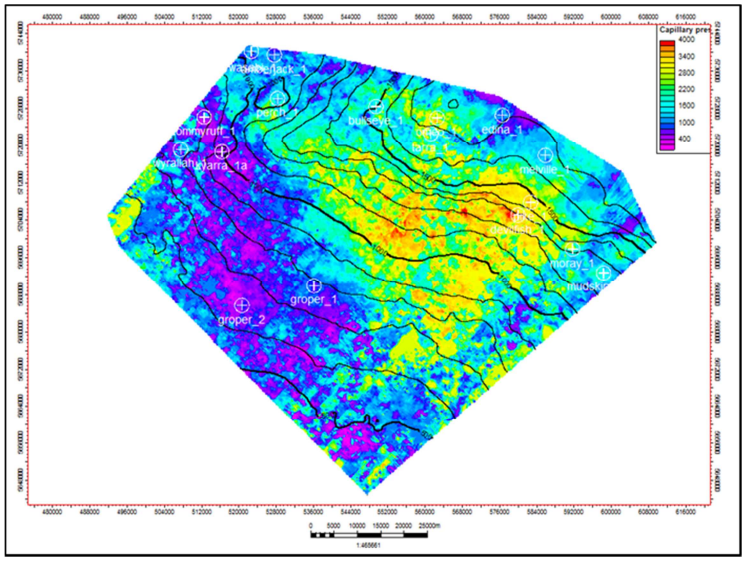

Figure 67. Predicted Capillary Pressure (Window of 12msec) based on geostatistical (co-kriging with best attribute) analysis. The time structure map is the top Latrobe structural map.

6.3 Exmouth Sub-basin

The capillary pressure samples that were analyzed in the Exmouth Sub-basin primarily belonged to the Muiron Member of the Barrow group. The Muiron Member is the distal facies of the Barrow Delta that mostly comprises fine silts and clay. The GR signature of the Muiron Member is a consistently high reading. This is a typical signature for shale-dominated facies for distal deltaic sequences.

The Muiron Member is a sealing unit that overlies the turbidity sands of the Macedon Member. The transition is abrupt and distinguished. This is because the turbidites are relatively fast depositional features compared to deltaic sequences. Turbidites are sudden flushes of sands/silts that have travelled down the submarine ramp/shelf and are deposited as fans within generally shalier facies (Zane et al., 2010). Therefore, the contact between the turbidite sands (Macedon Member) and their overlying sealing shale is sharp (Figure 68).

Although the outstanding GR character of the Muiron Member makes it easily distinguishable on logs, its massive and blocky character leaves little room to correlate with its sealing capacity. Neither gamma ray nor compressional sonic show any relation to the sealing capacity of the sealing sequences (Figure 69). However, if we limit the investigation to the Muiron Member only, and combine the two diagrams in Figure 69 (to build a pseudo-3D plot- DT values in color), we can see that, despite a lack of direct trend between GR readings and their corresponding P_c values, two separate groups of samples on the diagram show a distinctive separation in their DT values (Figure 70-left).

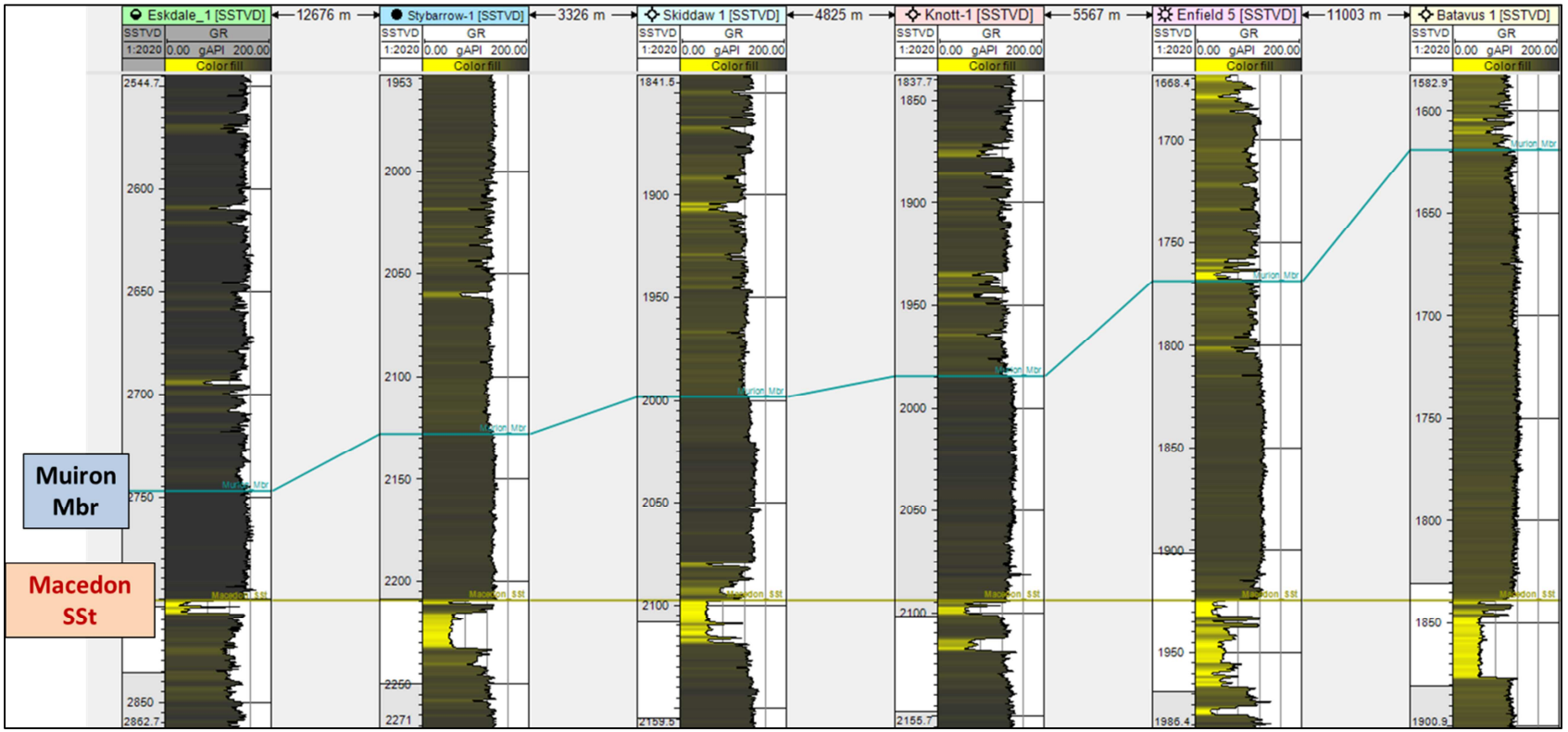

Figure 68. Well section in Exmouth Sub-Basin. The Muiron Member shows a monotonous GR signature which is typical of marine shale. Yet the sealing potential of the Muiron shale varies across the field.

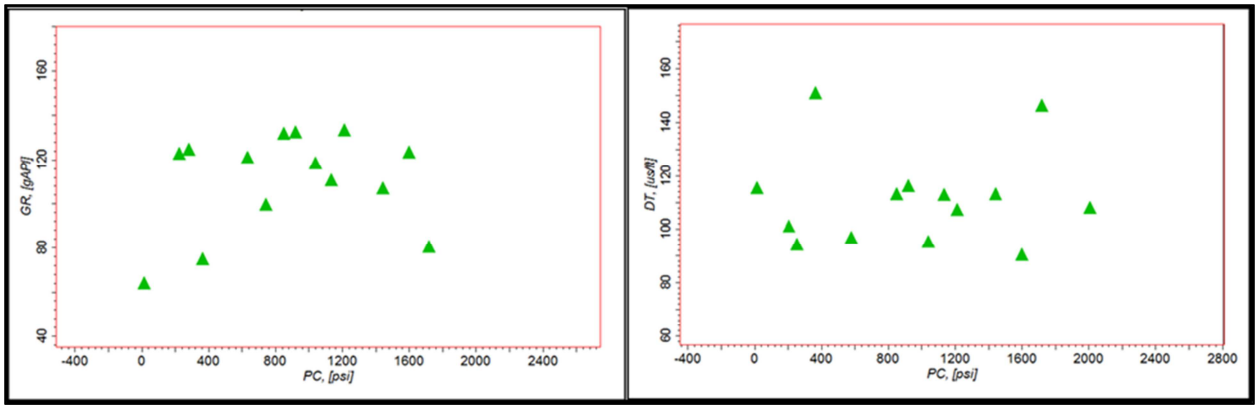

Figure 69. Shown are: left-GR and right-Sonic (Compressional) values of the sealing sequences in Exmouth sub-basin

Despite the lack of any trend within the distinguished group on Figure 70 (which eliminated the predictability of this approach), those samples that have a relatively higher sealing capacity can be grouped. Similar grouping can be made on the plot of P_c-RHOB-DT (Figure 70, right). The combination of DT and RHOB readings can be combined to limit the lowest readings of capillary pressure.

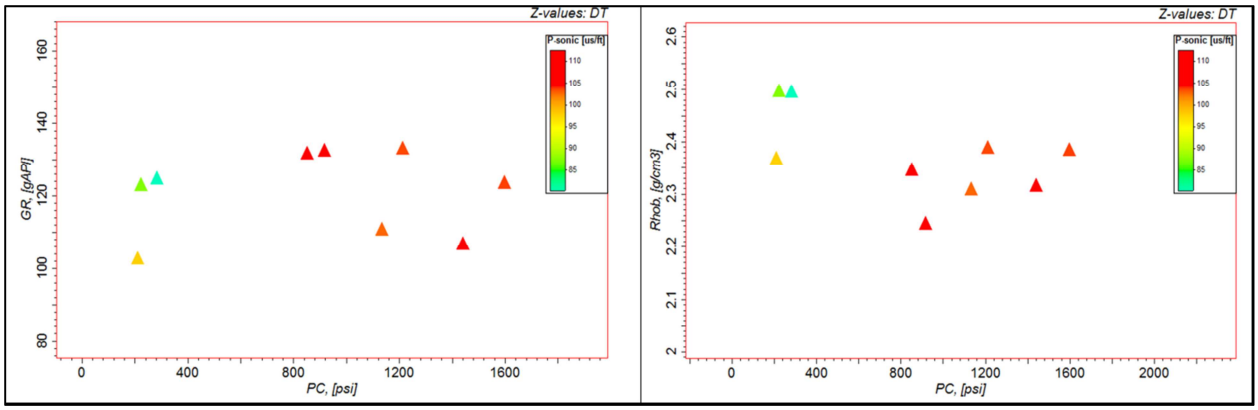

Figure 70. Psudo-3D plot of Capillary pressure against gamma ray (left) and RHOB (right) for samples of the Muiron member. Compressional sonic is the third vector and in color.

The only log reading that shows a reasonable trend with the increasing capillary pressure values is DT-shear (Figure 71, left). When plotted for the values of Muiron Member samples, the DT-shear log slowly increases with the sealing capacity. A combination of this trend and the groupings of DT-compressional and RHOB in Figure 70 will enable the separation of highest quality seals (Figure 71,

right). This suggests that combination of AI and EI (Elastic Impedance) may be zoned to highlight good sealing capacity. The relationship is investigated by comparing the inversion product Vp/Vs and the range of P_c values (Figure 72).

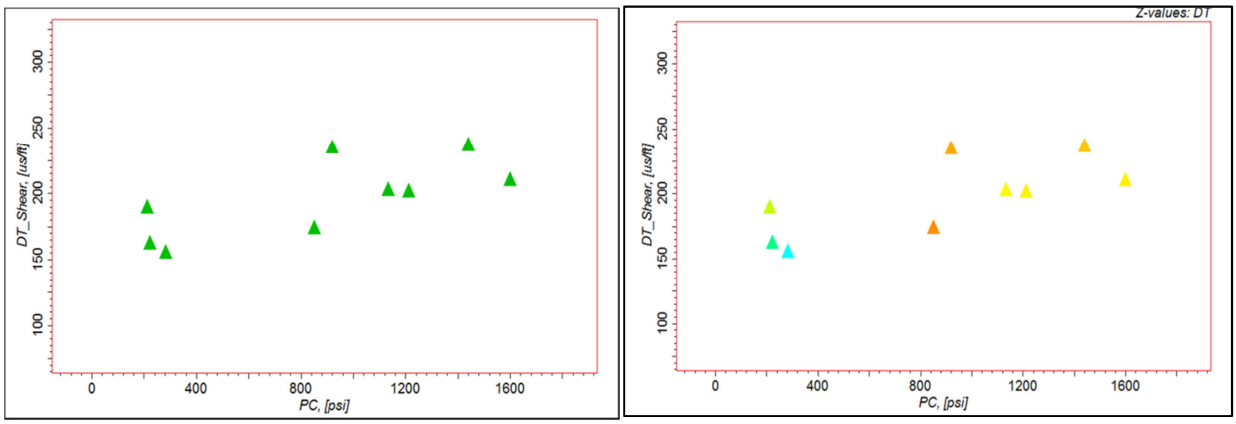

Figure 71. Plot of sealing capacity against shear sonic log (in Muiron member) shows a reasonable linear trend (left). When combined with DT-compressional, it can potentially separate the highest quality seals.

Although a mathematical function can be fit to the plot of Vp/Vs and P_c, it lacks any meaningful trend to make it useful for prediction purposes. This means a blind mathematical fit will lead the prediction process to where ratio V_p/V_s=2 could mean sealing capacity of either ~300^{psi} or ~1500^{psi}. Such effect is due to how sonic logs measure the compressional and shear velocities of rocks. These findings can be used to train the neural network. It is important to remember that shear and compressional data can be extracted/estimated more readily from the surface seismic data compared to other well such as GR or resistivity data. However, estimation of non-elastic logs using seismic data is still possible through Rock-physics modelling, neural networks and seismic attributes (Hampson et al., 2001; Mayer and Larson, 2014; Timko, 2003; Werthmüller et al., 2013).

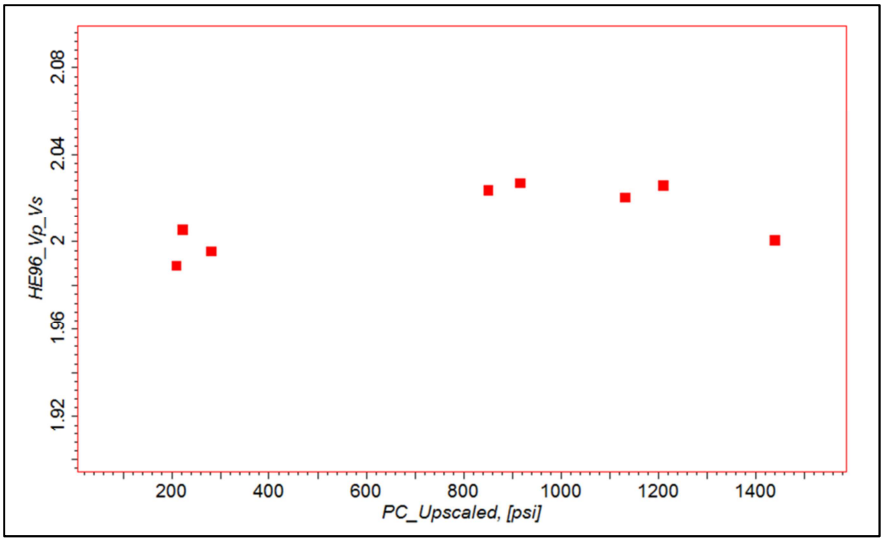

Figure 72. Comparison of compressional to shear ratio (Vp/Vs) and the capillary pressure for Murion member. A good mathematical fit can be run through the data but no predictable trend is observed.

As was the case with the Gippsland basin, the best approach to extract the velocity and density data from the seismic is through seismic inversion. Post-stack seismic inversion is usually good at returning the Z_p (compressional acoustic impedance) and, to a degree of accuracy, the Z_s (shear acoustic impedance).

Since the area of study is covered with good quality 3D seismic volumes, the post-stack inversion is the preferred approach. The pre-stack inversion of HE96 lines was tied in with the 3D results to better estimate the Z_s values.

The gamma ray estimation appears to be less critical in the case of Muiron Member samples, as explained above. Nevertheless, to estimate the GR away from the wells, and not entirely relying on geostatistics, multi-attributes of seismic were calculated and run through the algorithm explained by Hampson et al. (2001). The attribute sets that were used for the prediction process were Chaos, Amplitude Envelope, Instantaneous Frequency, Average Frequency, First Derivative, Amplitude-weighted Frequency, Dominant Frequency, Instantaneous Phase and RMS amplitude.

6.3.1 Pre-stack attributes

Despite the promising trend that is visible between the sealing potential (P_c) and shear sonic velocities, the extracted Z_s values from the post-stack inversion do not preserve such a trend. The reason can be attached to the fundamentals of how shear acoustic impedance is calculated in the post-stack inversion. Post-stack inversion is mainly aimed at compressional acoustic impedance and the shear impedance is a scaled version of Z_p when a model-based inversion is used. As a result, the distribution of the Z_s versus P_c looks very similar to that of Z_s versus P_c. This similarity is intensified even further in case of 3D seismic data due to the 3D migration process that homogenizes the medium in the process. Figure 73 shows that the post-stack Z_s values show no correlation with the sealing capacity.

A well-known way to estimate the shear impedance of the subsurface strata is the pre-stack seismic inversion. For the area of study (Exmouth Sub-basin), the pre-stack inversion was performed on the select sub-group of the HE96 survey that are parallel to the direction of $\sigma_{H\text{-}max}$. The inversion requires that a low-frequency model is calculated. This model was constructed based on the well data. The well data also provides the means to estimate the relationship between the Z_p, Z_s and density (Hampson et al., 2005). Each two of these parameters generally has a linear relationship in the logarithmic coordinate. There are enough DT-shear logs to have a confident estimate of Z_s in the study area.

There are 9 seismic lines that fit in the area of study and give a reasonable coverage of the area (Figure 18). When tied to wells and inverted, an estimate of the Z_p and Z_s values for the target levels is generated. Figure 73 shows that, although not a very high correlation, but the pre-stack estimation of Z_s shows a steady increasing trend with P_c. This is consistent with the observation made between P_c and DT-Shear logs (Figure 71-left). The calculated pre-stack impedances were along 2D line trajectories and not all the wells had a direct nearby value. Geostatistical interpolation was used to fill in between the lines and derive an upscale estimate of the impedance in immediate vicinity of the well and its P_c values.

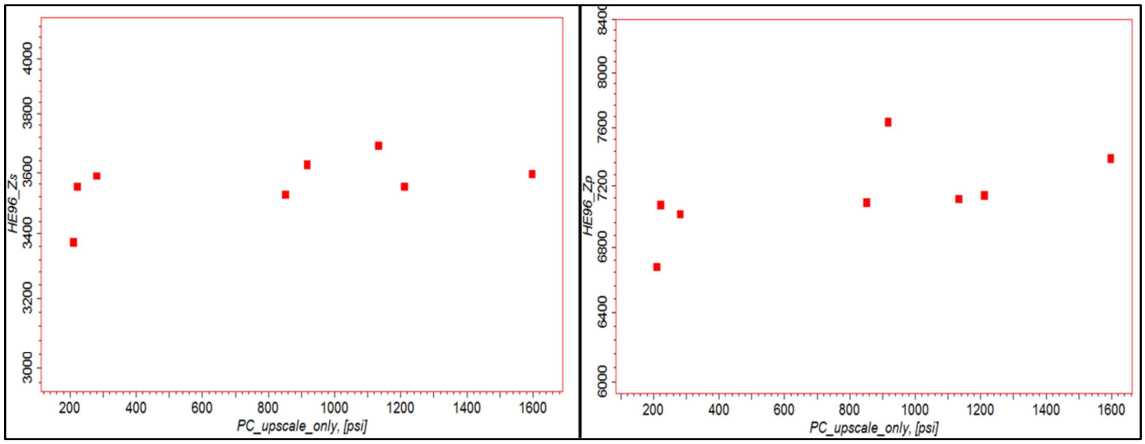

Figure 73. Cross plot of Z_s versus P_c (left) shows a weak climbing trend. The same trend can be envisaged on the right hand plot of Z_p versus P_c. The similarity of the trends implies linear dependence of the two attributes.

The similarities between the trends and values of the two plots of Figure 73 imply that the two attributes are not linearly independent. Therefore they are not really two useful (and independent) seismic attributes. In terms of information value, they are a unique attribute (Barnes, 2016; Chopra and Marfurt, 2014). Hence additional help is needed from other seismic attributes.

6.3.2 Post-stack attributes

Compared with the case study of the southern Gippsland, the Exmouth Sub-basin benefits from the coverage by 3D seismic volumes. The two seismic cubes that cover the AOI are the Vincent 3D and HCA2000. These two volumes underwent amplitude balancing and phase-matching, and were post-stack merged to generate a mega-cube. The mega-cube makes the calculation of seismic attributes easier as it requires a single run.

Out of the major groups of the attributes, less attention was given to geometric attributes. This is due to the nature of such attributes that reveal the structural features such as faults and fractures. They are still required to limit the analysis between the structural elements and avoid interferences when computing the attributes which are more sensitive to the "noise" such as instantaneous attributes. The sealing capacity is related to the internal structuring of the rock units and is perhaps best

related to stratigraphic seismic attributes. Such attributes are generally categorized under wavelet or instantaneous attributes. However, they still need to be averaged within the sequence or across selected intervals of the sequence to be a more robust indicator of the lateral variations in properties.

In the first instance, a set of attributes that show some relationship to the sealing potential are selected for further analysis. Next, further calibration of the attributes is accomplished by utilizing all logs. This enhances the initial trend observed. The attributes are now suitable to use in the neural network estimation of the target value.

Sealing rocks are generally associated with shales and shale sequences. They are easily observed on seismic data due to their continuity over large areas and monotonous or "washed-out" reflection character. Hence shale sequences can easily be analyzed with instantaneous seismic attributes, particularly when computed within selected sequences. Instantaneous attributes computed in such manner are sometimes called sequence attributes. Variation in shale properties is often best observed with frequency-based instantaneous attributes (Nourollah et al., 2010; Urosevic et al., 2002). Hence the first seismic attribute to analyze was instantaneous *Q* (*Instantaneous Quality* is the ratio of frequency to amplitude decay rate). Within the Muiron Member, unlike the case of southern Gippsland, the seismic Q shows a consistent drop against increasing sealing potential (Figure 74).

The presence of 3D seismic data is a factor for obtaining smoother results in the seismic Q results, but the primary reason is more likely to be the quality and composition of shales in the Muiron Member compared to that of the Lakes Entrance. The Muiron Member is composed of marine shales with high clay contents that show a consistent high gamma ray reading for the entire section (Figure 68), while Lakes Entrance varies in composition from bottom to top and becomes more marly (Figure 59). This compositional change is also the reason two different types of seismic quality attributes work for each shaly unit.

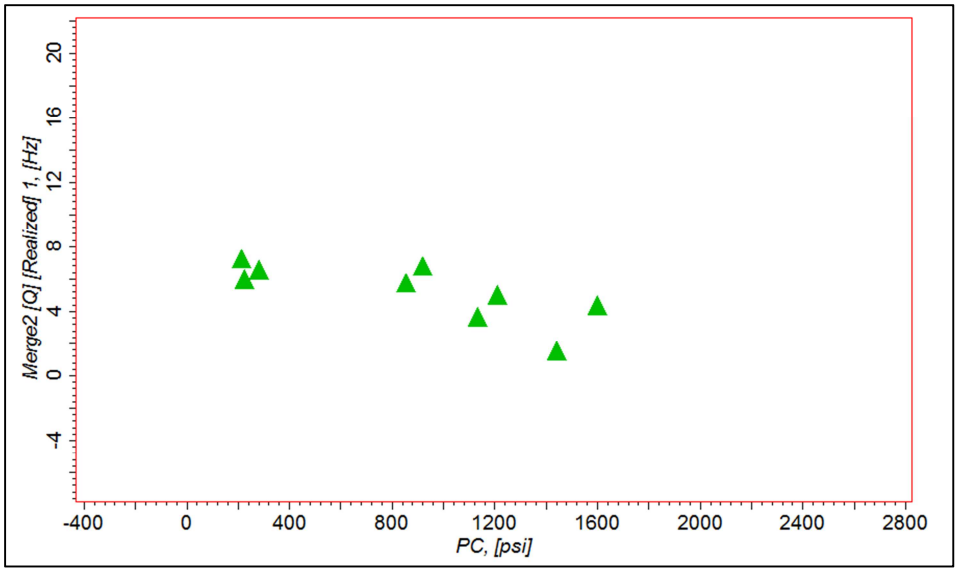

Figure 74. The seismic attribute "Q" (quality) decreases as the sealing potential increases. A reasonable correlation of ~75% can result from a second order polynomial fit.

The Q factor that is measured by the instantaneous Q attribute is a relative Q factor. The declining trend in Figure 74 implies the declining seismic quality (frequency content and energy) with increasing sealing potential of the Muiron shale. It likely points out that higher concentration of phyllosilicate minerals, which are known for their seismic absorption (Barnes, 2016; Hamilton, 1972; Johnston, 1981), are present and perhaps share more or less the same layering direction. Therefore, they disperse less of the incident seismic and absorb more.

Figure 74 shows that for the Muiron Member, the Instantaneous Q can act as a weighing factor to map the sealing values away from the wells. When the P_c values at wells are geostatistically co-kriged with the up-scaled instantaneous Q attribute, a more integrated map of the sealing potential of Muiron Member is generated. Figure 75 shows the average sealing capacity of the Muiron Member as the result of such process.

It can be observed that Muiron Member sealing quality improves towards the east and over the Enfield Field. In contrast, the seal is of lower quality over the Eskdale-1 and -2 wells on average. Although Figure 75 shows that the sealing potential is much higher towards the SE, it does not rule out thinner high quality seals within the Muiron Member (Figure 76).

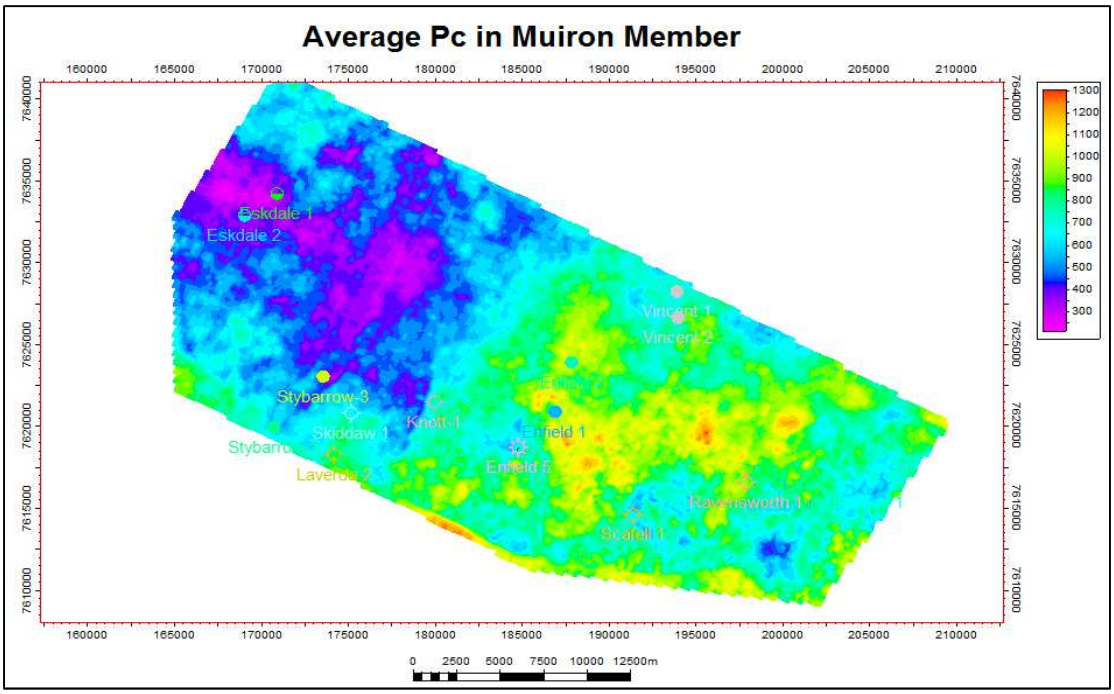

Figure 75. Average sealing potential that is calculated for the Muiron member when Instantaneous Q is co-Krigged with Pc.

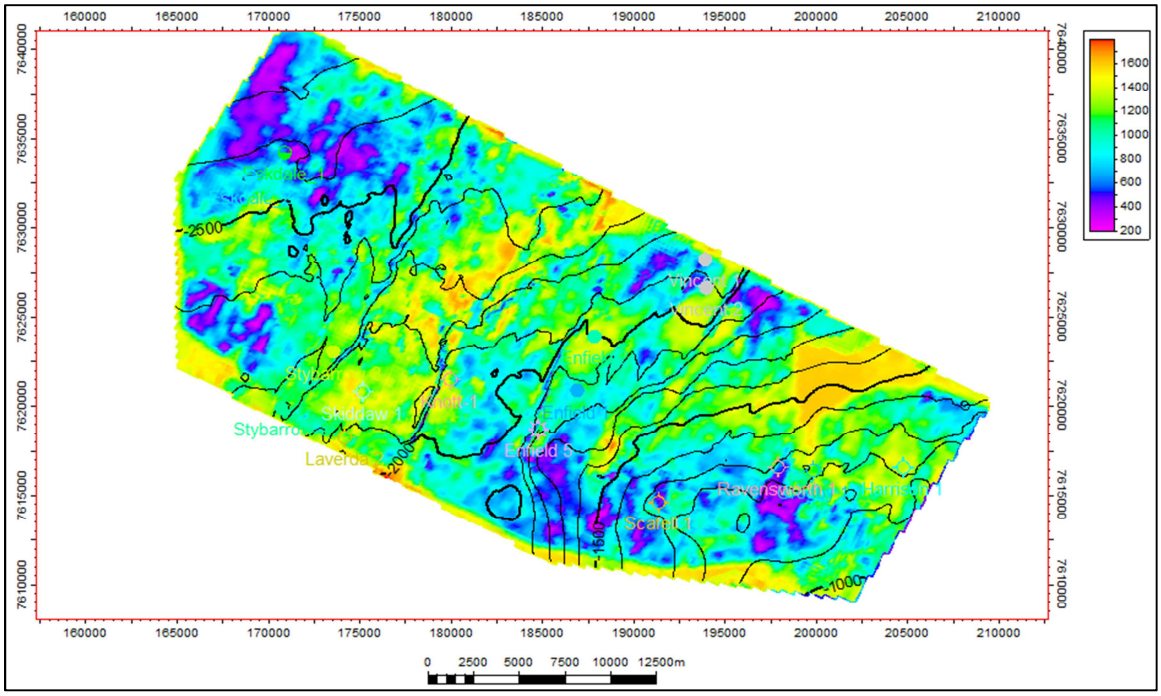

Figure 76. Extraction of Pc values (co-krigged with Instantaneous Q) at Muiron minus 20msec

7 Chapter 7: Analysis of the Case Studies

The sealing potential of two shaly sealing formations studied, have apparent differences in terms of tectonic history, depth of burial, geological age and the clay content. Capillary pressure and the pore throat radius have an inverse linear relationship and can be used interchangeably. However, pore throat values are small and it might be easier to use Pc instead. To illustrate the potential of each area to withstand a hydrocarbon column, the measured capillary pressure (Pc) of each sample is converted to its equivalent height using equation (5). Appendix 5 illustrates the hydrocarbon column heights that can be held for each sample within the two areas of study.

7.1 Calibration to saturated shale

Most shale samples are dried in the laboratory before their corresponding stiffness being measured. Saturated shales show significant decrease in the bulk and shear modulus (Aminul Islam and Skalle, 2013; Ghorbani et al., 2009; Josh et al., 2012). Triaxial drained and undrained tests on saturated shale samples by Aminul Islam and Skalle (2013) shows that Lame constants are approximately λ=4.53 and μ=1 at 25MPa which is far below the recorded values for dry shales by Blangy et al. (1993). It might look appealing to back calculate the fully aligned coefficients (a_1,a_2 and a_3) for saturated/in situ shales using equations (45) to (52) and calibrate them with C_{ij} values of Table 5, however this approach will faces problems as the distribution of water (as wetting phase) is not uniform within the shale. Most water absorption happens along the shale domains in thin layers and reduces the isotropic Lame constants. The vertically connected pipes or capillaries have a large impact on C_{11} and should be considered as an anisotropic effect. Therefore the addition of saturation to the dry model and calibrate it with the seismic or core measurements is the primary approach that is taken in this research. Table 5 shows the stiffness coefficients of the Muderong shale (Carnarvon Basin, Australia) reported by Dewhurst and Siggins (2006). Based on these values, ε is calculated to be 0.238 and 0.226 for 5MPa and

52.5MPa measurements respectively. Dewhurst et al. (2002b) also report very good alignment of shale and silt particles to the bedding plane. This means the a_i values of (50) to (52) are closer to the perfect alignment values of W_{400} and W_{200}. Using the W_{400}-W_{200}-ε plot of Figure 12, the corresponding range of W_{ij} for the Muderong shale sample is $0.0153<W_{200}<0.024$.

C_{ij}	GPa – at 5MPa	GPa – at 52.5MPa
C_{11}	19.5	26.6
C_{33}	13.2	18.3
C_{44}	3	4.5
C_{12}	6.7	9
C_{13}	7.6	16.2

Table 5. Elastic coefficients of the Muderong Shale at two confining pressures as measured by Dewhurst and Siggins (2006).

The measurements of the Muderong shale stiffnesses are helpful because:

- it belongs to the same geological settings as one of the case studies where we have some capillary pressure measurements; and
- The measurements were made on a saturated shale sample which resembles the real geological settings.
- MICP measurements were performed on the same sample. Therefore it can provide a calibration point.

An alternative to fully model the saturated shale is to use the forward modelled W_{ijk} values from the above mentioned method in conjunction with the lithology (clay mineral content) and assign an approximate W_{200}-W_{400} set. The studied Muderong shale sample has an approximate P_c value of 6000^{psi}

(Dewhurst et al., 2002b) that is much higher than the highest measurement in the Exmouth or Gippsland case studies. The corresponding ε value for this sample from Table 5 is almost 24%. Close to 75% of the sample is comprised of clay minerals and the W_{200}-W_{400} set is modelled (Chapter 2.9.2) to be close to 70% of the maximum values. Using equations (45) to (52) yields the C_{ij} values of the near-ideal dry seal as C_{11}=38.3GPa, C_{33}=22.1GPa, C_{12}=17.2GPa andC_{13}=13.8GPa. The ε value for the modelled dry Muderong should be nearly 0.36. The reduction is due to saturation of pore space (17%) which corresponds well with the prediction of Dvorkin et al. (2007) (refer to their Figure 3). In order to correct the compressional modulus (M=C_{11}) of the 70% aligned shale to the measured values, the ideally aligned wet shale will have C_{11}=27.9GPa, C_{33}=18.9GPa, C_{12}=9.6GPa, C_{13}=10.9GPa and C_{55}=4.3GPa. Figure 77 shows the modelled group and phase velocity behavior of the ideal shale sample.

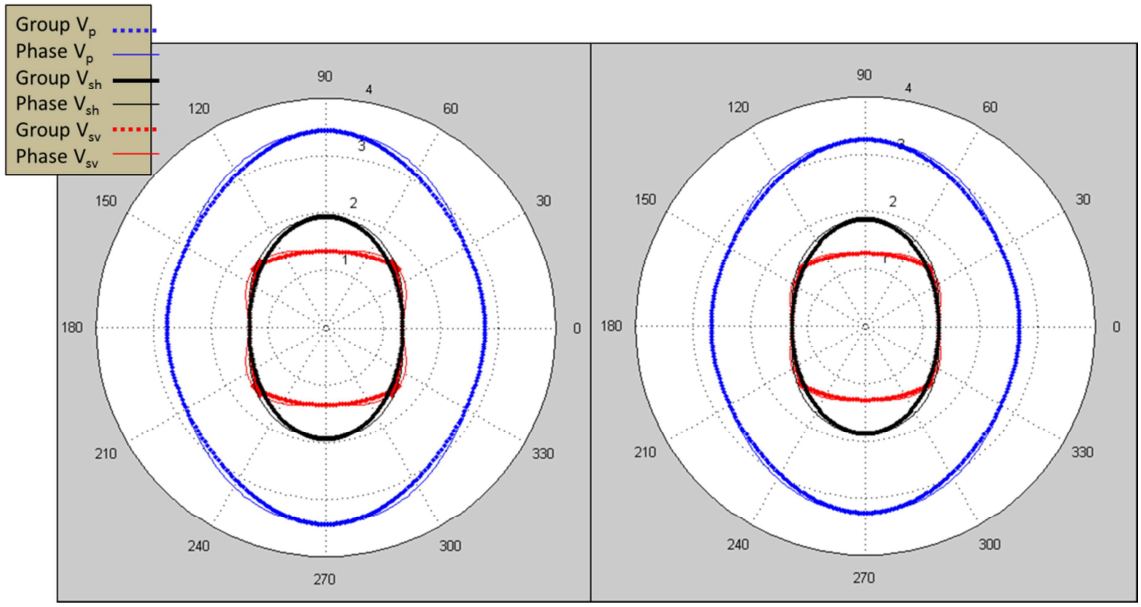

Figure 77. Group and phase velocities modelled for the ideally aligned wet shale (left) is close to that of the pressured Muderong shale (right). Vertical velocity is along direction 0-180.

7.2 Analysis of ε-P_c plots

In order to have a better understanding of the variations of the sealing potential with ε, Figure 43 & Figure 53 are compiled in one plot. Figure 78 shows a comparison of the sealing capacities of the

two case studies versus their corresponding ε values. The two dashed trend lines represent the data trends and allow a simpler comparison between the two groups of data. The distinct difference between the two groups (and their trend line) reveals the higher seismic anisotropy of the shale samples from the Exmouth Sub-basin (Green trend line in Figure 78) compared to the samples of the Lakes Entrance Formation (Red trend line in Figure 78). Such difference in anisotropy is visible from the core and cuttings samples of the two locations. The samples from the Muderong Shale and Muiron Member generally show a higher alignment compared to the ones from the Lakes Entrance Formation. However, both groups show independent increasing trend with increasing capillary pressure (tighter capillary pipes). The rate of increase in the anisotropy is also interesting. Increasing P_c is accompanied by a rapid rise in the corresponding ε values in the Exmouth data while a gentler slope is observed with the data from the Gippsland. Such behavior is in concert with the predictions of Chapter 3 where better-aligned shales are more affected by the introduction of capillary pipes compared with less well aligned shales.

It is also clear that absolute values of ε are not to be used as "blind" predictors for the sealing potential. For P_c values of about 3000 ^{psi} the two data groups show a difference of 20% in their corresponding values. Therefore it is important to know the background lithology and the level of shale domain alignment before the modelling. Another observation that can be made from the comparison plot of Figure 78 is the relative dispersion of points from the Exmouth Sub-basin compared to the Gippsland Basin. This is due to the relative scarce suitable seismic data in the Exmouth (vintage 2D lines-survey HE96) opposed to newer and denser seismic in the southern Gippsland (GDPI10). Such setback in the seismic data from the Exmouth is well compensated by abundance of points from the well with P_c measurements. Reprocessing of available 3D seismic over the area of study in Exmouth should improve the data dispersion.

The difference in lithology of the two seals in Exmouth and Gippsland plays an important role in the separation of their sealing-anisotropy trend. Smectite is the weakest of clay minerals (and one of weakest of all minerals) in terms of its geomechanical strength. Common clay minerals that are constituents of shales are Illite, Kaolinite, Smectite and chlorite. The higher the smectite content, the weaker the shale is. Although the Muderong shale and Muiron members have high contents of Smectite (up to 30%), they are still well below the recorded Smectite contents from the core samples of the Lakes Entrance Formation. Goldie Divko et al. (2010b) report the Smectite contents from the Groper-2, Wrasse-1 and Groper-1 to be 41%, 70% and 81% respectively. Such high Smectite content is one of the reasons that $\mathbf{F(P_c,\ \varepsilon)_{Gippsland} < F(P_c,\ \varepsilon)_{Exmouth}}$. Clay minerals generally have a structural water layer in between their cation sheets. Interestingly, Smectite family has dual water layer which significantly reduces their shear strength (μ). Such potential to adsorb water results in the increase of the shear compliance (B_T) and hence, the higher the smectite content the lower the $F(P_c, \varepsilon)$ of the shale will be.

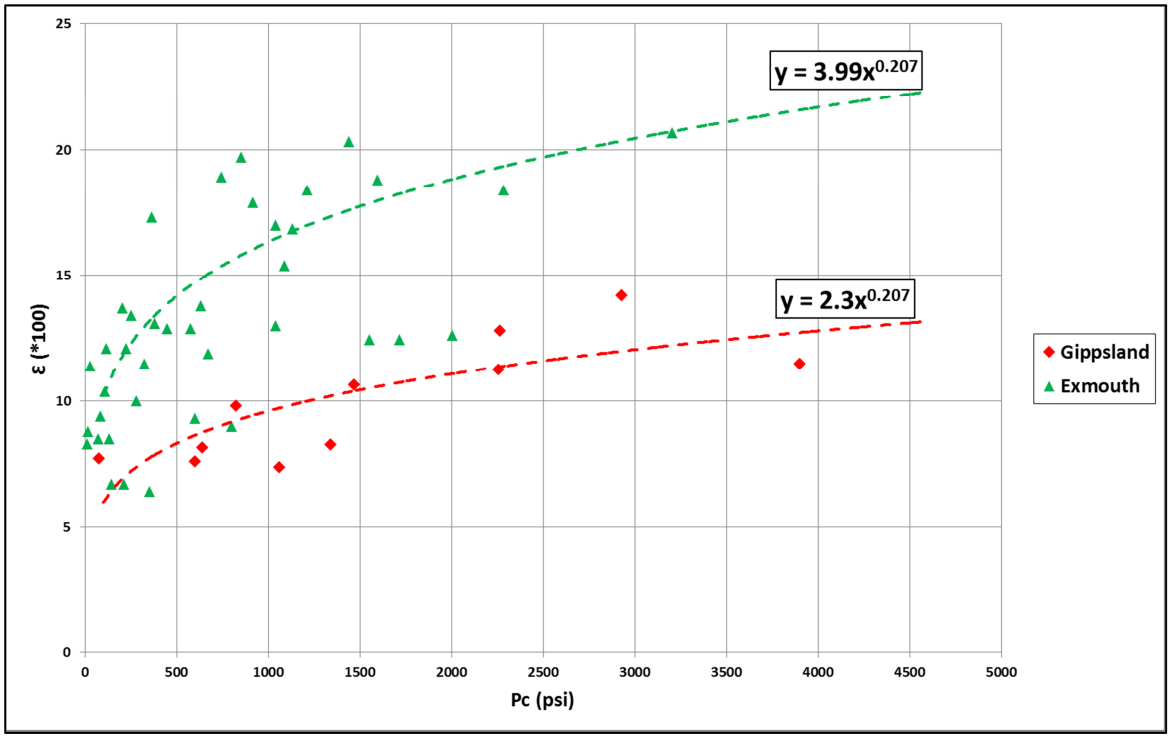

Figure 78. Cross plot of Epsilon versus capillary pressure to compare the data from Gippsland and Exmouth.

Analyses of Chapter 2.9.2 shows that ε values of a shale will decrease with increasing porosity (φ) of capillaries and B_T, the decrease in I_w (sorting index), B_N and their Lame constants (λ, μ). A combination of these parameters logically results in the decline of ε as well. Although a second order polynomial fit was chosen as trend lines (chapter 5.2.7), both groups show obvious slowing of their rate of increase of ε for P_c. In fact, the curves appear to reach a horizontal or gently sloped asymptote. Since the second order polynomial predicts a decline in larger P_c values, a power function (ax^b) is a more appropriate choice to retain the trends as well as the predictability of the series. Power functions were shown to be appropriate trends in relating mudrock properties (Lashkaripour, 2002). The results of the modelling in Chapter 2.9.2 also point towards logarithmic and power functions. A second order polynomial (Chapter 5) is in fact a trimmed Taylor expansion of this power function. The "ideal" wet seal (The Muderong shale sample) has the ε value of ~0.24 (Kanitpanyacharoen et al., 2015). The MICP measurements on the same sample evaluated the capillary pressure to be in the vicinity of 6000^{psi} (Dewhurst et al., 2002b). Therefore the slope of the $F(P_c, \varepsilon)$ should stay positive and the function itself should predict a sealing potential of $\sim 6000^{psi}$ for ε=0.24. The trend function for the Gippsland basin appears to be a fraction (~0.57) of the one for the Exmouth sub-basin. This is due to the higher (up to twice) content of Smectite in its samples which result in a generally lower "λ+2μ" values.

Another observation that can be made on the results of Figure 78 is the role of depth of burial and age of the shale formation in relation to their sealing potential. These factors affect the $F(\varepsilon, P_c)$ function by alignment of the clay domains through burial process and diagenesis .Burial diagenesis causes the alteration of weaker and less stable minerals such as Smectite to more stable /harder clay minerals such as Illite (Smectite Illitization) (Boles and Franks, 1979). Harder shale frame means the isotropic terms of equations (45) to (52) or "λ+2μ" are generally higher. This is equivalent to a vertical translation of the $F(\varepsilon, P_c)$ function as is observed on Figure 78. The Lakes Entrance Formation is shallower (less than 1800m depth) and younger (Oligocene) compared to the Muiron member and

Muderong shale which were deposited during Cretaceous and buried (during their history) more than 2000m. Figure 79 shows a general overview of the burial stages of the mudrock and the processes which affect its diagenesis. The two prominent processes which can affect the order of shale domains and its anisotropy are the history of compaction and the degree of Illitization. While the history can be quite complex for some shales (Delle Piane et al., 2015) with increasing depth of burial the overall trend is for the shale domains to get better aligned perpendicular to the axis of symmetry and become harder (Also see Appendix 7).

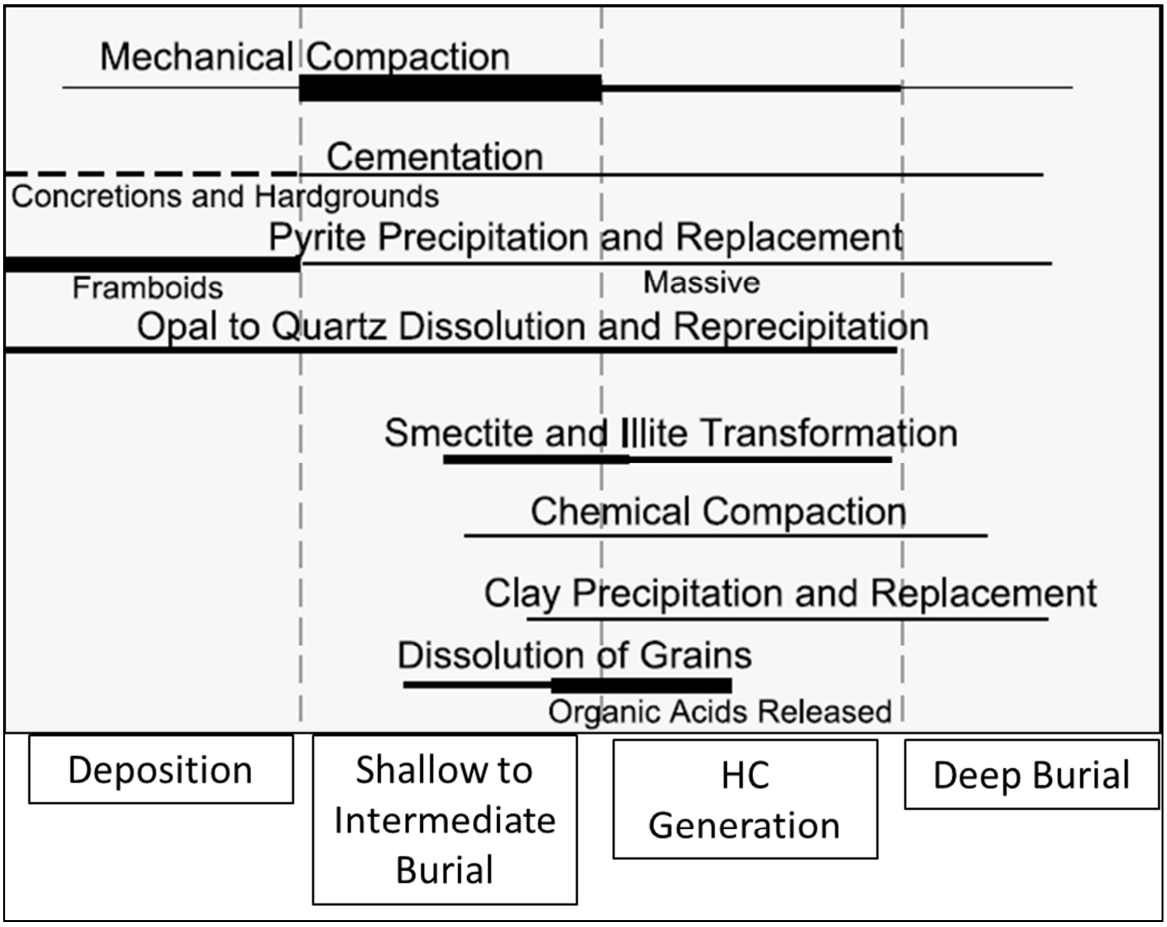

Figure 79. Summary of major stages in the burial diagenesis of mudrock (Modified after Loucks et al. (2012))

7.3 Analysis of the seismic attributes

Multiple sets of seismic attributes were tested on both case studies. The first step proved that there is no meaningful link between the gamma ray response of a shale sequence and its sealing potential. Out of the ranges of attributes, those that are categorized as frequency dependent or quality related appeared to have a better link to the sealing potential of the shales. Ordinary approaches to forward model the shale response using the Gassmann's equation is doomed to fail since most the assumption (linearity, pore connectivity, homogeneity) in those equations are violated (Josh et al., 2012). However, it is still interesting to find out the reason some classes of attributes are more likely to be responsive to sealing potential variations. It was shown in Chapter 2.9.2 that the (near) vertical capillaries which are responsible for the sealing potential have impact on three factors: Porosity (φ), domain misalignment (I_w) and compliance (B_N, B_T). How/which seismic attributes will be able to sense the variation of each or combination the above mentioned parameters?

Shales are highly porous rocks but with very low permeability. It means that their porous space is not connected and the water layer/molecules in between the clay sheets are tied to the adjacent shale domain and have limited mobility. When an impinging seismic wave passes through rocks, attenuation occurs due to cross-flow of the fluid in the pore space or between layers (Dvorkin and Mavko, 2006). The non-effective pore spaces in shale are abundant enough to absorb a lot of the seismic energy and convert it to heat through their limited viscous flow. This is the reason the *Quality Factor* (Q) values of some shales are among the lowest compared to other rocks (Sheriff and Geldart, 1995). This cannot be generalized but what is known from very detailed laboratory measurements is that over-pressured shales show significant increase in attenuation (Ciz et al., 2005). It could be speculated that some amount of unbound fluid could be responsible for friction or possibly squirt related losses. Similar arguments could be put towards fractured clays where some additional losses may be related to scattering mechanism. Measurements of the rock quality factor over shale samples

from the Canning Basin shows that Q factor is higher in shale samples with higher cross-bedding permeability (Delle Piane et al., 2014).

The decay in a lossy medium is frequency dependent in a way that higher frequencies get absorbed more quickly. Hence attributes that may be directly indicative of more attenuative shales are peak frequency measured across a part of entire shale sequence. Other attributes of interest are spectral slope or out of instantaneous attributes so called instantaneous Q that may me computed as: -IF/(ΔE/E), where IF – is instantaneous frequency and E is the envelope (Taner, 2001).

Bandyopadhyay et al. (2009) introduced the maximum inverse quality factor for a VTI medium to take the form

$$Q_{ij-max}^{-1} = \frac{C_{ij}^{\infty} - C_{ij}^{0}}{2\sqrt{C_{ij}^{0} C_{ij}^{\infty}}} \tag{63}$$

Where C^{∞} and C^{0} are the high and low frequency limits of the stiffness constants. And in the same manner as ε is defined by Thomsen (1986):

$$\varepsilon_{Q^{-1}} = \frac{Q_{11}^{-1} - Q_{33}^{-1}}{2Q_{33}^{-1}} \tag{64}$$

It is interesting to see that seismic quality of shales can have similarity to its physical anisotropic properties "ε". Equations (63) (89)and (64) show the dependency of the seismic quality in materials on its frequency content as well as the anisotropy of the quality perpendicular and parallel to it.

When analyzing shale sequence it is important to realise that shale sequence heterogeneity due to change in the shale volume, mineralogy, organic content, etc. will affect frequency-based attribute computations. Hence these attributes should not be measured in isolation. Rather additional attributes that may be indicative of shale heterogeneity should be computed in parallel. Therefore, heterogeneity attribute and/or stratigraphy-related seismic attributes such as "chaos" can give a general indication of

how the internal heterogeneity of the shale varies. Another methodology of interest is the spectral decomposition. This attribute is great in separating different variations across seismic frequencies. The general interest will be to see the difference between the low frequencies and high(er) frequencies. in relation to the sealing capacity of shales.

"Trace Gradient" attribute which returned a reasonable correlation with P_c in the Gippsland case study calculates the amplitude gradient along the trace. Although it is a relatively simple attribute, it gives a quick look at how amplitude varies through the shale sequence. Weaker seals could have less attenuation. By better alignment of shale domains and higher attenuation of seismic energy, the rate of attenuation of seismic amplitude should decrease. Narrow frequency bands inputs to "trace gradient" attribute generally increases its ability to detect sealing potential. However, the setback is its sensitivity to amplitude change and the sampling interval.

A more sophisticated attribute which contributes the frequency content of the seismic data as well as its apparent quality is the "instantaneous Q" (Chapter 6). A formulation of this attribute is

$$Inst.\ Q = \frac{f}{\frac{dA}{dt}} \tag{65}$$

Where A is the amplitude of the seismic.

Instantaneous Q has its strength in including the frequency into the attenuation estimation and therefore is more applicable to evaluating seals. Better seals should show higher attenuation and therefore Instantaneous Q should show a decreasing trend as verified in Figure 74.

Application and interpretation of seismic attributes of shale sequences faces some problems due to fundamental difference of shales and porous sands. While porous space in sands is generally connected, it cannot be assumed true in shales. The viscous cross-flow of liquids across and along shale

domains faces not only nanometer-scale pore-throats, but it faces the adsorption effect of clay platelets. Smectite is well-known to have a high adsorption capability and the higher the amount of Smectite is more likely to disturb a frequency-dependent fluid flow. Therefore the attributes which partly relate to I_w such as the “Trace Gradient” might have a better chance of success. The other reason which limits the usage of post-stack seismic attributes is the very same process which helps increase the signal/noise ratio: stacking. Stacking almost removes the effects of offsets while the incident angle on/within a shale boundary at far offset (high angle) should face a different attenuation compared to the near offset image (equation (64)).

8 Application: Gas Chimney

Chimneys are expressed as vertical chaotic disturbances on seismic sections related to the propagation of fluids (especially gas) through fissures and fractures in rocks. They can be indicative of mud diapirism, active gas seepage, migration pathways or hydrocarbon reservoirs (Aminzadeh et al., 2002). Chimneys can also be indicative of seal bypass systems (Cartwright et al., 2007). When a seal is breached, the overlying formations fracture and allow the reservoir fluids to pass to shallower levels. A combination of these fractured rocks with some degree of fluid saturation accounts for the seismic signature of what is referred to as a chimney. A classic gas chimney in the Gippsland Basin was studied by Nourollah et al. (2010). Seismic attributes were shown to be of significance in identifying and locating the gas chimney. The study however, stopped short of elaborating on the seal capacity of the area. In this chapter, the developed techniques of this research will be applied to the studied chimney in the Gippsland Basin to learn more about the top seal capacity.

8.1 Area of Study

The northern margin of the Gippsland Basin is host to several oil and gas discoveries. In contrast to the southern platform, the northern margin is composed of a number of smaller terraces which run sub-parallel to the Lake Wellington Fault system. The geological settings and structural history of the basin is explained in Chapter 4. The primary target for exploration is the top Latrobe Group sands (or Gurnard Formation), although the examples of success are in older sands of the Chimaera Formation in the nearby Longtom field. Proven seal for the petroleum system is the Lakes Entrance Formation and Early Oligocene Wedge (Goldie Divko et al., 2010a; Norvick and Smith, 2001; Rahmanian et al., 1990).

Four wells have been drilled in the AOI: Flathead-1 (1969), Whale-1 (1981), Moby-1 (2004) and Maclean-1 (2005). All four wells intersect the seal and reservoir, but only the first three have vertical (checkshot or VSP) and sonic velocity data. Moby 3D full stack and partial offset stack volumes cover the

area of study with older 2D lines partly transecting through the AOI. Processed stacked and partial offsets of the Moby 3D was available for this study. Although the gas chimney is obvious on the seismic, no public domain report or interpretation of the top seal integrity is available for the area. Structural interpretation of the (near) top seal and the top primary reservoir (Latrobe Group) seismic horizons were conducted to identify the modelling target. Despite the lack of MICP samples from the wells, the gas chimney acts as a valid calibration point for the seal failure. Since the geological setting of the AOI is very close to one of the case studies (Southern Gippsland), the findings of that study can be directly applied here.

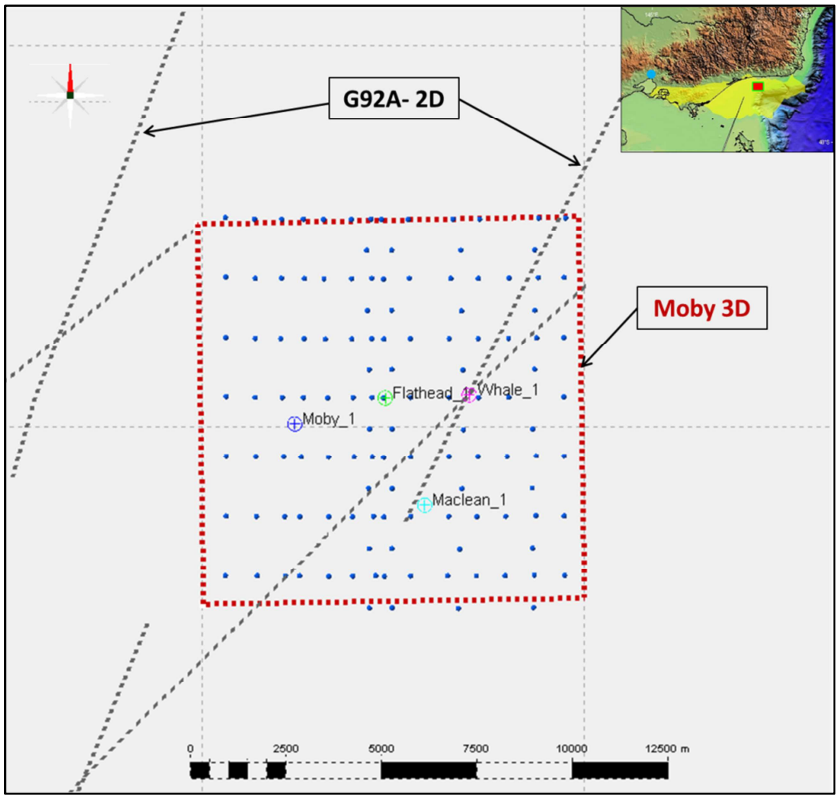

Figure 80. Location map of the Moby 3D survey in the Gippsland basin and the four wells within the area of study. The blue circles within the Moby 3D area are the analysis points for ETA.

8.2 The Chimney

The main gas chimney is located north and north east of Flathead-1. There are other smaller leakage signatures that are visible in the vicinity of the main chimney which are either associated with it or are independent features. The gas leakage appears to have stemmed from the Strzelecki group and breached the seal (Figure 81.). Where the chimney is in full form, it has reached the seabed and its signature can be detected on amplitude-related attributes. The movement of the chimney through the overlying sediments has caused ruptures and fractures that have only encouraged the upward movement of the gas. Sub-vertical fracture sets may well be associated with the chimney, however, a number of such feature are likely due poor seismic imaging quality around chimney areas.

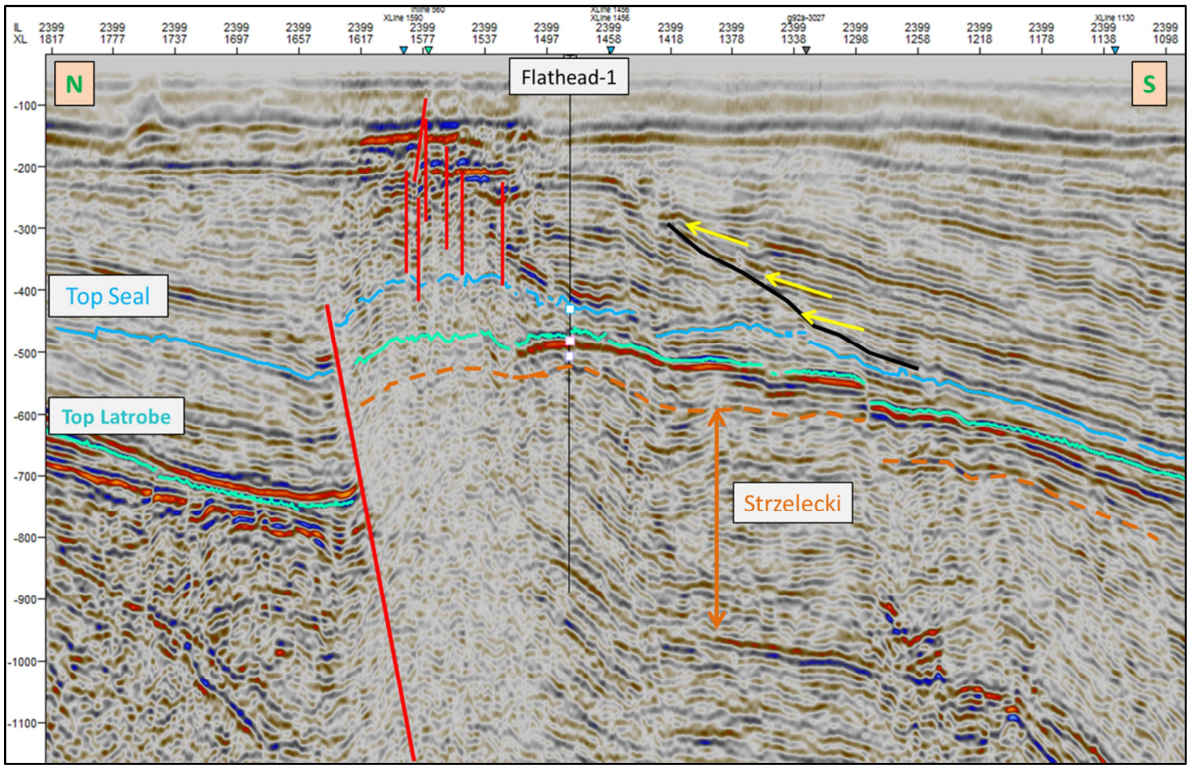

Figure 81. Seismic Inline 2399 east of Flathead-1 one shows the main gas chimney in the area of study. The well is projected some 200meters. Gas infusion through the seal package and the associated brightened reflectors in the shallow is visible.

A reflection intensity attribute is probably the best to map the variation of amplitudes due to presence of gas in the shallow sediments. The response of this attribute on the sea bed horizon shows the lateral extent of the main chimney (Figure 82). Not all the outstanding values of the amplitude at seabed are associated with gas chimneys underneath them. However, the more circular and bunched features such as the ones to the NW of the main chimney are somehow related to a leakage feature. Such feature can be indicative of either a fault or a weak top seal. Various onlapping packages have eroded into the top seal sequence and reduced its effective thickness. In some areas, especially to the NW of the main chimney, the cluster of high amplitude features suggests the onlapping erosion surfaces have assisted in weakening the top seal sequence or in providing more efficient escapes routes for the gas underneath.

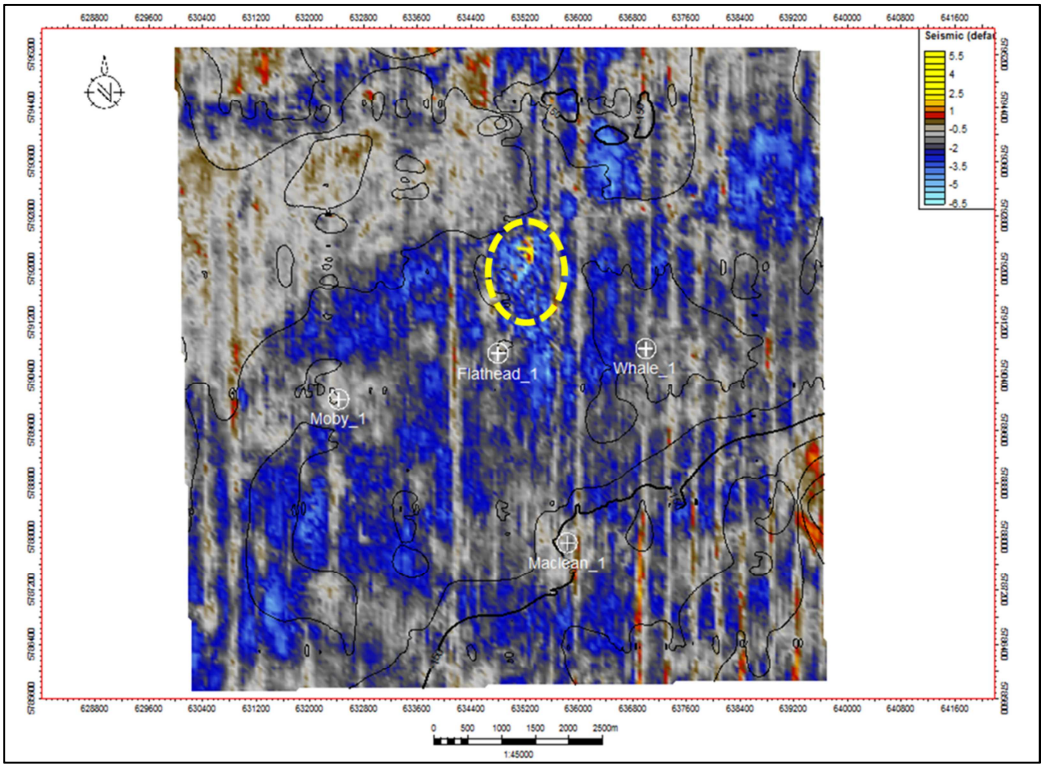

Figure 82. Reflection intensity of the sea bed. The coherent signature of high values of this attribute at the center of the map is associated with the gas chimney. The acquisition foot prints are evident as vertical (N-S direction) lines.

Interestingly, the thinnest seal is not directly related to the obvious chimneys. This is in concert with the fact that the top seal capacity is not necessarily related to the thickness of the seal. However the Lakes Entrance Formation is relatively thin and gets even thinner at the crest of the Moby high (Figure 83). The Lakes Entrance Formation thickens to the north of the inverted normal fault (Figure 81). Over the crest and south of the structure, the seal thickness varies within a range, but without significant variation. Depth to top Lakes Entrance is as shallow as ~400m (near Flathead-1) and increases to in the south to more than ~800m.

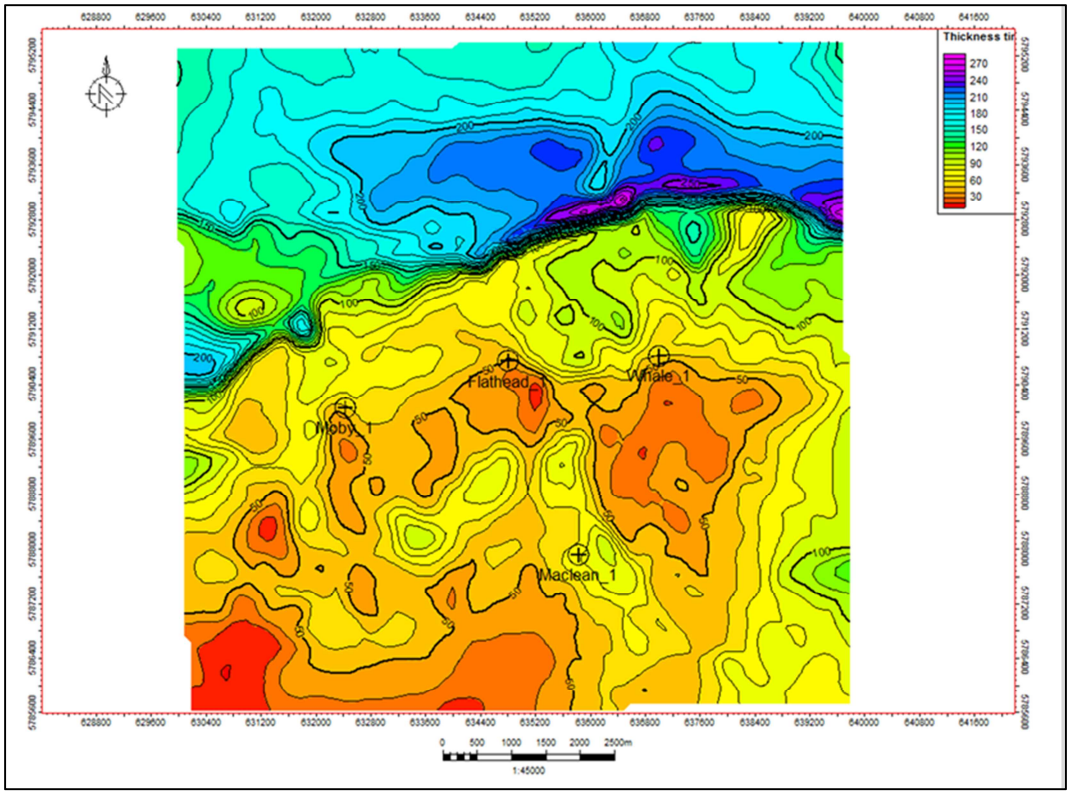

Figure 83. TWT thickness map of the top seal shows a relatively thinner sequence on the paleo-high.

8.3 The Sealing Potential

Despite the lack of MICP measurements to calibrate the sealing capacity, powerful tools were introduced in the previous chapters to assess the seal. The chimney sites can also act as calibration point

in the sense of where the seal has failed. Rather than re-surveying and testing numerous seismic attributes, the outcomes of Chapter 6.3 are directly applied. Hence, testing was carried out over narrow frequency bands for seismic Q as well as testing for the seismic anisotropy parameter ε. The input seismic data were the stack seismic and the far-offset stack cubes. The near-offset stack was not useful in the analysis due to lack of signal at shallow times. However, the full-offset stack should add enough near and mid-offset influence to offer a relatively independent signal from that of the far-offset cube. Spectral decomposition of seismic data offers the narrow frequency bands which are required to implement equations (64) and (65). Of interest are the extreme practical ends of the frequency spectrum. For the available data, the selected corridors are 20Hz and 60Hz. The data contains useful information beyond the selected thresholds, however, very low and very high frequency data from conventional seismic need to be utilized with care.

Figure 84 shows a comparison of the seismic *Quality (Q)* of the two end members of the offset range within the same frequency bracket. This analysis is useful to reveal relative (sub-) vertical cross-flow. The main chimney site (north of Flathead-1) shows a relatively higher Q values in comparison with those of the surrounding areas. This observation is consistent with the seismic evidence of the eruptive nature of the gas chimney and its associated fractures (Figure 81). The (squirt/viscous) flow along the shale layers (far-offset response) is easier than the movement perpendicular to the layers (near-offset response), but this is notably concurring over the main chimney site. Both maps highlight areas of potential sealing risk south of Moby-1 and Flathead-1. However, these areas show consistency in having higher seismic Q values at far-offsets. This is likely related to the increased stiffness in that direction, hence lower attenuation or higher Q. Lower risk of sealing breach is assigned to the areas where both offsets indicate a relatively low seismic quality (Q) values (warmer colors in Figure 84).

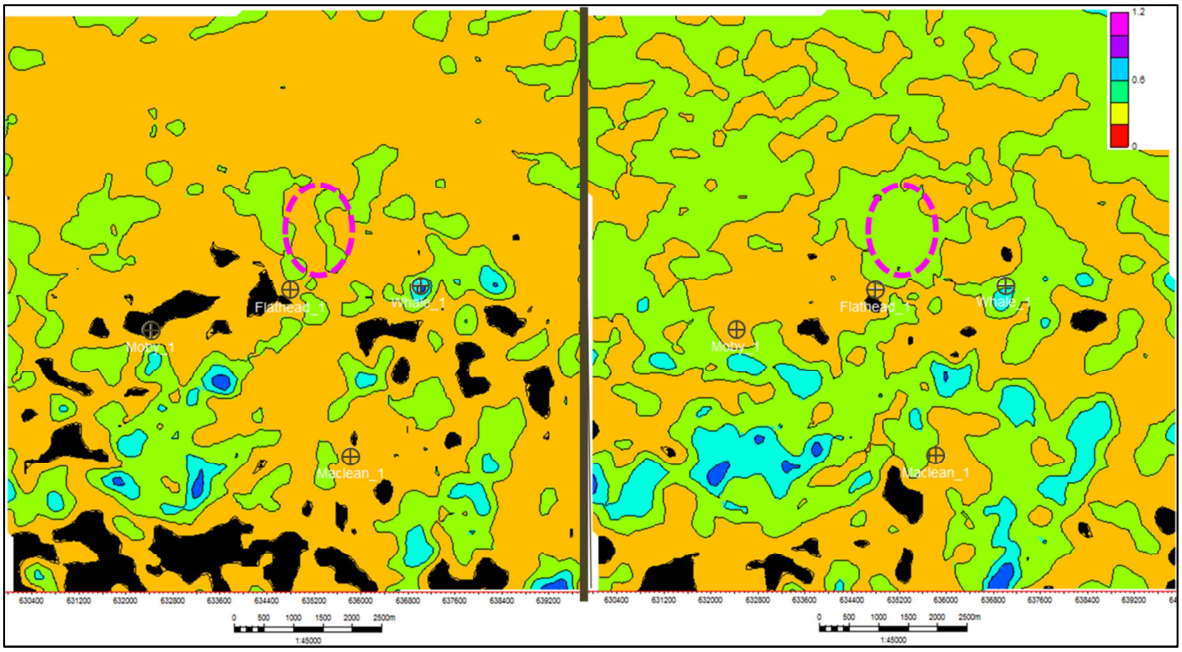

Figure 84. Averaged Seismic Q response of the Lakes Entrance sequence at 20Hz window from a stack seismic (Left) and the far stack (right) reveals potential sealing risks especially around the main chimney site north of Flathead-1. The dashed polygon is the location of the main gas chimney as in Figure 82.

The pores/conduits act as agents of cross-flow. To test the impact of the size of pores/conduits, a comparison between the low and high frequency windows is made (Figure 85 and Figure 84). The main chimney site shows a higher quality seismic response at 60Hz in comparison with the 20Hz. This means seismic is attenuated less in the 60Hz window in comparison with that at 20Hz bracket. Hence, there are pores and conduits which help the fluid (gas) flow across the seal, but they are not large enough to have a significant impact on the high frequencies. Yet both frequencies (especially 60Hz) indicate a distinct difference between the chimney area and the surrounding areas. Interestingly, there are some areas (south of the crest of the structure) which appear to have weak seals on the 20Hz map, but they are less distinct on the 60Hz map. They are representative of weak seals, but not too weak (in relative terms) to be significant on high frequencies.

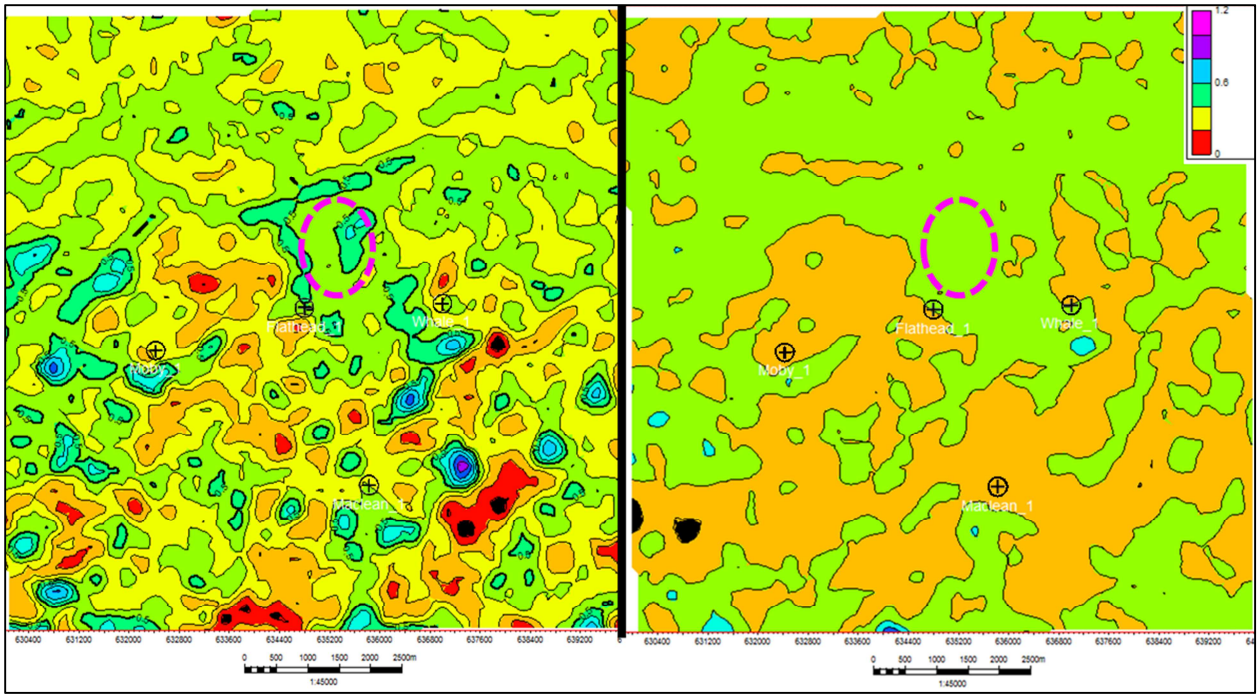

Figure 85. Average seismic Q over the sealing sequence for the 60Hz bracket of stack seismic cube (left) and the far-offset (right). The location of the main chimney is shown with the dashed polygon.

Again I use anisotropy parameter ε as a proxy to the relative sealing potential. Using the formulations which were introduced in the previous chapters, ε is deduced from the input V_{nmo}, ETA and V_0 parameters. Figure 86 shows the distribution of average ε over the Lakes Entrance Formation. The range of ε varies between 3 and 13, with the majority of the values to be less than 11. This is notably lower than the range that was observed in the Exmouth sub-basin, but is well within the mid-to-low ranges for the Lakes Entrance Formation. There is an overall match between the variations of ε and what was observed from the seismic attributes. It correctly predicts a relatively lower seal capacity at the main chimney location as well as some weakly sealed areas in the southern half of the map. The map of ε is relatively smoother and reveals that the lower seal quality areas occur in NE-SW trending stripes. This observation matches the relative structural uplifting in the same direction. Such uplifting caused a more reworked sedimentation, larger input of clastic particles and lower depth of burial which will all contribute to the diminishment of the sealing capacity. Furthermore, it is likely that the episode of

marine transgression and deposition/erosion of the sealing sequence was happening in the SE-NW direction (in the area of study). As a result, reworked (more disturbed) bands of the sealing sediments repeat in the same way that the Latrobe sands were deposited in the proximal environments within the Gippsland Basin.

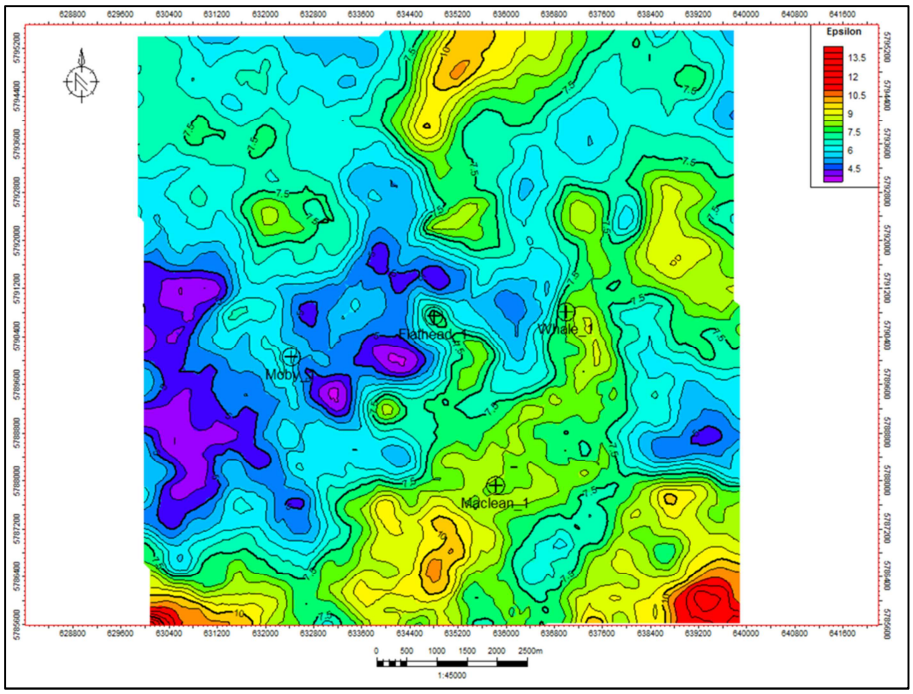

Figure 86. Map of anisotropy parameter epsilon averaged over the sealing sequence.

Using the inverse function of $F(_c, \varepsilon)$, the sealing potential of the Lakes Entrance in the area of study can be estimated. Figure 87 shows the estimated sealing potential overlain on the Lakes Entrance depth structure contours. The NE-SW stripes of low sealing capacity can be observed, indicating high risk areas, particularly southwest of Flathead-1 and Moby-1. It is interesting to observe that the lowest sealing capacity areas do not correspond to the location of the main chimney. The reason is that a seal leaks when the buoyancy pressure of the underlying fluid column is higher than its sealing capacity. This normally happens at the crest of the structures where buoyant fluids (oil-gas) migrate to. Therefore, in relative terms, the seal must be at its best capacity in the critical areas such as the crest of the structure,

but can be weaker on the flanks. This did not happen on the Flathead high, resulting in the formation of the main chimney.

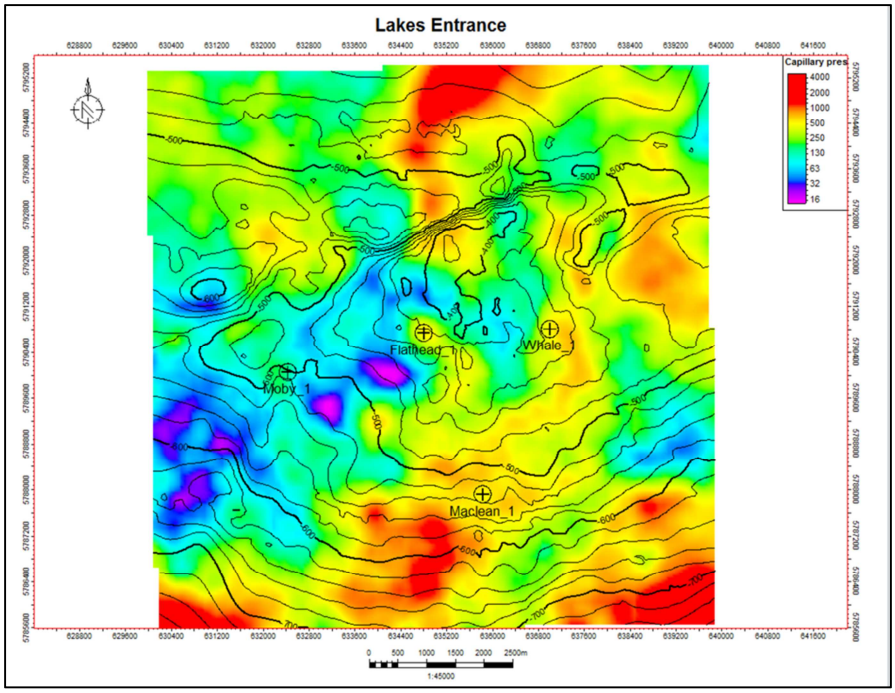

Figure 87. Average sealing potential of the Lakes Entrance Formation shows relative low capacity sealing bands over the crest of the structure stretched towards SW. contours are the top Lakes Entrance depth.

An immediate result from the map of Figure 87 is to estimate the highest hydrocarbon column height that could have existed in the AOI given the sealing capacity. The chimney is just an indication of failure in the face of pressure that exceeds the sealing capacity. There could be a remnant HC column underneath the breached seal. The highest sealing capacity at the crest of the structure is around 110^{psi}. This is a very weak seal which translates to the unlikelihood of having any commercial hydrocarbon potential for such values in the AOI (at least for reservoirs to be sealed by the Lakes Entrance). There are however some areas where a relatively competent seal is capping a local structural high. An example is the closure NW of Moby-1 where the average sealing capacity is in excess of 300^{psi} with some layers of the seal reaching as high as 500^{psi}. A local flat spot can be recognized on the seismic data in this locality (Figure 88).

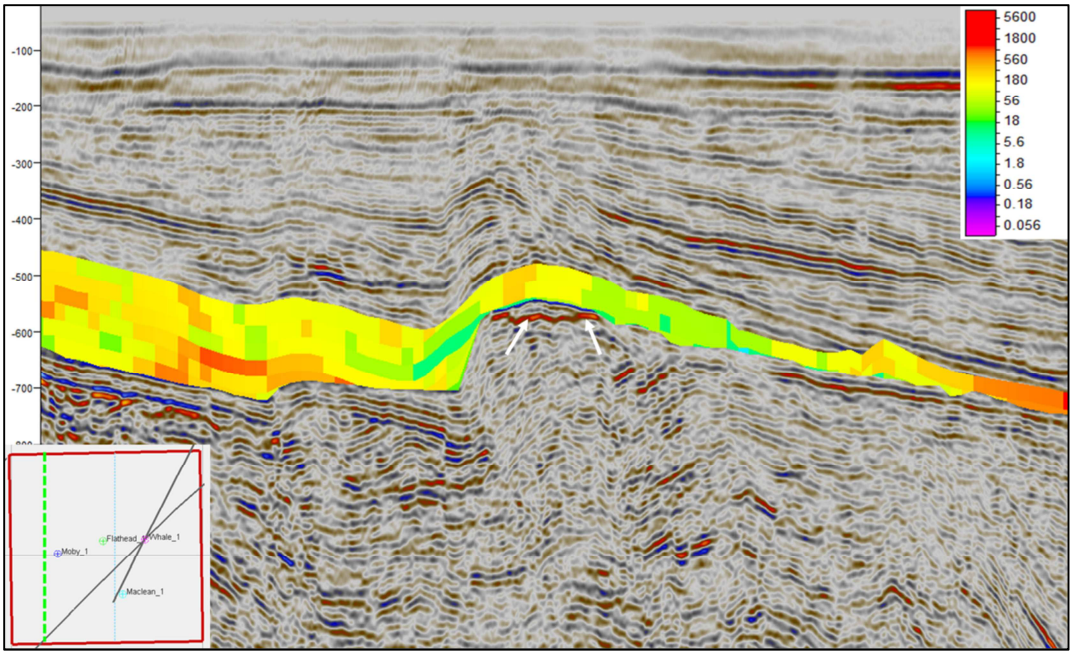

Figure 88. Inline 2119 of the 3D cube crosses over a local structure NW of Moby-1. The overlain predicted sealing capacity shows a relatively better seal compared to the surrounding areas. A flat spot in the structure can be observed (white arrows).

The observation that the seabed does not have any significant pockmarks (Cathles et al., 2010) matches the findings that the top seal was never strong enough to hold a large column of gas. Therefore the gas reached a critical height (for the weak seal) and escaped (better to say oozed) through the seal. The first movement of gas was perhaps quick enough after the gas chimney front reaches half way through the overlying sediment thickness (Cathles et al., 2010). Thereafter, it made some geomechanical changes to the remaining rocks between the forefront of the uprising gas chimney and the seabed, caused some fractures and escaped. However, this was not in an eruptive way as the seal was never strong enough. Leakage has continued ever since and is still detectable nowadays (Goldie Divko et al., 2010b).

9 Chapter 9: Conclusions and Future Work

This research has embarked on the better utilization of seismic data to estimate the sealing potential of sealing sequences. Although a well-studied subject in terms of core data and the geological aspects, sealing potential of rock sequences has not been directly analyzed from seismic data. This is related to the intricate nature of shales which makes them very difficult to study even in a controlled laboratory conditions. Hence remote prediction of sealing capacity of shales is necessarily very difficult. At the same time, prediction of the sealing capacity of a shale sequence is of huge interest to the CCS (Carbon Capture and Storage) industry to evaluate the top seal capacity of potential and producing fields or prospects. Despite such interests, the difficulty of obtaining shale samples, and its expensive nature (since it requires a well), have made seal capacity studies far less common compared to reservoir characterization.

Surface seismic data have been proven as a relatively cheap source to describe subsurface rock and fluid properties. This is exploited in the study by attempting to relate subtle changes in seismic data that is attributed to the microstructural property of shales (pore space). Rock physics modelling reveals that certain elements of the seismic anisotropy of shale sequences are related to its sealing capacity. The model introduced several aspects of capillary pipes into the perfect (impervious) shale. The volume and geometry of these pipes, the spatial orientation of the shale platelets and the relative compliance were determined to be of the highest impact. A combination of their contribution is a direct measure of the connectivity of the capillary system.

In order to field-test the modelled relationship, two cases studies from Exmouth Sub-basin and the Gippsland Basin were undertaken to investigate the potential of seismic anisotropy in predicting the sealing capacity of shale sequences. Both areas are prolific hydrocarbon basins containing proven petroleum systems. The historical accumulation of geological and geophysical data makes them suitable

candidates for this study. The sealing sequences of the two case studies are of different geological age and hence have a different burial history. Such differences make either of the case studies an independent field test.

9.1 Seismic Anisotropy and Sealing Potential

The rock physics modelling of the shale is different from what is usually performed on the porous reservoir rocks. Figure 89 shows a schematic of how the presence of different types of inclusions impacts the anisotropy of shale domains. The degree of change in the background matrix (shale domain) depends on the shape of the inclusion and its proportional volume (Appendix 6). The structure of shale is a saturated mixture of partly weakened (due to presence of inclusions) and the less (or practically none-) affected matrix shale domains. Once the micromechanical constituents (domains) are averaged according to their spatial distribution function, they can reflect the macroscopic elastic properties of a shale. Highly detailed modelling efforts of anisotropic behavior of samples can quickly get exhaustive even at today's era of powerful computers (Matthies, 2018 personal communication). However, limited numerical models based on analytic rock physics show that the anisotropic parameter ε should increase with higher sealing threshold in shales.

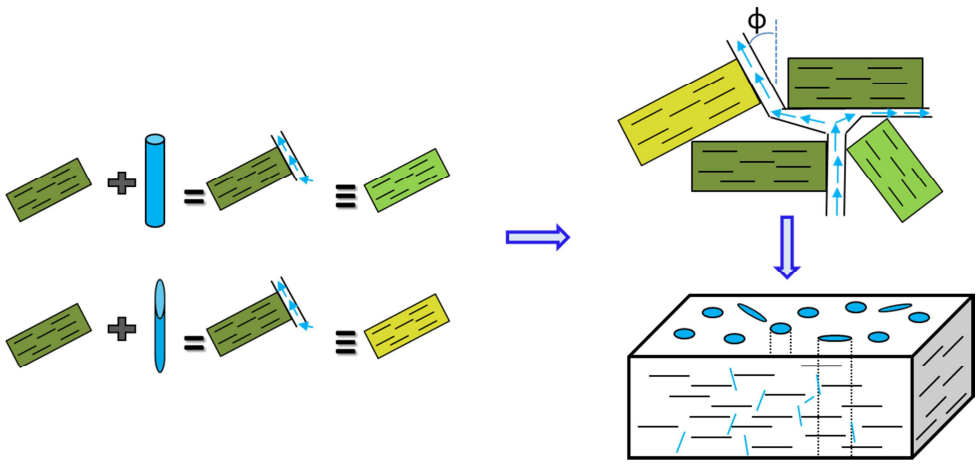

Figure 89. Addition of inclusions in the shape of near cylinders or crack-like pores to the shale domains causes excess compliance. When combined with the probabilistic distribution function it can model the sealing potential of the shale.

It is important to understand the roles of the Legendre's moments W_{200} and W_{400} (Appendix 3). The W_{200} is the moment of *alignment* in regards to the bedding plane. A higher W_{200} normally indicated better alignment. This moment has a higher weight in the calculations of elastic modules (and subsequently ε). W_{400} might seem like a higher-order moment of alignment, but it is not. The results of modelling in Chapters 3.5 and 3.6 show that ε may locally reduce slightly with increasing values of W_{400}. This is due to the nature of W_{400} which is a moment of *tortuosity* or "resemblance to a sphere: sphericity". Figure 90 how a more realistic distribution of pore shapes compares with its equivalent porosity of spheres. Both cases have equivalent conductivity, but have different elasticity (Kachanov and Sevostianov, 2005). Although the changes of the 4th order moment (W_{400}) can well be overwhelmed by the changes in the 2nd order moment (W_{200}), it has an important role in defining the overall shape of the pores. Interestingly, the shape of the pore spaces (at the same porosity) has no impact on the conductivity so the seismic attributes might have a higher degree of freedom in the evaluation of vertical and horizontal permeability.

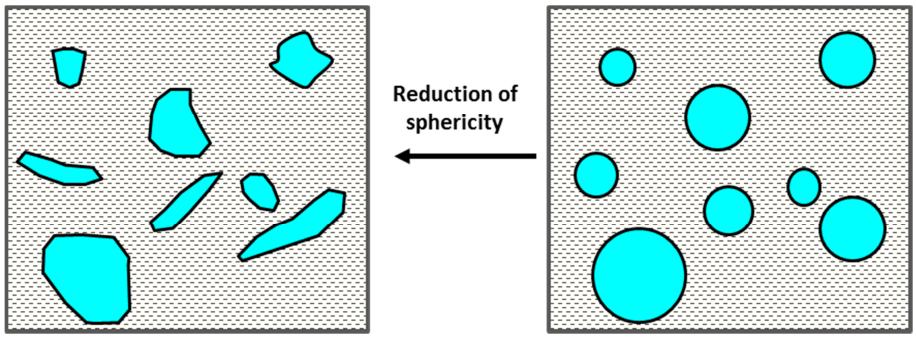

Figure 90. The deviation of pore shapes from spheres (maintaining the same porosity) has impact on the anisotropy and the moments of the Legendre expansion. (Figure is modified after Kachanov and Sevostianov (2005))

Both case studies show that capillary pressure measurements to determine the sealing capacity of shale-dominant formations can be propagated away from wells in a 3D geological model using seismic data. The calculated seismic anisotropy parameter, *ε,* appears to be a suitable covariant property and can be utilized to guide the distribution of sealing capacity measurements away from wells. Using

seismic data and its associated anisotropy measurements generally provides far more data points compared to the few MICP measurements at wells. Ɛ shows a general increase with increasing sealing potential that is estimated by P_c. This covariant increase generally follows a power function, however, the slope and incident of this power function is determined by mineralogy, burial history, internal structure of shales and their effective porosity. The $F(P_c,\varepsilon)$ of the two case studies were analyzed (Chapter 6.3) to cast light on the impact of contributing parameters. Presence of elastically weak minerals such as Smectite group lowers the slope of increase of $F(P_c, \varepsilon)$. Burial history impacts on the Illitization of the clay minerals and their orientation, therefore an important factor in the overall response of the seismic anisotropy of the sealing sequence.

Faults should be treated with care as VTI anisotropy values within the fault zone tend to be erroneous. It is best to initially reduce the effect of faulting on velocity analysis through processes such as DMO (Dip Move Out) or PSDM (Pre-Stack Depth Migration) (Yilmaz, 2001). Fault zones, including jointed areas, introduce HTI (Horizontal Transverse Isotropy) and thus act against VTI anisotropy (Jenner, 2011). Although the proposed method is suggested to high-grade the description of shales in the 3D model and across fault surfaces/zones, it is not a replacement for advanced algorithms that estimate fault seals (such as shale gouge ratio and smearing) (Yielding et al., 1997; and Bretan et al., 2003). A better knowledge of the sealing potential of shale units can enhance the existing techniques and algorithms in their approach to fault seal analysis.

The sealing capacity of the Lakes Entrance Formation in offshore Gippsland and the Muiron Member in the Exmouth Sub-basin were modelled using the established relationships with the seismic properties. The variation of the sealing potential at both sites was measured against the drilling success/failures. Where applicable, the sealing capacity was shown to be related to the depositional history of the shale sequences. Introduction of more terrestrial or clastic materials caused a reduction in

the overall sorting of shale platelets and reduced their sealing. The variation maps of the sealing potential for each site can be easily used as part of the play fairway maps for further exploration, development or carbon capture and storage (CCS) purposes.

9.2 Seismic Attributes

Seismic attributes (post-stack) prove to be of high value in delineating the seismic facies and high-grade the seismic quality. This is a key element in studying seals and understanding their geological distribution. Gamma ray, though a strong tool in detecting shale units, appears to be independent of the sealing potential of shales. It is also demonstrated within both case studies that the relative position of the sample within the parasequence has little bearing to its sealing capacity. However, this result does not rule out the value of identifying the sequences and map them across the target area. The minimum variation of API readings for the seismically predicted gamma ray was large for the Lakes Entrance Formation. This was possibly due to presence of other gamma ray-emitting elements (heavy minerals and organic matters). Using banded gamma ray readings for Potassium, Thorium and Uranium, it is possible to have a first order prediction of the mineralogy (or it variation) of the shale sequence.

The sealing potential of shale sequences showed some relationship to the frequency-limited attributes. As discussed in Chapter 6, the seismic attributes which help identify I_w, φ and B_N/B_T or any combination of them will be suitable candidates for seal capacity prediction. In general, those attributes that measure subtle changes in seismic energy and/or frequency seem to be suited to model the sealing potential. Which sub-category of these attributes is to be used depends on the seismic data and the composition of the seal. Chaos or similar attributes may provide a first estimate of potential disturbances in the shale sequence. Seismic (pseudo-) quality factor “Q” (as a proxy to rock quality factor) was shown to be different at sealing and leaky shales at various frequency bands. Comparison of

narrow high and low frequency bands (such as 15Hz and 65Hz) in combination of near and far stacks may also assist the evaluation.

9.3 Seismic data analysis

The case study of the Exmouth Sub-basin showed that PSTM-processed seismic data can be used to extract the Thomsen anisotropy data where there is adequate well-controlled velocity data. The estimation of anisotropy is more difficult at depth, and the results show a higher degree of dissipation. When the geology is relatively simple and the depth of investigation is not very deep (as is the case of Gippsland case study), PSTM provides appropriate data for the analysis. However, more complex geology, dipping beds and presence of faults stretch the abilities of the PSTM processing and depth processing should be considered.

Pre-stack depth migration (PSDM) is a more time-consuming, but more accurate, method to estimate the anisotropy parameters ε and δ. The only way to truly separate the effect of non-hyperbolic velocity from anisotropy (and to model ε and δ) is to perform anisotropic pre-stack depth migration (APSDM). Use of depth processing in the Exmouth Sub-basin will likely improve the accuracy of the results and generate a higher correlation between ε and P_c.

9.4 Seismic predictability of shale sealing potential

The two case studies were completed over separate sedimentary basins. Each study area has distinguishing features, such as water depth, structural history and depositional environment. The general outcome of the research is that anisotropy of shale sequences appears to be related to their sealing potential.

Although anisotropy and sealing capacity are defined by two different processes, the fact that better laminated shale units show more anisotropy and are perhaps better seals suggest a relationship

between anisotropy and sealing capacity. The sealing capacity and the depth of burial do not show a meaningful relation in the area of studies. However, the current depth of burial might not be the right parameter to choose. The burial history of the seal should be investigated, as the depth of burial will impact how well-oriented the fabric of the shale sequence would be. The burial depth will also likely encourage the growth of shale platelets within the existing pores and tighten the space available to let hydrocarbon pass. This essentially means a higher sealing potential.

The increase in the anisotropy parameter, ε, relates to the increasing sealing capacity that is measured through capillary pressure testing. However, this relationship is site-specific, which means the rate of change in ε versus P_c will likely be different for two study areas (as shown in chapter 6.3). The best practice to map the sealing potential of an area will be to model the parameter ε in 3D and calibrate it with at least one P_c value in the area of study. The 3D volume for ε will then serve as a trend to predict the sealing capacity of the sequence.

In the case where no calibration point is available (for capillary pressure), the ε values can be used to qualitatively indicate the better seals and weaker seals without specifying numbers. Analogues will perhaps help in narrowing the potential number that might be expected for specific ε ranges. Such usages can provide valuable de-risking tools in frontier exploration areas, CO_2 sequestration and evaluation of stratigraphic traps. When few P_c samples are available or the evaluation of anisotropy is not certain, probabilistic tools such as Monte Carlo simulators can define the most likely ranges on individual and combined components.

Using the established trend for $F(P_c, \varepsilon)$ of the southern Gippsland case study, the site of gas chimney in northern terrace of the Gippsland Basin was evaluated. The chimney area has been mentioned in several studies before and seismic attributes were used to define the location and extent of it. In light of the findings of this research, seismic attributes and anisotropy were used to evaluate the

variations of the sealing potential of the Lakes Entrance formation. The chimney site was used as a calibration point where the seal has failed to maintain a gas column. The results were shown to be consistent with the findings of the exploration wells and previous studies. The predicted sealing potential of the Lakes Entrance is not high enough to hold any commercial column of hydrocarbon over the uplifted section of the area of study. However, there were locally competent seals where generated hydrocarbon filled up local highs and showed a flat spot.

9.5 Future Studies

This research has aimed to establish a relation between the seismic anisotropy and the sealing capacity of shale sequences and field tested the methodology with two case studies. The application of the method was also tested on a gas chimney site. The origin of the seismic anisotropy of shales is still under research to establish whether it has depositional or tectonic/compaction origins (Pervukhina and Rasolofosaon, 2017). In either case, the mechanical/elastic behavior of shales appear to be related to how the shale domains are packed within the rock (Aylmore and Quirk, 1960). However, the prevailing mineralogy of the shales appears to have an impact on the anisotropy and its variations. The impact of specific mineral types on the capillary effects of shales and how it ties to the findings of this study can be an interesting research. Compaction and diagenesis (as another source for the anisotropy of shales) was also studied for its relation to the porosity and structure of shales (Bachrach, 2011). How the diagenesis history of shales can be tied to their sealing potential and their seismic response is another interesting research topic.

There are many sites where analysis of the sealing potential could be beneficial for hydrocarbon exploration. Any prolific basin which provides ample seismic and well data could be used to expand the current findings. Known locations of gas chimneys are indicative of breaches in the sealing system and can be investigated through the proposed method. Although the quality of seismic is not great over the

chimneys themselves, there should be enough data in the vicinity of them (compared to distal areas) that would establish a trend and help the evaluation of the seal. Additional data such as 3D VSP and/or C-wave studies may be utilized to help such analysis. There is also a strongly growing need for the CCS industries. The knowledge of the seal capacity is of absolute importance to CO_2 storage. The type of seismic data analysis presented in this research might increase public confidence of CO2 sequestration and that way contribute to its widespread acceptance.

10 References

Aki, K., and Richards, P. G., 1980, Quantitative seismology: Theory and methods, W. H. Freeman and Co.

Alexandrov, K. S., and Ryzhova, T. V., 1961, The elastic properties of crystals: Soviet Physics Crystallography, v. 6, p. 228-252.

Alford, R. M., 1986, Shear data in the presence of azimuthal anisotropy, 56th Annual International Meeting, SEG: Dilley, Texas, SEG.

Alkhalifah, T., 1997, Velocity analysis using nonhyperbolic moveout in transversely isotropic media: GEOPHYSICS, v. 62, no. 6, p. 1839-1854.

-, 2011, Scanning anisotropy parameters in complex media: GEOPHYSICS, v. VOL. 76, no. NO. 2.

Alkhalifah, T., and Rampton, D., 2001, Seismic anisotropy in Trinidad: A new tool for lithology prediction: The Leading Edge, v. 20, no. 4, p. 420-424.

Alkhalifah, T., and Tsvankin, I., 1995, Velocity analysis for transversely isotropic media: GEOPHYSICS, v. 60, no. 5, p. 1550-1566.

Alkhalifah, T., Tsvankin, I., Larner, K., and Toldi, J., 1996, Velocity analysis and imaging in transversely isotropic media: Methodology and a case study: The Leading Edge, v. 15, no. 5, p. 371-378.

Alsharhan, A. S., and Nairn, A. E. M., 2003, Chapter 12 - THE HYDROCARBON HABITAT OF THE ZAGROS BASIN, *in* Alsharhan, A. S., and Nairn, A. E. M., eds., Sedimentary Basins and Petroleum Geology of the Middle East: Amsterdam, Elsevier Science B.V., p. 651-736.

Aminul Islam, M., and Skalle, P., 2013, An Experimental Investigation of Shale Mechanical Properties Through Drained and Undrained Test Mechanisms: Rock Mechanics and Rock Engineering, v. 46, p. 1391-1413.

Aminzadeh, F., Connolly, D., and Groot, P. d., Interpretation of gas chimney volumes, *in* Proceedings 72nd Annual International Meeting2002, Volume Expanded Abstracts, p. 440-443.

Amiri Besheli, S., 2006, Using Seismic Anisotropy for AVO Based Reservoir Characterization [PhD: Curtin University of Technology.

Amiri Besheli, S., and Urosevic, M., 2006, The effect of seismic anisotropy on AVO study: Abstracts - Geological Society of Australia, v. 82.

Andrews, G. E., Askey, R., and Roy, R., 1999, Encyclopedia of Mathematics and its Applications, Cambridge University Press.

Aplin, A., and Macquaker, J. H. S., 2011, Mudstone diversity: Origin and implications for source, seal, and reservoir properties in petroleum systemsShale Heterogenity and Petrophysical Properties: AAPG Bulletin, v. 95, no. 12, p. 2031-2059.

Armstrong, P. N., Chmela, W., and Leaney, W. S., 1995, AVO Calibration using borehole data: First Break, v. 13, no. 8, p. 319-328.

Auld, B. A., 1973, Acoustic fields and waves in solids, John Wiley & Sons.

Avseth, P., Dræge, A., van Wijngaarden, A., Johansen, T., and Jørstad, A., 2008, Shale rock physics and implications for AVO analysis: A North Sea demonstration: The Leading Edge, v. 27, no. 6, p. 788-797.

Aylmore, L. A. G., and Quirk, J. P., 1960, Domain or turbostratic structure of clays: Nature, v. 187, p. 1046-1048.

Bachrach, R., 2011, Elastic and resistivity anisotropy of shale during compaction and diagenesis: Joint effective medium modeling and field observations: GEOPHYSICS, v. 76, no. 6, p. E175-E186.

Backus, G. E., 1962, Long-wave elastic anisotropy produced by horizontal layering: Journal of Geophysical Research, v. 67, no. 11, p. 4427-4440.

Bailey, W. R., Underschultz, J., Dewhurst, D. N., Kovack, G., Mildren, S., and Raven, M., 2006, Multi-disciplinary approach to fault and top seal appraisal; Pyrenees–Macedon oil and gas fields, Exmouth Sub-basin, Australian Northwest Shelf: Marine and Petroleum Geology, v. 23, no. 2, p. 241-259.

Bandyopadhyay, K., Dvorkin, J., and Mavko, G., 2009, Attenuation and attenuation-anisotropy in laminated rocks: SEG Houston 2009 International Exposition and Annual Meeting.

Banik, N. C., 1984, Velocity anisotropy of shales and depth estimation in the North Sea basin: GEOPHYSICS, v. 49, no. 9, p. 1411-1419.

-, 1987, An effective anisotropy parameter in transversely isotropic media: GEOPHYSICS, v. 52, no. 12, p. 1654-1664.

Barnes, A. E., 2016, Handbook of Poststack Seismic Attributes, Society of Exploration Geophysicists.

Bear, J., 1972, Dynamics of Fluids in Porous Media, Dover.

Beloborodov, R., Lebedev, M., and Pervukhina, M., 2017, The coupling of elastic properties and hydraulic permeability in artificial shales, SEG Technical Program Expanded Abstracts 2017, Society of Exploration Geophysicists, p. 3816-3820.

Bernecker, T., and Partridge, A. D., 2001, Emperor and Golden Beach Subgroups: the onset of Late Cretaceous Sedimentation in the Gippsland Basin, SE Australia, *in* Hill, K. C., and Bernecker, T., eds., Eastern Australasian Basins Symposium, A Refocused Energy Perspective for the Future, Petroleum Exploration Society of Australia, p. 391-402.

Berryman, J. G., 1979, Theory of elastic properties of composite materials: Applied Physics Letters, v. 35, no. 11, p. 856-858.

-, 1992, Single-scattering approximations for coefficients in Biot's equations of poroelasticity: The Journal of the Acoustical Society of America, v. 91, no. 2, p. 551-571.

BHP Billiton, 2004, Ravensworth-1/1CH Well Completion Report-Interpretive Volume: BHP Billiton Petroleum Pty. Ltd.

-, 2005, Harrison-1 well completion report: BHP Billiton Petroleum Pty. Ltd., W20915A2.

Blangy, J. P., Strandenes, S., Moos, D., and Nur, A., 1993, Ultrasonic velocities in sands—revisited: GEOPHYSICS, v. 58, no. 3, p. 344-356.

Blevin, J., Cathro, D., Nelson, G., Vizy, J., and Lee, J. D., 2013, Survey GDPI10 Interpretation Project, Southern Flank, Gippsland Basin: Department of Primary Industries.

Boggs, S. J., 1992, Petrology of Sedimentary Rocks, Cambridge University Press.

Boles, J. R., and Franks, S. G., 1979, Clay diagenesis inWilcox sandstones of southwest Texas: Implication of smectite diagenesis on sandstone cementation: Journal of Sedimentary Research, v. 49, p. 55-70.

Bolshikh, S. F., 1956, On the approximate representation of the traveltime of reflected waves in the case of a multilayered medium: Applied Geophysics, v. 15, p. 3-14.

Bortfeld, R., 1961, Approximations to the reflection and transmission coefficients of plane longitudinal and transverse waves: Geophysical Prospecting, v. 9, no. 4, p. 485-502.

Bouvier, J. D., Kaars-Sijpersteijin, C. H., Kluesner, D. F., Onyejekwe, C. C., and Van der Pal, R. C., 1989, Three-dimentional seismic interpretation and fault sealing investigations, Nun River field, Nigeria: AAPG Bulletin, v. 73, p. 1397-1414.

Bretan, P., Yielding, G., and Jones, H., 2003, Using calibrated shale gouge ratio to estimate hydrocarbon column heights: AAPG Bulletin, v. 87, p. 397-413.

Brown, A., 2003, Capillary effects on fault-fill sealing.pdf: AAPG Bulletin, v. 87, no. 3, p. 381-395.

Brown, A. R., 1996, Seismic attributes and their classification: The Leading Edge, v. 15, no. 10, p. 1090-1090.

Budiansky, B., and Rice, J. R., 1973, Conservation Laws and Energy-Release Rates: Journal of Applied Mechanics, v. 40.

Bunch, M. A., Dobrzinski, N., and Vidal-Gilbert, S., 2009, CO2 storage potential in the onshore Gippsland Basin-Phase 1: Site screening and capacity estimation: CO2CRC.

Cartwright, J., Huuse, M., and Aplin, A., 2007, Seal bypass systems: AAPG Bulletin, v. 91, no. 8, p. 1141-1166.

Castagna, J. P., Batzle, M. L., and Eastwood, R. L., 1985, Relationships between compressional-wave and shear-wave velocities in clastic silicate rocks: GEOPHYSICS, v. 50, no. 4, p. 571-581.

Cathles, L. M., Su, Z., and Chen, D., 2010, The physics of gas chimney and pockmark formation, with implications for assessment of seafloor hazards and gas sequestration: Marine and Petroleum Geology, v. 27, no. 1, p. 82-91.

Chen, Q., and Sidney, S., 1997, Seismic attribute technology for reservoir forecasting and monitoring: The Leading Edge, v. 16, no. 5.

Chopra, S., and Marfurt, K. J., 2007, Seismic Attributes for Prospect Identification and Reservoir Characterization, Geophysical Development Series.

-, 2014, Churning seismic attributes with principal component analysis: SEG Denver 2014 International Exposition and Annual Meeting.

Ciftci, B., Langhi, L., Strand, J., and Goldie Divko, L., 2014, Efficiency of a faulted regional top seal, Lakes Entrance Formation, Gippsland Basin, SE Australia: Petroleum Geoscience, v. 20, no. 3, p. 241-256.

Ciz, R. M., Urosevic, M., and Dodds, K. J., 2005, Pore pressure prediction based on seismic attributes response to overpressure: APPEA Journal, v. 1, p. 1-10.

Collet, O., and Gurevich, B., 2013, Fluid dependence of anisotropy parameters in weakly anisotropic porous media: GEOPHYSICS, v. 78, no. 5, p. WC137-WC145.

Constantine, A. E., 2001, Sedimentology, stratigraphy and palaeoenvironment of the Late Jurassic–Early Cretaceous Strzelecki Group, Gippsland Basin [PhD: Monash University.

Courant, R., and Hilbert, D., 1953, Methods of Mathematical Physics, New York, Interscience Publishers, Inc.

Crampin, S., 1994, The fracture criticality of crustal rocks: Geophysical Journal International, v. 118, no. 2, p. 428-438.

Crampin, S., Evans, R., and Atkinson, B. K., 1984, Earthquake prediction: A new physical basis: Geophysical Journal of the Royal Astronomical Society, v. 76, p. 147-156.

Cruse, T., 2004a, Skiddaw-1 & 2 well completion report, Interpretive volume: BHP BILLITON PETROLEUM PTY. LTD.

-, 2004b, WA-12-R Crosby-1 Well Completion Report- Interpretive Volume.

Daniel, R. F., 2005, Carbon Dioxide Seal Capacity Study, Gippsland Basin, Victoria: CO2CRC.

Daniel, R. F., and Kaldi, J. G., 2008, Evaluating seal capacity of caprocks and intraformational barriers for the geosequestration of CO2, PESA Eastern Australian Basins Symposium III: Sydney.

David, E. C., and Zimmerman, R. W., 2011, Compressibility and shear compliance of spheroidal pores: Exact derivation via the Eshelby tensor, and asymptotic expressions in limiting cases: International Journal of Solids and Structures, v. 48, p. 680-686.

Delle Piane, C., Almqvist, B. S. G., MacRae, C. M., Torpy, A., Mory, A. J., and Dewhurst, D. N., 2015, Texture and diagenesis of Ordovician shale from the Canning Basin, Western Australia: Implications for elastic anisotropy and geomechanical properties: Marine and Petroleum Geology, v. 59, p. 56-71.

Delle Piane, C., Sarout, J., Madonna, C., Saenger, E. H., Dewhurst, D. N., and Raven, M., 2014, Frequency-dependent seismic attenuation in shales: experimental results and theoretical analysis: Geophysical Journal International, v. 198, no. 1, p. 504-515.

Dewangan, P., and Grechka, V., 2003, Inversion of multicomponent, multiazimuth, walkaway VSP data for the stiffness tensor: GEOPHYSICS, v. 68, no. 3, p. 1022-1031.

Dewhurst, D., Clennell, B., Siggins, T., Raven, M., Kuila, U., and Bolås, H., 2007, Elastic and petrophysical properties of shales, ASEG Extended Abstracts 2007: 19th Geophysical Conference, Australian Society of Exploration Geophysicists (ASEG), p. 1-5.

Dewhurst, D. N., and Hennig, A. L., 2003, Geomechanical properties related to top seal leakage in the Carnarvon Basin-NW shelf Australia: Petroleum Geoscience, v. 9, p. 255–263.

Dewhurst, D. N., Jones, R. M., and Raven, M. D., 2002a, Microstructural and petrophysical characterization of Muderong Shale-apps to top seal risking: Petroleum Geoscience, v. 8, p. 371–383.

-, 2002b, Microstructural and petrophysical characterization of Muderong Shale: application to top seal risking: Petroleum Geoscience, v. 8, p. 371–383.

Dewhurst, D. N., and Siggins, A. F., 2006, Impact of fabric, microcracks and stress field on shale anisotropy: Geophysical Journal International, v. 165, no. 1, p. 135-148.

Djikpesse, H. A., 2015, C13 and Thomsen anisotropic parameter distributions for hydraulic fracture monitoring: Interpretation, v. 3, no. 3, p. SW1-SW10.

Duncan, G., Hurren, C., Hill, R., Stanley, M., Woodward, J., and Lumley , D., 2013, The Stybarrow Field - a 4D Case Study: ASEG Extended Abstracts, v. 2013, no. 1, p. 1-5.

Dvorkin, J., and Mavko, G., 2006, Modeling attenuation in reservoir and nonreservoir rock: The Leading Edge, v. 25, no. 2, p. 194-197.

Dvorkin, J., Mavko, G., and Gurevich, B., 2007, Fluid substitution in shaley sediment using effective porosity: Geophysics, v. 72, no. 3, p. O1-O8.

Eshelby, J. D., 1957, The determination of the elastic field of an ellipsoidal inclusion, and related problems: Proceedings of the Royal Society of London. Series A. Mathematical and Physical Sciences, v. 241, no. 1226, p. 376.

Fox, F. G., 1959, Structure and Accumulation of Hydrocarbons in Southern Foothills, Alberta, Canada: AAPG Bulletin, v. 43, no. 5, p. 992-1025.

Gassmann, F., 1951, Uber die elastizitat poroser medien: Veirteljahrsschrift der Naturforschenden Gesellschaft, v. 96, p. 1-23.

Ghorbani, A., Zamora, M., and Cosenza, P., 2009, Effects of desiccation on the elastic wave velocities of clay-rocks: International Journal of Rock Mechanics and Mining Sciences, v. 46, no. 8, p. 1267-1272.

Glinsky, M. E., Asher, B., Hill, R., Flynn, M., Stanley, M., Gunning, J., Thompson, T., Kalifa, J., Mallat, S., White, C., and Renard, D., 2005, Integration of uncertain subsurface information into multiple reservoir simulation models: The Leading Edge, v. 24, no. 10, p. 990-999.

Goldie Divko, L., Campi, M. J., Tingate, P. R., O'Brien, G. W., and Harrison, M. L., 2009a, Geological Carbon Storage Potential of the Onshore Gippsland Basin, Victoria, Australia,.

Goldie Divko, L., Hamilton, J., and O'Brien, G. W., 2010a, Evaluation of the Regional Top Seal for the Purpose of Geologic Sequestration in the Gippsland Basin, Southeastern Australia, AAPG Convention: New Orleans, Louisiana.

Goldie Divko, L., O'Brien, G. W., Harrison, M. L., and Hamilton, P. J., 2010b, Evaluation of the regional top seal in the Gippsland Basin: Implications for geological carbon storage and hydrocarbon prospectivity, 463-486 p.:

Goldie Divko, L., O'Brien, G. W., Tingate, P. R., and Harrison, M. L., 2009b, Geological Carbon Storage in the Gippsland Basin, Australia: Containment Potential: Geological Carbon Storage in the Gippsland Basin, Australia: Containment Potential.

Grechka, V., 2009, Applications of Seismic Anisotropy in the Oil and Gas Industry, European Association of Geoscientists and Engineers.

Grechka, V., and Kachanov, M., 2006, Seismic characterization of multiple fracture sets: Does orthotropy suffice?: GEOPHYSICS, v. 71, no. 3, p. D93-D105.
Gurevich, B., 2003, A new model for fluid substitution in fractured reservoirs, ASEG Extended Abstracts, p. 1-5.
Hamilton, E. L., 1972, Compressional-wave attenuation in marine sediments: Geophysics, v. 37, no. 4, p. 620-646.
Hampson, D. P., Russell, B. H., and Bankhead, B., 2005, Simultaneous inversion of pre-stack seismic data, SEG Annual Meeting: Houston, SEG.
Hampson, D. P., Schuelke, J. S., and Quirein, J. A., 2001, Use of multiattribute transforms to predict log properties from seismic data: GEOPHYSICS, v. 66, no. 1, p. 220-236.
Han, D. h., Nur, A., and Morgan, D., 1986, Effects of porosity and clay content on wave velocities in sandstones: GEOPHYSICS, v. 51, no. 11, p. 2093-2107.
Hearmon, R. F. S., 1961, An Introduction to Applied Anisotropic Elasticity, Oxford University Press.
Helbig, K., 1984, Anisotropy and dispersion in periodically layered media: GEOPHYSICS, v. 49, no. 4, p. 364-373.
Hill, R., 1963, Elastic properties of reinforced solids: Some theoretical principles: Journal of the Mechanics and Physics of Solids, v. 11, p. 357-372.
-, 1965, A self-consistent mechanics of composite materials: Journal of the Mechanics and Physics of Solids, v. 13, no. 4, p. 213-222.
Hilterman, J. F., 2001, Seismic Amplitude Interpretation, Society of Exploration Geophysicists, v. Distinguished Instructor Short Course.
Hoffman, N., Arian, N., and Carman, G., 2012, Detailed seal studies for CO2 storage in the Gippsland Basin, Eastern Australasian Basins Symposium IV: Brisbane, QLD.
Holdgate, G. R., and Mcnichol, M. D., 1992, New directions–old ideas: hydrocarbon prospects of the Strzelecki Group, onshore Gippsland Basin, *in* Barton, C. M., ed., Energy, Economics and Environment: Gippsland Basin Symposium, Melbourne, p. 121-131.
Hornby, B. E., 1998, Experimental laboratory determination of the dynamic elastic properties of wet, drained shales: Journal of Geophysical Research, v. 103, no. B12, p. 29945.
Hornby, B. E., Schwartz, L. M., and Hudson, J. A., 1994, Anisotropic effective-medium modeling of the elastic properties of shales: GEOPHYSICS, v. 59, no. 10, p. 1570-1583.
Horne, S. A., 2013, A statistical review of mudrock elastic anisotropy: Geophysical Prospecting, v. 61, no. 4, p. 817-826.
Hudson, J. A., and Knopogg, L., 1989, Predicting the overall properties of composite materials with small-scale inclusions of cracks: Pure and applied geophysics, v. 131, p. 551-576.
Jakobsen, M., Hudson, J. A., Minshull, T. A., and Singh, S. C., 2000, Elastic properties of hydrate-bearing sediments using effective medium theory: Journal of Geophysical Research: Solid Earth (1978–2012), v. 105, no. B1, p. 561-577.
James, A., 2004, Eskdale-1 well completion report, Interpretive Volume: BHP Billiton Petroleum Pty. Ltd.
Jenner, E., 2011, Combining VTI and HTI anisotropy in prestack time migration: Workflow and data examples: The Leading Edge, v. 30, no. 7, p. 732-739.
Jennings, J. B., 1987, Capillary pressure techniques: Application to Exploration and Development Geology: AAPG Bulletin, v. 71, no. 10, p. 1196-1209.
Johnston, D. H., 1981, Attenuation: A state-of-the-art summary, *in* Toksoz, M. N., and Johnston, D. H., eds., Seismic wave attenuation, Volume 2, SEG, p. 123-135.
Johnston, J., and Christensen, N. I., 1995, Seismic anisotropy of shales: Journal of Geophysical Research: Solid Earth (1978–2012), v. 100, no. B4, p. 5991-6003.
Jones, L. E. A., and Wang, H. F., 1981, Ultrasonic velocities in Cretaceous shales from the Williston Basin: Geophysics, v. 46, no. 288-297, p. 11.

Josh, M., Esteban, L., Delle Piane, C., Sarout, J., Dewhurst, D. N., and Clennell, M. B., 2012, Laboratory characterisation of shale properties: Journal of Petroleum Science and Engineering, v. 88-89.

Kaarsberg, E. A., 1959, Introductory Studies of Natural and Artificial Argillaceous Aggregates by Sound-Propagation and X-ray Diffraction Methods: The Journal of Geology, v. 67, no. 4, p. 447-472.

Kachanov, M., 1992, Effective Elastic Properties of Cracked Solids: Critical Review of Some Basic Concepts: Applied Mechanics Reviews, v. 45, no. 8, p. 304-335.

Kachanov, M., and Sevostianov, I., 2005, On quantitative characterization of microstructures and effective properties: International Journal of Solids and Structures, v. 42, no. 2, p. 309-336.

Kachanov, M., Tsukrov, I., and Shafiro, B., 1994, Effective Moduli of Solids With Cavities of Various Shapes: Applied Mechanics Reviews, v. 47, no. 1S, p. S151-S174.

Kaldi, J. G., and Atkinson, C. D., 1997, Evaluating seal potential: example from the Talang Akar Formation, offshore northwest

Java, Indonesia, Seals, traps, and the petroleum system, Volume 67, p. 85-101.

Kanitpanyacharoen, W., Vasin, R., Wenk, H.-R., and Dewhurst, D. N., 2015, Linking preferred orientations to elastic anisotropy in Muderong Shale, Australia: GEOPHYSICS, v. 80, no. 1, p. C9-C19.

Kanitpanyacharoen, W., Wenk, H. R., Kets, F., Lehr, C., and Wirth, R., 2011, Texture and anisotropy analysis of Qusaiba shales: Geophysical Prospecting, v. 59, no. 3, p. 536-556.

Katahara, K. W., 1996, Clay mineral elastic properties: SEG Technical Program Expanded Abstracts, p. 1691-1694.

Kendall, J. M., Fisher, Q. J., Crump, S. C., Maddock, J., Carter, A., Hall, S. A., Wookey, J., Valcke, S. L. A., Casey, M., Lloyd, G., and Ismail, W. B., 2007, Seismic anisotropy as an indicator of reservoir quality in siliciclastic rocks: Geological Society, London, Special Publications, v. 292, no. 1, p. 123-136.

Kim, K. Y., Wrolstad, K. H., and Aminzadeh, F., 1993, Effects of transverse isotropy on P-wave AVO for gas sands: GEOPHYSICS, v. 58, no. 6, p. 883-888.

Koefoed, O., 1955, ON THE EFFECT OF POISSON'S RATIOS OF ROCK STRATA ON THE REFLECTION COEFFICIENTS OF PLANE WAVES*: Geophysical Prospecting, v. 3, no. 4, p. 381-387.

Kostenko, O. V., Naruk, S. J., Hack, W., Poupon, M., Meyer, H.-J., Mora-Glukstad, M., Anowai, C., and Mordi, M., 2008, Structural evaluation of column-height controls at a toe-thrust discovery, deep-water Niger Delta: AAPG Bulletin, v. 92, no. 12, p. 1615-1638.

Krushin, J. T., 1997, Seal Capacity of Nonsmectite Shale, *in* Surdam, R. C., ed., AAPG Memoir 67, Volume 67, American Association of Petroleum Geologists, p. 31-47.

Lashkaripour, G. R., 2002, Predicting mechanical properties of mudrock from index parameters: Bulletin of Engineering Geology and the Environment, v. 61, no. 1, p. 73-77.

Laubach, S. E., Olson, J. E., and Gale, J. F. W., 2004, Are open fractures necessarily aligned with maximum horizontal stress?: Earth and Planetary Science Letters, v. 222, p. 191-195.

Levin, F. K., 1980, Seismic velocities in transversely isotropic media, II: GEOPHYSICS, v. 45, no. 1, p. 3-17.

Levin, V. M., and Markov, M. G., 2005, Elastic properties of inhomogeneous transversely isotropic rocks: International Journal of Solids and Structures, v. 42, no. 2, p. 393-408.

Li, X. Y., 1999, Fracture detection using azimuthal variation of P-wave moveout from orthogonal seismic survey lines: GEOPHYSICS, v. 64, no. 4, p. 1193-1201.

Lonardelli, I., Wenk, H.-R., and Ren, Y., 2007, Preferred orientation and elastic anisotropy in shales: GEOPHYSICS, v. 72, no. 2, p. D33-D40.

Longley, I. M., Buessenschuett, C., Clydsdale, L., Cubitt, C. J., Davis, R. C., Johnson, M. K., Marshall, N. M., Murray, A. P., Somerville, R., Spry, T. B., and Thompson, N. B., 2003, The North West Shelf of Australia - A Woodside Perspective: Search and Discovery.

Loucks, R. G., Reed, R. M., Ruppel, S. C., and Hammes, U., 2012, Spectrum of pore types and networks in mudrocks and a descriptive classification for matrix-related mudrock pores: AAPG Bulletin, v. 96, no. 6, p. 1071-1098.

Mackenzie, J. K., 1950, The elastic constants of a solid containing sperical holes: Proceedings of the Royal Society of London, v. 63B, p. 2-11.

Matthies, S., 2012, GEO-MIX-SELF calculations of the elastic properties of a textured graphite sample at different hydrostatic pressures: Journal of Applied Crystallography, v. 45, no. 1.

Mayer, F., and Larson, G., 2014, Resistivity and density estimation from multicomponent seismic data: Case study from the Lower Cretaceous McMurray Formation, Athabasca Oil Sands: SEG Technical Program Expanded Abstracts, v. 2014.

Miller Douglas, E., and Spencer, C., 1994, An exact inversion for anisotropic moduli from phase slowness data: Journal of Geophysical Research: Solid Earth, v. 99, no. B11, p. 21651-21657.

Moriya, S., 2011, Effective permeability to water in petroleum column from capillary pressure data: implications for hydrodynamic effects on capillary seal capacity: Petroleum Geoscience, v. 17, no. 4, p. 397-404.

Morris, P. R., 1969, Averaging Fourth-Rank Tensors with Weight Functions: Journal of Applied Physics, v. 40, no. 2, p. 447-448.

-, 1970, Elastic constants of polycrystals: International Journal of Engineering Science, v. 8, no. 1, p. 49-61.

Müller, R. D., Dyksterhuis, S., and Rey, P., 2012, Australian paleo-stress fields and tectonic reactivation over the past 100 Ma: Australian Journal of Earth Sciences, v. 59, no. 1, p. 13-28.

Mura, T., 1987, Micromechanics of defects in solids, Martinus Nijhoff Publishers.

Nishizawa, O., and Yoshino, T., 2001, Seismic velocity anisotropy in mica-rich rocks: an inclusion model: Geophysical Journal International, v. 145, no. 1, p. 19-32.

Norvick, M. S., and Smith, M. A., 2001, Mapping the plate tectonic reconstructions of southern and southeastern Australia and implications for petroleum systems: The APPEA Journal, v. 41, no. 1, p. 15-35.

Norvick, M. S., Smith, M. A., and Power, M. R., 2001, The plate tectonic evolution of eastern Australasia guided by the stratigraphy of the Gippsland Basin, *in* Hill, K. C., and Bernecker, T., eds., Eastern Australasian Basins Symposium, A Refocused Energy Perspective for the Future, Petroleum Exploration Society of Australia, p. 15-23.

Nourollah, H., 2011, Applications of property modelling from 2D seismic data to reservoir identification and sealing potential for petroleum exploration and CO2 sequestration: Exploration Geophysics, v. 42, no. 4, p. 239.

Nourollah, H., Keetley, J., and O'Brien, G., 2010, Gas chimney identification through seismic attribute analysis in the Gippsland Basin, Australia: The Leading Edge, v. 29, no. 8, p. 896-901.

Nourollah, H., Urosevic, M., and Keetley, J., 2015, Seal potential of shale sequences through seismic anisotropy: Case study from Exmouth Sub-basin, Australia: Interpretation, v. 3, no. 4, p. T257-T267.

Nye, J. F., 1985, Physical properties of crystals, Oxford University Press.

O'brien, N. R., 1986, The effects of bioturbation on the fabric of shale: Journal of Sedimentary Petrology, v. 57.

Ortega, J. A., Ulm, F. J., and Aboulseiman, Y., 2007, The effect of the nanogranular nature of shale on their poroelastic behavior: Acta Geotechnica, v. 2, p. 155-182.

Partridge, A. D., Kelman, A. P., Khider, K., Le Poidevin, S., and Mantle, D. J., 2012, Gippsland Basin, Biozonation and Stratigraphy, *in* 40, C., ed., Geoscience Australia.

Perrodon, A., and Masse, P., 1984, Subsidence, sedimentation and petroleum systems: Journal of Petroleum Geology, v. 7, no. 1, p. 5-26.

Pervukhina, M., and Rasolofosaon, P. N. J., 2017, Compaction trend versus seismic anisotropy in shaly formations: Geophysical Prospecting, v. 65, no. 5, p. 1351-1365.
Pevzner, R., Bona, A., Gurevich, B., Yavuz, I., Shaiban, A., and Urosevic, M., 2010, Seismic anisotropy estimation from VSP data: CO2CRC Otway project case study, SEG Technical Program Expanded Abstracts 2010, p. 353-357.
Picknell, J. J., Swanson, B. F., and Hickman, W. B., 1966, Application of air-mercury capillary pressure data in the study of pore structure and fl uid distribution: SPE Journal, v. 6, p. 55-61.
Postma, G. W., 1955, WAVE PROPAGATION IN A STRATIFIED MEDIUM: GEOPHYSICS, v. 20, no. 4, p. 780-806.
Purcell, W. R., 1949, Capillary pressures - their measurement using mercury and the calculation of permeability therefrom: Petroleum Transactions: American Institute of Mining, Metallurgical and Petroleum Engineers, v. 186, p. 39-48.
Pyrcz, M. J., and Deutsch, C. V., 2014, Geostatistical Reservoir Modeling, Oxford University Press.
Rahmanian, V. D., Moore, P. S., Mudge, W. J., and Spring, D. E., 1990, Sequence stratigraphy and the habitat of hydrocarbons, Gippsland Basin, *in* Brooks, J., ed., Classic Petroleum Provinces, Volume Special Publications, Geological Society, London, p. 525-541.
Reuss, A., 1929, Berechnung der Fließgrenze von Mischkristallen auf Grund der Plastizitätsbedingung für Einkristalle: Z. Angew. Math. Mech., v. 9, p. 49-58.
Roe, R. J., 1965, Description of Crystallite Orientation in Polycrystalline Materials. III. General Solution to Pole Figure Inversion: Journal of Applied Physics, v. 36, no. 6, p. 2024-2031.
Rose, M. E., 1957, Elementary Theory of Angular Momentum, New York, John Wiley &Sons, Inc.
Rüger, A., 1996, Reflection coefficients and azimuthal AVO analysis in anisotropic media: Colorado School of Mines.
Ruth, P. J. v., Nelson, E. J., and Hillis, R. R., 2006, Fault reactivation potential during CO2 injection in the Gippsland Basin, Australia: Exploration Geophysics, v. 37, p. 50-59.
Sales, J. K., 1993, Closure vs. sealing strength—a fundamental control on the distribution of oil and gas: Basin modeling: advances and application, Norwegian Petroleum Society Special Publication, Volume 3, Norwegian Petroleum Society, p. 399-414.
Sales, J. K., 1997, Seal strength vs. trap closure—a fundamental control on the distribution of oil and gas, *in* Surdam, R. C., ed., Seals, traps, and the petroleum

system, Volume AAPG Memoir 67, AAPG.
Sarout, J., and Guéguen, Y., 2008a, Anisotropy of elastic wave velocities in deformed shales: Part 1 — Experimental results: GEOPHYSICS, v. VOL. 73, no. NO.5.
-, 2008b, Anisotropy of elastic wave velocities in deformed shales: Part 2 — Modeling results: GEOPHYSICS, v. 73, no. 5, p. D91-D103.
Sayers, C. M., 1989, Seismic anisotropy of the inner core: Geophysical Research Letters, v. 16, no. 3, p. 267-270.
Sayers, C. M., 1994a, The elastic anisotrophy of shales: Journal of Geophysical Research: Solid Earth (1978–2012), v. 99, no. B1, p. 767-774.
-, 1994b, P-wave propagation in weakly anisotropic media: Geophysical Journal International, v. 116, p. 799-805.
Sayers, C. M., 1999, Stress-dependent seismic anisotropy of shales: Geophysics, v. 64, p. 93-98.
Sayers, C. M., 2005, Seismic anisotropy of shales: Geophysical Prospecting, v. 53, no. 5, p. 667-676.
Sayers, C. M., 2008, The effect of low aspect ratio pores on the seismic anisotropy of shales, SEG Technical Program Expanded Abstracts 2008, p. 2750-2754.
-, 2010, Geophysics Under Stress, Society of Exploration Geophysicists, Geophysics Under Stress.

Sayers, C. M., and Boer, L. D. d., 2014, Shale anisotropy and the elastic anisotropy of clay minerals, SEG Technical Program Expanded Abstracts 2014, p. 2829-2833.
Sayers, C. M., and Kachanov, M., 1995, Microcrack-induced elastic wave anisotropy of brittle rocks: Journal of Geophysical Research, v. 100, no. B3, p. 4149-4156.
Schoenberg, M., and Douma, J., 1988, Elastic wave propagation in media with parallel fractures and aligned cracks: Geophysical Prospecting, v. 36, p. 571-590.
Schoenberg, M., and Sayers, C. M., 1995, Seismic anisotropy of fractured rock: Geophysics, v. 60, p. 204-211.
Schowalter, T. T., 1979, Mechanics of secondary hydrocarbon migration and entrapment: AAPG Bulletin, v. 63, p. 723–760.
Scibiorski, J., Micenko, M., and Lockhart, D., 2005, RECENT DISCOVERIES IN THE PYRENEES MEMBER, EXMOUTH SUB-BASIN: A NEW OIL PLAY FAIRWAY: The APPEA Journal, v. 45, no. 1.
Sevostianov, I., and Kachanov, M., 2002, Explicit cross-property correlations for anisotropic two-phase composite materials: Journal of the Mechanics and Physics of Solids, v. 50, no. 2, p. 253-282.
Sheriff, R. E., and Geldart, L. P., 1995, Exploration seismology, Cambridge University Press.
Shuey, R. T., 1985, A simplification of the Zoeppritz equations: GEOPHYSICS, v. 50, no. 4, p. 609-614.
Smith, G. C., 1988, Oil and gas, *in* Douglas, J. G., and Ferguson, J. A., eds., Geology of Victoria, Volume 5, Geological Society of Australia, p. 514-531.
Sneider, R. M., Sneider, J. S., Bolger, G. W., and Neasham, J. W., 1997, Comparison of Seal Capacity Determinations: Conventional Cores vs. Cuttings, *in* Surdam, R. C., ed., AAPG Memoir 67, Volume 67, The American Association of Petroleum Geologists, p. 1-12.
Sondergeld, C. H., and Rai, C. S., 2011, Elastic anisotropy of shales: The Leading Edge, v. 30, no. 3, p. 324-331.
Taner, M. T., 2001, Seismic attributes: CSEG Recorder, v. 26, no. 9, p. 48-56.
Taner, M. T., and Koehler, F., 1969, VELOCITY SPECTRA—DIGITAL COMPUTER DERIVATION APPLICATIONS OF VELOCITY FUNCTIONS: GEOPHYSICS, v. 34, no. 6, p. 859-881.
Taya, M., and Chou, T.-W., 1981, On two kinds of ellipsoidal inhomogeneities in an infinite elastic body: An application to a hybrid composite: International Journal of Solids and Structures, v. 17, no. 6, p. 553-563.
Taya, M., and Mura, T., 1981, On Stiffness and Strength of an Aligned Short-Fiber Reinforced Composite Containing Fiber-End Cracks Under Uniaxial Applied Stress: Journal of Applied Mechanics, v. 48, no. 2, p. 361-367.
Teng, L., and Mavko, G., 1996, Fracture signatures on P wave AVOZ, *in* Geophysicists, S. o. E., ed., 66th Annual Meeting, p. 1818-1821.
Thomsen, L., 1986, Weak elastic anisotropy: GEOPHYSICS, v. 51, no. 10, p. 1954-1966.
-, 2002, Understanding Seismic Anisotropy in Exploration and Exploitation, SEG, SEG/EAGE Distinguished Instructor Short Course.
Timko, D., 2003, Pseudo Gamma Ray Volumes Estimated from Offset Seismic: Recorder, v. 28, no. 7.
Tindale, K., Newel, N., Keall, J., and Smith, N., 1998, Structural evolution and charge history of the Exmouth subbasin, northern Carnarvon basin, western Australia, *in* Purcell, P. G., and Purcell, R. R., eds., The sedimentary basins of western Australia 2: Proceedings of The Petroleum Exploration Society of Australia Symposium, p. 447–472.
Tosaya, C. A., 1982, Acoustic properties of clay-bearing rocks [PhD: Stanford University.
Tutuncu, A. N., 2010, Anisotropy, Compaction And Dispersion Characteristics of Reservoir And Seal Shales, American Rock Mechanics Association.
Ulm, F. J., and Aboulseiman, Y., 2006, The nanogranular nature of shale: Acta Geotechnica, v. 1, no. 3, p. 77-88.

Urosevic, M., Chambers, B., Gurevich, B., and Koster, K., 2004, Resolving Ambiguity in Fracture Induced Anisotropy Interpreted from Various Data, 66th EAGE Conference & Exhibition, Volume C044, EAGE.

Urosevic, M., Fu, L.-Y., and Dodds, K. J., 2002, Seismic expression of abnormal geo-pressure in the Barrow sub-basin: APPEA Journal, v. 42, no. 2.

Vasin, R. N., Wenk, H. R., Kanitpanyacharoen, W., Matthies, S., and Wirth, R., 2013, Elastic anisotropy modeling of Kimmeridge shale: Journal of Geophysical Research: Solid Earth, v. 118, no. 8, p. 3931-3956.

Vavra, C. L., Kaldi, J. G., and Sneider, R. M., 1992, Geological Applications of Capillary Pressure A review: AAPG Bulletin, v. 76, no. 6, p. 840-850.

Vernik, L., and Nur, A., 1992, Ultrasonic velocity and anisotropy of hydrocarbon source rocks: Geophysics, v. 57, p. 727-735.

Voigt, W., 1887, Theoretische Studien über die Elasticitätsverhältnisse der Krystalle, Dieterichsche Verlags-Buchhandlung, Göttingen.

Walsh, J. B., 1965, The effect of cracks on the compressibility of rocks: Journal of Geophysical Research, v. 70, p. 381-389.

Wardlaw, N. C., and Taylor, R. P., 1976, Mercury capillary pressure curves and the interpretation of pore structure and capillary behaviour in reservoir rocks: Bulletin of Canadian Petroleum Geology, v. 24, p. 225-262.

Weinberger, C., and Cai, W., 2004, Lecture Note 2. Eshelby's Inclusion I, *in* University, S., ed.

Werthmüller, D., Ziolkowski, A., and Wright, D., 2013, Background resistivity model from seismic velocities: GEOPHYSICS, v. 78, no. 4, p. E213-E223.

Willis, S., 1999, Viincent-1 Well Completion Report, Interpretive Data, WA-271-P: Woodside Energy Ltd.

Winterstein, D. F., 1990, Velocity anisotropy terminology for geophysicists: GEOPHYSICS, v. 55, no. 8, p. 1070-1088.

Winterstein, D. F., and Paulsson, B. N. P., 1990, Velocity anisotropy in shale determined from crosshole seismic and vertical seismic profile data: GEOPHYSICS, v. 55, no. 4, p. 470-479.

Withers, P. J., 1989, The determination of the elastic field of an ellipsoidal inclusion in a transversely isotropic medium, and its relevance to composite materials: Philosophical Magazine A, v. 59, no. 4, p. 759-781.

Woodside, 2001, Laverda-1 well completion report: Woodside Energy Ltd.

Yielding, G., Freeman, B., and Needham, D. T., 1997, Quantitative fault seal prediction: AAPG Bulletin, v. 81, no. 6, p. 897-917.

Yilmaz, O., 2001, Seismic data analysis, Society of Exploration Geophysicists.

Zane, R. J., Donald, R. L., and Uchytil, S. J., 2010, Two fundamentally different types of submarine canyons along the continental margin of Equatorial Guinea: Marine and Petroleum Geology, v. 28, p. 843-860.

Zhdanov, M. S., Endo, M., Yoon, D., Čuma, M., Mattsson, J., and Midgley, J., 2014, Anisotropic 3D inversion of towed-streamer electromagnetic data: Case study from the Troll West Oil Province: Interpretation, v. 2, no. 3, p. SH97-SH113.

Every reasonable effort has been made to acknowledge the owners of copyright material. I would be pleased to hear from any copyright owner who has been omitted or incorrectly acknowledged.

1 Appendix 1

One of the strengths of the MICP method is that the samples that are subjected to this type of measurement can be of any shape and size (as long as they fit in the measurement capsule). Such a characteristic is very useful as the majority of wells don't recover cores of proper plugs and measurements can be performed on cuttings. Recovery of cores and samples from shaley formations is particularly difficult as they can get lost during drilling/percolation. Therefore the capability of MICP measurement to be performed on cuttings is very useful in the evaluation of shale sealing capacity.

1.1 Sample size correction

Although it is best to have a sufficiently large sample to perform the MICP analysis, cuttings are sometime the only available options. Measurements on cuttings need a correction so that their measurements can compare with the plugs where the sealing capacity is measured perpendicular to the bedding and under more optimum conditions (Sneider et al., 1997). In this correction, a global empirical adjustment is applied to the cuttings so that their values are comparable to those that might have been obtained from plugs. Table 6 shows the adjustment values that should be added to the pressure values measured for cuttings.

Seal Type	Min. (psi)	Max. (psi)	Average (psi)
A*	1402	3120	2315
A	923	4009	1810
B	423	1040	455
C	22	363	140
D	27	91	30

Table 6. Empirical pressure adjustment factors for different seal type (after Sneider et al. (1997)). Seal classes are on the left column ranging from the best (A*) to the poorest (D).

1.2 Blank Cell Correction

The MICP measurements use the injection pressure of up to 60,000 psia (~414 MPa). Such pressure will certainly affect the sample and will cause compression. This compression happens to not only the sample, but also the measuring instruments. Although it is small, but this compression is measurable and is recorded as part of the intrusion/extrusion data. The amount of compression can vary depending on the lithology, porosity and internal structuring of the samples. Porosity of the samples has the most significant impact on this correction factor. The amount of correction can generally vary to up to 4% of the raw measurements in shales. This correction (called the blank cell correction) is usually performed in the lab using either an instrument software or user-defined functions by comparison with a non-porous sample.

1.3 Conformance Correction

When the sample is placed in penetrometer, it will be encroached by the non-wetting phase (mercury) on a macroscopic scale. However, the non-wetting phase does not prefer to replace the wetting phase (air) in a microscopic scale. Therefore, the initial steps of pressure that are applied will be spent on forcing the mercury to cover the micro-fractures, surface cavities and fissures of the sample. Once this step is achieved, mercury will be looking for the largest pores to enter the pore space under the next step of applied pressure. The conformance correction converts the lab measurement to the actual intrusion values of the non-wetting phase in the pore space. This correction takes into account the encroachment of mercury within the irregularities and non-pore space micro-fractures that are falsely seen as mercury injection. The conformance correction brings to zero any pressure measurement before the commencement of mercury intrusion to the inter-granular pore space. The conformance correction then gradually decreases as the intrusion increases until it equates zero at the point of 100% saturation

In order to select the conformance (closure) pressure for a particular sample, the plot of percent saturation of non-wetting phase versus pressure is prepared. On the plot that shows the incremental pore space filled with mercury (Figure 91), there will be a sudden increase in the rate of mercury volume. This plot should more or less match with the injection plot that shows the saturation of the non-wetting phase versus pressure. The sudden increase in the influx of mercury into the pore space occurs where the injection/drainage plot shows a deflection on the graph (larger blue point in Figure 91). This is the point that is reference for the conformance correction.

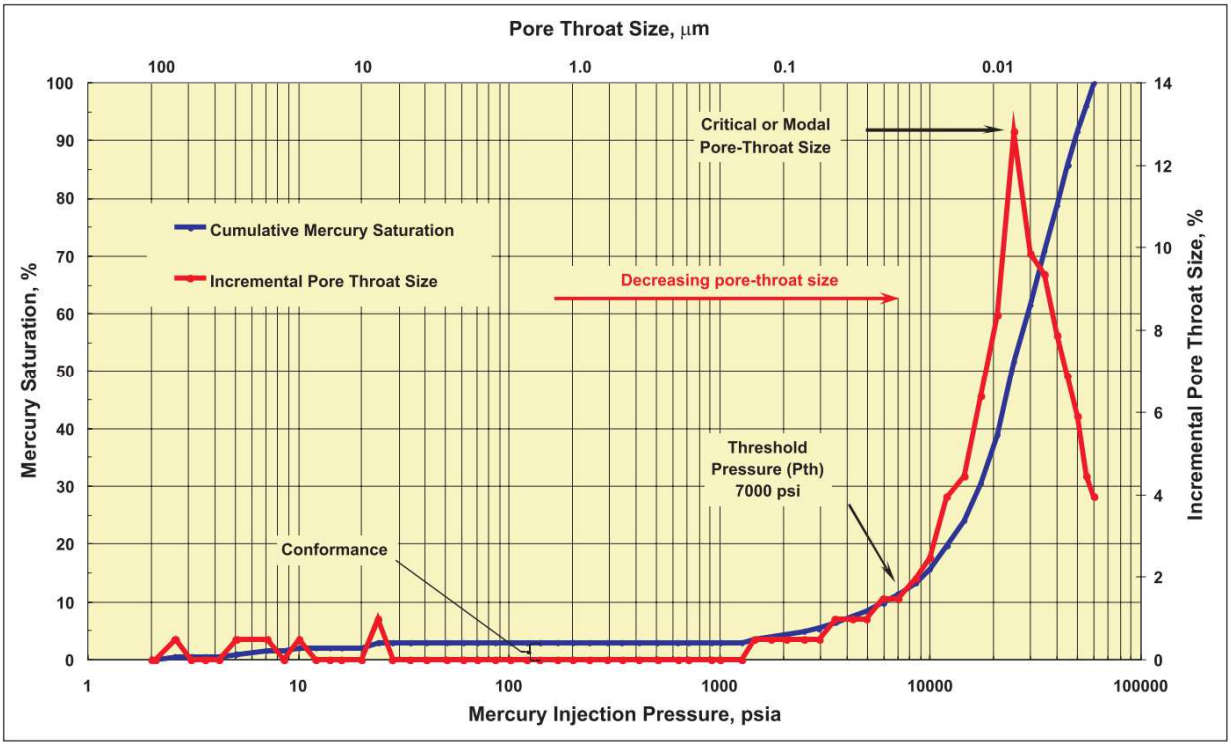

Figure 91. An example of Mercury injection test results. The red curve depicts the incremental filling of the pore space as the non-wetting pressure increases (after Daniel and Kaldi (2008))

2 Appendix 2

For an inclusion with the dimensions $a_1<a_2<a_3$ and the Poisson ratio of ν, the component of the Eshelby's tensor are:

$$S_{1111} = \frac{3}{8\pi(1-\nu)} a_1^2 I_{11} + \frac{1-2\nu}{8\pi(1-\nu)} I_1$$

$$S_{1122} = \frac{1}{8\pi(1-\nu)} a_2^2 I_{12} + \frac{1-2\nu}{8\pi(1-\nu)} I_1$$

$$S_{1133} = \frac{3}{8\pi(1-\nu)} a_3^2 I_{13} + \frac{1-2\nu}{8\pi(1-\nu)} I_1 \qquad (66)$$

$$S_{1212} = \frac{a_1^2 + a_2^2}{16\pi(1-\nu)} I_{12} + \frac{1-2\nu}{16\pi(1-\nu)} (I_1 + I_2)$$

All other non-zero components are obtained by the cyclic permutation of (1, 2, 3). The components which cannot be obtained by the cyclic permutation are zero (e.g. S_{1112}, S_{1223}, etc). The "I" integrals are expressions of the standard elliptic integrals (Mura, 1987):

$$I_1 = \frac{4\pi a_1 a_2 a_3}{(a_2^2 - a_3^2)(a_1^2 - a_3^2)^{\frac{1}{2}}} \{F(\theta, k) - E(\theta, k)\}$$

$$I_3 = \frac{4\pi a_1 a_2 a_3}{(a_2^2 - a_3^2)(a_1^2 - a_3^2)^{\frac{1}{2}}} \left\{ \frac{a_2 (a_1^2 - a_3^2)^{\frac{1}{2}}}{a_1 a_3} - E(\theta, k) \right\} \qquad (67)$$

Where $F(\theta, k) = \int_0^\theta \frac{dw}{(1 - k^2 sin^2 w)^{\frac{1}{2}}}$, $E(\theta, k) = \int_0^\theta (1 - k^2 sin^2 w)^{\frac{1}{2}}$

$$\theta = sin^{-1}(1 - \frac{a_3^2}{a_1^2})^{\frac{1}{2}} \quad , \quad k = \left\{ \frac{(a_1^2 - a_2^2)}{(a_1^2 - a_3^2)} \right\}^{\frac{1}{2}}$$

Also, the following relationship stays for the "I" integrals:

$$I_1 + I_2 + I_3 = 4\pi$$

$$3I_{11} + I_{12} + I_{13} = \frac{4\pi}{a_1^2}$$

$$3a_1^2 I_{11} + a_2^2 I_{12} + a_3^2 I_{13} = 3I_1 \tag{68}$$

$$I_{12} = \frac{(I_2 - I_1)}{(a_1^2 - a_2^2)}$$

Various shapes can be modelled using the above formulations. For an elliptic cylinder, $a_3 \to \infty$ and for a spherical inclusion $a_1 = a_2 = a_3$.

3 Appendix 3

The function $Z_{lmn}(\zeta)$ is given (Roe, 1965; Rose, 1957) by the solution of the differential equation:

$$(1-\zeta^2)\frac{d^2Z}{d\zeta^2} - 2\zeta\frac{dZ}{d\zeta} + \left[l(l+1) - \frac{m^2 - 2mn\zeta + n^2}{1-\zeta^2}\right]Z = 0 \tag{69}$$

We have to make the substitutions

$$\begin{gathered} i = \frac{(1-\zeta)}{2} \\ Z = Ni^{\frac{m-n}{2}}(1-i)^{\frac{m+n}{2}}f(t) \end{gathered} \tag{70}$$

Then equation (69) will transform to:

$$t(t-1)\left(\frac{d^2f}{dt^2}\right) + [(m-n+1) - 2mt]\left(\frac{df}{dt}\right) + [l(l+1) - m(m+1)]f = 0 \tag{71}$$

which is a second-order linear equation. The solution to the above equation is (for m ≥ n):

$$\begin{gathered} f(t) = F_1(-l+m, l+m+1; m-n+1; t) \\ F_1(\alpha,\beta;\mu;t) = 1 + \frac{\alpha.\beta}{1.\mu}t + \frac{\alpha(\alpha+1)\beta(\beta+1)}{2!\,\mu(\mu+1)}t^2 + \cdots \end{gathered} \tag{72}$$

For the situation where α is a negative integer, the series in equation (72) terminates after a finite number of terms. This means the function will be a polynomial that is called a Jacobi Polynomial (Andrews et al., 1999; Courant and Hilbert, 1953). The constant "N" in equation (70) is determined from

$$\int_{-1}^{1} Z_{lmn}^2(\zeta)d\zeta = 1 \tag{73}$$

For m=n=0, the generalized Legendre functions are

$$Z_{l00}(\zeta) = \sqrt{\frac{2l+1}{2}}P_l(\zeta) \tag{74}$$

The basic isotropic ODF (Orientation Distribution Function) is W_{000} and defined as

$$W_{000} = \frac{1}{4\sqrt{2}\pi^2} \tag{75}$$

For the VTI medium, the required orientation parameters are

$$W_{200} = \sqrt{\frac{5}{2}} \int_{-1}^{1} W(\zeta)\, P_2(\zeta) d\zeta$$
$$W_{400} = \sqrt{\frac{9}{2}} \int_{-1}^{1} W(\zeta)\, P_4(\zeta) d\zeta \tag{76}$$

Where ζ=cos θ and

$$P_2(\zeta) = \frac{1}{2}(3\zeta^2 - 1)$$
$$P_4(\zeta) = \frac{1}{8}(35\zeta^4 - 30\zeta^2 + 3) \tag{77}$$

4 Appendix 4

The clay platelet orientation distribution function can be evaluated using several methods such as direct measurement of velocities of samples (at different angles), inversion of pole figures from X-ray diffraction measurements (Kanitpanyacharoen et al., 2015; Roe, 1965) or SEM (Scanning Electron Microscope) images (Hornby et al., 1994). The method that is used to analyze the micro-images consist of digitization of the image(s) and scanning them along different angles (from the axis of symmetry) to construct a coherency energy attribute for that direction. This is similar to running a surface attribute on seismic data. (Hornby et al., 1994) proposed the energy indexing formula to be:

$$\chi = \left[\sum_{n=1}^{N-1} a(i+n,j)\right]^2 \tag{78}$$

Where I and j are indexes of image intensity of the matrix (a) and N is the number of pixels in a representative clay platelet.

Cumulative scores/counts per rotation angles (Δω) will be added and the normalized criteria can be expressed as (Hornby et al., 1994):

$$\int_{-\frac{\pi}{2}}^{\frac{\pi}{2}} f(\omega)d\omega = 1 \tag{79}$$

Where f is the orientation distribution of platelet normals.

This ODF (orientation distribution function) is the background information for the shales sample. There are many concerns over the accuracy of using such data as to whether it truly represents the in-situ data (Sarout and Guéguen, 2008b) especially considering the difficulty of measuring wet shale elastic properties. Assuming the SEM results practically acceptable, the distribution of connected pore spaces over this background ODF is usually found during the MICP tests. The MICP data usually provides

the ranges of (connected) pores, their probabilistic distribution against their size and the cumulative porosity (for example Figure 34). The cumulative porosity is mathematically the integral of the incremental pore size distribution. The combination of the two forms the overall ODF that can be used in a numerical model.

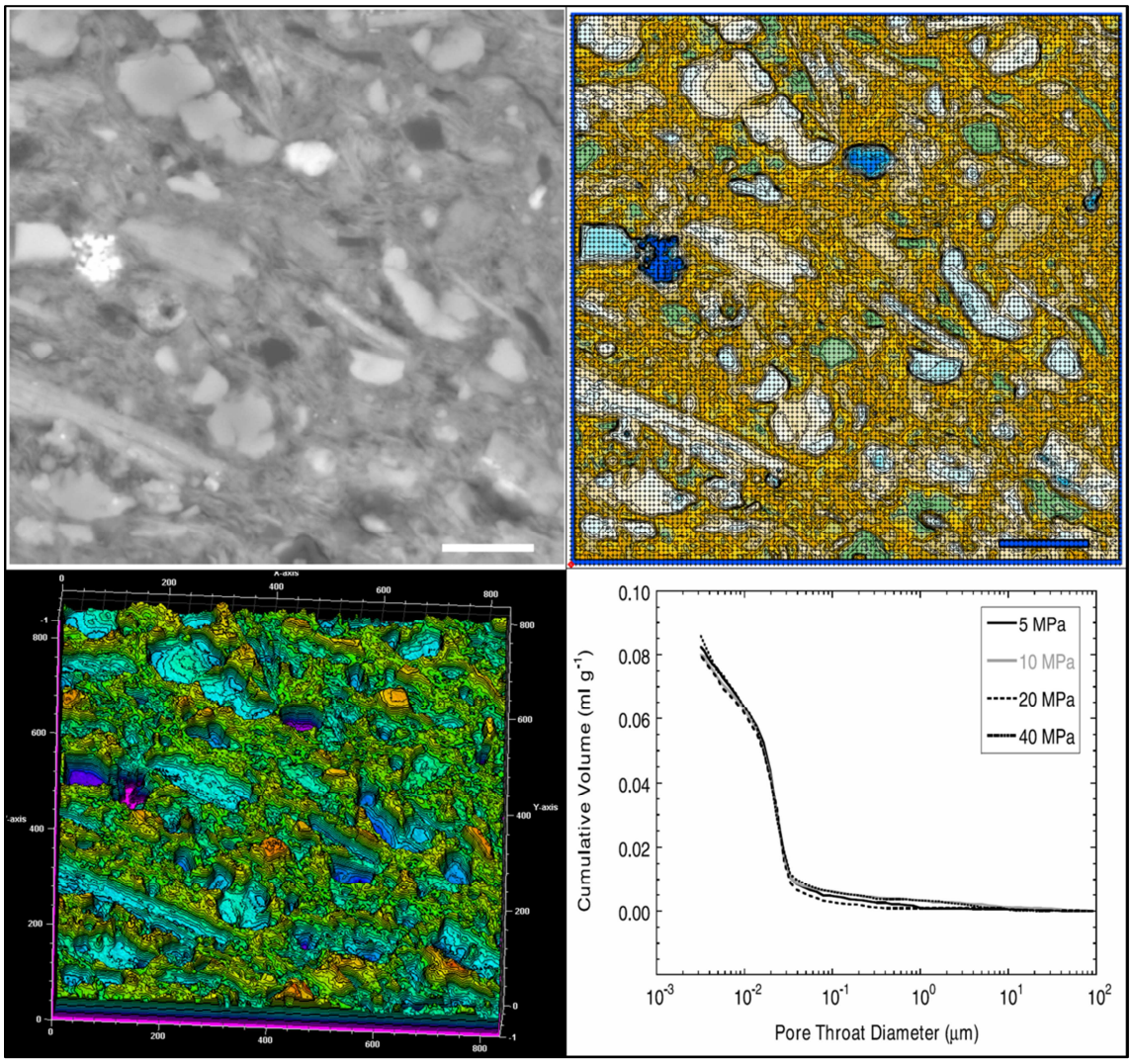

Figure 92. An SEM image of the Muderong Shale (Dewhurst et al., 2002b) and the digitized contoured version (top right). The same contour image can be analyzed for energy attribute (bottom left). When the information on the pore throat (bottom right) are added to the orientation of domains, the overall seismic response may be modelled.

5 Appendix 5

To calculate the impact of an inclusion on the longitudinal Young's modulus, we can imagine an ellipsoidal inclusion in an infinite matrix which undergoes the stress σ_0 along the large axis of the inclusion (Figure 93). The overall volume of the matrix is V and the volume of the inclusion is a fraction (f) of V and is denoted by V_f.

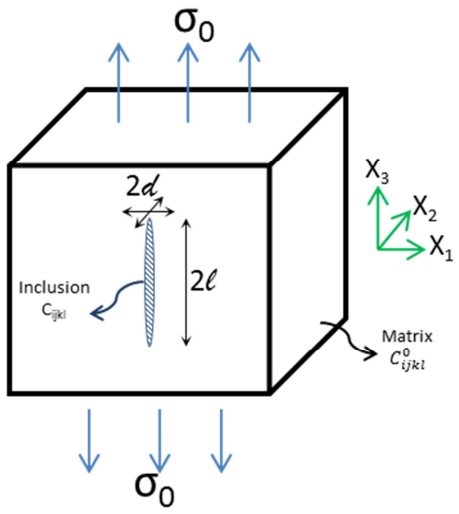

Figure 93. A schematic infinite composite under uniaxial stress

One of the methods to calculate the overall stiffness of a composite is to compute the elastic energy. Modifying from equation (5) of (Taya and Mura, 1981) by removing the end-fiber crack terms:

$$\frac{{\sigma^0}^2}{2E_L}V = \frac{{\sigma^0}^2}{2E_0}V - E_{int}^f \tag{80}$$

Where E_0 and E_L are the Young's moduli of the matrix and the composite respectively. E_{int}^f is the interaction energy (between the applied stress and the inclusion) of the inclusion and is given by:

$$E_{int}^f = -\frac{1}{2}\sigma^0 \varepsilon_{33}^* V_f \tag{81}$$

Using Eshelby's equivalent inclusion method (Appendix 1), we can write:

$$\sigma_{ij}^0 + \sigma_{ij} = C_{ijkl}^0(\varepsilon_{kl}^0 + \bar{\varepsilon}_{kl} + \varepsilon_{kl} - \varepsilon_{kl}^*)$$

Where (82)

$$\varepsilon_{kl} = S_{klmn}\varepsilon_{mn}^* \quad \text{and} \quad \sigma_{ij}^0 = C_{ijkl}^0\varepsilon_{kl}^0$$

Solving for $\varepsilon_{33}^* \; and \; \varepsilon_{11}^*$(eigenstrain in the inclusion):

$$\varepsilon_{33}^* = \left\{\frac{B_4 - \nu_0 B_3}{A} + \frac{f(B_3S_1 + B_4S_2)}{AS}\right\}\frac{\sigma^0}{E_0}$$
$$\varepsilon_{11}^* = \left\{\frac{B_2 - \nu_0 B_1}{A} + \frac{f(B_1S_1 + B_2S_2)}{AS}\right\}\frac{\sigma^0}{E_0} \quad (83)$$

Where

$A = C_{11}C_{22} - C_{21}C_{12}\,,\; B_1 = 2(C_{12} - D_1C_{22})\,, B_2 = D_2(C_{12} - D_1C_{22}),\; B_3 = 2(D_1C_{21} - C_{11})$

$B_4 = C_{21} - D_2C_{11}, D_1 = 1 + \left(\frac{\mu-\mu^0}{\lambda-\lambda^0}\right), D_2 = 1 + 2\left(\frac{\mu-\mu^0}{\lambda-\lambda^0}\right)$

Now, substituting in equation (81), we have:

$$\frac{1}{E_L} = \frac{1}{E_0} - \frac{f}{E_0}\left(\frac{B_4 - \nu_0 B_3}{A} + \frac{f(B_3S_1 + B_4S_2)}{AS}\right) \quad (84)$$

From which, $\frac{E_L}{E_0}$ can be calculated (for direction X_3). Equation (84) shows the reduction in the Young's modulus due to the presence of the inclusion. This reduction is related to the components of the Eshelby's tensor that are related to the dimensions of the inclusion. The calculation of $\frac{E_L}{E_0}$ for the horizontal case is done the same way as above, noting that $\varepsilon_{33}^0 = -\nu_0\frac{\sigma_0}{E_0}$ and $\varepsilon_{11}^0 = \frac{\sigma_0}{E_0}$.

The total potential energy in an inhomogeneous body is defined as (Eshelby, 1957):

$$P = P_0 + E_{int} \quad (85)$$

Where P_0 is the potential energy without the inclusion and E_{int} is defined in equation (81). Comparison of equations (84) and (85) show that the energy is dependent on the volume of the inclusion that the stress is acting upon. The energy release rate (Budiansky and Rice, 1973) is the rate of change of the potential energy in regards to the effective area/diameter. For a capillary pipe, the surface area facing σ_{33} is approximately a circle with radius $d=r_c$ while for σ_{11} this is a rectangle with an area of $2lr_c$ ($l>>rc$). This shows that the release rate is faster in the direction of σ_{11} compared to σ_{33}.

6 Appendix 6

The problem of imbedding a network of pipes and possible crack-like pores into the shale matrix can be approached by an alternative method. This is analogous to the approach taken by Rüger (1996) in rotating the VTI medium and deducing the HTI response. The explicit analytic solution for the crack-like pores in a VTI medium is only available (Withers, 1989) for the case that the equatorial plane of the inclusion is parallel to the VTI symmetry plane. We can follow the modelling of the flat lying cracks/crack-like pores in shale (Sarout and Guéguen, 2008b) and then rotate the model so that the connected pore space resemble a capillary network.

The capillary network is likely a mixture of connected equant and crack-like pores. The results of the field data observations (case studies) and the geological understanding of the capillary network encourages this model (Figure 94). The exact mixture of the equant and crack-like pores is not known a priori and should be deduced experimentally. However, a statistical approach can help reduce the uncertainty (or evaluate it). The connected equant pores are needle-like inclusions are a degenerate case of the cracks (Kachanov et al., 1994). Therefore the introduced shape factor for the change between the crack and needle can be applied as a correction term on top of the rotated model.

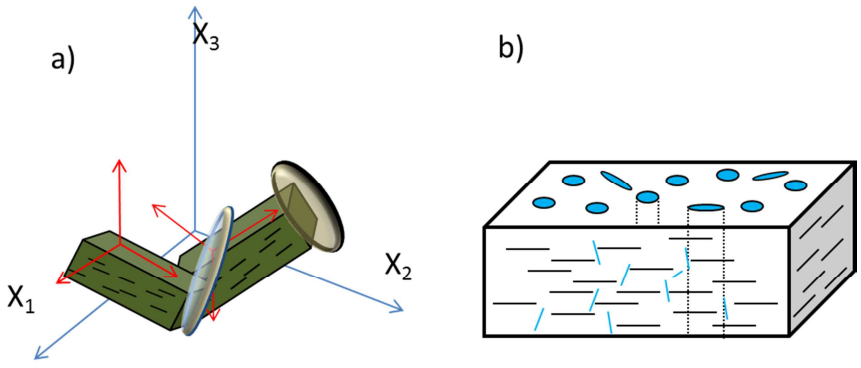

Figure 94. The network of capillaries is likely a combination of crack-like (brown in a) and equant/tube pores (blue in a).

The result of modelling of cavities in a VTI medium by Levin and Markov (2005) indicates that the impact of channel like pores on the anisotropy is noticeably less than cracks. This is a fact that was mentioned in this thesis to avoid the HTI effects of cracks. However, the crack-like pores are not exactly like cracks, they are prolate spheroids (David and Zimmerman, 2011) adjacent to the associated shale domain. Therefore a more realistic model can be imagined in Figure 94b. As Discussed in chapter 3 and shown by Withers (1989), the presence of vertical cracks in the VTI medium has a noticeable impact on the anisotropy of the solid. Figure 95 shows that ε' can be roughly approximated by switching the curves for C_{11} and C_{33}.

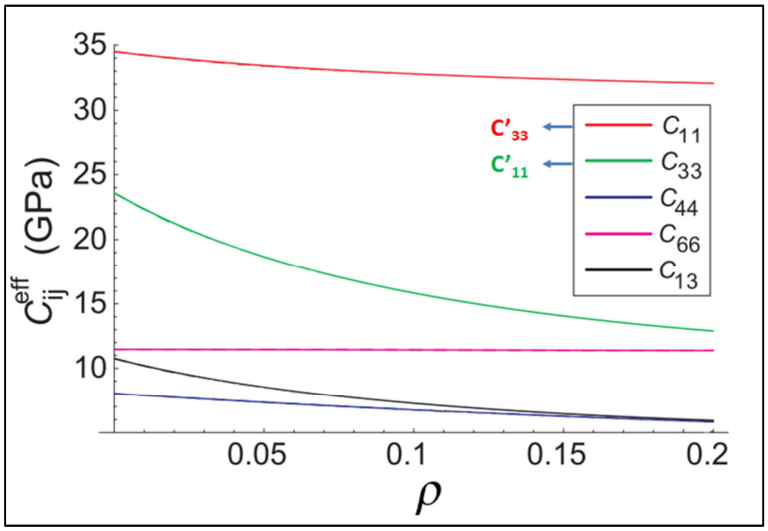

Figure 95. Variation of elastic moduli of a wet shale containing flat lying cracks (Sarout and Guéguen, 2008b). If the cracks are vertical the orientation of C_{11} and C_{33} switch. The previous curves give a first approximation of the behavior of the shale under stress. ρ is the crack density.

The approximation of the approach taken in Figure 95 gets better when we replace a fraction of the crack-like discontinuities with equant/rounded pores. Kachanov et al. (1994) showed the variation of the effective Young modulus depends on the shape (or departure from the circle) of the inclusion Figure 96. This makes sense when as the Eshelby's tensor does not depend on the volume of the inclusion but on its aspect ratio and the elastic moduli of the matrix.

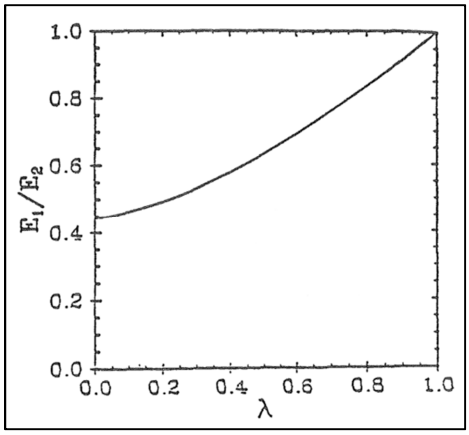

Figure 96. Variation of anisotropy as the holes are inflated from cracks to circles. λ denotes the aspect ratio of the inclusion. Picture is taken from Kachanov et al. (1994).

When the Probabilistic Distribution Function (PDF) of the inclusions is implemented, a statistical distribution of weakened shale domains (due to the excess compliance) within the apparently unaffected matrix domains should yield the desired distribution. Show the schematic of incorporation of the excess compliance in the shale matrix.

The presence of the pore causes extra strain to the representative volume element (RVE) which is the shale domain. Following Sarout and Guéguen (2008b), we can write:

$$\varepsilon^{total} = \varepsilon^{total} + \Delta\varepsilon = (S^0 + \Delta S) : \sigma^0 \tag{86}$$

The excess compliance was shown to be (Sevostianov and Kachanov, 2002):

$$\Delta S = \frac{V^*}{V}\left[(S^* - S^0)^{-1} + C^0 : \left(I - s^{esh}\right)\right]^{-1} \tag{87}$$

Where V^* and V are the volumes of the inclusion and the RVE respectively. S^* is the compliance of the RVE, C^0 and S^0 are the elastic moduli of the matrix. S^{esh} is the Eshelby's tensor.

Equation (87) simply shows that the excess compliance is directly determined by the shape of the inclusion (through Eshelby's tensor), its compliance and the percentage of that inclusion.

7 Appendix 7

The confining pressure has a vivid impact on the anisotropic properties of shales. Shale structure can be modelled as the shale domains with interbedded low-aspect-ratio pores parallel to these platelets. Increase of the confining pressure will first close the crack-like pores parallel to the bedding (Walsh, 1965). Therefore causing a reduction in the observed anisotropy parameter ε (Sarout and Guéguen, 2008a). On the other hand, the pressure applied to a shale sample in the laboratory resembles the geopressure during burial. The burial causes the shale to adopt a compaction fabric (Dewhurst and Siggins, 2006) and will likely increase the alignment of the shale platelets (Bachrach, 2011). However, the study of Pervukhina and Rasolofosaon (2017) shows there is not a first-order relation between the burial/compaction and anisotropy of shales.

Apparent depth of burial (as opposed to absolute depth that is estimated through basin modelling) may be measured through the depth below the mudline of the samples. The depth of burial was plotted against the measured capillary pressure threshold in both case study areas (southern Gippsland and the Exmouth) (Figure 97). Results show little correlation between the two parameters in either of the two cases. However, the Gippsland data show a slightly better correlation between the depth below mudline and the P_c. This observation was made on a larger dataset through the basin by Hoffman et al. (2012). Compaction causes reduction in the porosity of shales and their associated hydraulic permeability (Beloborodov et al., 2017). This reduction is shown to have an exponential form. The compaction is responsible for the change of shape in the pore spaces as shown by Bachrach (2011):

$$W_{200}(\phi) = W_{200}^{max}(1 - \frac{\phi}{\phi_0})^{n_{200}}$$
$$W_{400}(\phi) = W_{400}^{max}(1 - \frac{\phi}{\phi_0})^{m_{400}} \quad (88)$$

Where φ_0 is the critical porosity and m and n are more parameters depending on the orientation distribution function of a sample.

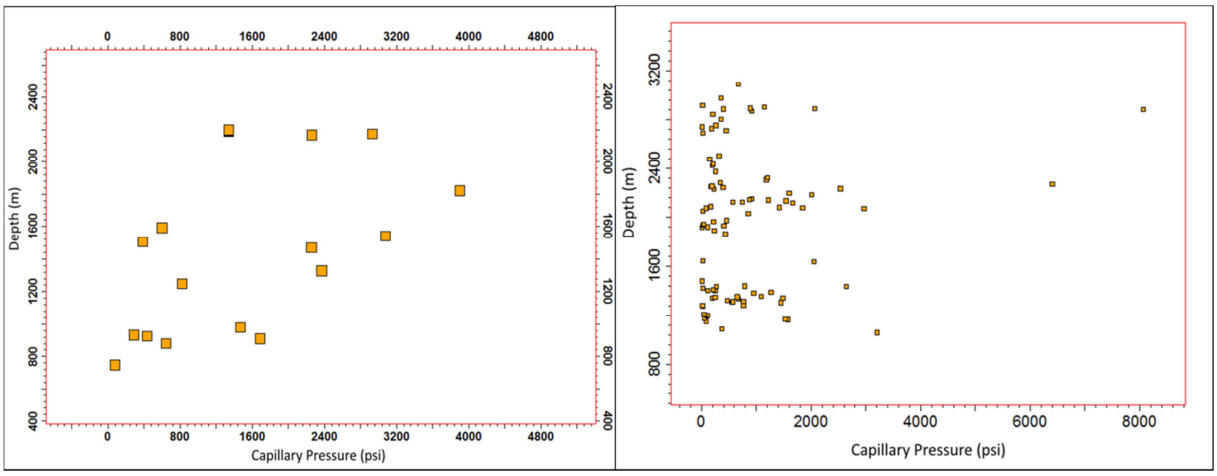

Figure 97. Plot of the sealing capacity measured through capillary pressure threshold versus depth below mudline in the Gippsland Basin (left) and the Exmouth (right) study areas. A weak correlation may be perceived for the increase of P_c with increasing depth of burial in the Gippsland while there is no such trend in the Exmouth data.

The anisotropy parameter ε seems to have a weak correlation with the depth of burial in the case study of the Gippsland basin. Therefore, it is likely that the compaction in the Gippsland basin is partly contributing to the anisotropy of the samples and is then seen to have a weak correlation with the sealing potential. While in fact, the seismic anisotropy of the samples is a better proxy to infer their sealing capacity as it better relates both to the packing of the grains structure and the orientation of inclusions. Lack of any trend between depth and the sealing capacity is likely due to the well-compacted state of the shale. Equation (88) shows the potential contribution of pore alignment to the anisotropy through the W_{200} and W_{400} moments. However, it generally discusses the total porosity (not effective) which includes the targeted porosity of this research. An approach to potentially separate the two might be through analyzing the weakening of the domains by presence of inclusions as presented in this study and observed in the field data. However, seismic response is also sensitive to the differential pressure and overpressured shales show increased attenuation (Ciz et al., 2005).

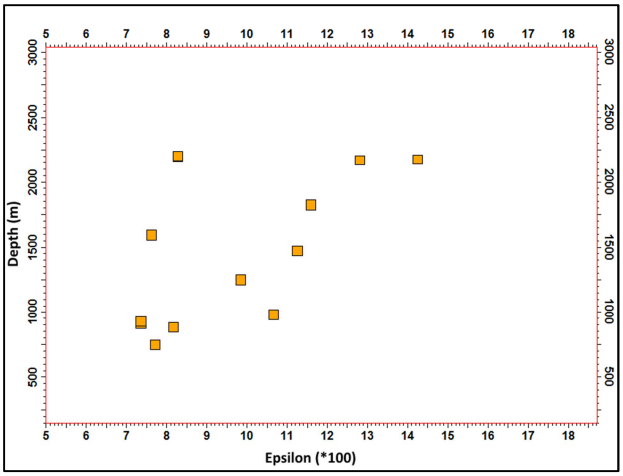

Figure 98. The plot of depth below mudline versus Ɛ shows a weak ascending trend. It is likely, shale grain alignment and pore space changes (as a result of compaction) are contributing to the trend.

8 Appendix 8

Seismic waves bounce (reflect) or change not at geological boundaries but at geophysical ones. Such geophysical boundaries form where a combination of density (ρ) and velocity of rock units change. The boundary condition that determines whether a new geophysical layer exists is called the Acoustic Impedance and is defined by

$$AI = \rho V \tag{89}$$

The change in Acoustic Impedance makes the down (or up)-going seismic wave to sense a difference and imprint a new reflector on the geophone record. The change in the acoustic impedance is called the Reflection Coefficient and is denoted by

$$RC = \frac{\rho_2 v_2 - \rho_1 v_1}{\rho_2 v_2 + \rho_1 v_1} \tag{90}$$

A zero offset stacked seismic section is a record of changes in the reflection coefficients of the subsurface layers. The goal of seismic inversion is to extract intrinsic earth properties (i.e. velocity and density) from a stacked seismic section or CDP seismic gathers. The seismic record on its own does not provide enough information to help us estimate the rock properties. Several steps are required in collecting and processing the accessory information that are required to complete the seismic inversion. Most of these steps are dependent on the inputs from the well such as well tops, logs and velocity measurements.

The convolutional model of the seismic trace states

$$T(i) = \sum_i R_i * W + n \tag{91}$$

Where T(i) stands for seismic trace, R(i) is the reflectivity of layer (i), W is the seismic source wavelet and “n” denotes the noise.

Estimation of the seismic source is not an easy task. It is certainly more difficult for onshore seismic data where dynamite and vibrators are the two most common sources. For marine seismic data, the far field signature of the gun array has been measured in modern seismic acquisitions. The far field signature of the air guns is equivalent to the source wavelet. If the seismic source wavelet is known, it can be directly used it in the convolutional model (equation (91)).

The reflectivity series shows where the seismic wave has encountered a geophysical boundary. The most accurate match to the earth's reflectivity series is constructed from well data. Density and sonic logs (compressional and/or shear) will be the ingredients of a multiple-free 1D reflection series that is the calibration point for the equivalent seismic one. This borehole-based approximation of earth reflectivity is called the "synthetic seismogram".

Examples of the seismic inversion in the southern Gippsland case study can be viewed in Figure 99 and Figure 100. Individual lines show interesting stratigraphic features and assist to identify the shaley sequences.

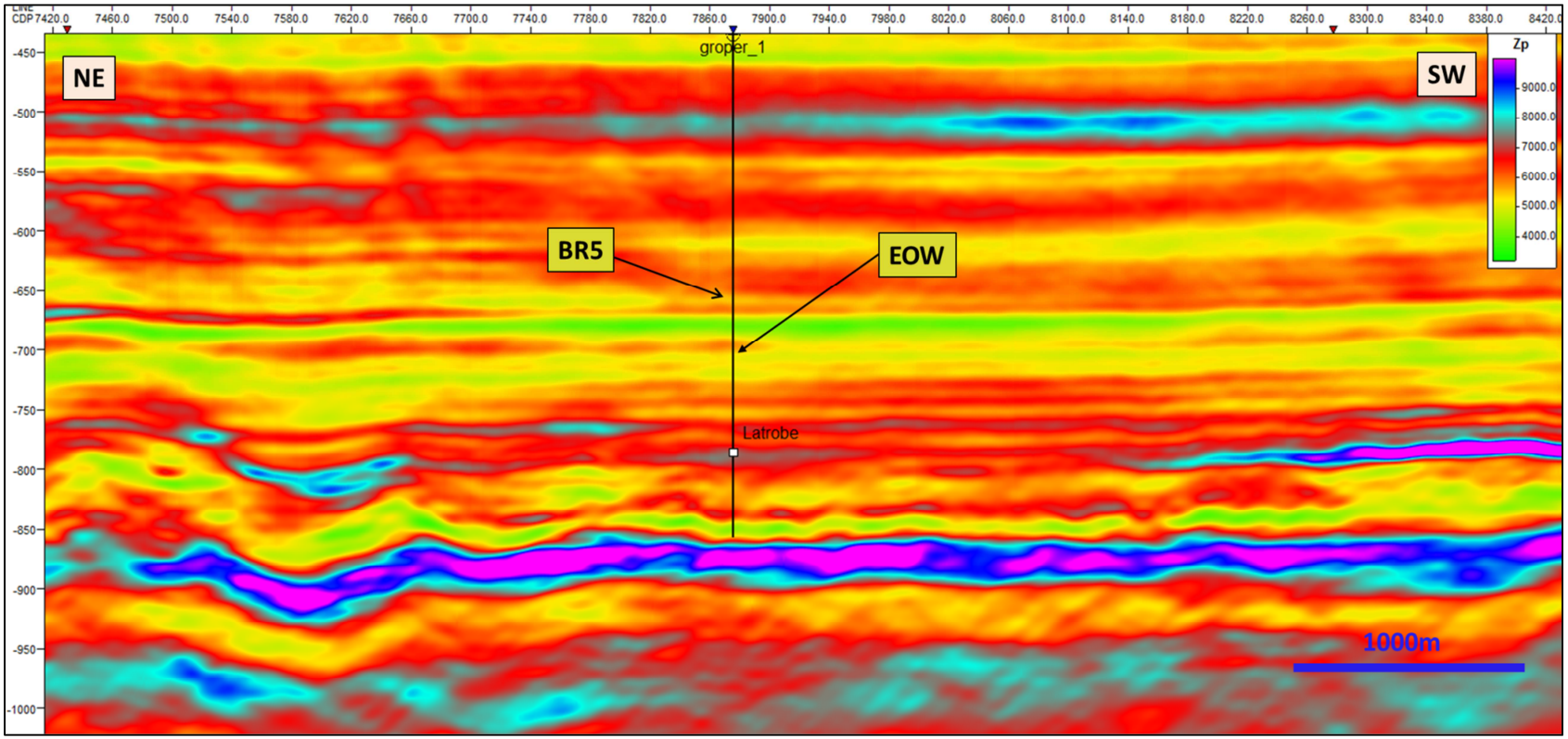

Figure 99. Inverted seismic line (S14) to Compressional Acoustic Impedance shows the clinoforms (prependicular to the section) of the EOW package as well as high Zp lenses within the seal and reservoir. The purple band in the lower half of the image represents the crystaline basement.

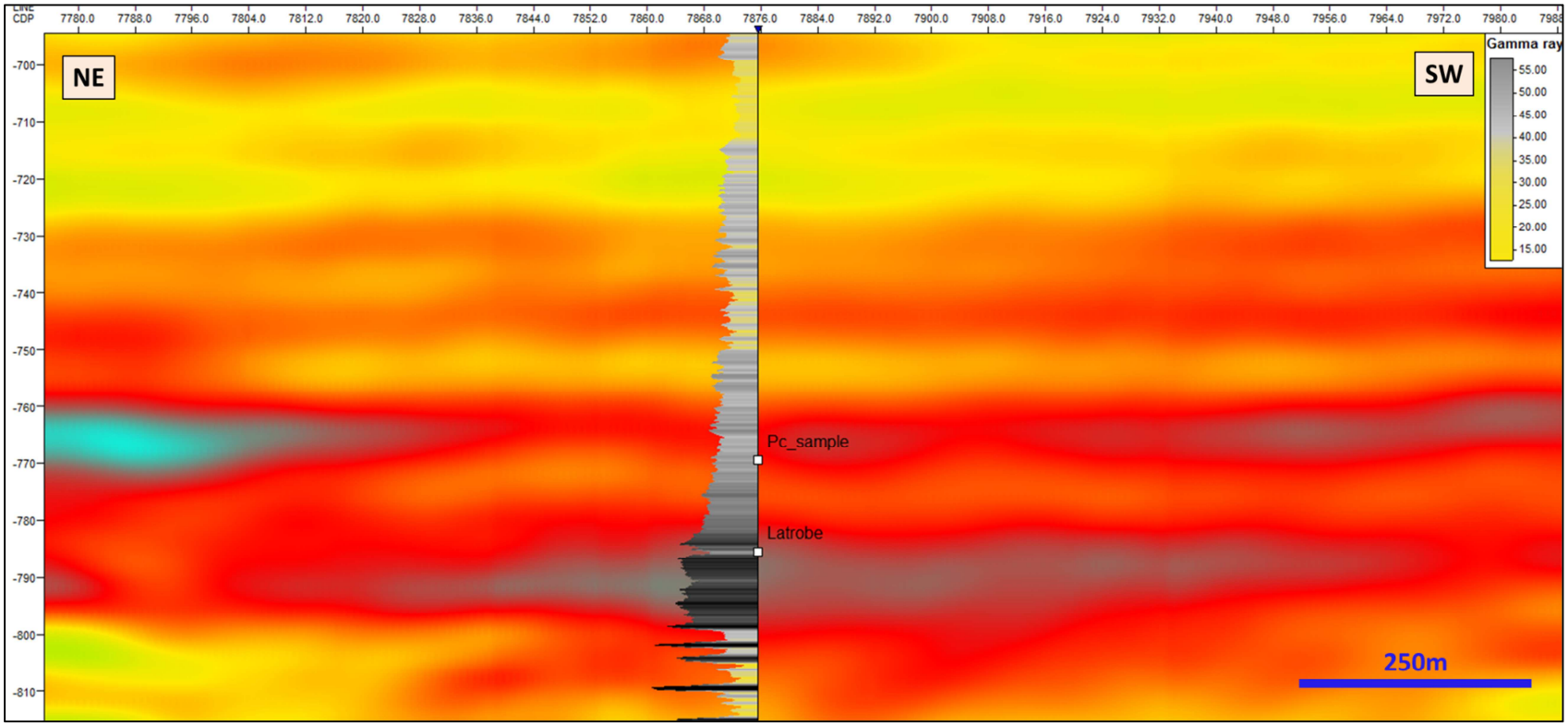

Figure 100. Blown up section of Figure 99 around Groper-1. The sequential character of gamma ray can be followed on the inverted seismic (Z_p). The location of the sample corresponds to a local decrease in the acoustic impedance and shows little correlation to the gamma ray reading. Compare with Figure 59.

9 Appendix 9

Shear wave velocities (V_s) can help reveal valuable geomechanical information about the rocks and their fluid contents. Even in the case of isotropy, shear velocity data can help distinguish between fluids (gas and non-gas) and fluid bearing rocks since shear waves can only propagate through solids. Measurements or estimation of shear velocities are necessary to evaluate the anisotropy parameter γ which in turn can be translated to in situ stress and micro cracks.

There are several ways used that the shear velocities can be calculated over the area of study:

- Wireline Logs
- Surface Seismic
- Global V_p/V_s relationship

9.1 Wireline logs

Wireline sondes can measure both compressional or shear wave velocities. Such sondes contain multiple sources, polarized in different directions and several sets of three-component receivers (cross-dipole tool). This allows for measuring compressional and both (split shear) modes. Shear wave anisotropy is computed by utilizing Alford's rotation (Alford, 1986). Compressional sonic are more common especially among older bore holes.

In the Area of study, only the most recently drill well, Wasabi-1, has shear velocity measurements (single directional Shear log). The rest of the wells have compressional DT or no sonic log at all. Although the shear velocity of sediments can vary, there is usually a relationship between the compressional and shear sonic properties. By modelling the compressional sonic in the AOI (area of study) and calibrate the DT-shear is at least one point, we can estimate the shear velocities of the entire area.

Figure 101 shows the relationship between $DT_{compressional}$ and DT_{shear} for the entire length of the well Wasabi-1. Although the derived equation from this plot can convert the two values together, it is worth noticing that when we limit our interval of analysis to a particular formation (with more uniform lithology) the trend becomes a linear trend.

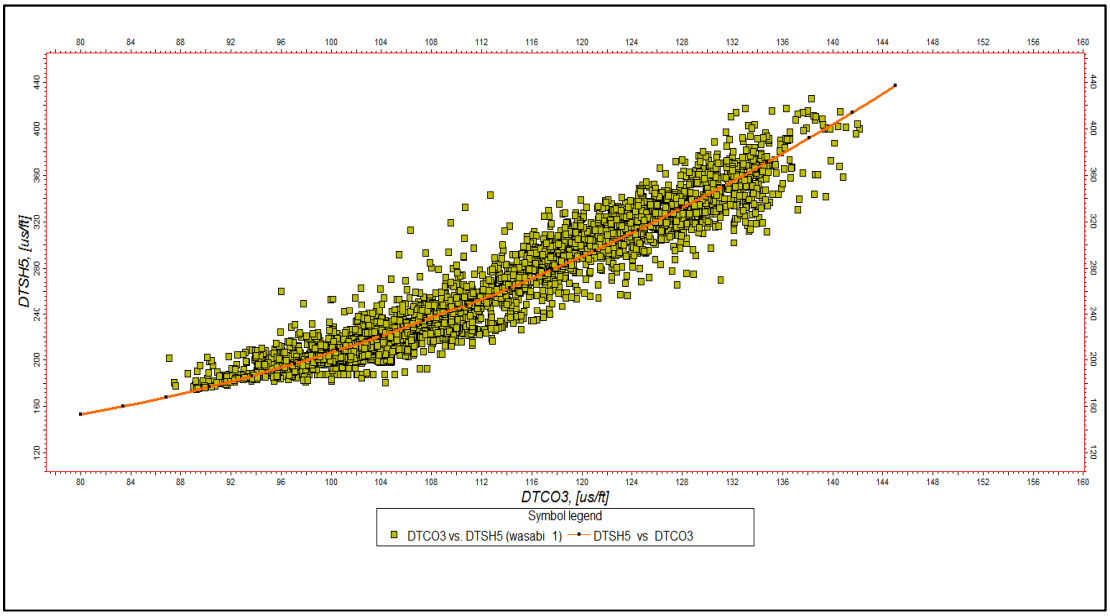

Figure 101. Plot of Compressional versus shear sonic for the entire Wasabi-1.

In this particular case, the values that correspond to the Lakes Entrance formation are plotted in Figure 102 show a linear trend.

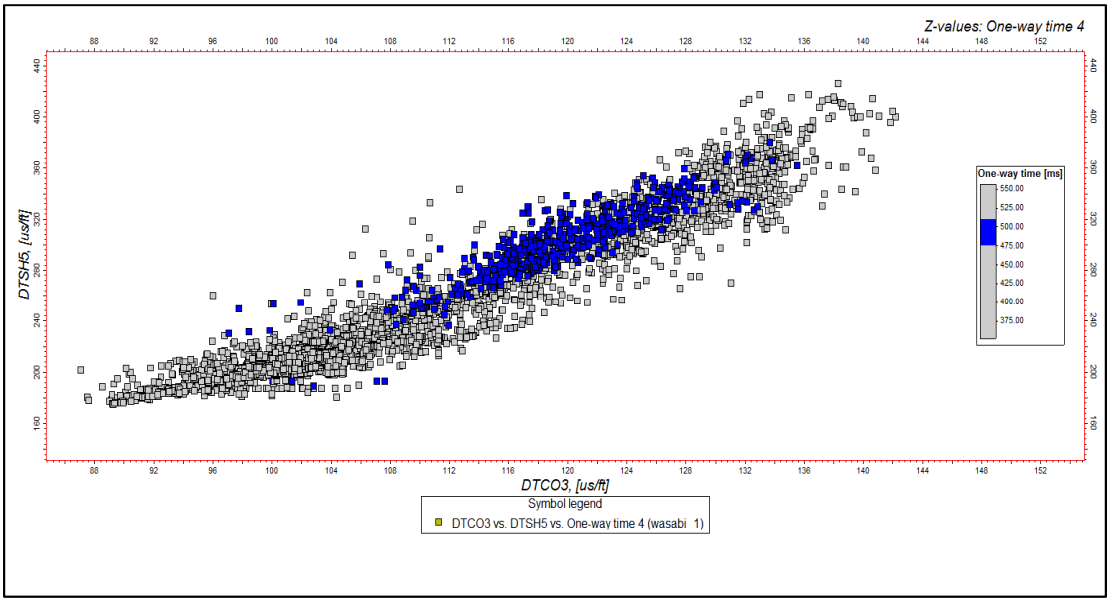

Figure 102. The log measurements corresponding to the Lakes Entrance formation are coloured in blue.

It is interesting that the values on Figure 102 that are colored in blue match very well with the those lithologies that have a high gamma ray value (Figure 103). Gamma ray values higher than 80 API units are considered as indication of shales and are colored in yellow to orange. Comparison with Figure 102 confirms that the sales belong to the Lakes Entrance formation.

The highest gamma ray values on Figure 103 (red color) correspond to the volcanics of the Latrobe group and should not be considered as part of the trend line of V_p/V_s in shales.

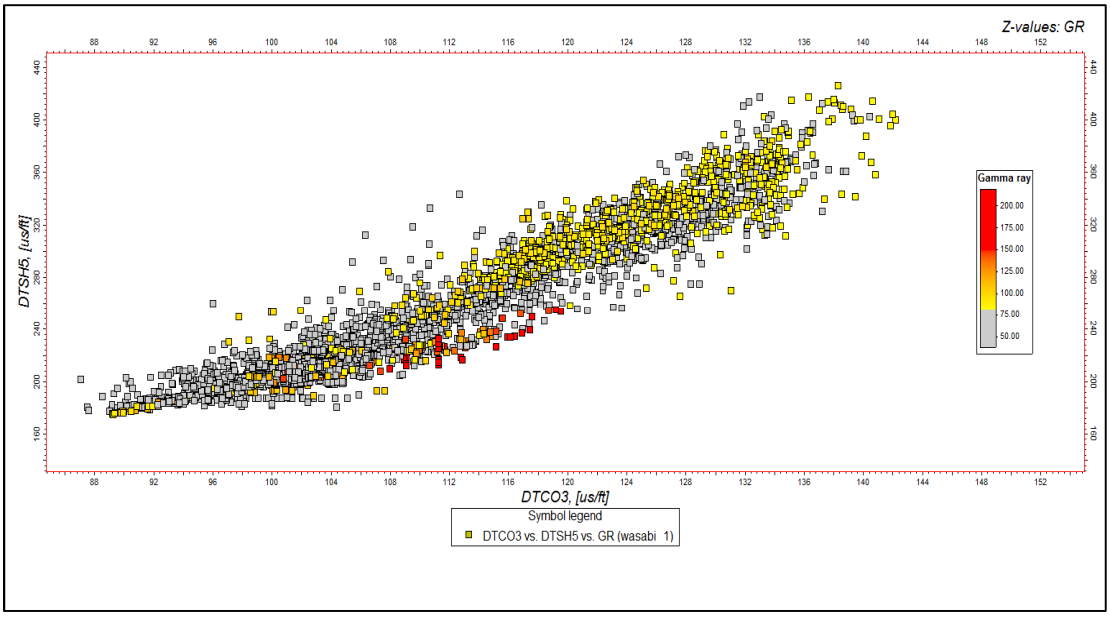

Figure 103. Sonic log measurements are coloured according to their gamma ray values. Gamma range of greater than 80 is assumed as probable shale lithology.

9.2 Surface Seismic

Surface seismic signal was not strong enough for the PSSP processing and this method was abandoned. Reliable results are based on OBC (ocean bottom cable) acquisition method where the second (upward) P-S conversion is omitted. Therefore the signal to noise ratio is much higher.

9.3 Global V_p/V_s relationship

Castagna et al. (1985) showed that the relationship between the compressional and shear waves in sediments stays close to a linear trend. The trends are different for sandstones, Limestones and shales. This trend for mudrocks with a good approximation is

$$V_p = 1.16V_s + 1.36 \qquad (92)$$

Where V_p and V_s stand for compressional and shear velocities respectively and are measured in km/s.

The sealing sequence in the AOI is the shales of the Lakes Entrance formation. Therefore the usage of equation (92) with reference to the local well calibration can be a reasonable approximation of the V_s values.

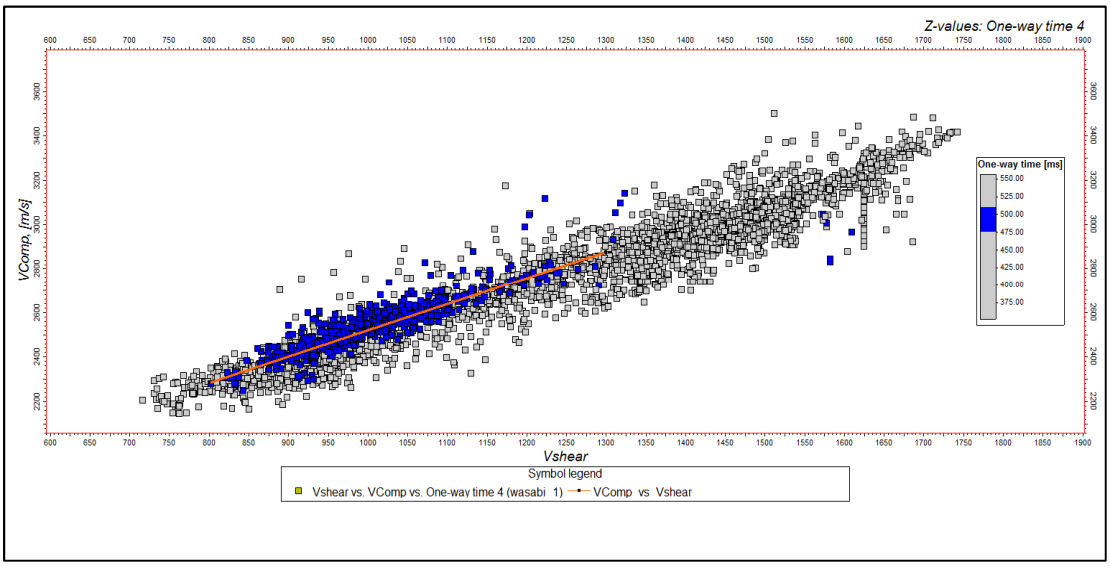

Figure 104. Calculated compressional and shear velocities from sonic logs at Wasabi-1.

In order to calibrate the global V_p/V_s relationship to the study area, the shear and compressional velocities from the sonic logs at the Wasabi-1 are calculated. The cross plot of $V_{compressional}$ versus V_{shear} is shown in Figure 104 where the values which belong to the Lakes Entrance formation are colored in blue. A regression line for the blue points of Figure 104 is

$$V_p = 1.18V_s + 1.33 \quad (93)$$

When measured in KM/seconds.

Equation (93) closely matches the global function that is suggested by Castagna et al. (1985) in equation (92).

10 Appendix 10

The HE96-2D comprises a set of dip and strike lines in the relatively deep water area of Exmouth Sub-basin. The target lines to process were those that ran in the azimuth of 120 degrees (the dip lines). Although the lines were shot in the Nineties, they are of reasonable quality and benefit from a longer offset compared to the 3D surveys in the area of study. The goal in the seismic processing was not to get the best structural stack, but to have an accurate estimate of the near and far velocity fields. However, some pre-processing stages have to be applied to the data in order to make it ready for further analysis. The following stages are adopted so that η and the near field velocity are computed.

The majority of offshore Gippsland basin is categorized as shallow water with bathymetry ranging from 20^{m} to less than 100^{m} deep. This is a different scenario from that of the Exmouth Sub-basin which was deep water. Shallow water seismic is distinguished from its deep-water counterpart by presence of direct arrivals and shallow water multiples. The dip direction of the majority of the faults that were active at the Latrobe time (Late Miocene) is approximately zero. This direction is different from the current direction of maximum stress. Geomechanical and well test studies have concluded that the current orientation of stress in the Gippsland Basin is about 135 degrees. The GDPI10 seismic survey benefits from the modern acquisition equipment, has large enough offset, and the strike lines are oriented at 135 degrees.

Table 7 summarises the major processing steps that were applied on the seismic data for each case study. Figure 105 shows a CDP gather before and after the processing steps were applied.

Processing Step	Gippsland	Exmouth
Amplitude recov.	Applied exp. Grain.- 6dB ampl. recovery	Applied exp. Grain.- 6dB ampl. recovery
Noise Filter	Linear noise (Tau-p) remov., noise burst suppres., shot and receiver Swell noise reduc, Freq. Filter.	High frequency suppr. , Swell noise remov., Tau-P linear noise remov.
Demultiple	SRME, Tau-P and Radon Forward Modelling	SRME, Radon filter
Velocity Analysis	Three passes, 2500m, 1000m and ~750m	Two passes, every 100 and 50 CDP's
ETA analysis	Two passes for each velocity round- Automatic and manual	Two passes for each velocity round- Automatic and manual
Migration	PSTM	PSTM

Table 7. Summary of the seismic processing steps for each case study

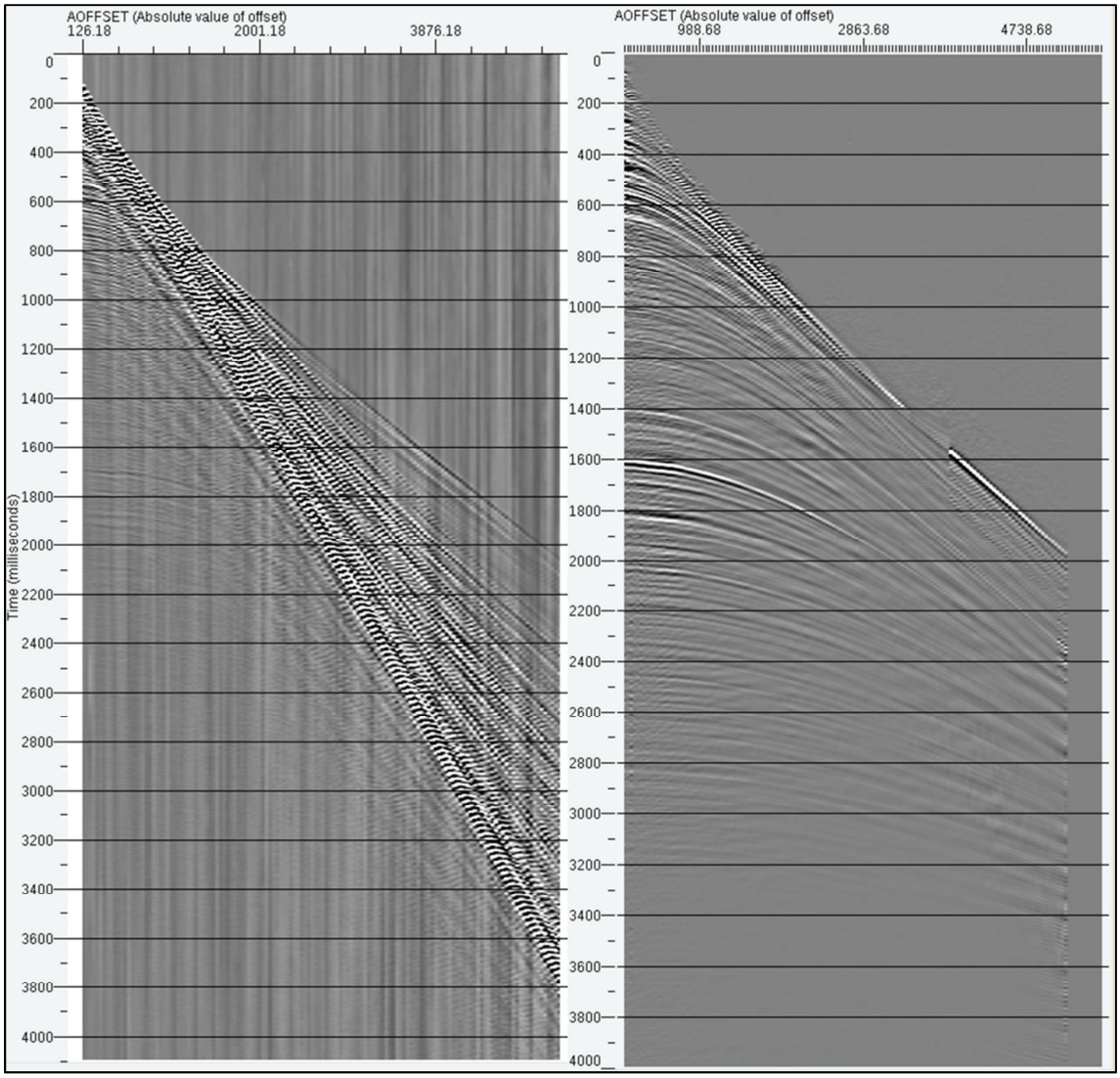

Figure 105. Comparison between Pre-processed CDP (left) and Post-processed CDP. Noise and multiples are suppressed. The image depicts a CDP from line GDPI-10-S5.

11 Appendix 11

Tables Table 8 and Table 9 show the variations of the gas column height values each sample can hold before it leaks. The density of brackish water was assumed to be 1.006 g/cc. Surface tension for gas is taken to be 50 dynes/m. Not all the samples come from the target shale units. Such measurements were ignored in the modelling.

Well Name	Number of Samples	Depth Range(m)	Gas Density (g/cc)	Min Height (m) -Gas	Max Height (m) - Gas
Skiddaw-1&2	9	2030-2184.5	0.1602	3	336
Stybarrow-2	9	1864-2308.5	0.1602	25	725
Ravensworth-1	10	1062-1412	0.0908	2	334
Scafell-1	14	1279-1440	0.114	7	519
Eskdale-1	13	1437-3093	0.1602	1	295
Crosby-1	6	1090.4-1210.9	0.0908	5	38
Stybarrow-1	28	1918-2437.6	0.1602	1	287
Eskdale-2	8	2714-2905	0.2974	25	1104

Table 8. Variation of Hydrocarbon (Gas) column height for the wells in the Exmouth sub-basin area.

Similar calculations are made for the samples of the Gippsland basin case study to reveal the range of the potential to retain hydrocarbon.

Well Name	Number of Samples	Depth Range(m)	Gas Density (g/cc)	Min Height (m) -Gas	Max Height (m) - Gas
Groper-1	3	909.15-932	0.1602	33	191

Groper-2	1	747.8	0.1602	-	8
Wasabi-1	4	1250-1540	0.1602	44	348
Melville	1	2190-2200	0.1602	-	152
Omeo-2a	1	2169	0.1602	-	256
Pike-1	1	1822.7	0.1602	-	441
Tummy-Ruff-1	1	880	0.1602	-	73
Mudskipper-1	1	1470	0.1602	-	255
Kyarra-1a	1	980	0.1602	-	166
Devilfish	1	1593	0.1602	-	68

Table 9. Variations of the sealing potential of the Lakes Entrance Formation in the area of study shown by calculation of hydrocarbon (gas) column height.